Imperial College of Science, Technology and Medicine
Department of Mechanical Engineering

Reduced Order Modelling of Large Finite Element Structures with Geometric and Contact Nonlinearities: Application to Blade-Casing Interaction in Aircraft Engines

Alessandra Vizzaccaro

February 2021

Submitted in part fulfilment of the requirements for the degree of PhD.

Conflict of interest

The author declares that they have no conflict of interest.

Originality statement

I certify that the intellectual content of this thesis is the product of my own work and that all the assistance received in preparing this thesis and sources have been acknowledged.

Copyright declaration

The copyright of this thesis rests with the author. Unless otherwise indicated, its contents are licensed under a Creative Commons Attribution-Non Commercial 4.0 International Licence (CC BY-NC).

Under this licence, you may copy and redistribute the material in any medium or format. You may also create and distribute modified versions of the work. This is on the condition that: you credit the author and do not use it, or any derivative works, for a commercial purpose.

When reusing or sharing this work, ensure you make the licence terms clear to others by naming the licence and linking to the licence text. Where a work has been adapted, you should indicate that the work has been changed and describe those changes.

Please seek permission from the copyright holder for uses of this work that are not included in this licence or permitted under UK Copyright Law

Abstract

The numerical simulation of structural vibration of aircraft engines components is of crucial importance for engine manufacturers both in the design stage and in the assessment of failures. Protracted vibration of rotor blades shortens their lives and might cause blade failure due to high cycle fatigue. To ensure the structural integrity of blades, accurate predictions of their dynamic behaviour are necessary. In this respect, numerical models based on linear approximations are no longer representative of the actual behaviour of the blade that is affected by several nonlinear forces. Finite element models of blades are usually large models with a high number of degrees of freedom and complex geometry. To compute the nonlinear dynamic behaviour of blade in a fast yet accurate manner, reduced order models are necessary. The main focus of this thesis is the assessment and investigation of reduced order modelling methods for geometrically nonlinear structures. It will be shown that reduced order modelling methods based on modal coordinates displays a slow convergence of the basis when applied to structures discretised with three dimensional finite elements. Direct methods based on modal derivatives have instead the advantage of being computed directly in physical basis and the computation of the reduced dynamics can be done non-intrusively from any generic finite element software. However, the applicability of these methods is restricted to the case of a clear separation between the mode of interest and the modes coupled with it through the nonlinear forces. Invariant manifold based methods are instead able to reproduce the correct dynamics even without a slow/fast separation between modes, thanks to the inclusion of velocity dependent terms in the nonlinear mapping. However, invariant manifold methods are based on modal coordinates thus making their applicability limited to relatively small structures. In this work, a direct method fully in physical coordinates able to compute the invariant manifold through normal form is proposed and its capabilities assessed.

Acknowledgements

Throughout the writing of this dissertation and during the years of my PhD, I have been supported and guided by several people that I want to thank.

First of all, my supervisor Loïc Salles. During this time, he has guided me through an incredible journey, keeping me motivated and curious, and offering me a constant support and help.

I am also thankful to Rolls Royce for the financial support and especially grateful for the great deal of technical support I received from my industrial relators, Caetano Peng and Chian Wong.

I want to express my extreme gratitude to Professor Cyril Touzé, who hosted me during my internship in ENSTA ParisTech. The time I spent in Paris has been so fruitful that a large portion of this thesis is the result of this collaboration.

Another collaboration that has produced crucial insights for this thesis has been the one with Professor Olivier Thomas, to whom I want to express all my gratitude.

Lastly, I want to thank all my colleagues, now friends, from Imperial College, with whom I shared this amazing experience.

This thesis is dedicated to my parents and my partner Andrea, as my gratitude for them, I failed to put into words.

Dedication

To my parents, for their unconditional love.

To my partner, for his unconditional patience.

”Well, in our country,” said Alice, still panting a little, ”you’d generally get to somewhere else - if you run very fast for a long time, as we’ve been doing.”

”A slow sort of country!” said the Queen. ”Now, here, you see, it takes all the running you can do, to keep in the same place. If you want to get somewhere else, you must run at least twice as fast as that!”

Lewis Carroll

Contents

Conflict of interest **i**

Abstract **iii**

Acknowledgements **iv**

1 Introduction **1**

1.1 Motivations 1

1.2 Framework 4

1.3 Nonlinear modal analysis 5

1.3.1 Positioning 7

1.3.2 Research questions 9

1.4 Outline 10

2 Methodology **12**

2.1 General procedure 12

2.2 Finite Element Model 14

2.2.1 Finite Element Discretisation 15

2.2.2 Geometric Nonlinear Forces 17

2.2.3 Contact Forces 18
2.2.4 Generic form of nonlinear FE discretised system 21
2.2.5 Modal coordinates 22
2.2.6 Stiffness Evaluation Procedure 25
2.3 Model Order Reduction 28
2.3.1 Reduction on Linear Modes 30
2.3.2 Hurty/Craig-Bampton method 31
2.3.3 Modal derivatives 32
2.3.4 Quadratic Manifold 34
2.3.5 Shaw and Pierre formulation of Invariant Manifold 35
2.3.6 Normal form approach for Invariant Manifold 38
2.4 Time discretisation 40
2.4.1 Central difference scheme 40
2.4.2 Harmonic Balance Method 42
2.5 Continuation 44
2.5.1 Predictor-Corrector continuation 45
2.5.2 Asymptotic numerical method 46
2.5.3 Application to forced responses and nonlinear modes 48
2.5.4 Application to nonlinear modes of systems with non conservative forces 51
2.6 Code architecture 52

3 Slow convergence of linear ROM **54**

3.1 Motivating Example: a clamped-clamped beam 56

3.2 The case of a flat thin structure 59

3.3 Static Condensation 61

3.4 Normal Form 62

3.4.1 Convergence with 3D elements 63

3.5 Static modal derivatives 68

3.6 A modified StEP for 3D elements 73

3.7 Numerical examples 77

3.7.1 Application to a clamped-clamped beam 78

3.7.2 Application to a clamped circular plate 78

3.8 Conclusion 81

4 The role of the slow/fast separation assumption **82**

4.1 Normal Form 85

4.2 Modal derivatives 89

4.3 Quadratic Manifold 90

4.4 Theoretical Comparison 92

4.5 Comparison on two degrees of freedom systems 100

4.5.1 A two-dof model representing a flat symmetric structure 101

4.5.2 A two-dof model representative of a shell structure 105

4.6 Shallow and Non-Shallow Arches 109

4.6.1 Amplitude-frequency relationships 112

4.6.2 Nonlinear modeshapes 113

4.7 Conclusion 116

5 Direct Normal Form for Large Scale FE Models 118

5.1 Normal Form 120

5.1.1 Single mode motion coefficients 122

5.2 Direct Normal Form 123

5.2.1 Second-order direct normal form 124

5.2.2 Third Order direct normal form 131

5.3 Internal Resonances 138

5.4 Damping and forcing 138

5.5 Practical implementation and algorithm 142

5.6 Numerical Results 144

5.6.1 A clamped-clamped beam with internal resonance 144

5.6.2 FE model of a fan blade 151

5.6.3 Frequency-response curve with damping and forcing 155

5.7 Conclusions 159

6 Structures with clearance nonlinearity 161

6.1 Problem statement 164

6.2 Comparison of time discretisation methods 169

6.2.1 Solution with harmonic balance method 169

6.2.2 Presentation of time finite element method 170
6.2.3 Comparison on a single oscillator testcase 173
6.3 Reduced order modelling for clearance nonlinearity 177
6.3.1 Contact derivatives 179
6.3.2 Presentation of the testcase 181
6.3.3 Comparison with Hurty/Craig-Bampton method 184
6.4 Damped nonlinear modes for self-excited vibration 185
6.4.1 2DOFs Model 186
6.4.2 Negative clearance system 188
6.4.3 Open clearance system 189
6.5 Conclusions 193

7 Conclusion **195**

7.1 Scientific Contributions 195
7.2 Industrial contribution 199
7.3 Code development and integration 201
7.4 Open questions and future developments 201

Bibliography **202**

A Details of the derivation of von Kármán beam model **218**

B Reduced-order models for two modes motion **222**

C Detailed description of the *fortran fun* library **225**

List of Tables

2.1 Code used for different stages of the workflow. 52

3.1 Order of appearance in the basis (#), eigenfrequencies, correction factors and shapes of the most relevant modes coupled with the first bending mode in y-direction for the clamped-clamped beam. The colors scale the modulus of the displacement field and arrows display the axial displacement for axial mode 34. 66

3.2 Corrected cubic coefficients with the three condensation methods and comparison with analytical values. Due to the symmetry of the mode shapes, the nonlinear coefficients which couple the first and the third modes have all nonzero values, and are therefore chosen for these computations. 78

3.3 Mode shapes of the 9 most relevant modes coupled with the first flexural asymmetric (1,0) mode. Only two of them are in-plane modes: (e) and (h), while all the others are thickness modes. (a2) is a side view of the top view (a1) of the first thickness mode, in order to show the strong dependence on thickness deformation. 80

3.4 Corrected cubic coefficient Γ^p_{ijk}, for two flexural modes, *i.e.* $i, j, k, p \in [2, 4]$, where 2 refers to the first (1,0) asymmetric mode while 4 refers to the second (2,0) asymmetric mode; anf for three different methods : the modified StEP, the static condensation where all the coupled modes are statically condensed, and the Modal derivative where the added modal derivative is then statically condensed to the master mode. 80

4.1 Table of coefficients of the reduced system given by the three methods 93

4.2 Table of coefficients of the reduced system given by the three methods 93

5.1 Linear modes frequencies and frequency ratios with mode 1 and 2. 145

5.2 First five eigenfrequencies of the fan blade and frequency ratios with the first mode. 151

6.1 Error on the maximum value of contact force for different values of β_ϵ. . . . 174

6.2 Error of HBM on the asymptotic nonlinear frequency for different value of β_ϵ. 174

7.1 Cases and methods capabilities. 197

List of Figures

1.1 Sketch of a Campbell diagram to predict resonant crossings (red) between the natural frequencies (yellow) and an engine order (black) around the operational range (green). 2

1.2 Results of experimental test described in [10] 3

1.3 Schematic example of nonlinear behaviour of a cantilever beam in large amplitude vibration. 5

1.4 Positioning of the present work in terms of accuracy and computational cost. 7

1.5 Comparison of the two main approaches with different level of accuracy to blade-casing interaction problems. 9

2.1 Workflow diagram of a numerical study of a nonlinear large-scale model . . 14

2.2 Definition of gap function for a point in the potential contact zone. 19

2.3 Normal contact conditions in case of hard or soft contact surface. 20

2.4 Tangential contact conditions in case of hard or soft friction conditions. . . . 21

2.5 Visual representation of the presented path following methods. 45

2.6 Periodic orbits lying on the invariant manifold. Amplitude of a tangent mode p against amplitude and velocity of the mode under investigation $(q, \dot{q})$. . . . 50

2.7 Schematic of the fortran fun library. 53

3.1 Clamped-clamped beam mesh 64

3.2 Nondimensional correction factor $\mathcal{C}^{1s}_{111}/\beta^1_{111}$ (Eq. (3.14)), associated to the first bending mode ($p = 1$) and to all the other modes ($s = 2, \dots N$) of the thick beam testcase, over the nondimensional mode number s/N. The Poisson ratio is $\nu = 0.3$. 64

3.3 Nondimensional correction factor $\mathcal{C}^{1s}_{111}/h^1_{111}$ (Eq. (3.14)), associated to the first bending mode ($p = 1$) and to all the other modes ($s = 2, \dots N$) of the thick beam testcase, over the sorted nondimensional mode number s/N, where the imposed order is by decreasing correction factor. 65

3.4 Convergence to the full model solution with the increase of coupled modes taken into account in the reduced model. (a) Frequency response curve of the beam at center, in the vicinity of the first bending mode eigenfrequency; case of the thick beam with 1287 dofs. Red: full model, and convergence curves with increasing number of modes retained in the truncation: 1 mode (yellow), 4 modes (green), 9 modes (blue), all modes statically condensed (dashed light blue). Solution with normal form in black. (b) Convergence of the evaluated corrected cubic stiffness coefficient Γ^1_{111}, defined in Eq. (3.13), with increasing number of linear modes kept in the truncation. 67

3.5 Application of normal form and static condensation to the case of a cantilever beam. 69

3.6 (a) Static modal derivative $\boldsymbol{\theta}_{11}$ associated to the first bending mode. (b) Four first non-bending modes contained in the SMD $\boldsymbol{\theta}_{11}$, found equivalently by projecting $\boldsymbol{\theta}_{11}$ on the linear mode basis, or by application of Eq. (3.21). The relative modal participation factors q_s of each of these modes numbered 34, 167, 328 and 330 (see also Table 1) is also numerically given, normalized by the total amplitude of the SMD $\boldsymbol{\theta}_{11}$ ($q_{SMD} = 1$), and exactly recovers the factors exhibited in Eq. (3.21). 71

3.7 Examples of prescribed displacement field of the M-StEP, in the transverse direction and in the middle surface / line of a plate / beam 74

3.8 First-mode displacements prescribed on the middle line of the clamped beam and the middle surface of the circular plate. For visualisation purpose, the mesh of the plate is less fine than the one use for the computations of the ROM coefficients. 78

3.9 (a) Normalised modal correction factor for the clamped circular plate, as a function of the normalised mode number (normalization by the number of dofs), for the first asymmetric (1,0) mode of the plate. (b) The correction factors are now sorted by decreasing values, and two cases are shown : the case of the first asymmetic mode, corresponding to sorting (a), and the case of the first axisymmetric mode, showing a faster convergence. Grey points are negligible modes in terms of coupling, magenta points are the important in-plane coupled modes while blue points are the important thickness modes. 79

4.1 Visualisation of the change of coordinates obtained with normal form method. Plot (a): the linear invariance is broken by the nonlinear couplings between modes. Plot (b): the change of coordinates embeds all the invariance-breaking terms so that the system in normal coordinates regain the invariance property. 85

4.2 Evolution of the ratios $\frac{\mathcal{C}_{\text{MD}}}{\mathcal{C}_{\text{SC}}}$, $\frac{\mathcal{C}_{\text{SMD}}}{\mathcal{C}_{\text{SC}}}$ and $\frac{\mathcal{C}_{\text{NF}}}{\mathcal{C}_{\text{SC}}}$, defined in Eqs. (4.27), as a function of the parameter $\rho = \omega_s/\omega_p$, from which the behaviour of the type of nonlinearity defined by the Γ coefficients in Eqs. (4.25), can be directly deduced. Dashed grey line is the (constant) value predicted by static condensation (all curves are normalized with respect to this value). Yellow curve: $\frac{\mathcal{C}_{\text{SMD}}}{\mathcal{C}_{\text{SC}}}$ predicted by static modal derivatives; orange curve: $\frac{\mathcal{C}_{\text{MD}}}{\mathcal{C}_{\text{SC}}}$ computed from modal derivatives, blue curve: $\frac{\mathcal{C}_{\text{NF}}}{\mathcal{C}_{\text{SC}}}$ given by normal form theory. . . . 97

4.3 Comparison of manifolds in phase space for the first example, and for three different values of $\rho = \omega_2/\omega_1$. The exact NNM, represented in violet (full system solution: FS), is compared to the reduction manifolds obtained by QM from MDs (dark orange), from SMDs (yellow), and normal form (blue). (a) $\rho = 1.25$, (b) $\rho = 2.5$, (c) $\rho = 10$ with slow/fast assumption fulfilled. . . . 102

4.4 Values of the coefficient Γ dictating the hardening/softening behaviour for the first two-dofs system. Comparison of Γ_{MD}, Γ_{SMD} and Γ_{NF}, given respectively by QM with MDs, with SMDs, and normal form, Eqs. (4.40), and for varying $\rho = \omega_2/\omega_1$ ratio. 103

4.5 First mode backbone curves as a function of modal amplitude q_1 (first row), and q_2 (second row), and for different values of $\rho = \omega_2/\omega_1$. Comparisons between the exact solution (FS: full system, violet), that predicted by QM with MDs (dark orange), SMDs (yellow) and normal form (NF, blue). 104

4.6 Two degrees of freedom model with quadratic springs characteristic and geometric nonlinearities. 105

4.7 Comparison of manifolds in phase space for the second two-dofs example, and for three different values of $\rho = \omega_2/\omega_1$. The exact NNM, represented in violet (full system solution: FS), is compared to the reduction manifolds obtained by QM from MDs (dark orange), from SMDs (yellow), and normal form up to the second order (blue manifold in the first line, plots a-b-c) and third order (green manifolds, second line in plots d-e-f) are given. (a-d) $\rho = 1.25$, (b-e) $\rho = 2.5$, (c-f) $\rho = 10$ with slow/fast assumption fulfilled. In all cases $\omega_1 = 1$. 107

4.8 First mode invariant manifolds cut on the $\dot{q}_1 = 0$ plane, evaluated with the quadratic manifold method (QM) (either with MD in dark orange, and SMD in yellow) and normal form (NF) approach, where the distinction between NF up to second order (blue line) and third-order (dashed green line) is reported, and compared to the numerical solution obtained with the full system (FS). In all cases $\omega_1 = 1$. 107

4.9 First mode backbone curves for the second two-dofs example with quadratic nonlinearity, as a function of modal amplitude q_1 (first row), and q_2 (second row), and for different values of $\rho = \omega_2/\omega_1$. Comparisons between the exact solution (FS: full system, violet), that predicted by QM with MDs (dark orange), SMDs (yellow) and normal form (NF, blue, NF third order, dashed green). 110

4.10 Mesh and deformation along the mode under study for three different test cases: (a) a flat beam, (b) a shallow arch and (c) a non-shallow arch. For each test case the mode under study corresponds to the first flexural mode in the plane $y - z$ where the curvature is imposed if present. 110

4.11 Comparison of backbone curves obtained from QM with MDs (dark orange), SMDs (yellow) and normal form approach (blue), for the three tested structures: (a) flat beam, (b) shallow arch, (c) non-shallow arch. Nondimensional amplitude of flexural displacement (along y, nondimensionalised with respect to the thickness) of the central node of each beam as a function of ω/ω_1 where ω_1 refers to the eigenfrequency of the first flexural mode studied shown in Fig. 4.10. The backbone curves are contrasted to the FRF obtained on the full system (FS, violet) with numerical continuation and a small amount of damping, see text. The vertical gray dashed lines represent the frequency at which the saddle-node bifurcation of the forced response occurs. 113

4.12 Comparisons of the additional terms perturbing the linear mode shape solutions (deformation orthogonal to ϕ_p) for the case of the flat beam, computed at the saddle-node bifurcation point marked in Fig. 4.11a, fixing the frequency at which they have been computed. (a) full model solution, representation of the axial component of displacement $\boldsymbol{U}_{\mathrm{FS}}^{\perp,sym}.\boldsymbol{e}_z$ of the centre line nodes, (b) normal form: $\boldsymbol{U}_{\mathrm{NF}}^{\perp}(t^*).\boldsymbol{e}_z$, (c) Modal derivative : $\boldsymbol{U}_{\mathrm{MD}}^{\perp}(t^*).\boldsymbol{e}_z$, (d) Static modal derivative $\boldsymbol{U}_{\mathrm{SMD}}^{\perp}(t^*).\boldsymbol{e}_z$. 115

4.13 Comparisons of the additional terms perturbing the linear mode shape solutions (deformation orthogonal to ϕ_p) for the case of the shallow arch, computed at the saddle-node bifurcation point marked in Fig. 4.11b, fixing the frequency at which they have been computed. (a) full model solution, representation of the displacement $\boldsymbol{U}_{\text{FS}}^{\perp,sym}$ of the centre line in the $y-z$ plane; vertical axis $\boldsymbol{U}_{\text{FS}}^{\perp,sym}.\boldsymbol{e}_y$ (transverse direction) and horizontal axis $\boldsymbol{U}_{\text{FS}}^{\perp,sym}.\boldsymbol{e}_z$ (axial direction), (b) normal form: $\boldsymbol{U}_{\text{NF}}^{\perp}(t^*)$, (c) Modal derivative : $\boldsymbol{U}_{\text{MD}}^{\perp}(t^*)$, (d) Static modal derivative $\boldsymbol{U}_{\text{SMD}}^{\perp}(t^*)$. Gray lines: position of the centre line of the beam at rest. Solution amplified of factor 15. 115

4.14 Comparisons of the additional terms perturbing the linear mode shape solutions (deformation orthogonal to ϕ_p) for the case of the non-shallow arch, computed at the saddle-node bifurcation point marked in Fig. 4.11c, fixing the frequency at which they have been computed. (a) full model solution, representation of the displacement $\boldsymbol{U}_{\text{FS}}^{\perp,sym}$ of the centre line in the $y-z$ plane; vertical axis $\boldsymbol{U}_{\text{FS}}^{\perp,sym}.\boldsymbol{e}_y$ (transverse direction) and horizontal axis $\boldsymbol{U}_{\text{FS}}^{\perp,sym}.\boldsymbol{e}_z$ (axial direction), (b) normal form: $\boldsymbol{U}_{\text{NF}}^{\perp}(t^*)$, (c) Modal derivative : $\boldsymbol{U}_{\text{MD}}^{\perp}(t^*)$, (d) Static modal derivative $\boldsymbol{U}_{\text{SMD}}^{\perp}(t^*)$. Gray lines: position of the centre line of the beam at rest. Solution amplified of factor 50. 116

5.1 Mesh selection and geometry of the straight clamped-clamped beam, as well as eigenmode shapes corresponding to bending modes number 1 to 4 and mode 6. The bending vibration direction is along x while the in-plane direction is z. 146

5.2 Illustration of the physical content of some of the quadratic and cubic tensors used in DNF approach. First line: $\bar{\boldsymbol{a}}_{11}$, $\bar{\boldsymbol{a}}_{13}$ (black lines) compared to static modal derivatives Θ_{11}, Θ_{13} and Θ_{33} (dashed green line). Second line: quadratic vectors $\bar{\boldsymbol{b}}_{11}$, $\bar{\boldsymbol{b}}_{13}$ and $\bar{\boldsymbol{b}}_{33}$. Third line: cubic vectors: $\bar{\boldsymbol{r}}_{111}$, $\bar{\boldsymbol{\mu}}_{111}$ and $\bar{\boldsymbol{\nu}}_{111}$.146

5.3 Amplitude-frequency backbone curve for the first NNM of the clamped-clamped beam. (a) reference full-order solution obtained with 9 harmonics (black line) and with 15 harmonics (purple). Stability is not reported. (b) comparison of the reference solution to different ROMs computed with the direct normal form (DNF). Light blue curve: direct normal form with a single master coordinate corresponding to mode 1. Dashed blue line: second-order direct normal form with two master coordinates 1 and 3, green line: third-order direct normal form with two master modes (1 and 3) and inclusion of the resonant monomials corresponding to 3:1 internal resonance. 148

5.4 Amplitude-frequency backbone curve for the second NNM of the clamped-clamped beam. (a) Reference solution obtained with 15 harmonics (purple) compared to ROM considering only master coordinate of mode 2 (DNF single master mode, light blue), and a ROM with the third-order normal form with modes 2 and 4 and the resonant monomials corresponding to 3:1 internal resonance (DNF third-order + 3:1, dashed red curve). (b) Reference solution is compared to a ROM obtained with the second-order normal form with 3 master coordinates corresponding to modes 2, 4 and 6 (dashed blue), and to a ROM obtained with the third-order normal form, 3 master coordinates, and resonant monomials corresponding to 3:1 between mode 2 and 4 and 2 and 6. 150

5.5 Blade mesh and first five modes. In Fig. 5.5a, the blade mesh is shown from two different views. Clamped faces highlighted in yellow. In Fig. 5.5b, the first five modes of the blade are reported. 152

5.6 Second-order correction vector shapes $\bar{\boldsymbol{a}}_{11}$ and $\bar{\boldsymbol{b}}_{11}$ used in the reduction procedure for the first mode of the fan blade ϕ_1. The vector $\bar{\boldsymbol{b}}_{11}$ presents a strong component of the mode ϕ_1, highlighting the important quadratic self-coupling term g_{11}^1 due to the curvature. In the table are listed the values of the parameters needed to construct the reduced-order dynamics for the fundamental mode. 154

5.7 Backbone curve of the fundamental mode of the fan blade. Amplitude of vibrations (in m) computed at the node where the force vector is shown, see Fig. 5.5a, and in the same direction x. 154

5.8 Frequency response functions of the fan blade subjected to harmonic forcing in the vicinity of the first bending eigenfrequency. (a) Only mass-proportional Rayleigh damping is taken into account, with $\zeta_M = 3 \cdot 10^{-1}$ and $\zeta_K = 0$. Amplitude of the forcing $F = 30N$. Comparison between full-order model (purple), and ROM composed of a single master mode computed with direct normal form, either with only linear damping term (DNF linear damping, blue curve), or by taking into account the nonlinear aggregated damping term (DNF nonlinear damping, yellow dashed curve). (b) Only stiffness-proportional damping with $\zeta_K = 2 \cdot 10^{-5}$ and $\zeta_M = 0$. Amplitude of forcing $F = 2N$. (c) Only stiffness-proportional damping with $\zeta_K = 10^{-5}$, $\zeta_M = 0$, amplitude of forcing $F = 10N$. 156

5.9 (a) Frequency response functions of the clamped-clamped beam subjected to harmonic forcing in the vicinity of the second eigenfrequency. Only stiffness-proportional damping is considered with $\zeta_K = 13 \cdot 10^{-6}$ and $\zeta_M = 0$. Amplitude of the forcing $F = 10N$. Full-order solution is compared to ROMs obtained with a single master coordinate (mode 2), with only linear damping term (blue curve) and with additional nonlinear damping term (dashed yellow curve). (b) close-up view near the maximum amplitude. 157

5.10 (a) Frequency response functions of the clamped-clamped beam subjected to harmonic forcing in the vicinity of the second eigenfrequency. Stiffness-proportional damping is considered with $\zeta_K = 3 \cdot 10^{-7}$ and $\zeta_M = 0$. Amplitude of the forcing $F = 30N$. Full-order solution is compared to different ROMs obtained with a two master coordinates corresponding to modes 2 and 4. Reference solution obtained with 15 harmonics (purple). All the ROMs are obtained with two modes and second-order normal form. Blue curve: only linear damping term considered. Yellow dashed curve: full consideration of nonlinear damping including cross-coupling terms. Brown curve: nonlinear damping neglecting the cross-couplings. (b) close-up view in the 3:1 resonance loop. 158

6.1 Rubbing between single blade and elastic casing 161

6.2 Nonlinear mode of the single oscillator with clearance nonlinearity. 167

6.3 Comparison on a softer contact case. Conservative solution of the nonlinear mode with $\beta_\epsilon = 4.5$. Frequency amplitude curve (a) and contact force at $\omega = 1.35$ (b). 173

6.4 Comparison between the forced response function evaluated with HBM and with FET: (left) 31 DOFs, (right) 151 DOFs 175

6.5 Comparison between the solution evaluated at $\lambda \approx 0.46$ with HBM and with FET: (a) Displacement over time, (b) relative error on displacement with respect to time-integration, (c) contact force over time, (d) relative error on contact force with respect to time-integration 176

6.6 Convergence of the error with the DOFs: error on displacement (left) and error on contact force (right) 177

6.7 Blade-like structure under test. Discretisation and axis orientation. Bounding box size: $(\Delta X, \Delta Y, \Delta Z) = (79.84, 40.07, 200)mm$. Positioning of nodes along the chord: from trailing edge (TE) to leading edge (LE). 182

6.8 Solution of mode 1 at low amplitude vibration. Linear solution at amplitude lower than the clearance. 182

6.9 Solution of nonlinear mode 1 at high amplitude vibration. Solution close to asymptotic nonlinear frequency. 183

6.10 Time response of tip nodes along nonlinear mode 4.(a) Linear solution at amplitude lower than the clearance. (b) Solution close to asymptotic nonlinear frequency. 183

6.11 Frequency amplitude plot of nonlinear mode 1 obtained with: full model (black), proposed method based on derivatives (blue), Hurty/Craig-Bampton method with 2 internal modes (red). Amplitude at trailing edge (a) and leading edge (b). 184

6.12 Frequency amplitude plot of nonlinear mode 1 obtained with: full model (black), proposed method based on derivatives (blue), Hurty/Craig-Bampton method with 5 internal modes (red). Amplitude at trailing edge (a) and leading edge (b). 185

6.13 2-DOFs simplified system. 187

6.14 Bifurcation diagram of the negative clearance system: isolated branches of periodic solution and stable equilibrium branches for different values of k_e. . 189

6.15 Bifurcation diagram of the positive clearance system: isolated branches of periodic solution and stable equilibrium branches for different values of k_e. . 190

6.16 Nonlinear modes of the system and trajectories in the vicinity of the internal resonance 1:2 191

6.17 Branch of self-excited solution underneath the internal resonance 1:2 between first and second mode of the system. Stable (solid) and unstable (dashed) branches of undamped (red) and damped (black) nonlinear mode. 192

C.1 Class read mk file 225

C.2 Class build physical system 226

C.3 Class time discretisation 227

C.4 Class initialisation 228

C.5 Class dynamical functions 228

Chapter 1

Introduction

1.1 Motivations

Vibration is a major source of failure in aircraft engines. The prolonged vibration of a component can lead to high cycle fatigue which may result in cracks in the points of maximum stress or, in the worst case scenario, failure of the component. The blades of a turbomachine are, among all, a particularly fragile component in that they are relatively thin structures directly exposed to the flow. A sustained regime of vibration would reduce their lives, thus jeopardising the whole assembly structural integrity. That is why special attention is required to ensure blades are not exposed to periodic forcing tuned with their natural frequencies.

The sources of excitation of blades can have multiple origins, the most common one being the aerodynamic flow itself. Previous stages of the machine can act like spatially periodic obstacles for the flow and generate an aerodynamic excitation with a frequency that is a multiple, depending on how many obstacles it has encountered, of the rotational speed. The design of modern engines aims at reducing the weight of the engine to the greatest extent possible thus making lightweight blades more prone to be excited even by low force levels.

Together with the excitation from the flow, purely mechanical forces can also arise. If the rotor is unbalanced or the casing is ovalised the rotating and stationary parts of the engine can come into contact. Running clearances between the tip of the blades and the inner surface of the casing are present but they have been drastically reduced in modern engines to improve aerodynamic efficiency. In fact, the leakage flows at the blades' tips represent the main loss in terms of aerodynamic efficiency, and for the manufacturers to remain competitive, these losses must be reduced to the greatest extent possible. In recent years, efforts made in this respect led to a drastic reduction of the operating clearances which resulted in an increased probability that the blade-tip and the casing come into contact. To reduce the violence of the possible impacts of the blade tip against the bare casing while maintaining the size of the clearance small, the inner surface of the casing is coated with a

layer of soft abradable material. In this way the energetic efficiency is kept high and, at the same time, the risk that possibly dangerous events occur is reduced. The abradable material is soft and allows the blade tip to wear without generating very high forces. Moreover, this solution acts as a self-adjusting clearance since the blade can wear the abradable material only in the specifying locations required by the operating conditions that the machine is undergoing, without affecting the overall efficiency. However, despite the presence of the abradable, the tip/abradable interaction has still the power to excite a resonance if the frequency of the rubbings is close to a natural frequency of the blade. At the blades' tip, the velocity is very high compared to other spots where rotor and stator might interact, as the blade root for example. The high kinetic energy of the rotational motion can then be transformed into vibratory motion through rubbing. If the rotor is unbalanced or the casing is ovalised, the frequency of these contacts will coincides with the rotational speed in the first case and two times the rotational speed in the second case.

Both aerodynamic and mechanical excitation have a frequency proportional to the rotational speed with an integer factor. A multiple of the rotational speed is called engine order and every time a natural frequency of the blades is equal to an engine order a resonance might occur. The Campbell diagram reports the engine orders and the natural frequencies with respect to the rotational speed thus permitting to identify potential resonances at the crossing points. A schematic representation of a Campbell diagram is depicted in Fig. 1.1. The first three modes of a blade are computed with a linear analysis and their frequencies are plotted together with all the possible engine orders against the rotational speed. A given operational speed range is then checked and if a crossing occurs, more accurate analysis are performed to assess its safety.

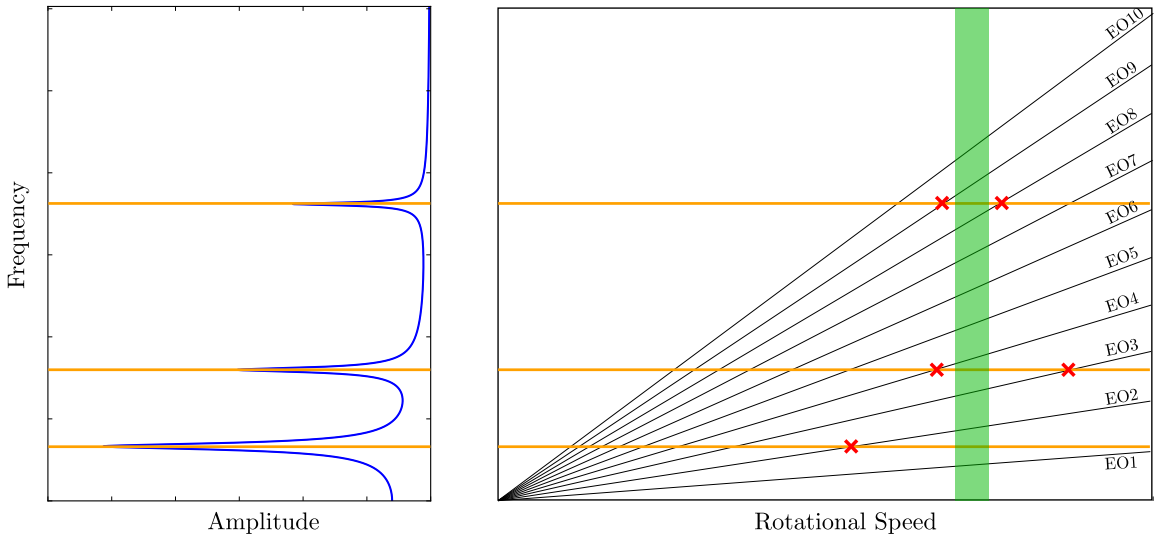
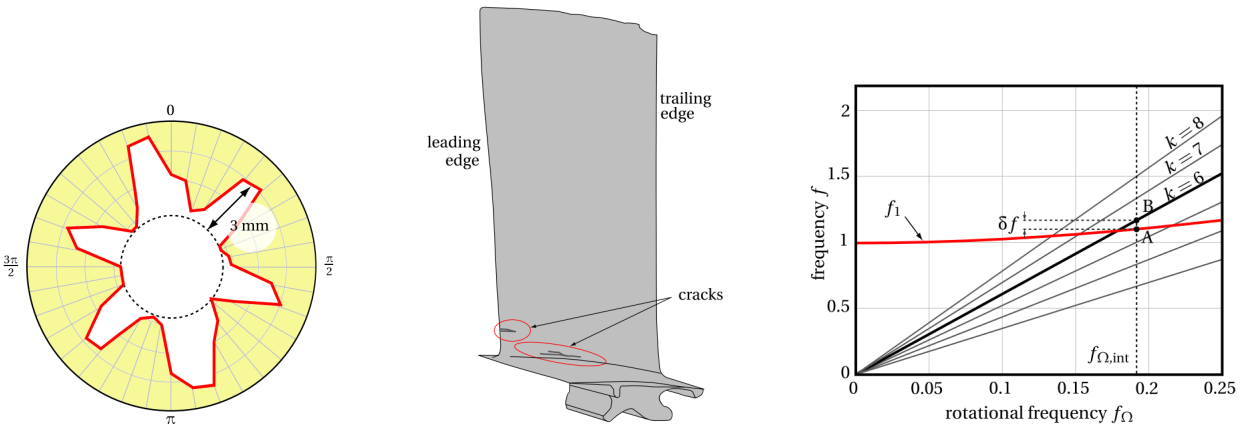


Figure 1.1: Sketch of a Campbell diagram to predict resonant crossings (red) between the natural frequencies (yellow) and an engine order (black) around the operational range (green).

Recent experiments by Batailly et al. [10] performed in the ONERA laboratory in Lille, tested a single compressor blade forced to rub against a rigid casing coated with a layer of abradable material. In the reported test, the rotational frequency was progressively

increased in the vicinity of the six engine order of the blade's first bending mode. After the test run, cracks at the root of the blade and blade missing parts (Fig. 1.2b) were observed, associated with a circumferentially periodic wear pattern on the sacrificial layer (Fig.. 1.2a). During the test, the blade experienced a significant level of natural vibrations thus making vibratory fatigue the most likely cause of the blade cracks.

The outcome of this test, demonstrated that, despite the presence of the abradable, a sustained regime of intermittent contacts can result in serious blade damages in a relatively short time span if a multiple of the rotational speed is tuned with a natural frequency. Moreover, the critical speed predicted by the Campbell diagram (Fig. 1.2c) showed a discrepancy with the actual critical speed at which the resonance occurred. The explanation for this discrepancy is rather simple in that the contact with the abradable introduced a stiffening effect on the blade that moved its natural frequency towards higher values. During the interaction, not only its natural frequency, but the whole blade dynamics is modified by the contacts. The abradable must be indeed seen as an unilateral contact constraint acting on the blade during the contact phase and exerting normal and tangential forces on it. To be predicted, the overall behaviour of such a system would require a nonlinear model that takes into account the nonlinearities introduced by the contact. The linear assumption underlying the Campbell diagram makes this tool limited when dealing with nonlinear systems, therefore for a more accurate solution, more refined numerical tools are necessary.



(a) Six-lobes wear pattern (b) Blade damages (c) Campbell diagram

Figure 1.2: Results of experimental test described in [10]

Not only these observations shed a new light on the potentially destructive effects that rub-induced vibrations can have on the engine but they also highlighted the limitations of linear modal analysis in dealing with such problems. It is therefore clear why the aircraft industry has the urge to develop new tools able to cope with the complexity of the phenomena observed. With the increasing computational efficiency of modern computers, aeroengines companies are allocating more and more resources on the improvement of the numerical predictions rather than relying solely on experiments. If it is true that level of accuracy expected from numerical models is very high it is also true that the computational power available for numerical simulation is unprecedented. In this context, nonlinear dynamics

tools that few decades ago could only be applied to toy models, can now be used to solve large scale realistic models.

1.2 Framework

This thesis deals with the numerical simulation of blade dynamics within the framework of nonlinear vibration. Several type of nonlinear forces can arise in the blade, from the purely structural ones coming from material nonlinearity, contacts and geometric nonlinearities to the aeroelastic ones coming from the nonlinearity of the flow.

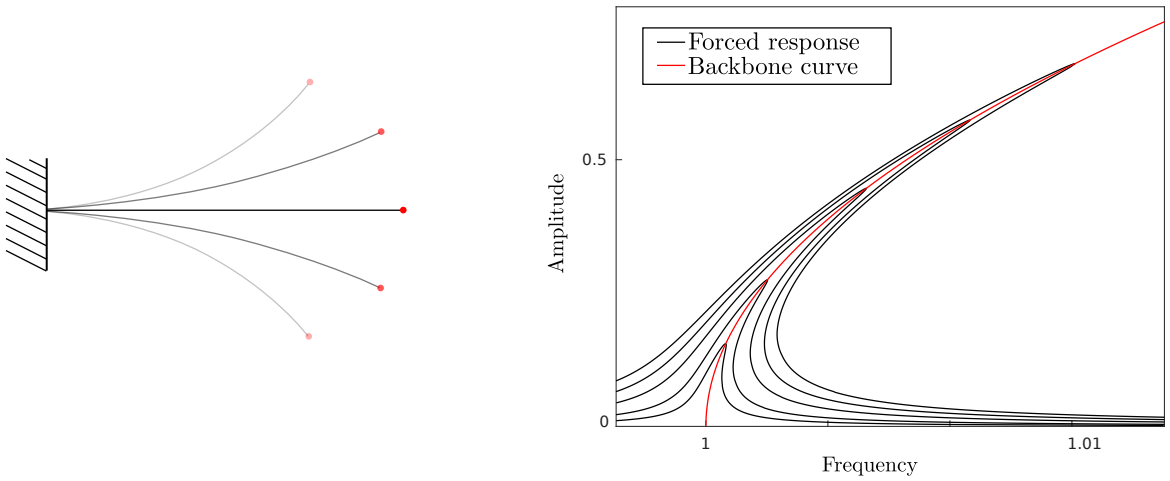
The main focus of this work are (i) the geometric nonlinearities arising when large displacement are exhibited and (ii) the contact nonlinearities due to the interaction with other mechanical components. The first type of nonlinearity is normally attributed to high amplitude vibration of long and flexible structures, such as fan blades, but it can have a key effect also at low amplitude vibration if the structure is overconstrained. As for the second one, contacts can occur between two rotor components, as in the case of underplatform dampers or between a rotor and a stator component, as in the case of blade casing contacts. Because of the high energy contained in the rotational motion, the latter type of contact is been shown to be potentially very dangerous and able to drive blade resonances.

Generally speaking, nonlinear forces have the effect of changing the mode shape and the natural frequency of linear modes. At very low amplitude, the structure behaves linearly and can be studied with the tools provided by modal analysis. However, as soon as the amplitude increases, the nonlinearities start having an effect and both the natural frequency and the mode shape become amplitude dependent.

From this point of view, the link between contact and geometric nonlinearities is manifold. The contact with the casing acts like a constraint on the blade and, during the contact phase, this constraint is able to activate a strong geometric nonlinear behaviours. Also, the contact interaction might excite a resonance of the blade that will lead to high amplitude vibration and large displacement, thus making geometric nonlinearities important. Moreover, geometric nonlinearities change the natural frequencies of free vibration so the actual rotational speed that will excite resonances not only changes because of the contact constraint but also because of the inherently geometric nonlinear behaviour. More importantly, an accurate detection of the contact is crucial to the accuracy of the simulation therefore the correct motion of the blade tip has to be computed by taking into account the shortening effect of geometric nonlinearities, *i.e.* the above mentioned dependence of the modeshapes by the amplitude. The dependence of the modeshapes with amplitude due to geometric nonlinear forces affects also the location of the first contact on the tip. If with a linear analysis a certain point along the tip is expected to touch first, when a nonlinear analysis is performed such location might be different. If the shortening effect is for example more pronounced at the leading edge and less at the trailing edge, the latter is more prone to touch than the former. Lastly, as demonstrated by Batailly at al. in [12], in the framework

of blade design, the so called clearance consumption which consists in the radial motion of the tip nodes as the blade vibrates along a mode is the key parameter to minimise to increase the robustness to contact interactions. In [12] it is shown that geometric nonlinearities can have effects on this parameter thus they have to be considered in the design process.

To better understand the concept of amplitude dependence of modeshapes and natural frequencies in nonlinear structures, a schematic representation of the dynamics of the first mode of a cantilever beam is depicted in Fig. 1.3. The tip of the beam does not move on a linear trajectory as one would predict with a linear analysis, but it undergoes a curvilinear one. The modeshape becomes nonlinear and shows a dependency with the amplitude of vibration. As for the resonance frequency, it also display a variation with the amplitude of excitation. Forced response with increasing excitation level are depicted in Fig. 1.3b in black. If one continuously tracks the resonant points, one would find that they lie on the red curve described as backbone curve. This curve follows the variation of the resonant frequency with respect to the amplitude.



(a) Amplitude dependent modeshape (b) Amplitude dependent frequency

Figure 1.3: Schematic example of nonlinear behaviour of a cantilever beam in large amplitude vibration.

1.3 Nonlinear modal analysis

The idea behind nonlinear modal analysis is to extend the framework of linear modal analysis to nonlinear vibration. In modal analysis the modeshapes and natural frequencies of a structure are computed once for all and they are used to reduce the behaviour of the structure to the sole modes responding to a given excitation. In particular, if the forcing frequency is close to a system's natural frequency, taking into account the sole resonant mode would provide accurate results. This approach can be extended to the case of nonlinear systems through nonlinear modal analysis. If one is able to compute the variations of modeshape and resonant frequency with the amplitude, i.e. is able to find the nonlinear mode, the overall behaviour of the structure subjected to a periodic excitation with

frequency close to a resonant frequency can be approximated by its resonant nonlinear mode.

Since the pioneering work of Rosenberg [125] that defined a nonlinear normal mode (NNM) as a family of periodic orbits, it also been defined as an invariant manifold in phase space, tangent to the linear eigenspace near the origin [137]. In recent years, the use of nonlinear modal analysis has become an established framework in engineering problems [67] and has been applied in to large finite element models [121].

Due to their dual definition, the concept of nonlinear mode has become a general concept that encompasses a wide range of numerical approaches. A general distinction can be firstly done between two strategies, both devoted to the computation of the nonlinear mode.

The nonlinear mode intended as a family of periodic orbits can be computed by applying continuation algorithm on the conservative system to find the periodic orbits as the amplitude of oscillation increases. In nonlinear modal analysis the periodic solution can be sought either with perturbation methods or with the so called boundary value problem method (BVP). When the size of the system is considerable and the nonlinearities are strong, BVP methods are usually required. Methods such Harmonic Balance Method, Shooting Method, Time Finite Element Method, and Collocation Method, to name a few, are common tools for this type of analysis. Such approach can be applied directly to the full equation of motion; however, if the model is large, the size of the nonlinear system to solve can be too large and the computational time too long. Model order reduction can then be necessary to decrease the number of degrees of freedom of the full system. Once all the periodic orbits are computed up to a certain amplitude, the invariant manifold can be then reconstructed if necessary. Depending on the type of nonlinear force present and on the size of the system, the strategies also vary. In the context of blade dynamics, nonlinear modes of large scale systems in presence of contact nonlinearities have been reported by [75, 76, 107], just to mention a few. The solution of the full model in presence of geometric nonlinearities is instead more challenging due to the fact that this type of nonlinearity is distributed throughout the whole structure; for this reason, much fewer attempts in this respect are available in the literature [17, 172]. As a matter of fact, when dealing with geometric nonlinear structures the application of reduced order models is usually the preferred approach.

Conversely, when the invariant manifold in phase space is sought, the nonlinear mode is found by directly computing this geometrical entity; with this approach, non conservative systems can also be studied as the assumption of periodic orbit is no longer included. Both analytical and numerical methods can be used to this end, where analytical methods are usually based on polynomial series expansions aimed at parametrising the geometry of the manifold [15, 42, 45, 137, 153] whereas numerical methods computes the solution of the partial differential equations that governs the manifold [114].

In the context of reduced order modelling (ROM), analytically computed invariant mani-

folds represent the minimal yet rigorously defined reduced model of the system. However, the application of analytical techniques is limited to structures with a limited number of degrees of freedom, mainly because the starting point of these ROMs is the system written in modal basis. Being this condition unattainable in the case of large models, most of the available methods for the reduction of geometrically nonlinear structures are based on approximations of the actual invariant manifold through simplifying assumptions that render the method applicable *directly* to the system in physical basis. Methods like implicit condensation [48], modal derivatives [53], and quadratic manifold [126] belong to this category and will be referred to as *direct* methods in the course of this thesis.

1.3.1 Positioning

The positioning of the present work is depicted in Fig 1.4. The time evolution of a nonlinear system can be characterised by transient or steady state response. A steady state response is reached when the transient decays and it is the state of utmost interest for engine manufacturers in that it can lead to high cycle fatigue. Even though in most analysis the periodic steady state is sought, in an industrial context, time-integration schemes are usually much more employed than BVP methods. In this work, we advocate for the use of BVP methods coupled with accurate ROMs and applied to large structures.

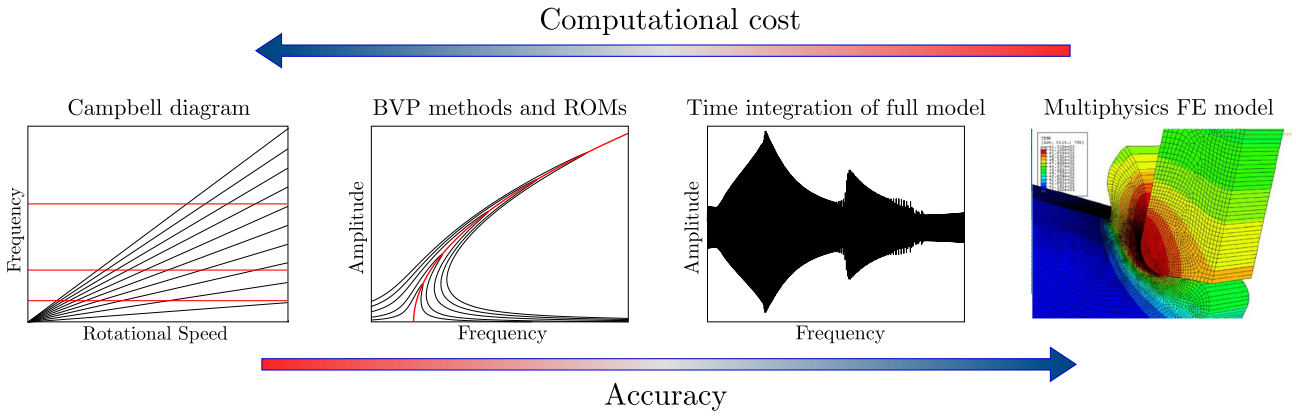


Figure 1.4: Positioning of the present work in terms of accuracy and computational cost.

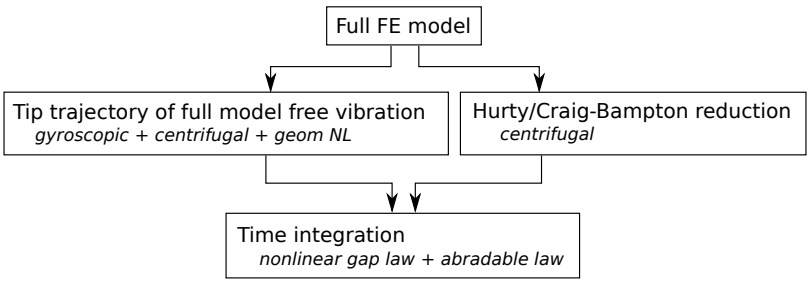
The accuracy provided by the coupled use of ROMs and BVP method is higher than that of the linear approximation because it is able to take into account the nonlinearities of the problem. Thanks to the reduction, the full model is reduced in its size and its reduced dynamics is computed by solving the periodic steady state with the chosen BVP method and then continued with respect to the parameter of interest with path following algorithm. In this way, the computational cost is drastically reduced compared to the simulation via time integration of the full model. For this reason, nonlinear modal analysis is the perfect candidate for assessment of blades in the preliminary design stage, as it represent a compromise between accuracy and fast computational time. Not only nonlinear modal analysis can produce accurate results within a much shorter computational time but it can also provide informations on bifurcations and stability that would be missed within a time integration

framework. Moreover, the use of reduced order models is able to isolate the specific features of interest from the rest, *i. e.* a particular mode or the interaction between two modes, thus providing much more insightful informations on the system. Informations gathered in this stage can be verified through more accurate methods in a later stage; time integration of the unreduced model is the most common verification method but also more accurate multiphysics simulations could be used.

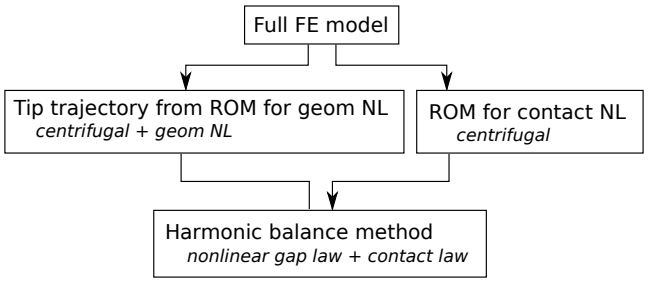
To better highlight the positioning of the present work in the context of blade-casing interaction, the typical workflow adopted by the industrial sponsor Rolls-Royce to study the problem is depicted in Fig. 1.5a. A model of the blade is meshed with three dimensional finite elements in the proprietary code SC03; a time integration analysis of the full model is firstly run with no contact conditions to identify the nonlinear trajectory of the tip of the blade when vibrating ; an accurate reduced order model of the blade classically reduced with Hurty/Craig-Bampton method with the inclusion of several - up to a few hundreds - internal modes is then build, taking into account centrifugal effects but discarding gyroscopic ones. Such reduced model is then solved with time integration with contact conditions that involve the wear of the abradable material and that takes into account the nonlinear trajectory of the tip by including a nonlinear gap law.

The workflow proposed in this work is reported in Fig. 1.5b. The calculation of the tip trajectory in free vibration when geometric nonlinearities are included in the model, could be done by means of a reduced order model for geometrically nonlinear structures; also, the reduction of the model for the computation with contact nonlinearities, could be done with minimal ROMs developed ad hoc for this type of nonlinearity. Finally, instead of time integration, a BVP method like HBM could be used to produce forced responses or backbone curves with a contact law that discards the wear and with the nonlinear gap law calculated from the geometrically nonlinear ROM. Ideally, if a unified treatment of geometric and contact nonlinearities would be developed, the two ROMs blocks could become a single one.

Both workflow have the aim of identifying potentially dangerous resonances or limit cycle oscillations. Thanks to the simplified dynamics produced by a reduction method, the results of a ROM are more interpretable than those obtained with time integration of a large model. Moreover, the analysis in presence of geometric nonlinearities could identify phenomena like internal resonances that could be missed by the time integration scheme. Finally, in the context of blade design, the trajectory of the tip along its nonlinear mode-shape, which is a by-product of the nonlinear ROMs that will be treated in this thesis, is a crucial parameter because it defines the nonlinear clearance consumption. By exploiting the computational advantages of a fast ROM for geometric nonlinearities, one could optimise the design of blades by minimising the clearance consumption directly.



(a) Time integration of full model workflow



(b) BVP methods and ROMs workflow

Figure 1.5: Comparison of the two main approaches with different level of accuracy to blade-casing interaction problems.

1.3.2 Research questions

The main objective of this thesis is to extend nonlinear modal analysis techniques and methods to an industrial framework. The main focus will be on reduced order modelling methods and on the assessment of their capabilities and limitations when applied to large finite element models. In particular, three dimensional finite elements will be used in this dissertation in that they are the only type of elements used in industry, mainly because of their flexibility in discretising the complex geometries of modern blades. Also, in the context of geometric nonlinearities, these elements are exact, as they do not rely on limiting assumption on the amplitude of vibration, unlike 1D and 2D elements for instance.

Given these premises, in this work we are mostly interested in predictive, offline and simulation-free ROMs. The main reason for this interest is the higher interpretability of such methods as compared to methods such as the POD or the PGD (Proper Generalized Decomposition) methods [3, 26, 73, 92] that rely on prior computations or output data from full-order model solutions. The methods treated in this thesis are based on an a priori construction of a basis, in the form of a nonlinear change of coordinates in most cases, that is defined starting from the equations of motion of the FE discretised system. It will be shown that such methods are able to achieve minimal reduced order models in a highly interpretable form, and also to reproduce the full model behaviour with great accuracy.

In this context, a summary of the scientific and industrial objectives that we attempt to achieve in this thesis is provided:

- How methods, like the modal ROMs, developed for and tested on simple structures

with well understood dynamics (flat beams and plates, shallow arches and shells), adapt to more generic models with complex geometry? Similarly, how these methods, always used on 1D and 2D finite elements models, behave when applied to structures discretised with 3D elements?

- Is there a link between modal and direct ROMs and can one give a mathematical and physical interpretation of direct ROMs? Can analogies and hidden similarities between different methods, guide us towards a better understanding of the performances and limitations of each method?

- Given the great suitability of direct ROMs for large structures, we would like to better understand what are the assumptions behind direct ROMs and how they affect the results. Which physical parameters are linked to these assumptions (separation of modes, internal resonances, shape of the structure flat/curved, number of modal couplings)? Can one generalise these assumptions and determine the range of applicability of such approximate ROMs?

- Given the rigorous mathematical foundation of the asymptotic calculations of invariant manifolds, we would like to use such methods on large structures, but they are intrinsically modal ROMs. Can the structure of direct ROMs be leveraged to build more rigorous ROMs? Can the assumptions of direct ROMs be lifted? Can modal ROMs be adapted to the case of a generic structure?

- Offline and simulation-free ROMs are rarely found in the literature for the case of contact nonlinearities. Can the same idea of predictive ROMs for geometric nonlinearities be applied to the case of contact nonlinearities? If so, can the treatment of those nonlinearities be unified in a model order reduction framework?

- The great popularity of nonlinear modal analysis makes it an unmissable tool for engineers, also in an industrial framework. Which phenomena relating to blade-casing interaction can be unveiled by the use of nonlinear modes? Can nonlinear modal analysis be used to isolate modes of interest and circumvent the lack of interpretability of multimode time responses?

1.4 Outline

The next chapter presents the reader with common tools from nonlinear dynamics for engineering applications. A particular attention will be dedicated to available reduced order modelling methods and their derivation. After having introduced the general methodology, in Chapter 3 the problem of slow convergence of ROM based on linear basis when dealing with three dimensional finite elements will be presented and two strategies to overcome the said problem will be introduced, namely the M-StEP method and the use of static modal derivatives. In Chapter 4, two methods based on a nonlinear change of coordinates,

the quadratic manifold method and the real normal form method, will be compared and the limitation given by the assumption of velocity independent manifold assessed. Also, the differences in the behaviour of static modal derivatives and modal derivatives will be demonstrated. In Chapter 5, the method of direct normal form is proposed with the aim of extending the concept of nonlinear normal modes based ROM to large finite element structures. The system is rewritten in physical coordinates and all the operations expressed in a non-intrusive manner. Lastly, in Chapter 6, the case of contact nonlinearities is treated. In this case the Hurty/Craig-Bampton method is compared to a proposed method consisting in the adaptation of the direct normal form method to contact nonlinearities that is more suitable for nonlinear modal analysis problems. Also friction-induced vibration are examined through damped nonlinear modes of a two degrees of freedom model.

Chapter 2

Methodology

The aim of this chapter is to present the reader with basic nonlinear dynamics notions that are deemed necessary to better understand the framework within which the scientific contributions of this dissertation have been developed.

The framework of this dissertation is nonlinear vibration of structures. Nonlinear vibration refers to the application of classical nonlinear dynamical system theory to mechanical systems. Dynamical system theory deals with systems of first order ODE in time. Conversely, vibration is normally referred to as a dynamical problem when mechanical systems are treated, which has, upon spatial discretisation, the form a system of second order ODE in time, where accelerations and velocity are present. Normally to solve a vibration problem the configuration space is used, where the displacement field is used to uniquely define the state of a system. When written as a dynamical system in first order, the so called phase space is used and displacement and velocity fields are both needed to define the state of the system. The two formulations are perfectly equivalent and one can always move from one to another. Nonlinear dynamical system theory is an established research field compared to the relatively more recent field of nonlinear vibration which is the reason why most of the methods used nowadays in nonlinear vibration are usually an adaptation of methods originally developed from dynamical systems.

This chapter provides an overview of the methodology that is usually applied to nonlinear vibration of mechanical systems. The huge variety of possible approaches and methods makes it impossible to provide an omni-comprehensive overview, therefore only the methods that will be used or investigated in the course of this work will be introduced here.

2.1 General procedure

A generic continuum mechanical problem can be modelled as a series of partial differential equations in time and space. The state of the system is unequivocally determined by its displacement and velocity fields, $\boldsymbol{u}(X, Y, Z, t)$, $\boldsymbol{v}(X, Y, Z, t)$ in time and space variables.

The strategies used to approach a large scale nonlinear vibration problem are various but the great majority of them shares a common structure. With the exception of the studies that use the wave approach [178], separation of variables is in fact the most viable way to tackle such problem. Inherited from modal analysis, the separation of variables consists in assuming the partial differential equations of the problem can be transformed into ordinary differential equation in the sole time variable upon a space discretisation by means of shape functions.

The flow diagram of the said strategy can be then summarised into four stages (see Fig. 2.1): (i) spatial discretisation, (ii) model reduction, (iii) time discretisation, (iv) variation of parameters.

The first stage consists in the spatial discretisation of the model geometry. Simplified models or semi-analytical models can be sometimes investigated in the preliminary study of a particular phenomenon, but in a broader engineering context, large scale finite element (FE) models are necessary to accurately reproduce the complexity of the model geometry. In the course of this thesis, 3D finite elements are of most interest being the most common way to discretise blade geometries. Some beam models will be also used, mostly to introduce the geometric nonlinear problem in a analytical way and to validate the results of the ROM on 3D FE discretised beam models. One and two dofs models will be also used to reduce the problem complexity and only focus on the phenomenon validation.

The second stage consists in reducing the size of the model. Due to the large size, the direct solution of the FE model is often impractical because it will lead to very long computational time. Moreover, once the system has reached a steady state, most of the energy is contained in the most excited modes. High frequency modes are normally much more damped than low frequency ones, making them decay faster and respond with very low amplitudes at steady state. For this reason, reduced models are usually build around the most responding modes thus dramatically reducing the computational cost of the following stages.

After having discretised and reduced the model, a system of ODEs in the sole time variable is obtained. For small systems, perturbation methods can be applied and an analytical solution can be derived. However, if the size of the model is still relatively large or the type of nonlinearity is not easily solvable by means of analytical methods, numerical methods are necessary to discretise the time and generate a nonlinear algebraic system of equations. The most common approach to solve the system of ODEs is time integration. A discretisation of the time variable into a series of time steps is performed and the solution at each time step is found using the previously calculated ones. In this way, transient dynamics as well as steady state dynamics can be solved with no assumption on the periodicity of the solution. If this approach is very simple and applicable to any system, its main drawback lies in its computational cost.

If the sought solution is a periodic steady state, much faster methods are available to solve the problem, harmonic balance method being the most classical one but other methods like

shooting [121] and collocation [31] are also very much used. All these methods enforce the periodicity of the solution therefore are only able to capture the steady state dynamics of the system. On the other hand they are able to provide a more insightful view of the system response when it comes to stability and bifurcation due to parameters variations.

As a matter of fact, the variation of the system response produced by a variation of a given parameters is the final aim of any analysis since not only a specific set of conditions is usually of interest but also a range of such conditions. The most classical example of parameter variation consists in the forced response function where the frequency of the excitation force is varied within a range and the resonances of the system are checked. This kind of analysis is done with a frequency sweep if the time is discretised with time integration whereas continuation algorithms are adopted if methods to compute the periodic solution are used.

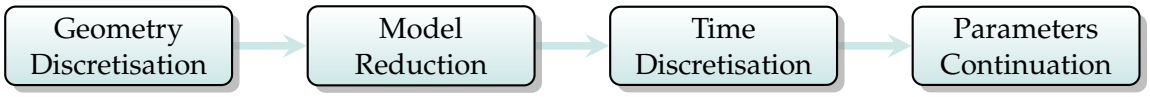


Figure 2.1: Workflow diagram of a numerical study of a nonlinear large-scale model

2.2 Finite Element Model

The finite element method [179] is the most common tool used in structural dynamics to discretise complex geometries. Here, we will briefly recall the general procedure that leads to the weak formulation of the original problem by means of the principle of virtual work.

In solid mechanics the structure is treated as a continuous body of domain Ω and domain boundary Σ, whose displacement field is $\boldsymbol{u}(\boldsymbol{X}, t)$. The reference position of each point P in the domain is the set of coordinates $\boldsymbol{X}_P$ at $t = 0$, whereas the actual position of the same point at the generic time t is given by the set of coordinates $\boldsymbol{x}_P(t)$. Since a Lagrangian formulation is normally used in solid mechanics, the principle of virtual work is usually expressed in reference configuration rather than in actual configuration and reads:

$$\int_\Omega \boldsymbol{S} : \delta\boldsymbol{E}\, d\Omega + \int_\Omega \rho\ddot{\boldsymbol{u}} \cdot \delta\boldsymbol{u}\, d\Omega = \int_\Omega \boldsymbol{b} \cdot \delta\boldsymbol{u}\, d\Omega + \int_\Sigma \boldsymbol{t} \cdot \delta\boldsymbol{u}\, d\Sigma \tag{2.1}$$

where $\rho(\boldsymbol{X})$ is the material density, $\boldsymbol{b}(\boldsymbol{X}, t)$ is the body force per unit volume, $\boldsymbol{t}(\boldsymbol{X}, t)$ the surface traction per unit surface; the first term on the left hand side represents the virtual work done by the internal stress being $\boldsymbol{S}$ the second Piola-Kirchhoff tensor and and $\boldsymbol{E}$ the Green-Lagrangian strain tensor. In finite strain theory, the Green-Lagrangian strain tensor is defined as:

$$\boldsymbol{E} = \frac{1}{2}\left((\nabla\boldsymbol{u})^{\mathrm{T}} + \nabla\boldsymbol{u} + (\nabla\boldsymbol{u})^{\mathrm{T}} \cdot \nabla\boldsymbol{u}\right) \tag{2.2}$$

where the first two terms are linear and the third term is quadratic with respect to $\boldsymbol{u}$.

When the displacement is expected to be smaller than any relevant dimension of the body, infinitesimal strain is assumed hence the quadratic part of the strain tensor is neglected.

This is the case, for instance, of stress analysis and vibration analysis where, if also the material is treated as linear and elastic, the resulting system of equation upon finite element discretisation will be linear. However, when large displacements occur, the quadratic component of the strain tensor has to be taken into account; this quadratic component is what generates geometric nonlinearities in the form of quadratic and cubic elastic forces. In such case, a linear elastic law can still be used, which is the case of the present work. Different models exist to express a linear relation between stress and strain of a linear elastic material, the most common one being the Saint Venant-Kirchhoff model. This model is derived from Cauchy linear elasticity and reads :

$$\boldsymbol{S} = \boldsymbol{A} : \boldsymbol{E} \tag{2.3}$$

with $\boldsymbol{A}$ is the fourth order stiffness tensor. If the material is also isotropic, only two constants are enough to define the constitutive equation:

$$\boldsymbol{S} = 2\mu\boldsymbol{E} + \lambda \mathrm{tr}(\boldsymbol{E})\boldsymbol{I} \tag{2.4}$$

with λ and μ, the two Lamé constants. They are related to the more common engineering quantities E_Y and ν, Young modulus and Poisson ratio respectively, through the following equalities:

$$\lambda = \frac{\nu E_Y}{(1-2\nu)(1+\nu)}, \qquad \mu = \frac{E_Y}{2(1+\nu)} \tag{2.5}$$

2.2.1 Finite Element Discretisation

The discretisation of the domain into finite elements permits to express the continuous displacement function $\boldsymbol{u}$ as a function of the discrete displacement $U^{(r)} \in \mathcal{R}$:

$$\boldsymbol{u}(\boldsymbol{X}, t) = \sum_r U^{(r)}(t)\boldsymbol{N}^{(r)}(\boldsymbol{X})\,. \tag{2.6}$$

Without going into the details of the choice of the shape functions, suffice to say that to deal with components with complex geometries, such as blades, the structure must be discretised with three dimensional finite elements. For this reason, all the considerations done in this thesis are finalised to the application of the studied methods to FE structures discretised with either tetrahedrons or hexahedrons. For this type of element, the shape functions $\boldsymbol{N}^{(r)} : \Omega_r \to \mathcal{R}^3$ are 3D functions that map the domain of the body Ω into $\mathcal{R}^3$. Each $\boldsymbol{N}^{(r)}$ has a portion of the domain Ω_r as a support and it is zero in the remainder of Ω; more specifically, such support is the volume of all the 3D elements containing the node whose displacement is $U^{(r)}$.

To be admissible, the shape functions must respect the Dirichlet boundary conditions given by:

$$\boldsymbol{e} \cdot \boldsymbol{u} = 0 \qquad \text{on } \Sigma_{\mathrm{D}}\,, \tag{2.7}$$

where Σ_D represents the portion of the boundary on which Dirichlet boundary conditions are imposed and $\boldsymbol{e}$ the direction on which the constraint is applied. In the FE solver, such condition can be enforced by either setting the relative degree of freedom to zero or by adding a reaction force as an unknown of the system in the form of a Lagrangian multiplier.

The virtual displacement $\delta\boldsymbol{u}$ is also expressed as a linear combination of the weighting functions and the virtual discrete displacements $\delta U^{(r)}$. Following the classical Galerkin method, such weighting functions coincide with the shape functions, leading to:

$$\delta\boldsymbol{u}(\boldsymbol{X},t) = \sum_r \delta U^{(r)}(t)\boldsymbol{N}^{(r)}(\boldsymbol{X})\,. \tag{2.8}$$

To derive an expression of the virtual work done by internal forces with respect to $U^{(r)}(t)$ and $\delta U^{(r)}(t)$, it is convenient to first express the virtual Green-Lagrangian strain tensor and the second Piola-Kirchhoff tensor in Einstein notation. For the sake of readability, let us limit the expansion of the tensors to their linear terms and denote them with the superscript L:

$$\delta E^{\mathrm{L}}_{ij} = \frac{1}{2}\left(\delta u_{i,j} + \delta u_{j,i}\right) \tag{2.9}$$

$$S^{\mathrm{L}}_{ij} = \mu\left(u_{i,j} + u_{j,i}\right) + \lambda\, u_{k,k}\,\delta_{ij}\,, \tag{2.10}$$

where δ_{ij} is the Kroneker delta and the notation $u_{i,j}$ stands for the derivatives of u_i with respect to X_j.

We are now able to express Eq. (2.1) in its discrete form. For each virtual displacement $\delta U^{(s)}$, one has:

$$\delta U^{(s)}\left(M^s_r\ddot{U}^{(r)} + K^s_r U^{(r)} = B_s + T_s\right) \tag{2.11}$$

with:

$$K^s_r = \frac{1}{2}\int_\Omega \left(\mu N^{(r)}_{i,j} + \mu N^{(r)}_{j,i} + \lambda N^{(r)}_{k,k}\,\delta_{ij}\right)\left(N^{(s)}_{i,j} + N^{(s)}_{j,i}\right)\,d\Omega \tag{2.12}$$

$$M^s_r = \int_\Omega \rho N^{(r)}_i N^{(s)}_i\,d\Omega \tag{2.13}$$

$$B_s = \int_\Omega b_i N^{(s)}_i\,d\Omega \tag{2.14}$$

$$T_s = \int_\Sigma t_i N^{(s)}_i\,d\Sigma \tag{2.15}$$

where the upper index s is used to denote the s-th row of each tensor. The same notation will be used for higher order tensors throughout this thesis.

Since Eq. (2.11) has to be verified for every value of the virtual displacement $\delta U^{(s)}$, it reduces to an algebraic system of equations and reads:

$$\boldsymbol{M}\ddot{\boldsymbol{U}} + \boldsymbol{K}\boldsymbol{U} = \boldsymbol{B} + \boldsymbol{T}\,. \tag{2.16}$$

Before moving to the definition of the nonlinear forces, the non-conservative linear terms that might appear in Eq. (2.16) must be first discussed. Inside the vector $\boldsymbol{B}$ of body forces, not only the external load but also centrifugal, gyroscopic, and viscous forces are included. The first two types of non-conservative forces are out of the scope of this thesis, therefore will not be treated here. As for the latter, they give rise to a damping term that makes the linear system of Eq. (2.16) become:

$$\boldsymbol{M}\ddot{\boldsymbol{U}} + \boldsymbol{C}\dot{\boldsymbol{U}} + \boldsymbol{K}\boldsymbol{U} = \boldsymbol{F}_{\text{ext}}\,, \tag{2.17}$$

where $\boldsymbol{C}$ is the damping matrix multiplying the velocity term $\dot{\boldsymbol{U}}$ and where the term $\boldsymbol{F}_{\text{ext}}$ includes the sole contribution of the external loads from body forces and surface tractions.

Before moving to the definition of nonlinear forces, it is necessary to remark that neglecting the effect of rotation is a strong assumption in the context of this thesis. However, most of the methods presented in this work could be extended to the case of gyroscopic and centrifugal forces with relatively little effort; this is considered as one of the future developments of this work as it will be discussed in the final Chapter.

As for the linear damping term, the assumption is less strong, in that it is common industry practice to treat the damping as a purely linear viscous term. Moreover, being the damping extremely difficult to predict with models and being its value small for metal structures, it is considered legitimate to assume that the damping matrix is in the simplest possible form, *i.e.* it is diagonalised by the eigenvectors of the conservative system [35]. Two of the most common types of damping for engineering structures are modal and Rayleigh damping; a modal damping matrix requires the knowledge of all the natural frequencies of the structure to be fully built, so in an industrial framework, it is only built for the first hundreds of modes of a blade, for example, and a Rayleigh damping is assumed for the higher modes. In the context of this thesis, a Rayleigh damping will be assumed in most of the testcases for its simplicity, and because the inclusion of modal damping in the methods presented would not affect the methodology *per se*.

2.2.2 Geometric Nonlinear Forces

Geometric nonlinearities are generated by the inclusion in the Green-Lagrangian strain tensor $\boldsymbol{E}$ of the quadratic component deriving from the term $\nabla \boldsymbol{u}^{\mathrm{T}} \cdot \nabla \boldsymbol{u}$. Quadratic components will then also appear in the second Piola-Kirchhoff $\boldsymbol{S}$ tensor, being it derived from $\boldsymbol{E}$. The full expression of both δE_{ij} and S_{ij}, is then the sum of the linear term given in Eq. (2.10) plus a quadratic term given by:

$$\delta E_{ij}^{\mathrm{Q}} = \frac{1}{2}\left(\delta u_{k,i}\, u_{k,j} + u_{k,i}\, \delta u_{k,j}\right) \tag{2.18}$$

$$S_{ij}^{\mathrm{Q}} = \mu\left(u_{k,i}\, u_{k,j}\right) + \frac{\lambda}{2} u_{k,l} u_{k,l} \delta_{ij}\,. \tag{2.19}$$

When plugged into Eq. (2.1), these terms produce two nonlinear terms in $\boldsymbol{U}$, a quadratic one and a cubic one, making the system of Eq. (2.17) become in the nonlinear case:

$$\boldsymbol{M}\ddot{\boldsymbol{U}} + \boldsymbol{C}\dot{\boldsymbol{U}} + \boldsymbol{K}\boldsymbol{U} + \boldsymbol{G}(\boldsymbol{U},\boldsymbol{U}) + \boldsymbol{H}(\boldsymbol{U},\boldsymbol{U},\boldsymbol{U}) = \boldsymbol{F}_{\text{ext}}\,, \tag{2.20}$$

where the functional notation for the quadratic and cubic terms can be expressed by means of a third-order tensor $G^s_{(rt)}$ and a fourth-order tensor $H^s_{(rtp)}$; the explicit indicial expressions of the functional notations read:

$$\boldsymbol{G}(\boldsymbol{U},\boldsymbol{U}) = \boldsymbol{G}_{(rt)} U^{(r)} U^{(t)} \tag{2.21}$$

$$\boldsymbol{H}(\boldsymbol{U},\boldsymbol{U},\boldsymbol{U}) = \boldsymbol{H}_{(rtp)} U^{(r)} U^{(t)} U^{(p)}\,, \tag{2.22}$$

and the explicit expression of the values of the coefficients of the tensors read:

$$\begin{aligned} G^s_{(rt)} = \frac{1}{2}\int_\Omega \left(\mu\left(N^{(r)}_{i,j} + N^{(r)}_{j,i}\right) + \lambda\, N^{(r)}_{k,k}\,\delta_{ij}\right)\left(N^{(s)}_{k,i}\, N^{(t)}_{k,j} + N^{(t)}_{k,i}\, N^{(s)}_{k,j}\right) d\Omega + \\ \frac{1}{2}\int_\Omega \left(\mu\left(N^{(r)}_{k,i}\, N^{(t)}_{k,j}\right) + \frac{\lambda}{2} N^{(r)}_{k,l} N^{(t)}_{k,l}\delta_{ij}\right)\left(N^{(s)}_{i,j} + N^{(s)}_{j,i}\right) d\Omega \end{aligned} \tag{2.23}$$

$$H^s_{(rtp)} = \frac{1}{2}\int_\Omega \left(\mu\left(N^{(r)}_{k,i}\, N^{(t)}_{k,j}\right) + \frac{\lambda}{2} N^{(r)}_{k,l} N^{(t)}_{k,l}\delta_{ij}\right)\left(N^{(s)}_{k,i}\, N^{(p)}_{k,j} + N^{(p)}_{k,i}\, N^{(s)}_{k,j}\right) d\Omega \tag{2.24}$$

2.2.3 Contact Forces

Contact forces [38, 83, 84, 177] are nonlinear boundary forces defined over a portion of the boundary Σ_C. Let us call Σ_C the potential contact zone as in [177]. For a given state of the system, Σ_C can be split into the active set $\bar{\Sigma}_C$ whose points are in contact and the inactive set $\Sigma_C \setminus \bar{\Sigma}_C$ whose points are not in contact.

The nonlinearity of contact forces stems from the fact that the contact conditions are state dependent. In particular, for each point belonging to the potential contact zone, a gap function defining the normal distance of the point from the contact surface can be derived:

$$g = \boldsymbol{u}\cdot\boldsymbol{e}_n + g_0 \tag{2.25}$$

where $\boldsymbol{e}_n$ the external normal of the contact surface, g the distance in actual configuration and g_0 that in reference configuration as shown in Fig. 2.2. Following this definition, for a given state, a point $\boldsymbol{X}$ is in the inactive set or in the active set based on the value of g:

$$\begin{cases} \boldsymbol{X} \in \bar{\Sigma}_C & \text{if } g \le 0 \\ \boldsymbol{X} \in \Sigma_C \setminus \bar{\Sigma}_C & \text{if } g > 0 \end{cases} \tag{2.26}$$

Since the contact conditions are defined by inequalities, contact forces are an unilateral constraint. However, on each subset of the potential contact zone, the contact conditions assume a simple form. In particular, in the inactive set, contact conditions assume the form

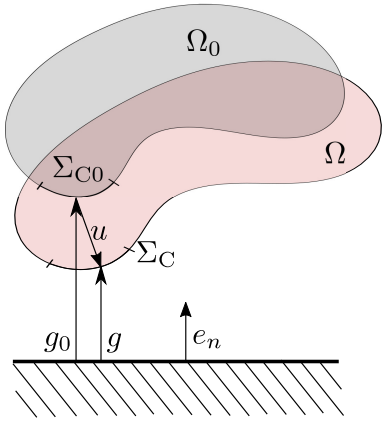


Figure 2.2: Definition of gap function for a point in the potential contact zone.

of Neumann boundary conditions; in the active set, contact conditions can either assume the form of Dirichlet boundary conditions if the contact surface impenetrable, or Robin boundary conditions if penetration is admitted.

When penetration of the contact surface is not allowed, they assume the form:

$$\begin{cases} g = 0 & \forall \boldsymbol{X} \in \bar{\Sigma}_C \\ t_n = 0 & \forall \boldsymbol{X} \in \Sigma_C \setminus \bar{\Sigma}_C, \end{cases} \tag{2.27}$$

with t_n reaction force exerted by the contact surface on the body directed along the direction of $\boldsymbol{e}_n$. These conditions are usually given in a more compact form through the Hertz-Signorini-Moreau conditions that read:

$$t_n \geq 0, \quad g \geq 0, \quad t_n g = 0 \tag{2.28}$$

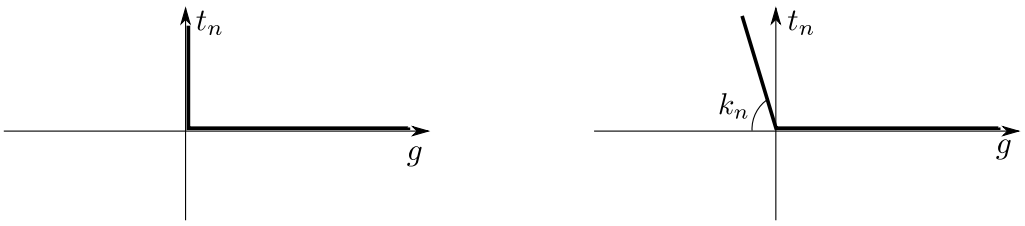
where the first inequality stems from the observation that the reaction force required to enforce the constraint $g = 0$ is always positive when the contact is active and zero when inactive; in a similar fashion, the second inequality states that for an impenetrable surface the distance cannot be negative; the last equality ensures that the two subsets are non-intersecting. The gap-force plot of this case is reported in Fig. 2.3a.

If the contact surface is elastic, penetration is allowed and the contact conditions assume the form:

$$\begin{cases} t_n = t_n(g, \dot{g}) & \forall \boldsymbol{X} \in \bar{\Sigma}_C \\ t_n = 0 & \forall \boldsymbol{X} \in \Sigma_C \setminus \bar{\Sigma}_C \,, \end{cases} \tag{2.29}$$

where $t_n(g, \dot{g})$ is a generic function that express the restoring force. In case of linear elastic restoring force, such condition coincides with a unilateral spring. The gap-force plot of this case is reported in Fig. 2.3b.

Such conditions are obtained for static problems. When dynamics is taken into account, if the contact surface is hard and penetration is not allowed, an impact law is needed to make



(a) Hard wall. (b) Linear elastic wall.

Figure 2.3: Normal contact conditions in case of hard or soft contact surface.

the problem well posed [83].

In case the contact surface is frictional, not only normal forces, but also tangential ones are generated when the set is active. In presence of friction, two states for the system are possible: stiction and sliding. The active set $\bar{\Sigma}_C$ must be then further split into the stiction set $\hat{\Sigma}_C$ and sliding set $\bar{\Sigma}_C \setminus \hat{\Sigma}_C$.

The contact conditions in the active set depend on the relative velocity between the two surfaces. For simplicity's sake, let us suppose that the relative motion is along a fixed direction defined by the unit vector $\boldsymbol{e}_t$. Introducing the tangential component of the friction force $t_t = \boldsymbol{t} \cdot \boldsymbol{e}_t$ and the tangential component of the relative velocity $v_t = \boldsymbol{v}_{rel} \cdot \boldsymbol{e}_t$, the contact conditions are expressed as:

$$\begin{cases} v_t = 0 & \forall \boldsymbol{X} \in \hat{\Sigma}_C \\ t_t = -\text{sign}[v_t]\, \mu t_n & \forall \boldsymbol{X} \in \bar{\Sigma}_C \setminus \hat{\Sigma}_C, \end{cases} \tag{2.30}$$

with μ friction coefficient. The relative velocity-force plot of this case is reported in Fig. 2.4a. Similarly to the Signorini conditions for the normal problem, the tangential conditions can be written in a more compact form through the Hertz-Kashun-Tucker conditions that reads:

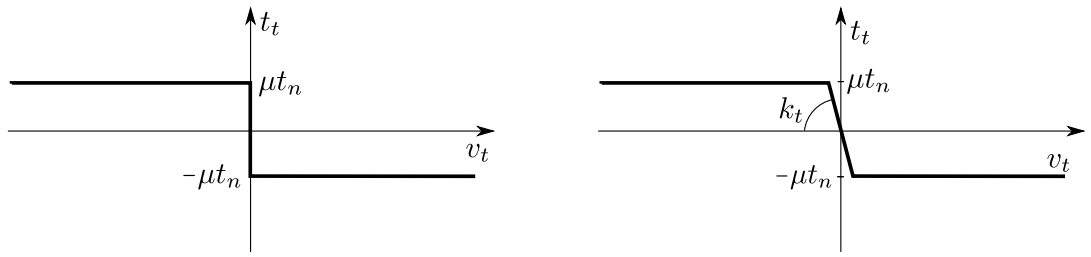
$$\|v_t\| \geq 0, \qquad \|t_t\| - \mu t_n \geq 0, \qquad \|v_t\|(\|t_t\| - \mu t_n) = 0 \tag{2.31}$$

Such conditions represent the pure Coulomb friction model. Many different dry-friction models have been developed and used depending on the problem at hand (see [38, 84] for a general overview). In tribological problems, the accuracy of the friction model is of crucial importance for a correct approximation of the underlying phenomena. Conversely, in dynamical problems, often a simple Coulomb is often enough to capture the overall behaviour of the system. A very common assumption used in dynamics is the one that leads to the regularised Coulomb model and consists in taking into account the tangential flexibility of the contact surface in the stiction set. In particular, if the contact surface is linear and elastic, it can be modelled as a bilateral spring with stiffness k_t. In such case, the

friction conditions read:

$$\begin{cases} t_t = -k_t v_t & \forall \boldsymbol{X} \in \hat{\Sigma}_C \\ t_t = -\text{sign}[v_t]\, \mu t_n & \forall \boldsymbol{X} \in \bar{\Sigma}_C \setminus \hat{\Sigma}_C, \end{cases} \tag{2.32}$$

The relative velocity-force plot of this case is reported in Fig. 2.4b.



(a) Pure Coulomb. (b) Regularised Coulomb.

Figure 2.4: Tangential contact conditions in case of hard or soft friction conditions.

For any given point $\boldsymbol{X} \in \Sigma_C$, normal and tangential contact forces will generate a boundary force $\boldsymbol{t} = \boldsymbol{t}(\boldsymbol{X}, \boldsymbol{u}, \boldsymbol{v})$ with a nonlinear relationship with the displacement and the velocity fields. Upon FE discretisation, such contact forces will then generate a nonlinear forcing term $\boldsymbol{T}_C = \boldsymbol{T}_C(\boldsymbol{U}_C, \dot{\boldsymbol{U}}_C)$ defined as:

$$T_C^s(\boldsymbol{U}_C, \dot{\boldsymbol{U}}_C) = \int_{\Sigma_C} t_i N_i^{(s)}\, d\Sigma_C \tag{2.33}$$

where the subscript C denotes the fact that the entries of $\boldsymbol{T}_C$ are non-zero only on the degrees of freedom belonging to Σ_C and they only depend on the displacement $\boldsymbol{U}_C$ and velocity $\dot{\boldsymbol{U}}_C$ of the degrees of freedom belonging to Σ_C.

Eq. (2.17) when contact forces are taken into account will then read:

$$\boldsymbol{M}\ddot{\boldsymbol{U}} + \boldsymbol{C}\dot{\boldsymbol{U}} + \boldsymbol{K}\boldsymbol{U} = \boldsymbol{F}_{\text{ext}} + \boldsymbol{T}_C(\boldsymbol{U}_C, \dot{\boldsymbol{U}}_C). \tag{2.34}$$

where the explicit dependence of the contact forces from the displacement and velocity used in the equation does not apply to the generic case, but it is only possible either in the regularised case, or if a primal method (for instance Nitsche method [103]) is used to eliminate the Lagrangian multipliers from the discretised equations.

2.2.4 Generic form of nonlinear FE discretised system

A compact form of a generic nonlinear system can be now formulated by including in a vector of nonlinear forces both the geometrically nonlinear restoring forces and the contact ones. The most classical form of such system is given in the configuration space and reads:

$$\boldsymbol{M}\ddot{\boldsymbol{U}} + \boldsymbol{C}\dot{\boldsymbol{U}} + \boldsymbol{K}\boldsymbol{U} = \boldsymbol{F}_{\text{ext}} + \boldsymbol{F}_{\text{NL}}(\boldsymbol{U}, \dot{\boldsymbol{U}}). \tag{2.35}$$

Equivalently, the system of Eq.(2.35) can be reformulated in the phase space when the velocity variable $\boldsymbol{V}$ is introduced and reads:

$$\begin{bmatrix} \boldsymbol{M} & \boldsymbol{0} \\ \boldsymbol{0} & \boldsymbol{I} \end{bmatrix} \begin{Bmatrix} \dot{\boldsymbol{V}} \\ \dot{\boldsymbol{U}} \end{Bmatrix} = \begin{bmatrix} -\boldsymbol{C} & -\boldsymbol{K} \\ \boldsymbol{I} & \boldsymbol{0} \end{bmatrix} \begin{Bmatrix} \boldsymbol{V} \\ \boldsymbol{U} \end{Bmatrix} + \begin{Bmatrix} \boldsymbol{F}_{\text{ext}} + \boldsymbol{F}_{\text{NL}}(\boldsymbol{U}, \boldsymbol{V}) \\ \boldsymbol{0} \end{Bmatrix}. \tag{2.36}$$

If the mass matrix is invertible, the system can be written in the more compact form:

$$\dot{\boldsymbol{Y}} = \boldsymbol{A}(\boldsymbol{Y}) \tag{2.37}$$

with:

$$\boldsymbol{Y} = \begin{Bmatrix} \boldsymbol{V} \\ \boldsymbol{U} \end{Bmatrix}. \tag{2.38}$$

These two forms will be referred to in the following if the nature of the nonlinear force is not specified.

2.2.5 Modal coordinates

In some cases, the system is required to be in modal coordinates for the reduction methods to be applied. To transform the system from its physical basis to its modal basis, the generalised eigenvalue problem has to be solved. A linear system with no forcing nor damping terms has the form:

$$\boldsymbol{M}\ddot{\boldsymbol{U}} + \boldsymbol{K}\boldsymbol{U} = \boldsymbol{0} \tag{2.39}$$

where both $\boldsymbol{M}$ and $\boldsymbol{K}$ are symmetric and positive definite matrices. The generalised eigenvalue problem associated to it, reads:

$$(-\omega_k^2 \boldsymbol{M} + \boldsymbol{K})\phi_k = \boldsymbol{0} \tag{2.40}$$

and permits to find all the eigenmodes, *i.e.* the couples natural frequency-eigenvectors $(\omega_k - \phi_k)$ that diagonalise the mass and stiffness matrices. If one disposed of all the N eigenmodes, with N number of degrees of freedom of the system, one could define the full eigenvectors matrix $\boldsymbol{\Phi}$ by assembling a square matrix whose columns are all the vectors ϕ_k and also the full eigenvalues matrix $\boldsymbol{\Omega}$ by assembling a diagonal matrix whose elements on the diagonal are all the corresponding natural frequencies ω_k. The diagonalisation would then read:

$$\boldsymbol{\Phi}^{\mathrm{T}} \boldsymbol{M} \boldsymbol{\Phi} = \boldsymbol{I} \tag{2.41}$$

$$\boldsymbol{\Phi}^{\mathrm{T}} \boldsymbol{K} \boldsymbol{\Phi} = \boldsymbol{\Omega}^2 \tag{2.42}$$

and by operating the linear change of coordinates:

$$\boldsymbol{U} = \boldsymbol{\Phi}\boldsymbol{q} \tag{2.43}$$

the system of Eq. (2.39) could be decoupled:

$$\ddot{\boldsymbol{q}} + \boldsymbol{\Omega}^2 \boldsymbol{q} = \boldsymbol{0} \tag{2.44}$$

Thanks to their decoupled nature, the newly defined coordinates q_k are independent to one another. Such coordinates are referred to as modal amplitudes in that they represent the response of each eigenmode.

In presence of damping, if the damping matrix is not diagonalised by the change of coordinates, the eigenvectors of the conservative system differ from those of the non-conservative one. However, in engineering applications, it is common to assume Rayleigh damping that is to say that the damping matrix is either mass proportional, stiffness proportional, or a combination of them [35]:

$$\boldsymbol{C} = \zeta_{\mathrm{M}} \boldsymbol{M} + \zeta_{\mathrm{K}} \boldsymbol{K} \,. \tag{2.45}$$

The non conservative system with damping and forcing in modal form will then read:

$$\ddot{\boldsymbol{q}} + (\zeta_{\mathrm{M}} \boldsymbol{I} + \zeta_{\mathrm{K}} \boldsymbol{\Omega}^2) \dot{\boldsymbol{q}} + \boldsymbol{\Omega}^2 \boldsymbol{q} = \boldsymbol{f} \tag{2.46}$$

with $\boldsymbol{f} = \boldsymbol{\Phi}^{\mathrm{T}} \boldsymbol{F}$ modal forcing obtained by projection.

Being in a polynomial form, the geometric nonlinear forces can be also more easily transformed in modal basis. If contact forces are not present, the nonlinear force vector in physical basis reads:

$$\boldsymbol{F}_{\mathrm{NL}}(\boldsymbol{U}) = -\boldsymbol{G}(\boldsymbol{U}, \boldsymbol{U}) - \boldsymbol{H}(\boldsymbol{U}, \boldsymbol{U}, \boldsymbol{U}) = -\boldsymbol{G}_{(rs)} U^{(r)} U^{(s)} - \boldsymbol{H}_{(rst)} U^{(r)} U^{(s)} U^{(t)} \tag{2.47}$$

Its modal basis projection reads:

$$\boldsymbol{f}_{\mathrm{NL}}(\boldsymbol{q}) = -\boldsymbol{\Phi}^{\mathrm{T}} \boldsymbol{G}(\boldsymbol{\Phi q}, \boldsymbol{\Phi q}) - \boldsymbol{\Phi}^{\mathrm{T}} \boldsymbol{H}(\boldsymbol{\Phi q}, \boldsymbol{\Phi q}, \boldsymbol{\Phi q}). \tag{2.48}$$

By defining $\boldsymbol{g}$ and $\boldsymbol{h}$ as the nonlinear tensor in modal basis, Eq. (2.48) can be written in the more compact form:

$$\boldsymbol{f}_{\mathrm{NL}}(\boldsymbol{q}) = -\boldsymbol{gqq} - \boldsymbol{hqqq} = -\boldsymbol{g}_{ij} q_i q_j - \boldsymbol{h}_{ijk} q_i q_j q_k \tag{2.49}$$

To relate the quadratic and cubic tensors in physical basis to those in modal basis, it is necessary to expand the term $\boldsymbol{\Phi q}$ into the sum of all eigenvectors multiplied by their modal amplitudes:

$$\boldsymbol{\Phi q} = \boldsymbol{\phi}_i q_i, \tag{2.50}$$

and substitute this sum into Eq. (2.48). By doing so, one obtains:

$$\boldsymbol{\Phi}^{\mathrm{T}}\boldsymbol{G}(\boldsymbol{\Phi q},\boldsymbol{\Phi q}) = \boldsymbol{\Phi}^{T}\boldsymbol{G}_{(rs)}\ \phi_i^{(r)} q_i\ \phi_j^{(s)} q_j = \boldsymbol{\Phi}^{T}\boldsymbol{G}(\phi_i,\phi_j)\ q_i q_j \tag{2.51a}$$

$$\boldsymbol{\Phi}^{\mathrm{T}}\boldsymbol{H}(\boldsymbol{\Phi q},\boldsymbol{\Phi q},\boldsymbol{\Phi q}) = \boldsymbol{\Phi}^{T}\boldsymbol{H}_{(rst)}\ \phi_i^{(r)} q_i\ \phi_j^{(s)} q_j\ \phi_k^{(t)} q_k = \boldsymbol{\Phi}^{T}\boldsymbol{H}(\phi_i,\phi_j,\phi_k)\ q_i q_j q_k. \tag{2.51b}$$

where the last simplification comes from the rearrangement of summations made in order to isolate the modal amplitudes. Finally, comparing the RHS of Eqs. (2.51) with that of Eq.(2.49), one finds the definition of the nonlinear tensors in modal basis:

$$\boldsymbol{g}_{ij} \doteq \boldsymbol{\Phi}^{T}\boldsymbol{G}(\phi_i,\phi_j) \tag{2.52a}$$

$$\boldsymbol{h}_{ijk} \doteq \boldsymbol{\Phi}^{T}\boldsymbol{H}(\phi_i,\phi_j,\phi_k). \tag{2.52b}$$

One must notice that the subscripts of the tensors $\boldsymbol{G}_{(rt)}$ and $\boldsymbol{H}_{(rtp)}$ are denoted with brackets because the indexes are here referred to the physical degrees of freedom. The entries of $\boldsymbol{G}$ and $\boldsymbol{H}$ with respect to the degrees of freedom are not of great interests. For this reason, we chose to keep the notation without brackets to denote the following quantities, of much greater interest for the future developments in this dissertation:

$$\boldsymbol{G}_{ij} \doteq \boldsymbol{G}(\phi_i,\phi_j) \tag{2.53a}$$

$$\boldsymbol{H}_{ijk} \doteq \boldsymbol{H}(\phi_i,\phi_j,\phi_k). \tag{2.53b}$$

The generic form of the system written in modal coordinates finally reads:

$$\ddot{\boldsymbol{q}} + \boldsymbol{\Xi}\dot{\boldsymbol{q}} + \boldsymbol{\Omega}^2\boldsymbol{q} + \boldsymbol{g}\boldsymbol{q}\boldsymbol{q} + \boldsymbol{h}\boldsymbol{q}\boldsymbol{q}\boldsymbol{q} = \boldsymbol{f}_{\text{ext}} + \boldsymbol{t}(\boldsymbol{q},\dot{\boldsymbol{q}}) \tag{2.54}$$

where the matrix $\boldsymbol{\Xi} = \boldsymbol{\Phi}^{\mathrm{T}}\boldsymbol{C}\boldsymbol{\Phi}$ that represent the generic damping matrix in modal coordinates is assumed to be diagonal. As discussed in [35], since in typical engineering structures the damping is very small, the hypothesis of damping matrix diagonalised by the modal coordinates is acceptable even if the damping matrix is not in the Rayleigh form.

As per the contact forces, not much attention has been paid to their transformation in modal coordinates because they are usually treated in physical basis directly. This is not the case for geometric nonlinear forces for which the modal basis is usually a preferred starting point, especially for structures with a relatively low number of degrees of freedom for which the full eigenvector matrix can be computed easily or for simple structures like beam and plates for which the discretisation is not done with finite elements but rather with geometrically exact theories [149]. The calculation of the tensors $\boldsymbol{g}$ and $\boldsymbol{h}$ can be done analytically in the latter case; conversely in the case of FE discretised structures, $\boldsymbol{g}$ and $\boldsymbol{h}$ have to be extracted from the FE software. This is possible to do, in a non-intrusive manner, by means of the stiffness evaluation procedure (StEP) that will be described in the next section.

2.2.6 Stiffness Evaluation Procedure

The linear parameters $\boldsymbol{\Omega}^2, \boldsymbol{\Phi}$ are easily obtained by modal analysis, available in any finite element code. The main issue is thus to compute the nonlinear coupling coefficients $\boldsymbol{g}$ and $\boldsymbol{h}$ in a non-intrusive manner from a commercial FE software. The StEP (Stiffness Evaluation Procedure) first introduced by Muravyov and Rizzi [97] is a non-intrusive method, allowing one to get these coupling coefficients from standard computations. The procedure consists in imposing a series of static displacements having the shapes of a linear mode and combinations of linear modes, and then extract the internal nonlinear forces arising in the structure. The main goal of the method, as originally proposed in [97], is to convert the original system from physical basis to modal basis, and to build a reduced order model composed of the sole linear modes of interest. However, due to the strong nonlinear couplings between modes, the original idea of the method cannot be applied in practice unless all the modes nonlinearly coupled with those of interest are also included in the reduced model. On the other hand, the StEP method provides an important basis for non-intrusive calculations. The problem of non-intrusiveness is indeed crucial because commercial FE software, widely used in industry, do not normally allow access to the elemental functions but they only provide the resulting output of a given computation. In this work, the StEP method will not be used to build a reduced order model, but rather as an efficient procedure to extract important coupling coefficients in a non-intrusive manner from a generic FE software. It will be shown, for example, that the same procedure can be used with other basis vectors than the linear modes, allowing to build more efficient ROMs non-intrusively. The presentation of the method will be now detailed as proposed in [97], and its extension to other bases will be treated separately (e.g. in Chapter 5).

Let us assume that one is interested in the value of the coefficients $\boldsymbol{g}_{ii}$ and $\boldsymbol{h}_{iii}$. If the following static displacements is prescribed to the structure:

$$\boldsymbol{U}_i = \lambda_i \boldsymbol{\phi}_i \quad \Rightarrow \quad \begin{cases} q_i = \lambda_i, \\ q_r = 0 \quad \forall r \neq i, \end{cases}, \tag{2.55}$$

since the modes are orthogonal, imposing a displacement along mode i is equivalent to consider that only the modal coordinate q_i is not vanishing. Here λ_i refers to the modal amplitude of the eigenvector $\boldsymbol{\phi}_i$ whose value has to be chosen so as to activate the geometrical nonlinearities. A value of λ_i such that the maximum value of the displacement vector $\lambda_i \boldsymbol{\phi}_i$ is $h/20$, with h being the thickness of the structure, is recommended in [36] in the case of clamped-clamped beams and plates.

Two static displacement have then to be imposed on the structure, with values respectively $\boldsymbol{U}_+ = \lambda_i \boldsymbol{\phi}_i$ and $\boldsymbol{U}_- = -\lambda_i \boldsymbol{\phi}_i$. The forces generated in the structure computed in the

software with the assumption of nonlinear behaviour are:

$$-\boldsymbol{F}(\boldsymbol{U}_+) = +\lambda_i \boldsymbol{K}\boldsymbol{\phi}_i + \lambda_i^2 \boldsymbol{G}(\boldsymbol{\phi}_i, \boldsymbol{\phi}_i) + \lambda_i^3 \boldsymbol{H}(\boldsymbol{\phi}_i, \boldsymbol{\phi}_i, \boldsymbol{\phi}_i), \tag{2.56a}$$

$$-\boldsymbol{F}(\boldsymbol{U}_-) = -\lambda_i \boldsymbol{K}\boldsymbol{\phi}_i + \lambda_i^2 \boldsymbol{G}(\boldsymbol{\phi}_i, \boldsymbol{\phi}_i) - \lambda_i^3 \boldsymbol{H}(\boldsymbol{\phi}_i, \boldsymbol{\phi}_i, \boldsymbol{\phi}_i). \tag{2.56b}$$

whereas those computed with the assumption of linear behaviour are simply $-\boldsymbol{F}(\boldsymbol{U}_\pm) = \pm\lambda_i \boldsymbol{K}\boldsymbol{\phi}_i$. The purely nonlinear component can be then extracted by difference and reads:

$$-\boldsymbol{F}_{\mathrm{NL}}(\boldsymbol{U}_+) = +\lambda_i^2 \boldsymbol{G}_{ii} + \lambda_i^3 \boldsymbol{H}_{iii}, \tag{2.57a}$$

$$-\boldsymbol{F}_{\mathrm{NL}}(\boldsymbol{U}_-) = +\lambda_i^2 \boldsymbol{G}_{ii} - \lambda_i^3 \boldsymbol{H}_{iii}. \tag{2.57b}$$

where the notation introduced in Eq. (2.53), where the subscripts denote the modal component of $\boldsymbol{G}$ and $\boldsymbol{H}$, has been used. Moreover, the contribution of the quadratic and cubic forces can be separated by computing:

$$-\boldsymbol{F}_{\mathrm{NL}}(\boldsymbol{U}_+) - \boldsymbol{F}_{\mathrm{NL}}(\boldsymbol{U}_-) = 2\,\lambda_i^2 \boldsymbol{G}_{ii}, \tag{2.58a}$$

$$-\boldsymbol{F}_{\mathrm{NL}}(\boldsymbol{U}_+) + \boldsymbol{F}_{\mathrm{NL}}(\boldsymbol{U}_-) = 2\,\lambda_i^3 \boldsymbol{H}_{iii}. \tag{2.58b}$$

Finally, being the full matrix of eigenvectors available in the considered case, the vectors $\boldsymbol{g}_{ii}$ and $\boldsymbol{h}_{iii}$ can be found by projection using Eq. (2.52).

The first step of the procedure consists in finding all the vectors $\boldsymbol{G}_{ii}$ and $\boldsymbol{H}_{iii}$ with equal indexes for all the modes. The second step is to find the vectors $\boldsymbol{G}_{ij}$, $\boldsymbol{H}_{iij}$ and $\boldsymbol{H}_{ijj}$, relative to the combination of two modes. To extract the sought vectors, three combinations of the two modes are needed; for example if one imposes $\boldsymbol{U}_{++} = \lambda_i\boldsymbol{\phi}_i + \lambda_j\boldsymbol{\phi}_j$, $\boldsymbol{U}_{--} = -\lambda_i\boldsymbol{\phi}_i - \lambda_j\boldsymbol{\phi}_j$, and $\boldsymbol{U}_{+-} = \lambda_i\boldsymbol{\phi}_i - \lambda_j\boldsymbol{\phi}_j$, then the values of $\boldsymbol{G}_{ij}$, $\boldsymbol{H}_{iij}$ and $\boldsymbol{H}_{ijj}$ can be calculated from:

$$4\lambda_i\lambda_j\boldsymbol{G}_{ij} = -\boldsymbol{F}_{\mathrm{NL}}(\boldsymbol{U}_{++}) - \boldsymbol{F}_{\mathrm{NL}}(\boldsymbol{U}_{--}) - 2\,\lambda_i^2\boldsymbol{G}_{ii} - 2\,\lambda_j^2\boldsymbol{G}_{jj} \tag{2.59a}$$

$$6\lambda_i^2\lambda_j\boldsymbol{H}_{iij} = +\boldsymbol{F}_{\mathrm{NL}}(\boldsymbol{U}_{+-}) + \boldsymbol{F}_{\mathrm{NL}}(\boldsymbol{U}_{--}) + 2\,\lambda_i^2\boldsymbol{G}_{ii} + 2\,\lambda_j^2\boldsymbol{G}_{jj} - 2\,\lambda_j^3\boldsymbol{H}_{jjj} \tag{2.59b}$$

$$6\lambda_i\lambda_j^2\boldsymbol{H}_{ijj} = -\boldsymbol{F}_{\mathrm{NL}}(\boldsymbol{U}_{++}) - \boldsymbol{F}_{\mathrm{NL}}(\boldsymbol{U}_{+-}) - 2\,\lambda_i^2\boldsymbol{G}_{ii} - 2\,\lambda_j^2\boldsymbol{G}_{jj} - 2\,\lambda_i^3\boldsymbol{H}_{iii} \tag{2.59c}$$

where the previously calculated same indexes vectors are used.

In the third and final step, the value of $\boldsymbol{H}_{ijk}$ is found by simply imposing the displacement $\boldsymbol{U}_{+++} = \lambda_i\boldsymbol{\phi}_i + \lambda_j\boldsymbol{\phi}_j + \lambda_i\boldsymbol{\phi}_k$ from:

$$\begin{aligned} 24\lambda_i\lambda_j\boldsymbol{H}_{ijk} = {} & -6\boldsymbol{F}_{\mathrm{NL}}(\boldsymbol{U}_{+++}) - 4\,\lambda_i^2\boldsymbol{G}_{ii} - 4\,\lambda_j^2\boldsymbol{G}_{jj} - 4\,\lambda_k^2\boldsymbol{G}_{kk} + \\ & - 8\,\lambda_i\lambda_j\boldsymbol{G}_{ij} - 8\,\lambda_i\lambda_k\boldsymbol{G}_{ik} - 8\,\lambda_j\lambda_k\boldsymbol{G}_{jk} - 4\,\lambda_i^3\boldsymbol{H}_{iii} - 4\,\lambda_j^3\boldsymbol{H}_{jjj} - 4\,\lambda_k^3\boldsymbol{H}_{kkk} + \\ & - 4\,\lambda_i^2\lambda_j\boldsymbol{H}_{iij} - 4\,\lambda_i\lambda_j^2\boldsymbol{H}_{ijj} - 4\,\lambda_i^2\lambda_k\boldsymbol{H}_{iik} - 4\,\lambda_i\lambda_k^2\boldsymbol{H}_{ikk} - 4\,\lambda_j^2\lambda_k\boldsymbol{H}_{jjk} - 4\,\lambda_j\lambda_k^2\boldsymbol{H}_{jkk} \end{aligned} \tag{2.60}$$

The geometric nonlinear forces in modal coordinates can be then finally obtained by projection of all the found vectors $\boldsymbol{G}$ and $\boldsymbol{H}$. One must notice that for each combination of

more than one mode, not all the values of $\boldsymbol{G}$ and $\boldsymbol{H}$ have been calculated; in fact, the value of $\boldsymbol{G}_{ij}$ for example is equal to $\boldsymbol{G}_{ji}$ as well as for example $\boldsymbol{H}_{ijk} = \boldsymbol{H}_{kji}$ and all other permutations. This property of symmetry stems directly from the symmetry of the tensors and derives from the fact that, being the nonlinear restoring forces derived from a potential, the symmetry of partial derivatives has to be verified. Another symmetry property less intuitive but also present and demonstrated in [97], is the symmetry between:

$$\boldsymbol{\phi}_k^{\mathrm{T}} \boldsymbol{G}_{ij} = \boldsymbol{\phi}_i^{\mathrm{T}} \boldsymbol{G}_{jk} \tag{2.61}$$

from which directly stems the following property on $\boldsymbol{g}$:

$$\boldsymbol{g}_{ij}^{k} = \boldsymbol{g}_{jk}^{i} \tag{2.62}$$

where the superscript is referred to the row number. The same property is verified by the tensor $\boldsymbol{h}$.

It is worth mentioning that, if the tangent stiffness matrix is accessible from the FE software, the number of computations could be further reduced by replacing the evaluation of nonlinear forces with that of the nonlinear tangent stiffness matrix, as proposed in [110]. Denoting with $\dfrac{\partial \boldsymbol{F}_{\mathrm{NL}}}{\partial \boldsymbol{U}}$ the nonlinear component of the tangent stiffness matrix, one could obtain all the vectors in only two steps. The first one that reads:

$$-\left.\frac{\partial \boldsymbol{F}_{\mathrm{NL}}}{\partial \boldsymbol{U}}\right|_{\boldsymbol{U}=+\lambda_i\boldsymbol{\phi}_i} \cdot \boldsymbol{\phi}_j = +\lambda_i \boldsymbol{G}_{ij} + \lambda_i^2 \boldsymbol{H}_{iij}, \tag{2.63a}$$

$$-\left.\frac{\partial \boldsymbol{F}_{\mathrm{NL}}}{\partial \boldsymbol{U}}\right|_{\boldsymbol{U}=-\lambda_i\boldsymbol{\phi}_i} \cdot \boldsymbol{\phi}_j = -\lambda_i \boldsymbol{G}_{ij} + \lambda_i^2 \boldsymbol{H}_{iij}. \tag{2.63b}$$

and that provides all the vectors $\boldsymbol{G}_{ii}$, $\boldsymbol{H}_{iii}$, $\boldsymbol{G}_{ij}$, $\boldsymbol{H}_{iij}$, and $\boldsymbol{H}_{ijj}$ for all the modes. The second step that reads:

$$-\left.\frac{\partial \boldsymbol{F}_{\mathrm{NL}}}{\partial \boldsymbol{U}}\right|_{\boldsymbol{U}=+\lambda_i\boldsymbol{\phi}_i+\lambda_j\boldsymbol{\phi}_j} \cdot \boldsymbol{\phi}_k = +\lambda_i \boldsymbol{G}_{ik} + \lambda_j \boldsymbol{G}_{jk} + \lambda_i^2 \boldsymbol{H}_{iik} + 2\lambda_i\lambda_j \boldsymbol{H}_{ijk} + \lambda_j^2 \boldsymbol{H}_{jjk}, \tag{2.64}$$

from which the $\boldsymbol{H}_{ijk}$ vectors can be deduced, being the only unknown of the equation. In this way, the third step of the classical StEP procedure is avoided; the third step is the most cumbersome one, in that it involves a number of forces evaluations that scales as the cubic power of the number of modes, so when a high number of modes is required, the speed-up provided by the use of the tangent stiffness is relevant. However, this speed-up comes at the expenses of the cost of storing the matrix before its projection onto the modes, so for a low number of modes, the classical StEP might be preferable. This consideration is not treated in [110] because the method was derived to be applied to all the modes of the structure.

Despite the reduction in the number of computations introduced by the symmetry or/and

the access to the tangent stiffness matrix, the application of the StEP method on all the modes of a large structure would still be infeasible due to the too high number of static computations required. However, it will be seen that this method is still very useful when coupled with model order reduction.

2.3 Model Order Reduction

The model obtained by FE discretisation is too large to be studied as it is. Moreover, only some of its features are of interest from an engineering perspective. Being the aim of reduced order modelling to reduce the number of unknowns of the model whilst maintaining the accuracy, each reduced model aims at decoupling the dominant features from the negligible ones so that the latter can be neglected.

For example, low frequency modes are normally more excited and less damped than very high frequency ones, thus making them the best candidates for reduction. For linear systems, the reduction on only some modes is what is done with modal analysis which can be seen as the simplest and most common form of model reduction. In modal analysis, only the modes of interest, usually the low frequency modes or the modes in the frequency band of the excitation frequency, are retained thus reducing the degrees of freedom of the system from many to few.

Such approach however, cannot be simply applied to nonlinear systems because the nonlinearities usually couple the modes, and other strategies must be adopted. Depending on which type of nonlinearity is present in the system, if distributed or localised, different approaches are available. Distributed nonlinearities are cumbersome to reduce because they affect all the degrees of freedom of the system. Despite being distributed, geometric nonlinearities have the advantage of being in the form of polynomials, hence they can be treated with perturbation or asymptotic expansion methods. Localised nonlinearities, on the other hand, affect only some nodes but in the case of contact they are defined in a piecewise linear or non-smooth manner. An overview of reduced order modelling methods that will be treated in this dissertation is presented in the following sections.

Generally speaking, each reduction method operates a *change of coordinates* that aims at reducing the number of DOFs of the original system and obtains a *reduced dynamics* system of equations of reduced dimension. In order to reduce the number of DOFs, a generic method for reduced order modelling (ROM) is a method that approximates the displacement vector $\boldsymbol{U}$ of size N with a smaller vector $\boldsymbol{\eta}$ of size $n \ll N$ by means of the said change of coordinates:

$$\boldsymbol{U} \approx \tilde{\boldsymbol{U}}(\boldsymbol{\eta})\,. \tag{2.65}$$

The distinction between linear and nonlinear methods depend on the nature of the dependency of $\boldsymbol{U}$ from $\boldsymbol{\eta}$, which, if nonlinear, it is also referred to as *nonlinear mapping*.

In linear reduction methods, said change of coordinates is instead simply obtained by the product of a reduction matrix $\boldsymbol{R}$ of size $N \times n$ and the reduced coordinates vector:

$$\tilde{\boldsymbol{U}}(\boldsymbol{\eta}) = \boldsymbol{R}\boldsymbol{\eta} \tag{2.66}$$

followed by a projection of the equation of motion onto the reduced space. If the method is a Galerkin method, such projection is performed on the same matrix $\boldsymbol{R}$. The reduced dynamics of the generic system of Eq. (2.35) will then read:

$$\boldsymbol{R}^{\mathrm{T}}\boldsymbol{M}\boldsymbol{R}\,\ddot{\boldsymbol{\eta}} + \boldsymbol{R}^{\mathrm{T}}\boldsymbol{C}\boldsymbol{R}\,\dot{\boldsymbol{\eta}} + \boldsymbol{R}^{\mathrm{T}}\boldsymbol{K}\boldsymbol{R}\,\boldsymbol{\eta} = \boldsymbol{R}^{\mathrm{T}}\boldsymbol{F}_{\mathrm{ext}} + \boldsymbol{R}^{\mathrm{T}}\boldsymbol{F}_{\mathrm{NL}}(\boldsymbol{R}\boldsymbol{\eta})\,. \tag{2.67}$$

Some nonlinear reduction methods like implicit condensation and quadratic manifold can as well fall into the category of projection methods in that the projection is executed on the tangent space around the equilibrium position:

$$\boldsymbol{\Gamma}(\boldsymbol{\eta}) = \left.\frac{\partial\tilde{\boldsymbol{U}}(\boldsymbol{\eta})}{\partial\boldsymbol{\eta}}\right|_{\boldsymbol{\eta}_0}\,. \tag{2.68}$$

The reduced dynamics equation in this case will then read:

$$\boldsymbol{\Gamma}^{\mathrm{T}}\boldsymbol{M}\ddot{\tilde{\boldsymbol{U}}} + \boldsymbol{\Gamma}^{\mathrm{T}}\boldsymbol{C}\dot{\tilde{\boldsymbol{U}}} + \boldsymbol{\Gamma}^{\mathrm{T}}\boldsymbol{K}\tilde{\boldsymbol{U}} = \boldsymbol{\Gamma}^{\mathrm{T}}\boldsymbol{F}_{\mathrm{ext}} + \boldsymbol{\Gamma}^{\mathrm{T}}\boldsymbol{F}_{\mathrm{NL}}(\tilde{\boldsymbol{U}})\,. \tag{2.69}$$

Conversely, invariant manifold methods avoid this projection by assuming the reduced dynamics form to be known a priori. Being them derived from the system written in first order formulation (see Eq. (2.37)), they share a common structure that can be summarised by the following steps. The first step is to assume a form for the nonlinear mapping in the generalised coordinates $\boldsymbol{Y}$ as a function of the invariant manifold coordinates $\boldsymbol{\eta}$:

$$\boldsymbol{Y} \approx \tilde{\boldsymbol{Y}}(\boldsymbol{\eta})\,. \tag{2.70}$$

Then, assume a form for the reduced dynamics on the manifold:

$$\dot{\boldsymbol{\eta}} = \boldsymbol{r}(\boldsymbol{\eta}) \tag{2.71}$$

and substitute them into the full equation of motion by noticing that:

$$\dot{\tilde{\boldsymbol{Y}}} = \frac{\partial\tilde{\boldsymbol{Y}}(\boldsymbol{\eta})}{\partial\boldsymbol{\eta}}\dot{\boldsymbol{\eta}} \tag{2.72}$$

Finally the nonlinear mapping $\tilde{\boldsymbol{Y}}$ and the reduced dynamics $\boldsymbol{r}$ will have to verify the equation of motion:

$$\frac{\partial\tilde{\boldsymbol{Y}}}{\partial\boldsymbol{\eta}}\boldsymbol{r} = \boldsymbol{A}(\tilde{\boldsymbol{Y}}) \tag{2.73}$$

Since the form of the mapping and of the reduced dynamics is not straightforward to guess

in the general case, this class of methods is normally applied to polynomial nonlinearities, such as geometric nonlinearities; in such case both $\tilde{\boldsymbol{Y}}$ and $\boldsymbol{r}$ are polynomials in $\boldsymbol{\eta}$ and and the balance expressed in Eq. (2.73) is performed in an asymptotic manner by balancing polynomials of increasing order.

A more detailed derivation of the methods that will be relevant for this dissertation is provided in the following subsections.

2.3.1 Reduction on Linear Modes

The simplest possible reduced order model one can build is the one obtained by modal analysis. If the system is linear, modal coordinates can diagonalise the system thus making every equation independent. A reduced order model can be then built by assuming that only some modes respond to a given forcing and that the displacement will be composed solely of those modes.

The actual change of coordinates operated by modal analysis will then have the linear reduction matrix of Eq. (2.66) equal to:

$$\boldsymbol{R} = \begin{bmatrix} \boldsymbol{\phi}_{M_1} & \boldsymbol{\phi}_{M_2} & \cdots & \boldsymbol{\phi}_{M_n} \end{bmatrix} \tag{2.74}$$

with $\boldsymbol{\phi}_{M_i}$ corresponding to the selected modes. As for the reduced dynamics, it will simply be equivalent to the M_i rows of Eqs. (2.46).

When nonlinearities are present though, the nonlinear forces introduce couplings between the modes. Focusing in particular on geometric nonlinearities, one can write the equation of motion in modal coordinates to better highlight the role of these couplings. Let us assume that only one mode, the p-th, receives a forcing and it is excited in the vicinity of its resonance. The equation of motion written by components and isolating the excited mode from the others read:

$$\ddot{q}_p + \xi_p \dot{q}_p + \omega_p^2 q_p + g_{ij}^p q_i q_j + h_{ijk}^p q_i q_j q_k = f_{\text{ext}}^p \tag{2.75a}$$

$$\ddot{q}_r + \xi_r \dot{q}_r + \omega_r^2 q_r + g_{ij}^r q_i q_j + h_{ijk}^r q_i q_j q_k = 0 \tag{2.75b}$$

Since the modal amplitude of the mode p is surely nonzero because of the forcing it receives, if the term q_p appears in another equation, it will produce a forcing-like term on that mode. Despite Eq. (2.75b) does not have any linear term in q_p, nonlinear ones can appear. In fact, if the terms g_{pp}^r and h_{ppp}^r are nonzero, in the equation of the r-th mode there will be terms proportional to q_p^2 and q_p^3 respectively. The terms g_{pp}^r and h_{ppp}^r are for this reason called invariant breaking terms because they break the invariance of the modal transformation.

Due to these terms, a reduced model composed of the sole mode p would lead to very wrong results. Only if the *coupled* modes are included in the reduced model the correct

behaviour can be retained. More details on this problem will be discussed extensively in Chapter 3.

2.3.2 Hurty/Craig-Bampton method

Hurty/Craig-Bampton method is a reduction method based on the splitting of the DOFs of the system into internal and boundary DOFs. The displacement at the boundary is kept as a DOFs in the reduced coordinates whereas the one of the internal DOFs is reduced. For this reason, it is commonly used in the treatment of localised nonlinearities and in substructuring.

When the nonlinearities are localised and if no other external force is applied to the system, the forces are non-zero only on selected DOFs. For example, in case of localised contact, only the contact nodes are subject to nonlinear forces whereas on all the other DOFs the force is zero.

A partition of the vector of displacement into two vectors:

$$\boldsymbol{U} = \begin{Bmatrix} \boldsymbol{U}_b \\ \boldsymbol{U}_i \end{Bmatrix} \tag{2.76}$$

with $\boldsymbol{U}_b$ vector of the so-called *boundary* DOFs on which the nonlinear forces are applied and $\boldsymbol{U}_i$ vector of the *internal* DOFs, yields the full system to:

$$\begin{bmatrix} \boldsymbol{M}_{bb} & \boldsymbol{M}_{bi} \\ \boldsymbol{M}_{ib} & \boldsymbol{M}_{ii} \end{bmatrix} \begin{Bmatrix} \ddot{\boldsymbol{U}}_b \\ \ddot{\boldsymbol{U}}_i \end{Bmatrix} + \begin{bmatrix} \boldsymbol{C}_{bb} & \boldsymbol{C}_{bi} \\ \boldsymbol{C}_{ib} & \boldsymbol{C}_{ii} \end{bmatrix} \begin{Bmatrix} \dot{\boldsymbol{U}}_b \\ \dot{\boldsymbol{U}}_i \end{Bmatrix} + \begin{bmatrix} \boldsymbol{K}_{bb} & \boldsymbol{K}_{bi} \\ \boldsymbol{K}_{ib} & \boldsymbol{K}_{ii} \end{bmatrix} \begin{Bmatrix} \boldsymbol{U}_b \\ \boldsymbol{U}_i \end{Bmatrix} = \begin{Bmatrix} \boldsymbol{T}_b(\boldsymbol{U}_b) \\ \boldsymbol{0} \end{Bmatrix} \tag{2.77}$$

It is then assumed that the internal DOFs can be expressed as the sum of a *static* and a *dynamic* component:

$$\boldsymbol{U}_i = \boldsymbol{U}_S + \boldsymbol{U}_D \tag{2.78}$$

the static component being evaluated from Eq. (2.77) by neglecting the inertia terms:

$$\boldsymbol{U}_S = -{K_{ii}}^{-1} K_{ib} \boldsymbol{U}_b$$

and the dynamic component being approximated by modal analysis applied to the internal substructure obtained by fixing all the boundary DOFs. The first m eigenmodes of the internal substructure are computed:

$$\left(-\omega_k^2 \boldsymbol{M}_{ii} + \boldsymbol{K}_{ii}\right) \boldsymbol{\phi}_k = 0 \tag{2.79}$$

and the dynamic component of $\boldsymbol{U}_i$ is reduced to these modes:

$$\tilde{\boldsymbol{U}}_D = \sum_{k=1}^{m} \boldsymbol{\phi}_k q_k \tag{2.80}$$

In this way, the new coordinates n_b interface DOFs $\boldsymbol{U}_b$ and m internal modes intensity DOFs $\boldsymbol{q}$:

$$\boldsymbol{\eta} = \begin{Bmatrix} \boldsymbol{U}_b \\ \boldsymbol{q} \end{Bmatrix} \tag{2.81}$$

and the linear reduction matrix is then:

$$\boldsymbol{R} = \begin{bmatrix} \boldsymbol{I} & \boldsymbol{0} \\ -{\boldsymbol{K}_{ii}}^{-1}\boldsymbol{K}_{ib} & \boldsymbol{\Phi} \end{bmatrix} \tag{2.82}$$

such that $\tilde{\boldsymbol{U}} = \boldsymbol{R}\boldsymbol{\eta}$.

The reduced dynamics of size $n_b + m$ is obtained by projection and reads:

$$\begin{bmatrix} \tilde{\boldsymbol{M}}_{bb} & \tilde{\boldsymbol{M}}_{bi} \\ \tilde{\boldsymbol{M}}_{bi} & \boldsymbol{I} \end{bmatrix} \begin{Bmatrix} \ddot{\boldsymbol{U}}_b \\ \ddot{\boldsymbol{q}} \end{Bmatrix} + \begin{bmatrix} \tilde{\boldsymbol{C}}_{bb} & \tilde{\boldsymbol{C}}_{bi} \\ \tilde{\boldsymbol{C}}_{bi} & \boldsymbol{I} \end{bmatrix} \begin{Bmatrix} \dot{\boldsymbol{U}}_b \\ \dot{\boldsymbol{q}} \end{Bmatrix} + \begin{bmatrix} \tilde{\boldsymbol{K}}_{bb} & \boldsymbol{0} \\ \boldsymbol{0} & \tilde{\boldsymbol{\Omega}}_{ii}^2 \end{bmatrix} \begin{Bmatrix} \boldsymbol{U}_b \\ \boldsymbol{q} \end{Bmatrix} = \begin{Bmatrix} \boldsymbol{T}_b(\boldsymbol{U}_b) \\ -{\boldsymbol{K}_{ii}}^{-1}\boldsymbol{K}_{ib}\boldsymbol{T}_b(\boldsymbol{U}_b) \end{Bmatrix} \tag{2.83}$$

where $\tilde{M}_{bb}, \tilde{M}_{bi}, \tilde{K}_{bb}$ are fully populated matrices and $\tilde{\Omega}_{ii}^2$ is the diagonal eigenvalues matrix of the internal modes.

This method is particularly suitable for problems with localised contact nonlinearities in that not only the static response to forces applied on the contact nodes is retained but also the dynamic one, with an accuracy that depends on the number of internal modes retained.

2.3.3 Modal derivatives

The modal derivatives have been first introduced with the aim of offering a framework that takes into account the dependence of mode shapes and eigenfrequencies on amplitude for nonlinear system. In this respect, the generalised eigenproblem solved in the linear case by modal analysis is rewritten in a nonlinear form by taking into account the conservative nonlinear forces and by assuming that, in the nonlinear case, the eigenmodes have a dependence on the amplitude of the solution $\boldsymbol{U}$. Note that, in this contribution, the mass matrix is assumed to be independent of the amplitude. However further development could include a dependence of the mass matrix on the amplitude in order to extend the use of MDs to other cases.

Let us denote the modal amplitudes coordinates as $\boldsymbol{q}$, the amplitude dependent eigenvectors as $\tilde{\phi}_k(\boldsymbol{q})$ and the associated amplitude dependent eigenvalues as $\tilde{\omega}_k^2(\boldsymbol{q})$. The nonlinear eigenproblem can be written as:

$$\left(\boldsymbol{K} - \frac{\partial \boldsymbol{F}_{\mathrm{NL}}}{\partial \boldsymbol{U}} - \tilde{\omega}_k^2(\boldsymbol{q})\boldsymbol{M}\right)\tilde{\phi}_k(\boldsymbol{q}) = \boldsymbol{0} \tag{2.84}$$

Assuming small motions in the vicinity of the equilibrium position $\boldsymbol{q} = \boldsymbol{0}$, and assuming that $\boldsymbol{U}$ is a function of the modal amplitudes q_j, this nonlinear eigenproblem can be Taylor

expanded with respect to q_j. The constant component of this expansion will coincide with the linear modal analysis eigenproblem so that $\tilde{\phi}_k(\mathbf{0}) = \phi_k$ and $\tilde{\omega}_k^2(\mathbf{0}) = \omega_k^2$. As per the linear component, it will read:

$$\left(\frac{\partial}{\partial q_j}\left(\boldsymbol{K} - \frac{\partial \boldsymbol{F}_{\mathrm{NL}}}{\partial \boldsymbol{U}} - \tilde{\omega}_k^2 \boldsymbol{M}\right)\tilde{\phi}_k\right)\Big|_{\mathbf{0}} = \left(\boldsymbol{K} - \omega_k^2 \boldsymbol{M}\right)\frac{\partial \tilde{\phi}_k}{\partial q_j}\Big|_{\mathbf{0}} - \left(\frac{\partial}{q_j}\frac{\partial \boldsymbol{F}_{\mathrm{NL}}}{\partial \boldsymbol{U}} + \frac{\partial \tilde{\omega}_k^2}{\partial q_j}\boldsymbol{M}\right)\Big|_{\mathbf{0}} \phi_k \tag{2.85}$$

The definition of modal derivatives aims at rendering Eq. (2.85) equal to zero. The system that permits to compute the modal derivatives can be then derived by rearranging the right hand side of Eq. (2.85). By noticing that $\phi_k = (\partial \boldsymbol{U}/\partial q_k)|_{\mathbf{0}}$ and that $(\partial \boldsymbol{F}_{\mathrm{NL}}/\partial \boldsymbol{U})(\partial \boldsymbol{U}/\partial q_k) = \partial \boldsymbol{F}_{\mathrm{NL}}/\partial q_k$ one can express the zero condition of the right hand side of Eq. (2.85) in the form:

$$\left(\boldsymbol{K} - \omega_k^2 \boldsymbol{M}\right)\frac{\partial \tilde{\phi}_k}{\partial q_j}\Big|_{\mathbf{0}} - \frac{\partial \tilde{\omega}_k^2}{\partial q_j}\Big|_{\mathbf{0}} \boldsymbol{M}\phi_k = \frac{\partial^2 \boldsymbol{F}_{\mathrm{NL}}}{\partial q_j \partial q_k}\Big|_{\mathbf{0}} \tag{2.86}$$

The unknowns of the system are the scalar $(\partial \tilde{\omega}_k^2/\partial q_j)|_{\mathbf{0}}$ and the vector $(\partial \tilde{\phi}_k/\partial q_j)|_{\mathbf{0}}$. The kj-th modal derivative $\boldsymbol{\theta}_{kj}$ is defined as the unknown vector that represents the derivative of $\tilde{\phi}_k$ with respect to a displacement enforced along the direction of the j-th eigenvector ([53, 56, 127, 173]), and writes:

$$\boldsymbol{\theta}_{kj} \doteq \frac{\partial \tilde{\phi}_k}{\partial q_j}\Big|_{\mathbf{0}}. \tag{2.87}$$

Since the modal derivative is premultiplied by the singular matrix $\boldsymbol{K} - \omega_k^2 \boldsymbol{M}$, to solve the system of Eq. (2.86), one must impose that the modal derivative is orthogonal to the kernel of the singular matrix, *i.e.* the system must be complemented by the additional condition:

$$\phi_k^{\mathrm{T}} \boldsymbol{M} \boldsymbol{\theta}_{kj} = \mathbf{0} \tag{2.88}$$

The last condition is sometimes seen as the first order term of a Taylor of the mass normalisation condition.

The system to be solved to find the modal derivatives is then finally obtained:

$$\begin{bmatrix} \boldsymbol{K} - \omega_k^2 \boldsymbol{M} & -\boldsymbol{M}\phi_k \\ -\phi_k^T \boldsymbol{M} & 0 \end{bmatrix} \begin{Bmatrix} \boldsymbol{\theta}_{kj} \\ (\partial \tilde{\omega}_k^2/\partial q_j)|_{\mathbf{0}} \end{Bmatrix} = \begin{Bmatrix} (\partial^2 \boldsymbol{F}_{\mathrm{NL}}/\partial q_j \partial q_k)|_{\mathbf{0}} \\ 0 \end{Bmatrix}. \tag{2.89}$$

In most of the studies concerned with application of modal derivatives to model order reduction, the so-called *static modal derivatives* are used instead. Let us denote them as $\boldsymbol{\theta}_{kj}^{(S)}$, they are obtained by neglecting the terms related to the inertia in (2.89), which then simplifies to:

$$\boldsymbol{K}\boldsymbol{\theta}_{kj}^{(S)} = \frac{\partial^2 \boldsymbol{F}_{\mathrm{NL}}}{\partial q_j \partial q_k}\Big|_{\mathbf{0}}. \tag{2.90}$$

A linear reduced order model whose reduction matrix $\boldsymbol{R}$ is composed of linear eigenvectors and modal derivatives can be then build. The reduction matrix reads:

$$\boldsymbol{R} = \begin{bmatrix} \boldsymbol{\phi}_{M_1} & \boldsymbol{\phi}_{M_2} & \cdots & \boldsymbol{\phi}_{M_n} & \boldsymbol{\theta}_{M_1M_1} & \boldsymbol{\theta}_{M_1M_2} & \boldsymbol{\theta}_{M_2M_1} \cdots \boldsymbol{\theta}_{M_nM_n} \end{bmatrix}, \tag{2.91}$$

and the reduced coordinates are composed by the amplitudes $\boldsymbol{q}$ of the linear eigenvectors plus the amplitudes $\boldsymbol{z}$ of the modal derivatives:

$$\boldsymbol{\eta} = \begin{Bmatrix} \boldsymbol{q} \\ \boldsymbol{z} \end{Bmatrix} \tag{2.92}$$

such that the change of coordinates is again $\tilde{\boldsymbol{U}} = \boldsymbol{R}\boldsymbol{\eta}$ and the reduced dynamics the projection of the equations of motion on $\boldsymbol{R}$.

2.3.4 Quadratic Manifold

Since the MDs are defined from a second-order Taylor expansion of the nonlinear eigenvalue problem, it is intuitive to use them in a quadratic nonlinear mapping. If one operates a Taylor expansion of the approximate solution $\tilde{\boldsymbol{U}}$ in the modal amplitudes $\boldsymbol{q}$ up to quadratic order, one finds:

$$\tilde{\boldsymbol{U}}(\boldsymbol{q}) = \tilde{\boldsymbol{U}}(\boldsymbol{0}) + \frac{\partial \tilde{\boldsymbol{U}}}{\partial q_k}\bigg|_{\boldsymbol{0}} q_k + \frac{1}{2}\left(\frac{\partial^2 \tilde{\boldsymbol{U}}}{\partial q_j \partial q_k}\right)\bigg|_{\boldsymbol{0}} q_k q_j, \tag{2.93}$$

where $\boldsymbol{q} = (q_{M_1}, ..., q_{M_n})$ is the vector of the modal amplitudes of the selected modes. By extending the definition of linear eigenvectors to the nonlinear ones, the nonlinear eigenvector spans the tangent space of the displacement with respect to the reduced coordinates, so that:

$$\frac{\partial \tilde{\boldsymbol{U}}}{\partial q_k} = \tilde{\boldsymbol{\phi}}_k(\boldsymbol{q}). \tag{2.94}$$

In Eq. (2.93), one can then substitute Eq. (2.94) and obtain:

$$\frac{\partial \tilde{\boldsymbol{U}}}{\partial q_k}\bigg|_{\boldsymbol{0}} = \boldsymbol{\phi}_k, \tag{2.95}$$

$$\frac{\partial^2 \tilde{\boldsymbol{U}}}{\partial q_j \partial q_k}\bigg|_{\boldsymbol{0}} = \boldsymbol{\theta}_{kj}, \tag{2.96}$$

However, this series of operations would lead to an inconsistent formulation in the case of MDs due to their asymmetry, as already outlined in [56]. In fact, since $\boldsymbol{\theta}_{kj} \neq \boldsymbol{\theta}_{jk}$, it implies that the symmetry of partial derivatives $\partial^2 \tilde{\boldsymbol{U}} / \partial q_j \partial q_k \neq \partial^2 \tilde{\boldsymbol{U}} / \partial q_k \partial q_j$ is not fulfilled. As shown in [56], since in the quadratic mapping each pair $\boldsymbol{\theta}_{kj}, \boldsymbol{\theta}_{jk}$ is multiplied by the same monomial $q_j q_k$, the mapping is actually independent on the asymmetric part of the MD. To overcome the asymmetry issue, and given the independence of the quadratic mapping

on the asymmetric part of each MD, the strategy proposed in [56] is to express both the mapping and its tangent space by means of symmetrized modal derivatives. The way the modal derivatives are symmetrised is by defining a new vector $\bar{\boldsymbol{\theta}}_{kj}$, as the average of the asymmetric MDs $\boldsymbol{\theta}_{kj}$ and $\boldsymbol{\theta}_{jk}$:

$$\bar{\boldsymbol{\theta}}_{kj} = \frac{\boldsymbol{\theta}_{kj} + \boldsymbol{\theta}_{jk}}{2} \tag{2.97}$$

and similarly for $\bar{\boldsymbol{\theta}}_{jk}$. In this way one has $\bar{\boldsymbol{\theta}}_{kj} = \bar{\boldsymbol{\theta}}_{jk}$. The quadratic mapping is then build as:

$$\tilde{\boldsymbol{U}}(\boldsymbol{q}) = \boldsymbol{\phi}_k q_k + \frac{1}{2}\bar{\boldsymbol{\theta}}_{kj} q_k q_j \,. \tag{2.98}$$

The change of coordinates operated in the quadratic manifold method is the composition of a linear part that coincides with the classical modal analysis reduction, and a quadratic part where the modal derivatives are used. Unlike the case outlined in the previous section where the modal derivatives were used in a linear reduction method and the new coordinates $\boldsymbol{z}$ were added, the quadratic manifold method only keeps the modal amplitudes as reduced coordinates, assuming that each $\boldsymbol{z}$ could be actually expressed as the product of two $\boldsymbol{q}$.

As per the projection of the full system to obtain the reduced dynamics, it is done on the tangent space Γ, obtained by deriving the change of coordinates with respect to the reduced coordinates and reads:

$$\boldsymbol{\Gamma}(\boldsymbol{q}) = \begin{bmatrix} \boldsymbol{\phi}_{M_1} + \bar{\boldsymbol{\theta}}_{jM_1} q_j & \boldsymbol{\phi}_{M_2} + \bar{\boldsymbol{\theta}}_{jM_2} q_j & \cdots & \boldsymbol{\phi}_{M_n} + \bar{\boldsymbol{\theta}}_{jM_n} q_j \end{bmatrix} . \tag{2.99}$$

2.3.5 Shaw and Pierre formulation of Invariant Manifold

Unlike the methods presented so far, the methods that aims at finding the invariant manifold have been initially developed starting from the system in modal coordinates, written in first order formulation:

$$\dot{\boldsymbol{p}} = -\boldsymbol{\Omega}^2 \boldsymbol{q} + \boldsymbol{f}_{\mathrm{NL}}(\boldsymbol{q}) \tag{2.100a}$$

$$\dot{\boldsymbol{q}} = \boldsymbol{p} \tag{2.100b}$$

where $\boldsymbol{q} = \boldsymbol{\Phi}^{-1}\boldsymbol{U}$ are the modal amplitudes, $\boldsymbol{p} = \boldsymbol{\Phi}^{-1}\boldsymbol{V}$ are their velocity.

The sought manifold is the nonlinear continuation of one linear mode, which will be referred to as the master mode. The problem of finding the nonlinear change of coordinates that describes the geometry of this manifold, reduces to find the unknown single valued functions $\tilde{\boldsymbol{q}}_S$ and $\tilde{\boldsymbol{p}}_S$ that describe the variations of the other modal coordinates as a function of the master mode amplitude q_M and velocity p_M:

$$\boldsymbol{q}_S = \tilde{\boldsymbol{q}}_S(q_M, p_M) \tag{2.101a}$$

$$\boldsymbol{p}_S = \tilde{\boldsymbol{p}}_S(q_M, p_M) \tag{2.101b}$$

where the subscript S represents the fact that the other modes are enslaved to the master one, hence they will be referred to as slave modes. By splitting the Eq.(2.100b) into master and slave modes, one obtains for the former:

$$\dot{q}_M = p_M \tag{2.102a}$$
$$\dot{p}_M = c_M(q_M, p_M, \tilde{\boldsymbol{q}}_S, \tilde{\boldsymbol{p}}_S)\,, \tag{2.102b}$$

and for the latter

$$\dot{\tilde{\boldsymbol{q}}}_S = \tilde{\boldsymbol{p}}_S \tag{2.103a}$$
$$\dot{\tilde{\boldsymbol{p}}}_S = \boldsymbol{c}_S(q_M, p_M, \tilde{\boldsymbol{q}}_S, \tilde{\boldsymbol{p}}_S) \tag{2.103b}$$

with $\boldsymbol{c}_S = -\boldsymbol{\Omega}_S^2 \tilde{\boldsymbol{q}}_S + \boldsymbol{f}_{\mathrm{NL}_S}$ and $c_M = -\omega_M^2 q_M + f_{\mathrm{NL}_M}$.

The time derivatives of the slave coordinates are expressed as a function of the master coordinates as :

$$\dot{\tilde{\boldsymbol{q}}}_S = \frac{\partial \tilde{\boldsymbol{q}}_S}{\partial q_M}\dot{q}_M + \frac{\partial \tilde{\boldsymbol{q}}_S}{\partial p_M}\dot{p}_M \tag{2.104a}$$
$$\dot{\tilde{\boldsymbol{p}}}_S = \frac{\partial \tilde{\boldsymbol{p}}_S}{\partial q_M}\dot{q}_M + \frac{\partial \tilde{\boldsymbol{p}}_S}{\partial p_M}\dot{p}_M \tag{2.104b}$$

Substituting into Eq. (2.103) and simplifying using Eq. (2.102), the time derivatives can be eliminated and the system reduced to:

$$\tilde{\boldsymbol{p}}_S = \frac{\partial \tilde{\boldsymbol{q}}_S}{\partial q_M}p_M + \frac{\partial \tilde{\boldsymbol{q}}_S}{\partial p_M}c_M \tag{2.105a}$$
$$\boldsymbol{c}_S = \frac{\partial \tilde{\boldsymbol{p}}_S}{\partial q_M}p_M + \frac{\partial \tilde{\boldsymbol{p}}_S}{\partial p_M}c_M \tag{2.105b}$$

The solution of this system can be evaluated either with a numerical method or with an analytical method. When the nonlinear force is in the form of a polynomial, the second approach is preferred in that it provides closed form expressions for the mapping functions $\tilde{\boldsymbol{q}}_S(q_M, p_M)$ and $\tilde{\boldsymbol{p}}_S(q_M, p_M)$. In such case, the mappings are also assumed to be in the form of polynomials and the solution is found order by order starting from the first one and then increasing. An example of such a calculation when the nonlinear forces are in the form of geometric nonlinearities can be derived. In particular, the balance of first order terms of Eq. (2.105), is trivial and leads to a zero linear component of the mappings $\tilde{\boldsymbol{q}}_S(q_M, p_M)$ and $\tilde{\boldsymbol{p}}_S(q_M, p_M)$. This is in agreement with the fact that the linear tangent of the manifold has to coincide with the linear master mode plane and the slave modes do not contribute to it.

Assuming the Taylor expansion of $\tilde{\boldsymbol{q}}_S(q_M, p_M)$ and $\tilde{\boldsymbol{p}}_S(q_M, p_M)$ up to second order to be:

$$\tilde{\boldsymbol{q}}_S(q_M, p_M) = \boldsymbol{a}_S\, q_M^2 + \boldsymbol{b}_S\, p_M^2 + \boldsymbol{c}_S\, q_M p_M \tag{2.106a}$$
$$\tilde{\boldsymbol{p}}_S(q_M, p_M) = \boldsymbol{\alpha}_S\, q_M^2 + \boldsymbol{\beta}_S\, p_M^2 + \boldsymbol{\gamma}_S\, q_M p_M\,, \tag{2.106b}$$

then the second order balance of Eq. (2.105) reads:

$$\boldsymbol{c}_S = \boldsymbol{0} \tag{2.107a}$$
$$\boldsymbol{\alpha}_S = \boldsymbol{0} \tag{2.107b}$$
$$\boldsymbol{\beta}_S = \boldsymbol{0} \tag{2.107c}$$
$$2\,\boldsymbol{a}_S - 2\,\omega_M^2 \boldsymbol{b}_S - \boldsymbol{\gamma}_S = \boldsymbol{0} \tag{2.107d}$$
$$\boldsymbol{\Omega}_S^{\boldsymbol{2}} \boldsymbol{a}_S - \omega_M^2 \boldsymbol{\gamma}_S = \boldsymbol{g}_{MM}^S \tag{2.107e}$$
$$\boldsymbol{\Omega}_S^{\boldsymbol{2}} \boldsymbol{b}_S + \boldsymbol{\gamma}_S = \boldsymbol{0} \tag{2.107f}$$

with $\boldsymbol{g}_{MM}^S$ slave modes component of the quadratic tensor that multiplies the term q_M^2. One must notice that the balance has been split into six equations, three for Eq. (2.105a) and three for Eq. (2.105b), each one relative to a different term $q_M^2, q_M p_M, p_M^2$, because the system has to be verified for any value of q_M, p_M. Once the second order component of the nonlinear mapping is found, the third order balance can be written and the procedure can continue iteratively up to a desired order. However, the number of subequations of the system (2.107), increases dramatically with the number of combination $q_M^l p_M^m$ so it is common practice to stop at relatively low orders. In most applications, the third order is enough to capture the most interesting features with a good accuracy.

Once the mapping functions $\tilde{\boldsymbol{q}}_S(q_M, p_M)$ and $\tilde{\boldsymbol{p}}_S(q_M, p_M)$ up to the prescribed order are found, the approximated invariant manifold is used for the nonlinear change of coordinates of the reduced order model:

$$\begin{Bmatrix} \boldsymbol{q} \\ \boldsymbol{p} \end{Bmatrix} = \begin{Bmatrix} q_M \\ \tilde{\boldsymbol{q}}_S(q_M, p_M) \\ p_M \\ \tilde{\boldsymbol{p}}_S(q_M, p_M) \end{Bmatrix} \tag{2.108}$$

where the reduced coordinates are $\boldsymbol{\eta} = (q_M, p_M)$. The reduced dynamics, unlike previous methods, is not obtained by projection but is already available. In fact it is simply Eq. (2.102) calculated with the found mapping functions $\tilde{\boldsymbol{q}}_S(q_M, p_M)$ and $\tilde{\boldsymbol{p}}_S(q_M, p_M)$. The reduced dynamics up to second order will then read:

$$\dot{q}_M = p_M \tag{2.109a}$$
$$\dot{p}_M = -\omega_M^2 q_M + g_{MM}^M q_M^2\,. \tag{2.109b}$$

2.3.6 Normal form approach for Invariant Manifold

The normal form approach is another possible way of approximating the invariant manifold geometry by means of a polynomial change of coordinates for geometric nonlinear forces. As the Shaw and Pierre method, also the normal form can be applied to different type of nonlinear forces but the focus of this thesis will be on geometric nonlinear one.

The main idea of the normal form is to define a nonlinear change of coordinates, from the modal coordinates to new ones defined as the *normal* coordinates. The nonlinear mapping is inherited from Poincaré and Poincaré-Dulac theorems, based on the idea of finding out a nonlinear relationship capable of eliminating as much as possible of nonlinear terms in the reduced system. In this contribution, the real normal form approach of [153, 154, 158] written for mechanical system will be outlined although the first developments of the normal form date back to previous works [57, 58].

The main difference with the Shaw and Pierre approach is that the normal coordinates (R, S) are not equal to the master mode amplitude and velocity but are tangent to them at the origin, in what it is defined as a near identity transformation:

$$\boldsymbol{q} = \boldsymbol{e}_M R + \tilde{\boldsymbol{q}}(R, S) \tag{2.110a}$$

$$\boldsymbol{p} = \boldsymbol{e}_M S + \tilde{\boldsymbol{p}}(R, S) \tag{2.110b}$$

being $\boldsymbol{e}_M$ the unitary vector along the master mode and $\tilde{\boldsymbol{q}}(R, S)$ and $\tilde{\boldsymbol{p}}(R, S)$ the purely nonlinear mapping functions. Unlike in the Shaw and Pierre formulation, the nonlinear mapping also affects the master mode amplitude and velocity (q_M, p_M) but the linear component of (q_M, p_M) is identical to (R, S).

Thanks to this new coordinates, the manifold can be better parametrised because the newly introduced normal coordinates are better suited to follow the manifold geometry. In particular, the graph representation of the manifold obtained by Shaw and Pierre formulation might collapse if the manifold presents a folding with respect to the master mode coordinates; this occurrence is extensively treated in [42].

The time derivatives of the original coordinates are expressed as a function of the normal coordinates as :

$$\dot{\tilde{\boldsymbol{q}}} = \frac{\partial \tilde{\boldsymbol{q}}}{\partial R}\dot{R} + \frac{\partial \tilde{\boldsymbol{q}}}{\partial S}\dot{S} \tag{2.111a}$$

$$\dot{\tilde{\boldsymbol{p}}} = \frac{\partial \tilde{\boldsymbol{p}}}{\partial R}\dot{R} + \frac{\partial \tilde{\boldsymbol{p}}}{\partial S}\dot{S} \tag{2.111b}$$

Assuming the Taylor expansion of $\tilde{\boldsymbol{q}}(R,S)$ and $\tilde{\boldsymbol{p}}(R,S)$ up to second order to be:

$$\tilde{\boldsymbol{q}}(R,S) = \boldsymbol{e}_M R + \boldsymbol{a}R^2 + \boldsymbol{b}S^2 + \boldsymbol{c}RS \tag{2.112a}$$
$$\tilde{\boldsymbol{p}}(R,S) = \boldsymbol{e}_M S + \boldsymbol{\alpha}R^2 + \boldsymbol{\beta}S^2 + \boldsymbol{\gamma}RS\,, \tag{2.112b}$$

then the second order balance of the equation of motion reads:

$$\boldsymbol{c} = \boldsymbol{0} \tag{2.113a}$$
$$\boldsymbol{\alpha} = \boldsymbol{0} \tag{2.113b}$$
$$\boldsymbol{\beta} = \boldsymbol{0} \tag{2.113c}$$
$$2\,\boldsymbol{a} - 2\,\omega_M^2 \boldsymbol{b} - \boldsymbol{\gamma} = \boldsymbol{0} \tag{2.113d}$$
$$\boldsymbol{\Omega^2 a} - \omega_M^2 \boldsymbol{\gamma} = \boldsymbol{g}_{MM} \tag{2.113e}$$
$$\boldsymbol{\Omega^2 b} + \boldsymbol{\gamma} = \boldsymbol{0} \tag{2.113f}$$

with $\boldsymbol{g}_{MM}$ quadratic component in R^2 of the nonlinear force on all the modes.

These equations look similar to those found by the Shaw and Pierre approach, the only difference being that in this case, the nonlinear mapping vectors $\boldsymbol{a}, \boldsymbol{b}, \boldsymbol{c}, \boldsymbol{\alpha}, \boldsymbol{\beta}, \boldsymbol{\gamma}$ are defined for all the modal coordinates, not just on the slave modes. In this way, the vectors have the capability of cancelling nonlinear terms on the equation of motion of the master mode too, in this case the quadratic term.

The reduced dynamics, also in this case, is not obtained by projection but is already available. In fact it is simply the remainder of the non-cancelled terms in Eq. (2.111). In this case, all the terms have been cancelled and the reduced dynamics up to second order is linear:

$$\dot{R} = S \tag{2.114a}$$
$$\dot{S} = -\omega_M^2 R\,. \tag{2.114b}$$

Although the aim of the method is to cancel all possible nonlinear terms, this is not always possible due to singular terms as a result of the so called trivial resonances. For example, in the balance of the third order terms, a singular denominator matrix would always appear, making impossible for the third order mapping tensors to cancel all the terms. The remaining terms will then become part of the reduced dynamics equations. More details will be given about this in the course of this dissertation, for now suffice to say that the reduced dynamics up to third order will read:

$$\dot{R} = S \tag{2.115a}$$
$$\dot{S} = -\omega_M^2 R - (A + h^M_{MMM})R^3 - BRS^2 \;=\; 0\,, \tag{2.115b}$$

with:

$$A = 2\, \boldsymbol{a}^{\mathrm{T}} \boldsymbol{g}_{MM} \tag{2.116a}$$

$$B = 2\, \boldsymbol{b}^{\mathrm{T}} \boldsymbol{g}_{MM}\,. \tag{2.116b}$$

Both normal form and Shaw and Pierre formulations permit to build a minimal reduced order model of only one degree of freedom in configuration space with high accuracy. Although not detailed here, these procedures can be easily generalised to the case of multiple master modes as will be seen in the following chapters. Moreover, both approaches can be extended to the case of non-conservative systems.

The only difference between the two methods is the fact that, in the normal form approach, the master coordinates are a nonlinear function of the normal coordinates, whereas, in the Shaw and Pierre approach, the two systems of coordinates coincide. The Shaw and Pierre approach construct the invariant manifold as a graph over the master coordinates whereas the normal form constructs the invariant manifold as an embedding, as detailed in [42]. If the invariant manifold presents a folding, the manifold build as a graph will not be able to approximate the correct manifold geometry and it will diverge. However, this occurrence is rare and it has only been shown on an ad-hoc academic example in [42], where the order of the expansion needed to capture the folding was equal to 19.

2.4 Time discretisation

The system of equations obtained by FE discretisation or by model order reduction is a system of ordinary differential equations in the sole time variable. In the case of a system particularly small in size and simple in its nonlinear forces, perturbation methods like multiple scales and averaging can be used to find analytical solutions. However this is not generally the case and numerical methods must be adopted. The next two sections are devoted to the most relevant methods for this dissertation, time integration via Newmark time stepping scheme and harmonic balance method. In the first case the time is discretised into time steps and no assumptions on the solution periodicity is made. In the second case, the periodic solution is sought and the time is discretised by means of trigonometric functions.

2.4.1 Central difference scheme

Newmark schemes [102] are particularly suitable for second order differential equations and their applicability to nonlinear smooth problems has been extensively studied in [35]. In the case of non-smooth problems, other methods should instead be used [23], but we restrict our analysis to the former case. In this work we will use a central finite difference scheme to approximate the acceleration and velocities in time.

If the time is discretised into equally spaced intervals of length Δt, the time variable becomes discrete $t_k = k\Delta t$. The unknown displacement is then calculated only at the discrete time points and stored into the vector $\mathbb{U}$:

$$\boldsymbol{U}(t_k) = \mathbb{U}_k \tag{2.117}$$

To compute the solution the equation of motion has to be solved. To do so, the velocity and acceleration at a given time point t_k must be also defined as a function of the displacement at previous and next steps. The two points central finite difference are used here to define the velocity:

$$\dot{\boldsymbol{U}}(t_k) = \frac{\mathbb{U}_{k+1} - \mathbb{U}_{k-1}}{2\Delta t} \tag{2.118}$$

and the acceleration:

$$\ddot{\boldsymbol{U}}(t_k) = \frac{\mathbb{U}_{k+1} - 2\mathbb{U}_k + \mathbb{U}_{k-1}}{\Delta t^2} \tag{2.119}$$

The resultant system to solve at each time step k, will then depend on three consecutive values of the displacement $(\mathbb{U}_{k-1}, \mathbb{U}_k, \mathbb{U}_{k+1})$:

$$\boldsymbol{M}\left(\frac{\mathbb{U}_{k+1} - 2\mathbb{U}_k + \mathbb{U}_{k-1}}{\Delta t^2}\right) + \boldsymbol{C}\left(\frac{\mathbb{U}_{k+1} - \mathbb{U}_{k-1}}{2\Delta t}\right) + \boldsymbol{K}\mathbb{U}_k = \boldsymbol{F}_{\text{ext}}(t_k) + \boldsymbol{F}_{\text{NL}}(\mathbb{U}_{k-1}, \mathbb{U}_k, \mathbb{U}_{k+1}) \tag{2.120}$$

If the nonlinear force depends on the sole displacement, its value at the time t_k will depend solely on $\mathbb{U}_k$. The vector $\mathbb{U}_{k+1}$ can be then calculated directly from Eq. (2.120). Otherwise, if a velocity dependence is present, a nonlinear solver must be used to solve Eq. (2.120).

The starting point of the scheme requires two initial conditions for $\mathbb{U}_0$ and $\mathbb{U}_1$. When a steady state periodic solution is sought, the closer the initial conditions to the sought solution, the faster the method will reach the steady state. In general, being the sought solution unknown, the choice of the initial conditions is usually just to set both at zero. In this way, the transient response of the system at rest to a sudden force has to decay before the steady is reached. Depending on the value of damping the process might take several periods.

If one wants to compute the response of a system to a given excitation, with excitation frequency in a given range, a so called frequency sweep is normally performed. The starting point is again the equilibrium state and the initial value of the forcing frequency equal to the first frequency in the range. When the steady state is reached, instead of starting a new computation with the new desired value of the forcing frequency, the value of the frequency is simply increased slowly with time. In this way, the effect of the transient response is minimised and the computational time saved. However, the solution found with this approach is not perfectly periodic because as the time goes, also the forcing frequency increases slightly thus making the period change. To minimise this error, the rate of growth of the forcing frequency should be kept slow enough to have a negligible influence on the

accuracy of the solution.

Time integration is widely used in contact problems, as it will be further commented in Chapter 6. It is also often used to verify the solution obtained with faster but more approximate methods such as Harmonic Balance Method, as it will be done in Section 6.2.3 of this thesis. Moreover, time integration is the standard verification method of the industrial sponsor Rolls-Royce, where more advanced stepping schemes are adopted; they are however out of the scope of this work therefore they will not be treated here.

2.4.2 Harmonic Balance Method

Harmonic balance method is a Galerkin method that seeks the periodic solution of the system of ordinary differential equation in time. The period is either the one coming from the forcing term in the case of non-autonomous systems, or it is the period of the limit cycle in case of autonomous systems. The time dependent displacement vector is assumed to be a superposition of trigonometric functions with pulsation $\Omega, 2\Omega, 3\Omega, \dots, H\Omega$ with H being the number of harmonics chosen for the time discretisation

$$\boldsymbol{U}(t) = \mathbb{U}_0 + \mathbb{U}_k^{(C)} \cos(k\Omega t) + \mathbb{U}_k^{(S)} \sin(k\Omega t) \tag{2.121}$$

with $k = 1, 2, \dots, H$.

The vectors $\mathbb{U}_k$ of length n equal to the size of the system are the Fourier components of the solution. They can be arranged in a unique vector of size $n \times (2H+1)$ as:

$$\mathbb{U} = \begin{Bmatrix} \mathbb{U}_0 \\ \mathbb{U}_1^{(C)} \\ \mathbb{U}_1^{(S)} \\ \dots \\ \mathbb{U}_H^{(C)} \\ \mathbb{U}_H^{(S)} \end{Bmatrix} \tag{2.122}$$

The vector containing all the shape functions can be also build as:

$$\boldsymbol{Q}(t) = \begin{Bmatrix} 1 & \cos(\Omega t) & \sin(\Omega t) & \dots & \cos(H\Omega t) & \sin(H\Omega t) \end{Bmatrix} \tag{2.123}$$

such that $\boldsymbol{U}(t) = (\boldsymbol{Q}(t) \otimes \boldsymbol{I}_N)\mathbb{U}$ where the symbol $\otimes$ represents the Kroneker product.

The velocity and acceleration vectors are found by deriving the sole vector $\boldsymbol{Q}(t)$. Since the weak form of the discretised system is obtained by projection of the equations of motion on the shape functions, it is convenient to define the following differentiation matrices of

size $2H+1$:

$$\boldsymbol{L}_2(\Omega) = \int_0^{\frac{2\pi}{\Omega}} \boldsymbol{Q}^{\mathrm{T}}(t)\ddot{\boldsymbol{Q}}(t)dt \tag{2.124a}$$

$$\boldsymbol{L}_1(\Omega) = \int_0^{\frac{2\pi}{\Omega}} \boldsymbol{Q}^{\mathrm{T}}(t)\dot{\boldsymbol{Q}}(t)dt \tag{2.124b}$$

$$\boldsymbol{L}_0(\Omega) = \int_0^{\frac{2\pi}{\Omega}} \boldsymbol{Q}^{\mathrm{T}}(t)\boldsymbol{Q}(t)dt \tag{2.124c}$$

Moreover to express the left hand side of the discretised equation of motion, it is convenient to define the so called dynamic stiffness matrix:

$$\mathbb{A}(\Omega) = \boldsymbol{L}_2(\Omega) \otimes \boldsymbol{M} + \boldsymbol{L}_1(\Omega) \otimes \boldsymbol{C} + \boldsymbol{L}_0(\Omega) \otimes \boldsymbol{K}\,, \tag{2.125}$$

and the vector of Fourier components of the external force:

$$\mathbb{F}_{\mathrm{ext}}(\Omega) = \int_0^{\frac{2\pi}{\Omega}} (\boldsymbol{Q}^{\mathrm{T}}(t) \otimes \boldsymbol{I}_N)\boldsymbol{F}_{\mathrm{ext}}(t)dt\,. \tag{2.126}$$

Finally the discretised form of the equation of motion can be written as:

$$\mathbb{A}\mathbb{U} - \mathbb{F}_{\mathrm{ext}} = \int_0^{\frac{2\pi}{\Omega}} (\boldsymbol{Q}^{\mathrm{T}}(t) \otimes \boldsymbol{I}_N)\boldsymbol{F}_{\mathrm{NL}}(\boldsymbol{U}(t))dt\,. \tag{2.127}$$

The left hand side of Eq. (2.127) is straightforward and only depends on Ω. As for the right hand side, it also depends on $\mathbb{U}$ through $\boldsymbol{U}(t)$. If the nonlinear forces are polynomials of $\boldsymbol{U}(t)$, the nonlinear force vector in the frequency domain can be calculated without need to go back into the time domain. Conversely, when contact forces are present, the so called alternating frequency time (AFT) procedure has to be performed [24]. The vector of unknowns in the frequency domain $\mathbb{U}$ has to be transformed into that in the time domain $\boldsymbol{U}(t)$ to compute $\boldsymbol{F}_{\mathrm{NL}}(\boldsymbol{U}(t))$. Only at this point, the value of the nonlinear forces in the frequency domain at the right hand side of Eq. (2.127) can be finally computed.

Eq. (2.127) can be rewritten in the form of a zero problem as:

$$\mathbb{R}(\mathbb{U}, \Omega) = \boldsymbol{0} \tag{2.128}$$

with $\mathbb{R} = \mathbb{A}\mathbb{U} - \mathbb{F}_{\mathrm{ext}} - \mathbb{F}_{\mathrm{NL}}$. In the next section, parametric continuation methods to find the solution of a zero problem as one parameter varies, for instance the frequency Ω, will be described. For the sake of readability the notation $\mathbb{R}, \mathbb{U}, \mathbb{A}, \ldots$ will be from now on substituted by the more readable notation $\boldsymbol{R}, \boldsymbol{U}, \boldsymbol{A}, \ldots$.

2.5 Continuation

Parametric continuation methods are a class of algorithms for evaluating the solution of a nonlinear zero problem as one parameter varies [1]. In engineering problems, the most common continuation parameter is the frequency, be it the forcing frequency when evaluating forced response curves or the natural frequency when evaluating nonlinear modes. The application of parametric continuation on the problems of interest in this work will be treated in Sec. 2.5.3 and Sec. 2.5.4. Here a generic presentation of the algorithm is provided.

The residual vector $\boldsymbol{R}$ of the discretised nonlinear system maps the vector of unknown of the system $\boldsymbol{U}$ and the control parameter λ. The system of equation to be solved simply writes:

$$\boldsymbol{R}(\boldsymbol{U}, \lambda) = \boldsymbol{0} \tag{2.129}$$

where the control parameter can be for instance the excitation frequency Ω but it might as well be equal to another parameter of the system. To solve Eq. (2.129) for a given range of values of the control parameters λ, is to find a solution $\boldsymbol{U}^*$ for each value of $\lambda = \lambda^*$.

The simplest algorithm for parametric continuation is the sequential continuation. Let us suppose to know the solution $\boldsymbol{U}_0^*$, root of $\boldsymbol{R}$ for the first value of the control parameter λ_0^*.

Then, the whole range of control parameter values can be covered by sequentially incrementing the control parameter of a small $\lambda_k^* = \lambda_{k-1}^* + \Delta\lambda$ and finding the solution vector $\boldsymbol{U}_k^*$ with a nonlinear solver such as Newton Raphson, using the previous value $\boldsymbol{U}_{k-1}^*$ as initial guess.

Although this method can potentially be used in a wide range of cases, if the solution path displays turning points a simple sequential continuation would not be able to follow the trajectory. An explicative case is that depicted in Fig. 2.5, where the fold point would make this algorithm fail. In such situation, path following algorithms are necessary to be able to follow the solution path.

Path following algorithms for parametric continuation share the same idea but instead of increasing the parameter of interest of a fixed quantity $\Delta\lambda$, the step between one solution and the next is taken along the solution path itself. Such algorithms treat the control parameter as an additional unknown thus making the system of equation undetermined. An additional constraint is then needed to make the system solvable. The additional constraint depends on the method used.

By defining the new quantity $\boldsymbol{Y} = \{\boldsymbol{U}, \lambda\}$, the system to be solved becomes:

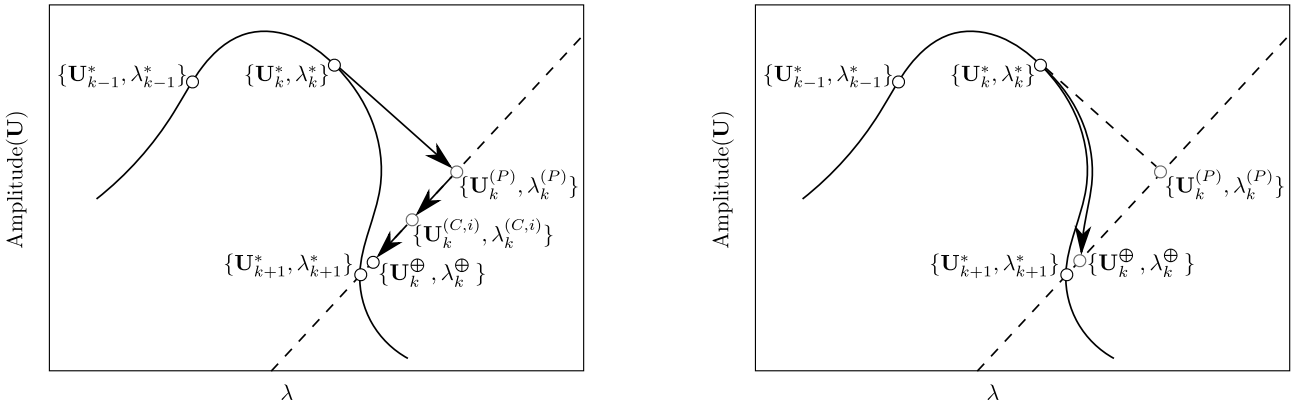
$$\boldsymbol{Y}_k^* : \quad \boldsymbol{R}(\boldsymbol{Y}_k^*) = \boldsymbol{0} \tag{2.130}$$

together with some additional equation:

$$g(\boldsymbol{Y}_k^*) = 0 \tag{2.131}$$

that depends on the method used.

Two different strategies are proposed here: predictor-corrector methods and asymptotic numerical methods. A visual representation of both methods is given in Fig. 2.5.



(a) Predictor-corrector method. (b) Asymptotic numerical method.

Figure 2.5: Visual representation of the presented path following methods.

2.5.1 Predictor-Corrector continuation

The most common continuation method is the predictor-corrector algorithm. This algorithm consists in two steps. Firstly, a predictor vector is calculated along the trajectory of the solution path at the actual solution point; it is commonly computed with a linear approximation as the tangent to the trajectory and in such case called Euler predictor. Then, from the predicted point, a series of correction is computed to find the next solution point on the path. The constraint imposed on the correction step depends on the method. In the pseudo-arc length method, the constraint equation enforces the orthogonality between predictor and corrector.

Let us suppose $\boldsymbol{Y}_k^*$ to be a solution of the system at a generic point of the continuation algorithm. Then the following system of equation is verified by $\boldsymbol{Y}_k^*$:

$$\boldsymbol{R}(\boldsymbol{Y}_k^*) = \boldsymbol{0} \tag{2.132}$$

Starting from the solution point $\boldsymbol{Y}_k^*$, the Euler prediction step $\boldsymbol{\Delta Y}_k^{(P)}$ is calculated as the tangent to the solution path at $\boldsymbol{Y}_k^*$ whose length is equal to a chosen step length a and its direction is the one that minimise the angle with the previous predictor step. First, the unitary vector tangent to the solution path is found by writing the undetermined system:

$$\left.\frac{\partial \boldsymbol{R}}{\partial \boldsymbol{Y}}\right|_{*,k} \cdot \boldsymbol{e}_k^{(P)} = \boldsymbol{0}\,, \tag{2.133}$$

that is made solvable by the addition of the normalisation condition:

$$(\boldsymbol{e}_k^{(P)})^{\mathrm{T}} \cdot \boldsymbol{e}_k^{(P)} = 1\,. \tag{2.134}$$

Then, the prediction step is found by multiplying the unitary vector by the chosen step length a and the sign of the cosine between the current unitary vector and the prediction step vector calculated at the previous continuation point:

$$\boldsymbol{\Delta Y}_k^{(P)} = \boldsymbol{e}_k^{(P)}\, a\, \mathrm{sign}((\boldsymbol{e}_k^{(P)})^{\mathrm{T}} \cdot \boldsymbol{\Delta Y}_{k-1}^{(P)})\,. \tag{2.135}$$

The predicted point $\boldsymbol{Y}_k^{(P)} = \boldsymbol{Y}_k^{*} + \boldsymbol{\Delta Y}_k^{(P)}$ is then used as a starting point for the correction steps. The correction consists in applying the Newton-Raphson method to find the new solution point $\boldsymbol{Y}_k^{\oplus}$ root of $\boldsymbol{R}$. Since the length of the residual is N but the length of the unknown vector is $N+1$ because also the parameter λ is unknown, the system is augmented with the condition of orthogonality between each corrector step $\boldsymbol{\Delta Y}_k^{(C,i)}$ and the predictor step. This condition is what makes the continuation algorithm able to overcome folding points as depicted in Fig. 2.5a.

The i-th Newton-Raphson iteration step reads:

$$\left.\frac{\partial \boldsymbol{R}}{\partial \boldsymbol{Y}}\right|_{(C,i-1,k)} \cdot \boldsymbol{\Delta Y}_k^{(C,i)} = -\boldsymbol{R}(\boldsymbol{Y}_k^{(C,i-1)})\,, \tag{2.136}$$

where $\boldsymbol{Y}_k^{(C,i-1)}$ is known from previous iterations and $\boldsymbol{\Delta Y}_k^{(C,i)} = \boldsymbol{Y}_k^{(C,i)} - \boldsymbol{Y}_k^{(C,i-1)}$ is the sought unknown. To be solvable, the system must be augmented with the condition of orthogonality between the correction step and the predictor one:

$$(\boldsymbol{\Delta Y}_k^{(C,i)})^{\mathrm{T}} \cdot \boldsymbol{e}_k^{(P)}\,. \tag{2.137}$$

At each step of the correction process, the residual is computed for the current value of the unknown vector $\boldsymbol{Y}_k^{(C,i)}$. Its norm is also computed and compared to the given tolerance value. If the current point meets the tolerance requirement, the sought $\boldsymbol{Y}_k^{\oplus}$ has been found and the iteration process stops:

$$\mathrm{norm}[\boldsymbol{R}(\boldsymbol{Y}_k^{(C,i)})] \leq \mathrm{tol} \quad \Rightarrow \quad \boldsymbol{Y}_k^{\oplus} = \boldsymbol{Y}_k^{(C,i)} \tag{2.138}$$

The targeted value of the unknown becomes the new solution point for the next predictor corrector step:

$$\boldsymbol{Y}_{k+1}^{*} = \boldsymbol{Y}_k^{\oplus} \tag{2.139}$$

2.5.2 Asymptotic numerical method

Another way of approaching the problem of continuation of solutions is the asymptotic numerical method [27]. The first step of the method is to express the residual equation as

a quadratic function of the unknowns with a procedure called quadratic recast [41]:

$$\boldsymbol{R}(\boldsymbol{Y}) = \boldsymbol{C} + \boldsymbol{L} \cdot \boldsymbol{Y} + \boldsymbol{Q}(\boldsymbol{Y}, \boldsymbol{Y}) \,. \tag{2.140}$$

It is possible to demonstrate that most known functions can be reformulated in this way by adding additional variables to the system, the so called auxiliary variables [27]. For piecewise smooth functions not directly recastable in quadratic form, a regularisation is introduced.

The second step of the method is to assume that the new targeted solution point is in the form of a polynomial in the arc-length variable a:

$$\boldsymbol{Y}_k^{\oplus}(a) = \boldsymbol{Y}_k^* + \boldsymbol{\Delta Y}_k^{(1)} a + \sum_2^m \boldsymbol{\Delta Y}_k^{(r)} a^r \tag{2.141}$$

with the constant component being equal to the present solution vector.

The residual calculated at $\boldsymbol{Y} = \boldsymbol{Y}_k^{\oplus}(a)$, also depends on the arc-length variable and can thus be expanded in Taylor series as:

$$\boldsymbol{R}(a) = \boldsymbol{R}(0) + \sum_1^m \frac{1}{r!} \left. \frac{\partial^r \boldsymbol{R}}{\partial a^r} \right|_{a=0} a^r + \mathcal{O}(a^{m+1}) \tag{2.142}$$

It is possible to demonstrate that thanks to the quadratic recast of the residual, each expansion term can be simplified to:

$$\left. \frac{1}{r!} \frac{\partial^r \boldsymbol{R}}{\partial a^r} \right|_{a=0} = \left. \frac{\partial \boldsymbol{R}}{\partial \boldsymbol{Y}} \right|_{*,k} \cdot \boldsymbol{\Delta Y}_k^{(r)} + \sum_{s=1}^{r-1} \boldsymbol{Q}(\boldsymbol{\Delta Y}_k^{(s)}, \boldsymbol{\Delta Y}_k^{(r-s)}) \tag{2.143}$$

with:

$$\left. \frac{\partial \boldsymbol{R}}{\partial \boldsymbol{Y}} \right|_{*,k} \cdot \boldsymbol{\Delta Y}_k^{(r)} = \boldsymbol{L} \cdot \boldsymbol{\Delta Y}_k^{(r)} + \boldsymbol{Q}(\boldsymbol{\Delta Y}_k^{(r)}, \boldsymbol{Y}_k^*) + \boldsymbol{Q}(\boldsymbol{Y}_k^*, \boldsymbol{\Delta Y}_k^{(r)}) \tag{2.144}$$

Since the expression of the residual of Eq.(2.142) has to be zero for all powers of a, each term is solved independently. In particular the first order unknown vector $\boldsymbol{\Delta Y}_k^{(1)}$ is found solving the linear system:

$$\left. \frac{\partial \boldsymbol{R}}{\partial \boldsymbol{Y}} \right|_{*,k} \cdot \boldsymbol{\Delta Y}_k^{(1)} = \boldsymbol{0} \tag{2.145}$$

plus the additional equation:

$$(\boldsymbol{\Delta Y}_k^{(1)})^{\mathrm{T}} \cdot \boldsymbol{\Delta Y}_k^{(1)} = 1 \tag{2.146}$$

thus making $\boldsymbol{\Delta Y}_k^{(1)} = \boldsymbol{e}_k^{(P)}$.

Whereas the generic order unknown vector $\boldsymbol{\Delta Y}_k^{(r)}$ is computed by solving:

$$\boldsymbol{L} \cdot \boldsymbol{\Delta Y}_k^{(r)} + \boldsymbol{Q}(\boldsymbol{\Delta Y}_k^{(r)}, \boldsymbol{Y}_k^*) + \boldsymbol{Q}(\boldsymbol{Y}_k^*, \boldsymbol{\Delta Y}_k^{(r)}) = -\sum_{s=1}^{r-1} \boldsymbol{Q}(\boldsymbol{\Delta Y}_k^{(s)}, \boldsymbol{\Delta Y}_k^{(r-s)}) \tag{2.147}$$

with the left hand side linear in $\boldsymbol{\Delta Y}_k^{(r)}$ and the right hand side only depending on previously calculated orders; to make the system solvable the additional equation is added:

$$(\boldsymbol{\Delta Y}_k^r)^{\mathrm{T}} \cdot \boldsymbol{\Delta Y}_k^1 = 0 \tag{2.148}$$

In this way, all the terms in the Taylor expansions are zero and the residual is of order $\mathcal{O}(a^{m+1})$. Instead of stopping the process at the value of m such that a tolerance is met, the strategy consists in fixing m (usually 20) and choosing the step length a in such a way that $\boldsymbol{R}(a_{max}) \leq tol$.

The asymptotic numerical method shares some similarity with the predictor-corrector method; first of all, the linear step coincides with the predictor step of the predictor corrector method; secondly, all the higher order terms are forced to be orthogonal to it through Eq. (2.148) as well as the corrector steps were in the predictor corrector method. However, in the asymptotic numerical method, each value of a between zero and a_{max}, $\boldsymbol{Y}_k^{\oplus}(a)$ is a solution of the system whereas for the predictor-corrector method only the last corrected vector was. For this reason, for high values of the order of expansion m the maximum step length a of the asymptotic numerical method is normally much larger than that of a predictor-corrector method because there is no loss of information between one step and the next.

2.5.3 Application to forced responses and nonlinear modes

Parametric continuation algorithm can be used to trace the response of the system to a variation of any possible parameter. However, in nonlinear vibration, the frequency of the response is the parameter of most interest in that it allows to build forced responses and nonlinear modes.

When a periodic forcing is applied, the system depends on time not only through the unknown displacement and velocity but also through the forcing term:

$$\boldsymbol{M}\ddot{\boldsymbol{U}}(t) + \boldsymbol{C}\dot{\boldsymbol{U}}(t) + \boldsymbol{K}\boldsymbol{U}(t) = \boldsymbol{F}_{\mathrm{ext}}(t) + \boldsymbol{F}_{\mathrm{NL}}(\boldsymbol{U}(t), \dot{\boldsymbol{U}}(t)). \tag{2.149}$$

When a system has an explicit dependence on time, it is said to be non-autonomous. Let us suppose that harmonic balance method is chosen to discretise the equation of motion, the residual will depend on the imposed forcing frequency Ω:

$$\mathbb{R}(\mathbb{U}, \Omega) = \mathbb{A}(\Omega)\mathbb{U} - \mathbb{F}_{\mathrm{ext}}(\Omega) - \mathbb{F}_{\mathrm{NL}}(\mathbb{U}, \Omega) \tag{2.150}$$

Parametric continuation along the forcing frequency can then be applied to the residual and the forced response function of the system computed. The forced response is usually the most sought outcome of the analysis in engineering application in that it allows to identify resonances and high amplitude responses of the system under study.

As anticipated in the introduction, another key outcome of nonlinear vibration studies are the nonlinear modes of the system. If no forcing term is applied, the system is autonomous. If no damping term is present and if the nonlinear forces are conservative, periodic orbits can exist as a solution of the following equation of motion:

$$\boldsymbol{M}\ddot{\boldsymbol{U}}(t) + \boldsymbol{K}\boldsymbol{U}(t) = \boldsymbol{F}_{\mathrm{NL,c}}(\boldsymbol{U}(t)). \tag{2.151}$$

Eq. (2.151) can be solved by periodic orbits of different amplitude from zero to infinity, each of which will have a different frequency ω because of the frequency-amplitude dependence that the nonlinear forces introduce. To find these orbits is to find the nonlinear normal modes of the system. Let us suppose that the nonlinear forces are weakly nonlinear, then any linear mode of the system, at a very low modal amplitude is almost a solution Eq. (2.151) because the nonlinear forces scales with the amplitude in a higher than linear manner. The nonlinear modes of the system could then be obtained by continuing the linear orbits from very low amplitude to increasing amplitudes. However, being the system conservative, for every value of the nonlinear frequency ω the zero vector is a solution of the equation of motion. From a computational point of view, if continuation is performed with the frequency as a control parameter, the trivial zero solution might attract the Newton-Raphson iterations thus preventing the continuation algorithm to capture the non-trivial orbits of interest. Moreover, for each periodic orbit solution of Eq. (2.151), the same orbit with a different phase is also a solution, which is the reason why a blind application of continuation algorithm to the system are not appropriate. To overcome this issues, several approaches can be adopted [121]. In this work we will use the same approach that is implemented in Manlab and Auto [27, 31] which consists in enlarging the system with one equation representing a phase constraint and one variable that represents the level of conservativeness of the system. Let us first write the residual that one obtains by time discretisation of Eq. (2.151):

$$\mathbb{R}(\mathbb{U}, \omega) = \mathbb{A}_c(\omega)\mathbb{U} - \mathbb{F}_{\mathrm{NL,c}}(\mathbb{U}, \omega) \tag{2.152}$$

where now the dynamic stiffness matrix $\mathbb{A}_c$ is the conservative one with no damping term. For this system, the vector $\mathbb{U} = \mathbf{0}$ is a solution of the residual for each value of ω. The strategy consists in the following steps. Firstly, one defines a dummy damping matrix $\boldsymbol{C}$ and add a fictitious damping to the system; a purely dissipative term will then appear in the form of a dissipative dynamic stiffness matrix:

$$\mathbb{A}_d(\omega) = \boldsymbol{L}_1(\omega) \otimes \boldsymbol{C} \tag{2.153}$$

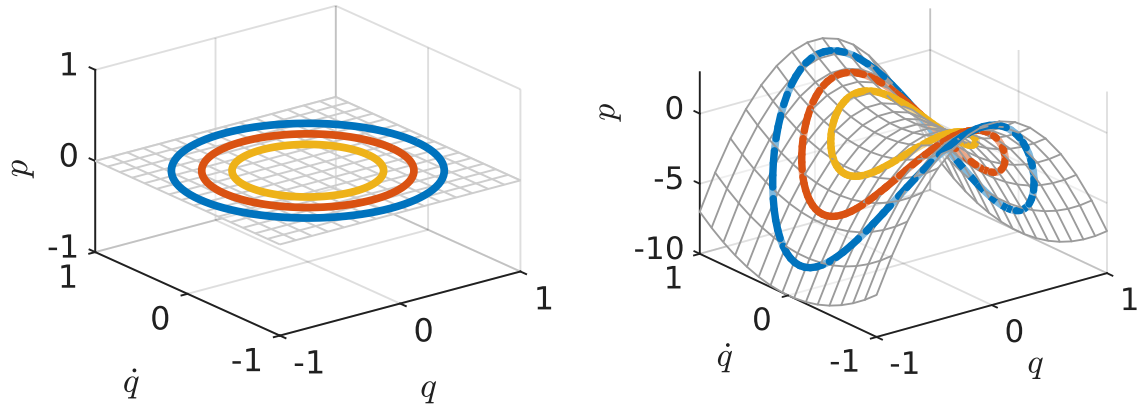
Secondly, a new variable λ is added to the system in the form of a multiplier of the user defined damping term. By adding this term to the residual one has:

$$\mathbb{R}(\mathbb{U},\omega) = (\mathbb{A}_c(\omega) + \lambda\mathbb{A}_d(\omega))\,\mathbb{U} - \mathbb{F}_{\mathrm{NL},c}(\mathbb{U},\omega) \tag{2.154}$$

Now, the trivial zero vector is a solution of the residual for any value of λ whereas the sought non-trivial solution only solves the system for $\lambda = 0$, *i.e.* when the system is conservative.

Lastly, one equation is added to the system to enforce the phase constraint. For example, imposing that the velocity of the solution at $t = 0$ has to be zero, is a common choice for such purpose. The residual enlarged by the phase constraint equation and the unknown vector enlarged by the variable λ, can be then solved with parametric continuation along the nonlinear frequency ω by providing $\lambda = 0$, $\omega = \omega_n$, and $\mathbb{U}$ along a linear mode as initial guess for the algorithm to start.

The continuation of a given nonlinear mode starting from its linear counterpart, permits to find the backbone curve and the invariant manifold of that mode. In fact, the nonlinear mode obtained by continuation will be a collection of periodic orbits of increasing amplitude that if continuously joined would provide the two dimensional invariant manifold associated with it. At low amplitude the invariant manifold is tangent to its linear counterpart [88] and it will depart from it as the amplitude increases. This geometrical entity is also referred to as Lyapunov subcenter manifold. A visual representation of this concept is provided in Fig. 2.6 where three orbits of increasing amplitude are plotted in the linear and nonlinear case respectively. The nonlinear forces couple the linear mode under analysis with other modes thus breaking the invariance property of the linear case.



(a) Linear invariant manifold

(b) Nonlinear invariant manifold

Figure 2.6: Periodic orbits lying on the invariant manifold. Amplitude of a tangent mode p against amplitude and velocity of the mode under investigation $(q, \dot{q})$.

2.5.4 Application to nonlinear modes of systems with non conservative forces

In the case of conservative nonlinear forces, periodic orbits that solve the autonomous system do exist. Conversely, in presence of non conservative nonlinear forces such as friction forces, the concept of periodic motion ceases to exist because the dissipation introduced by nonlinear forces will decrease the vibration amplitude of each solution along its motion. However a subspace tangent to each linear mode and such that if initial conditions belong to that subspace, the motion will remain on that subspace, still exists [42, 137]. To compute the nonlinear modes of non conservative systems, several strategies are available [55, 71, 77, 133]. In this work we will focus on the extended periodic motion concept firstly developed by Krack in [71]. The main reason behind this choice is the ease of implementation of the method that allows extending an existing continuation code with little effort. The interested reader is referred to [148] for a comparison between the extended periodic motion concept and complex nonlinear modes [77] for systems with non conservative nonlinear forces.

In the extended periodic motion concept, if the nonlinear forces dissipate energy, a term injecting energy in the system in the form of a fictitious negative damping can balance the losses due to the nonlinear forces and enforce the existence of periodic orbits. Similarly to the case of nonlinear mode, the definition by the user of a fictitious damping matrix will generate an additional dynamic stiffness matrix in the form of $\mathbb{A}_d(\omega)$. A multiplier of this matrix ζ, can be then seen as a fictitious damping ratio needed for periodic solutions to exist. The residual of such system reads:

$$\mathbb{R}(\mathbb{U}, \omega) = \left(\mathbb{A}_c(\omega) - \zeta \mathbb{A}_d(\omega)\right) \mathbb{U} - \mathbb{F}_{\mathrm{NL,nc}}(\mathbb{U}, \omega) \tag{2.155}$$

Once the phase constraint equation is added to the system, continuation can be performed in the same way than for a nonlinear mode with the only difference being that now ζ will be zero only if the nonlinear forces are neither dissipating nor injecting energy to the system, and strictly positive when the nonlinear forces are dissipative. The series of solution obtained in this way are sometimes also referred to as damped nonlinear mode. A final consideration about this method is about the choice of the fictitious damping matrix. The great advantage of the method lies in its simplicity and ease of implementation; however, the accuracy of the results is affected by the fact that the addition of a damping term changes the geometry of the found invariant manifold and might lead to a discrepancy between the found manifold and the actual one. Despite being an approximation of the actual invariant manifold, in an engineering context, the results provided by the method are still of great use for identifying the frequency-amplitude relationship and the amount of energy loss per cycle.

2.6 Code architecture

This chapter has presented the reader with a general overview of the methods and approaches that will be extended and used in the course of this work.

The general procedure outline described here will be used in the next chapters to study different structures and their nonlinear behaviours. A particular attention will be paid to the reduced order modelling methods introduced in Sec. 2.3, and, in the course of the next chapters, they will be scrutinised and their capabilities and limitations discussed.

The next three chapters are devoted to the study of geometrically nonlinear structures modelled with finite elements, whereas Chapter 6 will be focused on contact nonlinearities. Since most of the computations done in this thesis have large parts of code in common, here we report the generic code architecture for the two cases treated (i) geometric and (ii) contact nonlinearities. In Table 2.1, the four stages of the workflow of Fig. 2.1 are reported together with the codes used at each stage.

	FE discretisation	Reduced Order Model	Time discretisation	Continuation
Geom NL	Salome-Meca	Code Aster	ManLab	ManLab
Contact NL	Salome-Meca	Code Aster	Fortran	Python

Table 2.1: Code used for different stages of the workflow.

Each finite element model has been modelled, meshed and analysed in the open source code Salome-Meca/Code Aster [28], an integrated software developed by EDF. The code allows for python scripting, so reduced order models can be computed directly in the input file. All the reduced order modelling techniques that have been mentioned in this chapter (StEP, Hurty/Craig-Bampton, modal derivatives, quadratic manifold, normal form), together with others that will be introduced in the remainder of the thesis (direct normal form, M-StEP, contact derivatives) have been implemented in the software.

In the case of geometrically nonlinear structures, the reduced dynamical models extracted from Code Aster in the form of a system of ordinary differential equations, are solved in the open source code ManLab [27], which uses Harmonic Balance method for discretising the time, and Asymptotic Numerical method for parametric continuation. The implementation of the quadratic manifold method and the direct normal form method in Code Aster and the routines for computing forced response curves and backbones in ManLab have been made publicly available by the author in a github repository [164].

In the case of contact nonlinearities, a code has been implemented in fortran to test different time discretisation methods and contact laws. The code aims at mimicking the structure of the in-house code FORSE/jm62, developed at Imperial College London Vibration UTC and used by the industrial sponsor Rolls Royce for analysis of problems with contact nonlinearities with Harmonic Balance method and pseudo arc-length continuation. The code

developed by the author is a fortran code that takes inputs and produces outputs in the same format as FORSE/jm62. The code is wrapped in python and generates a python library (fortran fun) that is called by a continuation code written in python. Future developments of the code will integrate the fortran library inside FORSE/jm62 so that the python continuation algorithm will be replaced by that of FORSE/jm62. A schematic view of the code is reported in Fig. 2.7 and a more detailed description of each class is provided in Appendix C.

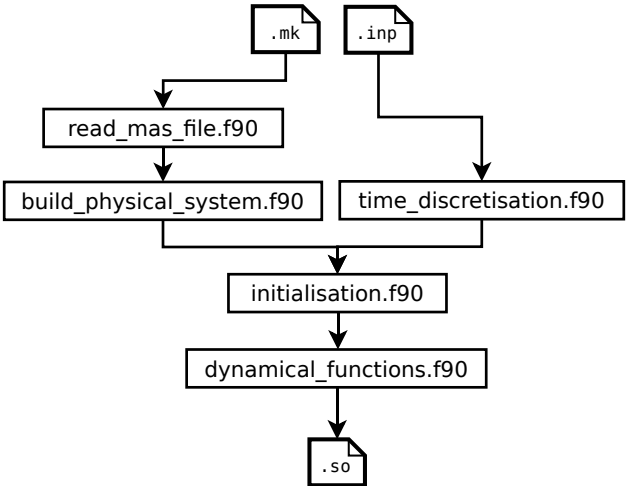


Figure 2.7: Schematic of the fortran fun library.

Chapter 3

Application of linear ROM for geometric nonlinearities and the problem of slow convergence of the linear basis

The aim of this chapter is to study the behaviour of ROMs for geometric nonlinearities when applied to 3D FE structures. The focus will be in particular on flat and symmetric structures. This type of structure can be solved with analytical models in the framework of geometrically-exact formulations. In the numerical implementation of this theory the main issue is the presence of rotational degrees of freedom [123]. The rotational degrees of freedom belong to a non-linear space, so that their general treatment is not trivial [144]. When modelled with 3D finite elements, no rotational degree of freedom is present thus no particular assumption is needed in their treatment. This is a great advantage when dealing with structures in large displacement and rotations but, as it will be shown, it comes with a price for some of the ROMs that will be presented. Not only 3D finite elements are more general with regards to the underlying assumption of the structural behaviour, but they are also more flexible when the geometry of the structure under investigation is complex. Since blades possess a complex geometry, they are normally discretised with three-dimensional finite elements, hexahedra in particular. It is then important to assess the validity of available ROMs when applied to 3D FE models. The investigation of flat symmetric structures in this context must not be seen as an interest in their dynamics, but more as a starting point for approaching the problem of ROMs for 3D finite elements. In fact, thanks to their symmetry, physical considerations about the coupling between modes arise in flat symmetric structures, thus providing a better ground for understanding the behaviour of geometric nonlinear forces in 3D finite elements.

We will refer to the reduction methods that require the system to be in the modal coordinates as *modal* ROMs in the following. In modal ROMs, when a particular nonlinear mode is of interest, the mode is taken as a master mode and its dynamics is studied. To do so, the blind application of StEP method with only one mode would produce wrong results be-

cause of the nonlinear couplings with other modes that will be referred to as either *slave* or *coupled* modes in the following. On the other hand, the application of StEP on all the modes of the structure would be infeasible due to too high number of operations that would be required.

To apply modal based ROMs to the structure is then first necessary to select only those modes that are known to be coupled with the master, and take them into account by applying a StEP procedure to those modes only [79]. In fact, flat symmetric structures allows to make assumptions based on the physics of the structure and find out that not all the modes are coupled to the low frequency bending modes through the nonlinear forces. In beams and plates modelled with 1D beam elements or 2D plate elements, the bending modes are coupled through quadratic nonlinearities only with a few well-known membrane modes. For example, a strong coupling between the first bending of a beam and the fourth axial mode is known to occur and a reduced order model obtained by application of StEP on those two modes only, would produce very accurate results [40]. Not only this approach allows to build small reduced models, but it also have the advantage of being non-intrusive from a computational point of view. For this reason, non-intrusive methods have been widely used to derive reduced-order models for geometrically nonlinear structures.

The Stiffness Evaluation Procedure (StEP) [97] presented in Sec. 2.2.6, relies on the static application of prescribed displacements in a finite-element context and permits to transform the system from physical to modal coordinates in a non-intrusive manner, i.e. without accessing the nonlinear forces at the finite element level. For its ease of implementation, it has been used in a number of different contexts [36, 79, 93, 94, 110]. The main advantage of this method is that it relies on classical static computations available in any finite element code, so that a user can derive the method without going into the code for programming new computations. Methods for which there is a need to implement the computations at the level of the element [135, 160] also exist.

Incidentally, the majority of papers where the StEP has been applied to thin structures, report results obtained with structures discretized with beam, plate or shell finite elements, as being mostly interested in slender structures. A few examples with hexahedral elements can be found in the literature, see *e.g.* [111, 170], where dual modes have been used in order to achieve convergence. An investigation of the behaviour of modal based ROMs when applied to a 3D FE model is not present in the literature.

Using 3D finite elements can be interesting in practice, sometimes mandatory. In engineering applications, structures are often defined with a 3D geometrical model, for which a 3D FE discretisation is straightforward. In other cases, some particular physical effects (piezoelectricity for instance) are sometimes implemented in existing FE codes only with 3D elements. Preliminary studies reveal a number of difficulties when applying the procedure to 3D finite elements, with more stringent inaccuracies and problems than those encountered with plate or shell elements. In particular, an unexpected slow convergence was observed when using the modal basis, and very high frequency modes appear to be

involved.

The objective of this chapter is to diagnose properly the issues one can encounter when selecting the modes for a modal basis to a structure discretized with 3D finite elements and present methods to overcome the problems. In the course of the chapter, it will be shown that the problem is intrinsically related to the use of the modal basis, and that the StEP can be used with other inputs than the modal basis, in order to get better results. We restrict our attention to thin structures that are symmetric in the thickness direction, such as straight beams or plates, for which there is a bending / longitudinal uncoupling at the linear level that greatly simplifies the understanding of the phenomena and enables to obtain reference results. We show that a particularly slow convergence of the modal expansion is observed and that the reason for this slow convergence is due to nonlinear couplings occurring with very high frequency modes involving 3D thickness deformations. Focusing on the case of flat structures, we first show by computing all the modes of the structure that a converged solution can be found by using either static condensation or normal form theory. We then show that static modal derivatives provide the same solution with fewer calculations. Finally, we propose a modified StEP, where the prescribed displacements are imposed solely on specific degrees of freedom of the structure, and show that this adjustment also provides efficiently a converged solution.

3.1 Motivating Example: a clamped-clamped beam

The particular nature of the nonlinear couplings in the case of flat symmetric structures such as beams and plates, relies on the simplifying facts that flexural and in-plane modes are linearly uncoupled, and their nonlinear couplings involve simple terms that can be easily traced from the von Kármán models. A classical example is the case of a clamped-clamped beam, for which geometric nonlinearities arise for a vibration amplitude in the order of the beam thickness. These simplifications have been used in numerous recent papers in order to explain why a number of methods for producing ROMs are able to predict very good results in this case, see *e.g.* [36,56,163]. In order to propose a simple two-dofs system mimicking these particular relationships, the von Kármán model for slender beams is used in order to produce a simplified system, whose coefficients can be related to meaningful quantities of the beam.

A non-prestressed beam of length L is thus considered, with a uniform rectangular cross section of area $S = bh$ (h being the thickness and b the width) and second moment of area $I = bh^3/12$, made in an homogeneous and isotropic material of Young's modulus E and density δ. Boundary conditions are clamped at $X = 0$ and $X = L$.

The equations of motion for the transverse displacement $W(X,T)$, and the longitudinal displacement $U(X,T)$ (X and T being the dimensional space and time variables), assuming

von Kármán theory, reads [36,100]:

$$\ddot{W} + \frac{EI}{\delta S} W'''' - \frac{E}{\delta}\left(U' W' + \frac{1}{2} W'^3\right)' = 0, \tag{3.1a}$$

$$\ddot{U} - \frac{E}{\delta}(U'' + W' W'') = 0. \tag{3.1b}$$

A particular feature of Eqs. (3.1) is that the longitudinal displacements are only quadratically coupled with the transverse, as shown in (3.1b). On the other hand, the only nonlinear terms appearing on the equations of motion for the flexural term W are: (i) a quadratic coupling involving a product between one in-plane and one transverse component, and a cubic term with only transverse components, see Eq. (3.1a).

Following [36], the equations of motion can be made nondimensional so that the resulting system depends only on two physically meaningful parameters: the slenderness ratio $\sigma = h/L$, and the wavelength β appearing naturally when solving the eigenvalue problem. Indeed, focusing on the linear problem for the transverse motion, the eigenvalue problem $\phi'''' = \omega^2 \frac{\delta S}{EI}\phi$ is solved by using a combination of sine, cosine, hyperbolic sine and hyperbolic cosine functions of kx, with k dimensional wavelength such that $k^4 = \frac{\delta S}{EI}\omega^2$ and $\beta = kL$. Assuming clamped boundary conditions the characteristic equation for β, from which the eigenfrequencies are deduced, reads : $\cos(\beta)\cosh(\beta) = 1$. The reader is referred to Appendix A for the details of this classical derivation.

Introducing the thickness h as characteristic length, so that the nondimensional displacements are as $w = W/h$ and $u = U/h$, normalizing time using $t = T(\beta^2/L^2\sqrt{EI/\delta S})$ and the space variable with the beam length, $x = X/L$; Eqs. (3.1) are rewritten as follows:

$$w_{,tt} + \frac{1}{\beta^4} w_{,xxxx} - \frac{12}{\beta^4 \sigma}\left(u_{,x} w_{,x}\right)_{,x} - \frac{6}{\beta^4}\left(w_{,x}{}^3\right)_{,x} = 0, \tag{3.2a}$$

$$u_{,tt} - \frac{12}{\beta^4 \sigma^2} u_{,xx} - \frac{12}{\beta^4 \sigma} w_{,x} w_{,xx} = 0. \tag{3.2b}$$

Let us now suppose that we are interested in studying the dynamics of the first bending mode of the beam. Such mode is a bending mode that only involves the flexural displacement w and no axial displacement u. However, in Eq. (3.2b), it is possible to see that the axial displacement is nonlinearly coupled to the flexural one. Due to the existence of this nonlinear coupling, a reduced order model composed of the sole bending mode would lead to wrong results and in particular to a much stiffer response of the system. A geometrical intuition for this behaviour can be given by imagining that a reduced model with the sole bending mode, would behave as a nonlinear structure that is forced to vibrate along its linear mode. This constraint would lead to a non-physical stiffening effect that would become the more visible the more the amplitude of oscillations increases. Therefore, in order to derive a reduced model from these equations, one has to select, together with the first bending mode of interest, the most important longitudinal modes coupled to the first

flexural. From previous studies, see *e.g.* [36, 40, 143], it is known that the fourth in-plane mode is strongly coupled to the first flexural. Not only the coupling is very strong, but it is also so much higher than the other couplings that a reduced model solely composed of these two modes is enough to capture the correct dynamics of the beam.

Let us denote as q_1 the modal amplitude of the first transverse mode and p_4 the modal amplitude of the fourth in-plane mode (see Appendix A for the details). Using a standard Galerkin projection (see *e.g.* [36]), Eqs. (3.2) can be rewritten as:

$$\ddot{q}_1 + q_1 + \frac{2G}{\sigma} p_4 q_1 + D q_1^3 = 0, \tag{3.3a}$$

$$\ddot{p}_4 + \frac{(4\pi)^2 12}{\beta^4 \sigma^2} p_4 + \frac{G}{\sigma} q_1^2 = 0, \tag{3.3b}$$

where D and G are the nonlinear coupling coefficients arising from the Galerkin projection, and involves integral on the length of products of derivatives of the mode shape functions, see [36] for the general calculation and Appendix A for the detailed expression of these two coefficients.

One can note in particular that, due to the choice of the nondimensional time to arrive at Eqs. (3.2), the eigenfrequency of the first flexural mode is 1, while the natural frequency of the fourth in-plane mode reads $\omega_2^2 = \frac{(4\pi)^2 12}{\beta^4 \sigma^2}$. Due to the normalisation selected (involving $\omega_1 = 1$ for the fundamental mode), the term in factor of p_4 in Eq. (3.3b) can be easily interpreted as the square of the ratio $\rho = \omega_2/\omega_1$; in the next chapter, the importance of this ratio for the fulfilment of the slow/fast assumption will be thoroughly discussed. For now, we just want to highlight that this ratio ρ, can be directly related to the slenderness ratio σ of the beam through the following expression:

$$\rho = \frac{4\pi\sqrt{12}}{\beta^2}\frac{1}{\sigma} \approx 1.95\frac{1}{\sigma}. \tag{3.4}$$

Even if the reduced model given by Eq. (3.3) is already very small having only two degrees of freedom, a further reduction could be done in this case by noticing that the frequency of the fourth in-plane mode is very high compared to that of the first bending for a thin enough structure. The inertia of the fourth in-plane mode can then be neglected and only its static contribution considered. This procedure is called static condensation and its generalisation will be better described in the next section. A direct relation between q_1 and p_4 can be found through this procedure and Eq. (3.3) will read:

$$\ddot{q}_1 + q_1 + (D - \frac{G^2\beta^4}{(4\pi)^2 6}) q_1^3 = 0 \tag{3.5}$$

The reduced order model built through static condensation is the minimal size possible and its dynamics is represented by that of a Duffing oscillator. It can be proved that for slender

structure with σ small enough, the behaviour obtained by solving the single oscillator of Eq. (3.5), is equivalent to that obtained by solving the two dofs model of Eq. (3.3). A quantitative evaluation of the error of the static condensation procedure as a function of the ratio ρ will be provided in the next chapter. For now we just want to point out that both Eq. (3.3) and Eq. (3.5) provides very good reduced models for the beam and that the solution obtained by solving these systems will be able to reproduce the free vibration behaviour of the full model with a great accuracy.

Similarly, if a finite element model of the beam made of 1D or 2D finite element was studied, a two degrees of freedom model composed of solely the first bending and fourth axial mode or a one dof model build with static condensation of the fourth axial mode with respect to the bending would have as well matched the solution of the full model [40]. Conversely, if 3D elements were used, a much higher stiffening effect would be encountered as it will be shown in this Chapter, suggesting that the inclusion of the fourth axial mode is not enough and other modes are coupled with the first bending. Like the quadratically coupled axial modes have to be included in the reduced model or they would generate an unnatural stiffening effect, similarly, 3D modes with a strong quadratic coupling must be considered or the reduced model will not be accurate. It will be shown that indeed a quadratic coupling does exist between low frequency bending modes and thickness modes. A justification for this behaviour that does not affect 1D and 2D elements can be seen in the fact that the linear modes of a 3D beam involve deformations of the section; such deformations are different from those of the nonlinear modes, in which nonlinear effects are also present. A reduced model that does not include the coupled thickness modes that are able to relax such deformations would behave like a nonlinear structure whose imposed section deformation is the one predicted by the linear modes, thus generating a non-physical stiffening effect.

3.2 The case of a flat thin structure

Let us recall the equation of a generic FE system with geometric nonlinearities expressed in modal coordinates, Eq. (2.54):

$$\ddot{\boldsymbol{q}} + \boldsymbol{\Xi}\dot{\boldsymbol{q}} + \boldsymbol{\Omega}^2\boldsymbol{q} + \boldsymbol{g}_{ij}q_iq_j + \boldsymbol{h}_{ijk}q_iq_jq_k = \boldsymbol{f}_{\text{ext}} \tag{3.6}$$

As stated in the previous chapter, the StEP method would require a very high number of operation to compute the full tensors $\boldsymbol{g}$ and $\boldsymbol{h}$ that scales as the third power of the number of degrees of freedom of the structure. This is the main weakness of modal ROMs and it will discussed in details in Ch. 5 and also in the last two sections of this chapter. However, we will see in the following that not all the entries of $\boldsymbol{g}$ and $\boldsymbol{h}$ are actually necessary but only those related to important coupled modes. For the moment though, let us assume that all the entries are available. Then, Eq. (3.6) would provide the equation of motion of the full model in modal coordinates.

In the present case of a 3D structure which has the shape of a beam / plate, it is possible to split the modes into two families in a similar fashion to what has been done in the previous section. The first family includes the bending modes, analogous to the ones obtained in the plate theory. Their frequencies are in the lower part of the spectrum, while their deformed shapes are dominated by transverse displacements. They, up to the accuracy of the plate theory, have the same displacement field in the middle plane / line, with no longitudinal displacement. The second family gathers all the other modes that we will denote as non-bending, that appear at higher frequencies in the spectrum. Some of them are analogous to the longitudinal modes of the plate theory, with the same transverse displacement field in the middle plane / line. Other modes are also present, linked to 3D effects and thus with no counterpart in the beam / plate theory, with mode shapes dominated by thickness deformations. For any mode of this second family, the displacement field in the middle plane / line has only longitudinal components, and thus no transverse component. Examples of coupled modes will be shown throughout the Chapter, especially in Tab. 3.1.

Let us decompose the displacement vector $\boldsymbol{q}$ by denoting as q_r, $r = 1, ..., N_B$ the bending coordinates, and p_s, $s = N_B + 1, ..., N$ the membrane coordinates: $\boldsymbol{X} = [q_1, ..., q_{N_B}, p_{N_B+1}, ..., p_N]^{\mathrm{T}}$. Then, Eq. (3.6) can be rewritten for each coordinates [36, 56] and involves quadratic and cubic coupling terms between the q_r and the p_s. We restrict ourselves to the case of a transverse low frequency excitation, for which the external forces remain normal to the middle plane of the plate. As a consequence, the dynamics is dominated by the bending modes, which are the only ones that receive external excitation. In this case, Eq. (3.6) can be simplified. First, all quadratic g^r_{ij} coefficients involving two bending coordinates i, j vanish, in order to fulfil the symmetry of the restoring force [36, 150]. In addition, one can assume that the bending coordinates, which are directly excited by the external forcing, are considered of the order magnitude of a small parameter ε: $q_r = O(\varepsilon)$, for all $r \in \{1, \dots, N_B\}$. On the other hand, non-bending coordinates, since they are not directly excited and shall vibrate at a lower order of magnitude, are assumed to scale as ε^2: $p_s = O(\varepsilon^2)$ for all $s \in \{N_B + 1, \dots, N\}$. Plugging these two scaling in Eq. (3.6) and keeping only the leading order, one arrives to, for the bending coordinates, $\forall\ r = 1, ..., N_B$:

$$\ddot{q}_r + \xi_r \dot{q}_r + \omega_r^2 q_r + \sum_{i=1}^{N_B} \sum_{s=N_B+1}^{N} 2\, g^r_{is} q_i p_s + \sum_{i=1}^{N_B} \sum_{j=1}^{N_B} \sum_{k=1}^{N_B} h^r_{ijk} q_i q_j q_k + O(\varepsilon^4) = f_r, \tag{3.7}$$

and for the membrane coordinate, $\forall\ s = N_B + 1, ..., N$:

$$\ddot{p}_s + \xi_s \dot{p}_s + \omega_s^2 p_s + \sum_{i=1}^{N_B} \sum_{j=1}^{N_B} g^s_{ij} q_i q_j + O(\varepsilon^3) = 0. \tag{3.8}$$

In the above equation, one can notice that because of the transverse excitation, the second member of Eq. (3.8) is zero.

Eqs. (3.7,3.8) approximate the dynamics of the structure in the present case of a 3D FE model. If an analytic von Kármán model was used, those equations would be exact, with

the terms $O(\varepsilon^3)$ and $O(\varepsilon^4)$ identically vanishing [36]. Those equations also show that the in-plane vibrations are quadratically coupled to the bending coordinates, while in the equations of motion of the transverse modes, only two nonlinear terms have to be taken into account: a quadratic coupling involving a product between a transverse and an in-plane coordinate, and a cubic term involving three transverse modes. This very specific form of equations renders the case of flat structures easier to solve than general shell problems that encompass all the possible nonlinear couplings as stated in Eq. (3.6).

3.3 Static Condensation

Since the non-bending modes have natural frequencies very large as compared to those of the directly excited bending modes, $\omega_s \gg \omega_r$, the dynamical part of Eqs. (3.8) can be neglected. The nonlinearities being more simple in this case, one can directly express the non-bending coordinate as function of the bending ones as:

$$p_s = -\sum_{i=1}^{N_B}\sum_{j=1}^{N_B} \frac{g_{ij}^s}{\omega_s^2} q_i q_j. \tag{3.9}$$

Substituting Eq. (3.9) into Eq. (3.7), one can rewrite the dynamics of the structure as a closed system involving only bending coordinates as:

$$\ddot{q}_r + \xi_r \omega_r \dot{q}_r + \omega_r^2 q_r + \sum_{i=1}^{N_B}\sum_{j=i}^{N_B}\sum_{k=j}^{N_B} \Gamma_{ijk}^r q_i q_j q_k = f_r, \tag{3.10}$$

where the corrected cubic Γ_{ijk}^r coefficients appear. Their general expression is:

$$\Gamma_{ijk}^r = h_{ijk}^r - \sum_{s=N_B+1}^{N} \mathcal{C}_{ijk}^{rs} \tag{3.11}$$

where the correction factors have been introduced and read:

$$\mathcal{C}_{ijk}^{rs} = 2\frac{g_{is}^r g_{jk}^s}{\omega_s^2} \tag{3.12}$$

If one is interested in deriving a reduced-order model for a single bending mode (say the master mode with label p), taking into account all the other non-bending mode, then Eq. (3.10) can be used and the leading nonlinear cubic term simply reduces to:

$$\Gamma_{ppp}^p = h_{ppp}^p - \sum_{s=N_B+1}^{N} \mathcal{C}_{ppp}^{ps} \tag{3.13}$$

with the correction factors:

$$\mathcal{C}_{ppp}^{ps} = 2\frac{g_{ps}^p g_{pp}^s}{\omega_s^2} = 2\frac{{g_{pp}^s}^2}{\omega_s^2} \tag{3.14}$$

These expressions show that the cubic term h^p_{ppp} of the standard modal expansion must be corrected by the summation of all non-bending modes quadratically coupled to the master one.

The quadratic coefficients g^p_{ij} have some symmetry relationships, provided that the nonlinear stiffness derives from a potential [97]. In particular, the following relationship holds: $g^p_{ps} = g^s_{pp}$, which leads to the second equation (3.14).

Recalling the derivation of the StEP method, the evaluation of g^s_{pp} requires only the computation of the nonlinear force when the displacement along the p-th linear mode is prescribed, whereas the calculation of the g^p_{ps} coefficients for each s-th mode would require as many evaluation of the nonlinear force as the number of non-bending modes. Nevertheless, it requires the projection of nonlinear force onto each membrane eigenvector ϕ_s, and thus their computation.

From a physical perspective, the coefficient g^s_{pp} can be seen as the projection onto the s-th membrane mode of the quadratic stiffness forces arising in the structure when a displacement along the linear p-th mode is imposed. Interestingly, this quadratic coefficient is related to a monomial q_p^2 on the s-th oscillator equation for p_s. Terms like this one have been named invariant-breaking terms in [153, 158], and they are defined as the monomials in the sole master modes that appear in the equation of motion of a slave mode. As soon as energy is given to a master mode p, the linear invariance will be broken and all s modes having a monomial in the sole q_p will no longer be vanishing. These invariant-breaking terms are then responsible for the loss of invariance of the linear eigenspaces, and they are found back naturally as correction factors when applying static condensation. They are also key in the formulation of invariant manifolds to define NNMs in phase space [136, 158].

3.4 Normal Form

In parallel to the static condensation emphasised here, one can use the reduction formulae given by the normal form approach, restricting the motion to a single Nonlinear Normal Mode (NNM) [153, 158, 160]. In this case, the reduced order model is directly constructed from Eqs. (3.6). The main advantage as compared to the above described static condensation is that there is no need to assume the particular structure of the equations obtained for flat structures (Eqs. (3.7,3.8)), thus generalizing the results to arches and shells. Recalling the system of equations (2.113) provided in Sec.2.3.6 where the normal form approach has been presented, it is possible to show that the vectors $\boldsymbol{a}$ and $\boldsymbol{b}$ of components a^s and b^s are the results of the system (2.113) when the master mode is the p-th mode:

$$a^s = -\frac{g^s_{pp}}{\omega_s^2}\frac{\omega_s^2 - 2\,\omega_p^2}{(\omega_s^2 - 4\,\omega_p^2)} \tag{3.15a}$$

$$b^s = +\frac{g^s_{pp}}{\omega_s^2}\frac{2}{\omega_s^2 - 4\,\omega_p^2} \tag{3.15b}$$

Similarly, recalling the definition of the reduced dynamics given in Eq. (2.115b) and Eq.(2.116), the reduced-order model reads:

$$\ddot{q}_p + \omega_p^2 q_p + \left(\sum_{s=N_B+1}^{N} -2\frac{g_{ps}^p g_{pp}^s}{\omega_s^2} \left(\frac{\omega_s^2 - 2\omega_p^2}{\omega_s^2 - 4\omega_p^2} \right) + h_{ppp}^p \right) q_p^3 + \left(\sum_{s=N_B+1}^{N} 2\frac{g_{ps}^p g_{pp}^s}{\omega_s^2} \left(\frac{2}{\omega_s^2 - 4\omega_p^2} \right) \right) q_p \dot{q}_p^2 = 0 \,. \tag{3.16}$$

Once again, one can observe that the correction brought to the cubic term h_{ppp}^p is solely given by the quadratic invariant-breaking terms. If one has been able to compute all the quadratic g_{pp}^s coefficients appearing in Eq. (3.16), then the model can be used to simulate the dynamics. Also, it is worth mentioning that since the non-bending modes have high frequencies, we can assume that $\omega_s \gg \omega_p$ (which is equivalent to neglect the membrane inertia). Then the term in factor of q_p^3 in Eq. (3.16) exactly reduces to the one obtained with static condensation in Eq. (3.10). On the other hand, the term in factor of $q_p \dot{q}_p^2$ has no counterpart in static condensation, but is an order of magnitude smaller since it scales as $1/\omega_s^4$, so that both models are almost equivalent when a slow/fast decomposition can be assumed. This extends the results of [29], in which the term q_p^3 is chosen as the leading term for experimental identification purposes. A complete comparison of static condensation and nonlinear normal modes is also provided in [140] in the context of clarifying the implicit condensation and expansion method. Finally, one can note that the formula used in Eq. (3.16) have been obtained thanks to a normal form approach on the conservative system [158], but they can be extended in order to take into account the damping of the slave modes in the master coordinate ROM, hence accounting for a finer prediction of the losses [154] as it will be shown in Chapter 5, a feature that once again is not possible with static condensation.

3.4.1 Convergence with 3D elements

In order to shed light on the couplings arising between the modes, a test case is chosen. It is a thick beam, with the same length $L = 1$ m but with a square cross section with $h = b = 30$ mm, as shown in Fig. 3.1. The cross section was chosen square to be able to easily observe the 3D deformations of the cross section. The material properties are $E = 210$ GPa for the Young's modulus and $\rho = 7800$ kg/m^3 for the density. and $\nu = 0.3$ for the Poisson ratio. A coarse mesh of 15 HEX20 elements along the axis and 2×2 in the cross section is chosen, to obtain full model with a reduced number of degrees of freedom (1287). The analyses on this beam are run in the software CodeAster [28]. For the sake of simplicity, we restrict attention to the convergence of the effective cubic coefficient of the first bending mode, Γ_{111}^1.

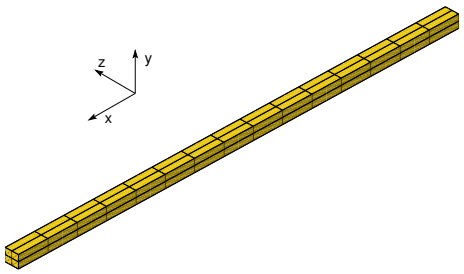
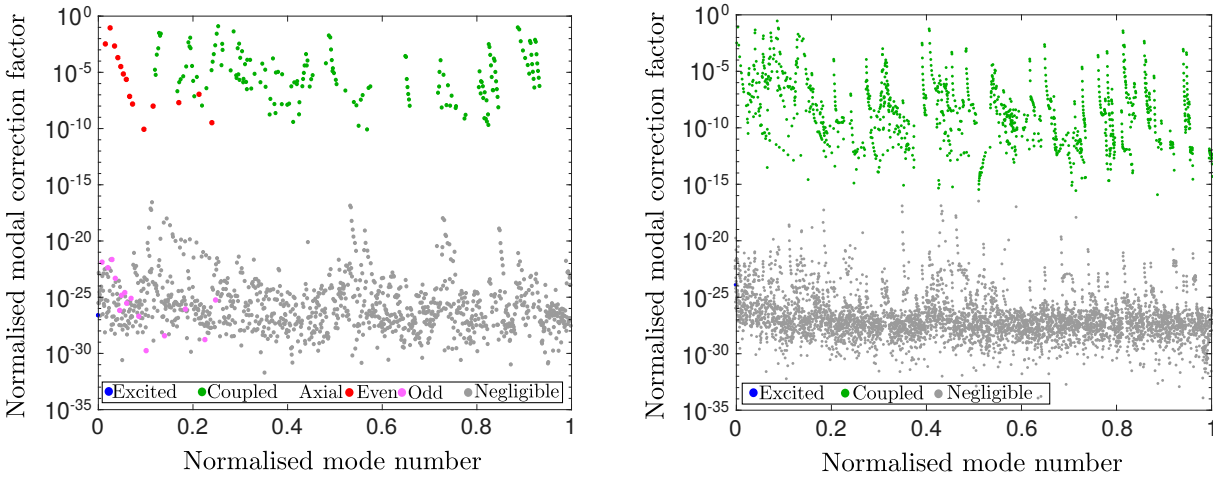


Figure 3.1: Clamped-clamped beam mesh

Fig. 3.2(a) shows the behaviour of the correction factor $\mathcal{C}^{1s}_{111}$ (defined in Eq. (3.14)), normalized by the cubic coefficient h^1_{111}, as a function of the mode number s, for the thick beam having 1287 dofs. This plot shows that the number of modes that are coupled to the first bending mode by invariant-breaking terms is very large, and uniformly distributed along the frequency spectrum. In order to facilitate the readings, the modes for which the correction factor is below 10^{-15} have been sorted as negligible. In this family of modes that are not important, one find backs all the odd axial modes, for symmetry reason. On the other hand, all even axial modes are strongly coupled to the first one. The most surprising result is that if one does considers only axial modes, then only a few portion of the couplings will be revealed and taken into account. Indeed, Fig. 3.2(a) shows that there is a very large number of modes having very large frequencies, and still being strongly coupled to the master bending mode.



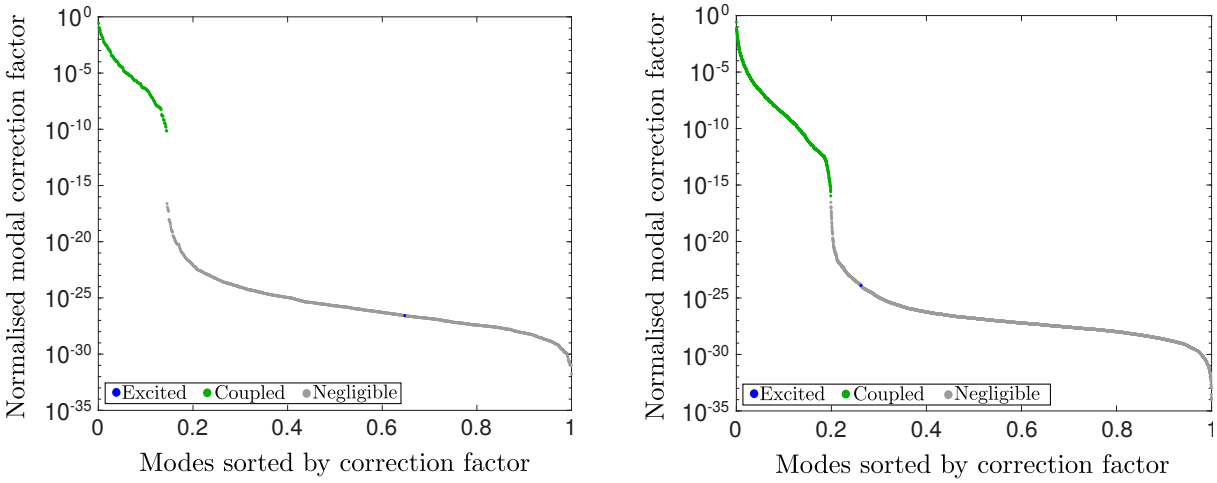
(a) Beam discretised with 1287 dofs

(b) Beam discretised with 5733 dofs

Figure 3.2: Nondimensional correction factor $\mathcal{C}^{1s}_{111}/\beta^1_{111}$ (Eq. (3.14)), associated to the first bending mode ($p = 1$) and to all the other modes ($s = 2, \dots N$) of the thick beam testcase, over the nondimensional mode number s/N. The Poisson ratio is $\nu = 0.3$.

In order to check the independence of this behaviour from the mesh refinement, a second mesh of 20 elements on the axis and 3 x 3 elements on the section has been defined on the same beam geometry. Fig. 3.2(b) reports a very similar behaviour for this second test case, where the distribution of coupled modes is uniform along the whole set of modes.

Fig. 3.3 shows the same data than Fig. 3.2, but with now the modes sorted by decreasing



(a) Beam discretised with 1287 dofs

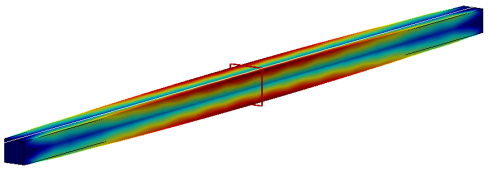
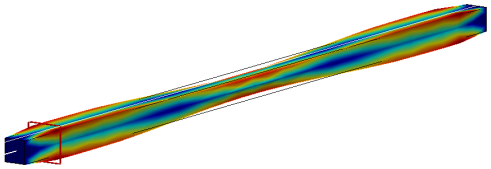
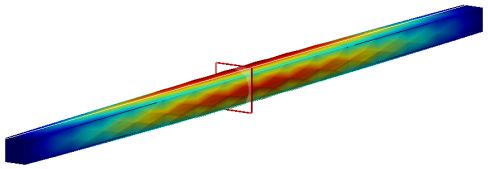
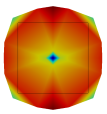
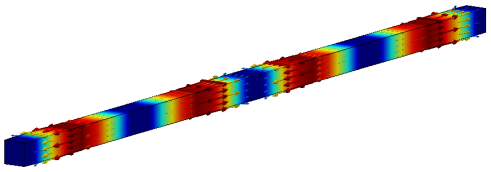
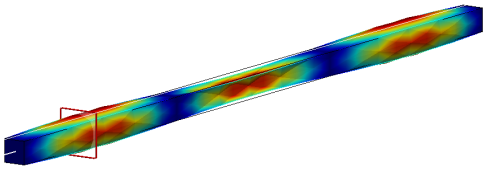
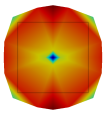
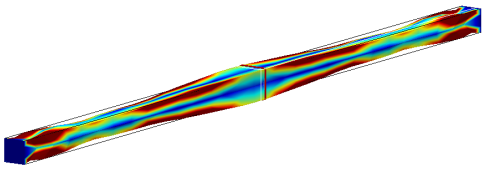
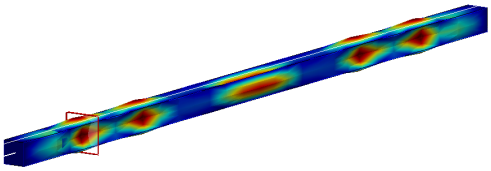
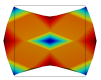
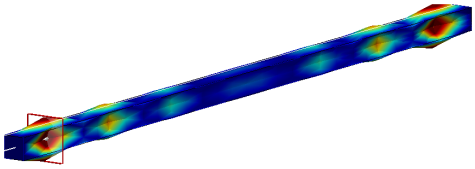
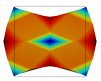
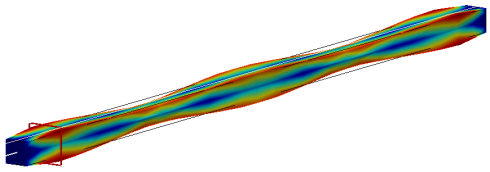
(b) Beam discretised with 5733 dofs

Figure 3.3: Nondimensional correction factor $\mathcal{C}^{1s}_{111}/h^1_{111}$ (Eq. (3.14)), associated to the first bending mode ($p = 1$) and to all the other modes ($s = 2, \dots N$) of the thick beam test-case, over the sorted nondimensional mode number s/N, where the imposed order is by decreasing correction factor.

correction factor. It is possible to observe that, by choosing 10^{-15} as a threshold for the significance of each contribution, a small percentage of modes, around 20%, is actually relevant. Consequently, the number of relevant modes depends on the mesh: the more refined it is, the more relevant modes are needed in the reduced model to achieve a given accuracy . Moreover, as seen on Fig. 3.2, these modes are spread over the entire spectrum, which would need the computation of all the eigenmodes of the structure, an operation impossible in practice for a complex structure with a larger number of dofs.

In order to gain insight into these coupled modes, Table 3.1 shows the associated mode shapes, sorted according to the importance of their contribution in the correction factor, thus following Fig. 3.3(a). The table shows the first nine eigenmode shapes, recalling in the first column their number of appearance when the modes are sorted according to the eigenfrequencies. One can observe that only one of these modes is a pure axial mode: the fourth one appearing in table 3.1, also being the 34^{th} by order of increasing frequencies. All the other ones involve important deformation in the thickness of the beam. They are thus called thickness modes, their presence being the direct consequence of 3D effects. The second column of Table 3.1 displays the eigenfrequencies, showing that they all are high-frequency modes. The last column shows the deformation of the section, showing the importance of thickness deformation.

The frequency-response curves obtained with a value of damping mass-proportional with a factor 3 and point force of $200N$ in the central node of the beam in the vicinity of its first eigenfrequency is investigated in order to illustrate how the static condensation and the normal form approach are able to retrieve the correct nonlinear behaviour. Fig. 3.4(a) shows the comparison of the solutions obtained by continuation, for different reduced-order models and the full model solution. The latter has been obtained by solving all

Coupled modes				
#	$\omega_s/(2\pi)[Hz]$	$\mathcal{C}^{1s}_{111}/\Gamma^{1}_{111}$	Shape	Section
330	1.137e5	3.22e-1		
328	1.125e5	1.34e-1		
1143	3.698e5	1.05e-1		
34	1.043e4	9.26e-2		
1147	3.699e5	7.01e-2		
370	1.202e5	4.60e-2		
167	7.644e4	3.35e-2		
172	7.653e4	2.93e-2		
324	1.112e5	2.89e-2		

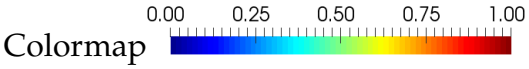
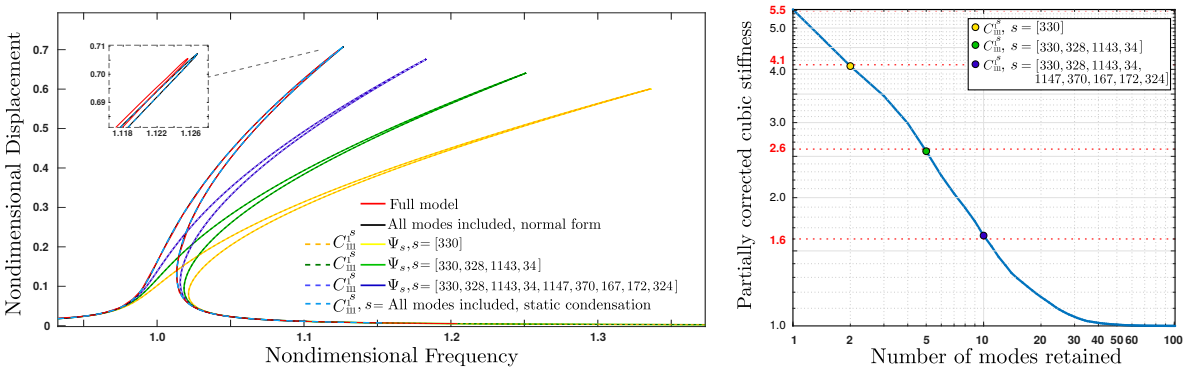


Table 3.1: Order of appearance in the basis (#), eigenfrequencies, correction factors and shapes of the most relevant modes coupled with the first bending mode in y-direction for the clamped-clamped beam. The colors scale the modulus of the displacement field and arrows display the axial displacement for axial mode 34.



(a) Forced response functions at beam centre node

(b) Convergence of partially corrected cubic coefficients

Figure 3.4: Convergence to the full model solution with the increase of coupled modes taken into account in the reduced model. (a) Frequency response curve of the beam at center, in the vicinity of the first bending mode eigenfrequency; case of the thick beam with 1287 dofs. Red: full model, and convergence curves with increasing number of modes retained in the truncation: 1 mode (yellow), 4 modes (green), 9 modes (blue), all modes statically condensed (dashed light blue). Solution with normal form in black. (b) Convergence of the evaluated corrected cubic stiffness coefficient Γ^1_{111}, defined in Eq. (3.13), with increasing number of linear modes kept in the truncation.

the degrees of freedom of the system with a parallel implementation of harmonic balance method and pseudo-arc length continuation [17]; the computation of the full forced response with 3 harmonics lasted approximately 36 hours. The convergence of the solution using static condensation with an increasing number of modes to compute the correction is also shown. Even if only few modes have a very high correction factor $\mathcal{C}^{s1}_{111}$, *i.e.* play a major role in the decrease of h^1_{111} (see Eq. (3.13)), it is the sum of the contributions from all the coupled modes that makes the reduced model converge to the solution of the full one. In Fig. 3.4(b), the strong stiffening effect coming from not having included enough coupled modes, is slowly reduced by their inclusion in the basis; however, only the response obtained by static condensation of all coupled modes (cyan dashed) approximates the solution correctly (almost overlapped with the full model solution in red). Similarly, the normal form solution with all the modes taken into account show also a direct convergence to the frequency-response curve. Although not shown in the Figure, the solution of the normal form with an incomplete basis would also show the same slow convergence than that of the static condensation, thus highlighting that this problem affects any modal ROM.

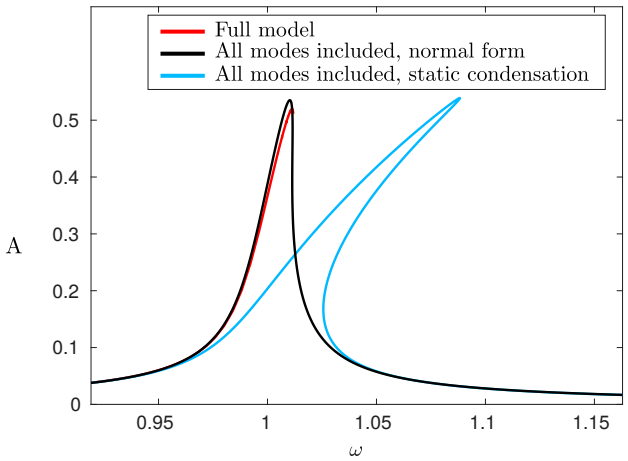
Fig. 3.4(b) shows the convergence of the corrected cubic coefficient Γ^1_{111} defined in Eq. (3.13) with the number of modes retained, i.e. the first mode plus the number of coupled modes condensed. When only one coupled mode is taken into account, the cubic coefficient h^1_{111} overestimates largely Γ^1_{111} (5.5 times). With 9 coupled modes the error on Γ^1_{111} is still significant (more than 60%). This strong overestimation of the cubic stiffness value results in the unrealistic stiffening effect observed in the forced response. The number of coupled modes that must be taken into account to ensure an acceptable accuracy makes the use the linear modes as projection basis without condensation impractical: 44 modes give a 1%

error and 68 an error of 0.1%. Not only a high number of degrees of freedom would be left in the reduced model thus making the reduced dynamics computation slow, but also the number of StEP method computations required to build the reduced dynamics with all the tensors entries would take a long time to run. The condensation of these modes onto the master one or the application of normal form, become a viable option to drastically reduce the computational burden without affecting the accuracy of the solution. In fact, it is worth underlining that the reduced model produced by static condensation and normal form is always in the form of a single oscillator, so all the computational burden of computing the eigenvectors is an offline cost.

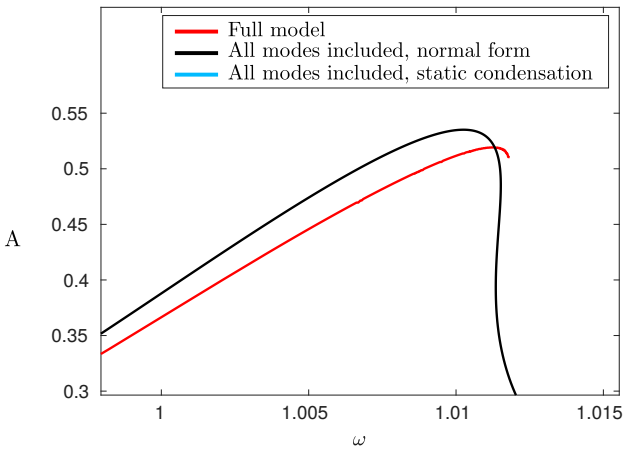
We have shown that in the case of 3D elements, a strong coupling with thickness modes occurred, thus rendering the convergence of the modal ROM particularly slow. When one is able to compute all the linear modes of the structure and their associated quadratic coefficients, then static condensation and normal form approach can be equivalently used to produce accurate ROMs in the case of a flat structure. In this case, the discretisation of the beam consisted in 1287 and 5733 dofs, thus making the computation of the full eigenvector matrix possible. However in large FE models, the computation of all the linear modes is out of reach. Before moving to the next section where we will investigate two alternative methods for which there is no need to compute all the linear modes, we want to show an example for which a substantial discrepancy between the static condensation method and the normal form method occur. So far the two methods have been shown to be completely equivalent. However, while the normal form is supported by a rigorous mathematical foundation that permits to compute the nonlinear mode of the system, the static condensation has to be seen as an approximate way of computing the nonlinear mode that is only applicable under certain assumptions. In Fig. 3.5 the same approach proposed so far has been applied on the same beam but with different boundary conditions; in this case, the beam is a cantilever so the structure thus is no longer symmetric. We see that the normal form is able to retrieve the correct dynamics of the structure at high amplitude vibration whereas the static condensation displays an overestimated stiffening effect. The reason for this lies in the importance that inertial effects assume in this case, thus making the assumption of negligible inertia of the static condensation no longer applicable. This results is known in literature as shown in [68].

3.5 Static modal derivatives

The previous sections have been devoted to the derivation of a reduced order model from a modal point of view. In fact, a modal projection of the quadratic nonlinear forces onto each mode ϕ_s is required to obtain the coefficients g^s_{pp}. The strong limitation of modal ROMs is the need for computing all the eigenvectors of the structure. Here we want to introduce the concept of static modal derivatives (see [53]) because its application provides the same results as the static condensation of all non-bending modes, but without requiring the computation of their associated eigenvectors.



(a) Forced response functions.



(b) Zoom on resonance.

Figure 3.5: Application of normal form and static condensation to the case of a cantilever beam.

The definition of modal derivatives have arisen from the recognition of the fact that in the nonlinear range, mode shapes and frequencies depend on amplitude [53]. Introducing this dependency in the eigenproblem defining the modes, one arrives at a quantity defined as the modal derivative [53, 173]. Following the definition of static modal derivatives $\boldsymbol{\theta}_{pp}$ (SMD) from Chapter 2, it reads:

$$\boldsymbol{\theta}_{pp} = \boldsymbol{K}^{-1}\left(-\frac{\partial^2 \boldsymbol{F}_{\mathrm{NL}}}{\partial q_p^2}\bigg|_{\mathbf{0}}\right) \tag{3.17}$$

The term in brackets coincides with two times the vector of quadratic forces when $\boldsymbol{U} = \boldsymbol{\phi}_p$, *i.e.* the previously defined vector $\boldsymbol{G}_{pp}$. The SMD can be then computed in a finite difference fashion as:

$$\boldsymbol{\theta}_{pp} = -\boldsymbol{K}^{-1}\left(\frac{\boldsymbol{F}_{\mathrm{NL}}(+\lambda\boldsymbol{\phi}_p) + \boldsymbol{F}_{\mathrm{NL}}(-\lambda\boldsymbol{\phi}_p)}{\lambda^2}\right). \tag{3.18}$$

Eq. (3.18) shows how the SMD can be easily computed from a set of applied static displacement, in an analogue manner to the StEP. The term in parenthesis in Eq. (3.18) can be seen as the numerical second order derivatives with respect to λ of the nonlinear force along mode p, evaluated at the equilibrium position. This can be easily evaluated in any FE software by imposing, on a nonlinear structure, a displacement proportional to the linear p-th mode with first positive and then negative sign in order to isolate the quadratic part of the nonlinear forces.

The SMD can thus be seen as an added displacement vector that enriches the basis constituted by the linear mode p, in a way that takes into account the nonlinear deformation of the structure. The use of SMDs as added vectors in the reduced order model basis is extensively documented in [56, 127, 143, 151, 173], and a complete comparison of quadratic manifolds derived from modal derivatives with normal form theory is given in [166] as well as in the next chapter. Here the focus is on the relationship between modal deriva-

tives and non-bending modes and on the equivalence between static condensation of all non-bending modes and static condensation of modal derivatives.

If one wants to draw an analogy with the previous calculations, the expression of the SMD in terms of $\boldsymbol{g}_{pp}$ has to be derived. To do so we first express the SMD in terms of the quadratic force vector in physical basis:

$$\boldsymbol{\theta}_{pp} = -2\,\boldsymbol{K}^{-1}\boldsymbol{G}_{pp} \tag{3.19}$$

Then, by introducing the full matrix of eigenvectors $\boldsymbol{\Phi}$, and by noticing that $\boldsymbol{\Phi}^{\mathrm{T}}\boldsymbol{K}\boldsymbol{\Phi} = \Omega^2$, from which it follows that $\boldsymbol{K}^{-1} = \boldsymbol{\Phi}\Omega^{-2}\boldsymbol{\Phi}^{\mathrm{T}}$, the value of $\boldsymbol{K}^{-1}$ is substituted in Eq. (3.19). Finally, the static modal derivatives related to the p-th linear mode can be expressed in terms of the vector of quadratic coefficients $\boldsymbol{g}_{pp}$ as:

$$\boldsymbol{\theta}_{pp} = -2\boldsymbol{\Phi}\boldsymbol{\Omega}^{-2}\,\boldsymbol{g}_{pp}\,, \tag{3.20}$$

where the relation $\boldsymbol{\Phi}^{\mathrm{T}}\boldsymbol{G}_{pp} = \boldsymbol{g}_{pp}$ has been used to make the vector $\boldsymbol{g}_{pp}$ appear.

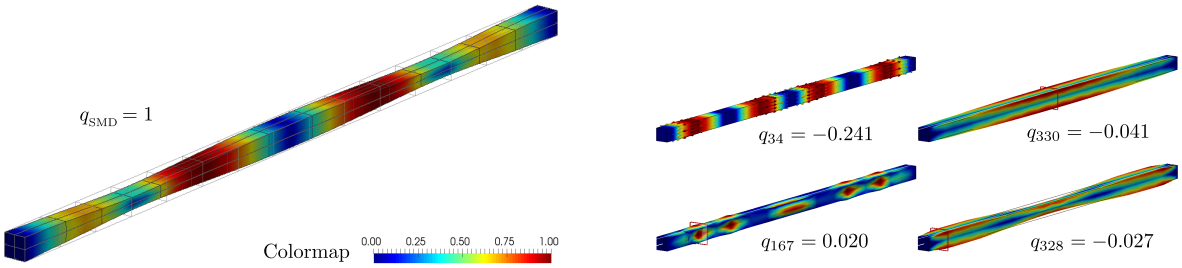
By expanding Eq. (3.20) over all the modes and by noticing that, for a flat structure, g^s_{pp} is non-zero only when s is a non-bending mode, one obtains this important relationship :

$$\boldsymbol{\theta}_{pp} = -\sum_{s=N_B+1}^{N} 2\phi_s \frac{g^s_{pp}}{\omega_s^2}. \tag{3.21}$$

The SMD thus appears as a linear combination of coupled modes with factor $-2g^s_{pp}/\omega_s^2$; therefore, it can be seen as a displacement field that takes into account the contribution of all non-bending modes into one equivalent vector. To show this property, the SMD relative to the first bending mode of the thick beam test case is depicted in Fig. 3.6a. The projection of the SMD onto the linear modes of the system recovers Eq. (3.21). The contributions from the non-bending modes that have been identified in previous calculations, the fourth axial mode as well as various thickness modes, appear in the SMD. For each mode s, the modal amplitudes q_s obtained from the projection coincides with those from Eq. (3.21) i.e. they are equal to $-2g^s_{pp}/\omega_s^2$.

These results recover and elaborate on those obtained in [56, 143], where it was shown that axial modes are contained in the SMDs of bending modes. The result is here extended to thickness modes and given a full expression since the exact participation factor of each mode is provided.

Once understood that the SMD allows gathering in a single vector the participation of all coupled modes, we want to show how to retrieve directly, from the calculation of the SMD, the correct nonlinear behaviour of the structure, when the motion is restricted to a single master mode. In the specific case of a flat structure, Eq. (3.9) shows that the amplitudes of the non-bending modes can be explicitly related to the squared amplitude of the single



(a) Static modal derivatives (b) Non-bending modes

Figure 3.6: (a) Static modal derivative $\boldsymbol{\theta}_{11}$ associated to the first bending mode. (b) Four first non-bending modes contained in the SMD $\boldsymbol{\theta}_{11}$, found equivalently by projecting $\boldsymbol{\theta}_{11}$ on the linear mode basis, or by application of Eq. (3.21). The relative modal participation factors q_s of each of these modes numbered 34, 167, 328 and 330 (see also Table 1) is also numerically given, normalized by the total amplitude of the SMD $\boldsymbol{\theta}_{11}$ ($q_{SMD} = 1$), and exactly recovers the factors exhibited in Eq. (3.21).

master mode labelled p, thanks to the static condensation, as:

$$p_s = -\frac{g^s_{pp}}{\omega_s^2} q_p^2. \tag{3.22}$$

The physical displacement $\boldsymbol{U}(q_p)$ that corresponds to the solution gathering together the master bending mode p and all its coupled modes can be written as:

$$\boldsymbol{U}(q_p) = q_p \boldsymbol{\phi}_p + \sum_{s=N_B+1}^{N} p_s \, \boldsymbol{\phi}_s. \tag{3.23}$$

In this last equation, replacing p_s by its value obtained from static condensation, Eq. (3.22), and then using Eq. (3.21) defining $\boldsymbol{\theta}_{pp}$ as a summation on the non-bending modes, one arrives easily at the fact that this physical displacement can be expressed as a function of the modal coordinate plus the participation of the SMD as:

$$\boldsymbol{U}(q_p) = q_p \boldsymbol{\phi}_p + \frac{1}{2} q_p^2 \boldsymbol{\theta}_{pp} \, . \tag{3.24}$$

which is exactly the expression of the change of coordinates of the quadratic manifold method for a single mode. More details about the quadratic manifold method will be provided in the next Chapter. Here, this expression is only used to replace the contribution of the p_s modes in a static condensation fashion.

If one wants now to derive a reduced-order model composed of a single master coordinate (say q_p here) and that contains the correct nonlinear behaviour, then the equation of motion would simply read:

$$\ddot{q}_p + \xi_p \dot{q}_p + \omega_p^2 q_p + \tilde{\Gamma}^p_{ppp} q_p^3 = f_p, \tag{3.25}$$

with $\tilde{\Gamma}^p_{ppp}$ a corrected cubic coefficient.

By making use of the displacement defined by Eq. (3.24) that contains the contribution of the master mode plus that of the SMD, then the cubic coefficient $\tilde{\Gamma}^p_{ppp}$ can be obtained directly in a StEP method manner. Since Eq. (3.21) shows that in our particular case (flat structure, one master mode), the SMD is completely equivalent to the static condensation of all coupled modes, then one will easily understand that there must be an equivalence between the two corrected coefficients $\tilde{\Gamma}^p_{ppp} = \Gamma^p_{ppp}$.

We now demonstrate that the coefficient $\tilde{\Gamma}^p_{ppp}$ introduced in Eq. (3.25), *i.e.* by using an imposed displacement composed of the master mode plus a quadratic part containing the SMD, is exactly equal to that given in Eq. (3.13), and obtained thanks to the static condensation. For that purpose, let us recall that the imposed displacement in the first case reads:

$$\boldsymbol{U}(q_p) = q_p\ \boldsymbol{\phi}_p + \frac{1}{2}\, q_p^2\ \boldsymbol{\theta}_{pp}. \tag{3.26}$$

The cubic coefficient $\tilde{\Gamma}^p_{ppp}$ can be computed by using the general formula from the StEP method, by replacing the imposed displacement by the one given in Eq. (3.26).

Denoting $\boldsymbol{U}(+\lambda) = +\lambda\boldsymbol{\phi}_p + \frac{1}{2}\lambda^2\boldsymbol{\theta}_{pp}$ and $\boldsymbol{U}(-\lambda) = -\lambda\boldsymbol{\phi}_p + \frac{1}{2}\lambda^2\boldsymbol{\theta}_{pp}$ one arrives at:

$$\tilde{\Gamma}^p_{ppp} = \boldsymbol{\phi}_p^{\mathrm{T}}\left(-\boldsymbol{F}_{\mathrm{NL}}(\boldsymbol{U}(+\lambda)) + \boldsymbol{F}_{\mathrm{NL}}(\boldsymbol{U}(-\lambda))\right)/2\lambda^3. \tag{3.27}$$

Using the explicit expression of the nonlinear forces, one has:

$$-\boldsymbol{F}_{\mathrm{NL}}(\boldsymbol{U}(+\lambda)) = \lambda^2\boldsymbol{G}_{pp}\ +\ \lambda^3\left(\boldsymbol{G}(\boldsymbol{\phi}_p,\boldsymbol{\theta}_{pp}) + \boldsymbol{H}_{ppp}\right)\ +\ \mathcal{O}(\lambda^4) \tag{3.28}$$

$$-\boldsymbol{F}_{\mathrm{NL}}(\boldsymbol{U}(-\lambda)) = \lambda^2\boldsymbol{G}_{pp}\ -\ \lambda^3\left(\boldsymbol{G}(\boldsymbol{\phi}_p,\boldsymbol{\theta}_{pp}) + \boldsymbol{H}_{ppp}\right)\ +\ \mathcal{O}(\lambda^4). \tag{3.29}$$

Thus the difference between the above nonlinear forces reads:

$$-\boldsymbol{F}_{\mathrm{NL}}(\boldsymbol{U}(+\lambda)) + \boldsymbol{F}_{\mathrm{NL}}(\boldsymbol{U}(-\lambda)) = 2\lambda^3\left(\boldsymbol{G}(\boldsymbol{\phi}_p,\boldsymbol{\theta}_{pp}) + \boldsymbol{H}_{ppp}\right)\ +\ \mathcal{O}(\lambda^5) \tag{3.30}$$

and the coefficient $\tilde{\Gamma}^p_{ppp}$, neglecting high order terms, reads:

$$\tilde{\Gamma}^p_{ppp} = \boldsymbol{\phi}_p^{\mathrm{T}}\boldsymbol{G}(\boldsymbol{\phi}_p,\boldsymbol{\theta}_{pp}) + \boldsymbol{\phi}_p^{\mathrm{T}}\boldsymbol{H}_{ppp} \tag{3.31}$$

The last term on the right hand side of Eq. (3.31) is the uncorrected cubic coefficient $h^p_{ppp} = \boldsymbol{\Phi}_p^{\mathrm{T}}\boldsymbol{H}_{ppp}$. As regards to the first term on the right hand side of Eq. (3.31), using the link between SMD and non-bending modes of Eq. (3.21) valid in case of a flat structure, they can be written as:

$$\boldsymbol{\phi}_p^{\mathrm{T}}\boldsymbol{G}(\boldsymbol{\phi}_p,\boldsymbol{\theta}_{pp}) = -\sum_{s=N_B+1}^{N}\boldsymbol{\phi}_p^{\mathrm{T}}\boldsymbol{G}(\boldsymbol{\phi}_p,\boldsymbol{\phi}_s)\,\frac{2g^s_{pp}}{\omega_s^2} = -\sum_{s=N_B+1}^{N} g^p_{ps}\,\frac{2g^s_{pp}}{\omega_s^2} \tag{3.32}$$

where the index s spans over all the non-bending modes.

It is now possible to express the corrected cubic coefficient as:

$$\tilde{\Gamma}^p_{ppp} = h^p_{ppp} - \sum_{s=N_B+1}^{N} g^p_{ps} \frac{2g^s_{pp}}{\omega_s^2} = \Gamma^p_{ppp} \tag{3.33}$$

and recover the same expression of the corrected coefficient given in Eq. (3.13) obtained with static condensation of all non-bending modes.

It is worth mentioning that the demonstration could have been done with another pathway. Indeed, the displacement introduced in Eq. (3.26) follows the general strategy proposed in [56, 127], consisting of using SMD to build a quadratic manifold approach in order to define a reduced-order models thanks to a nonlinear mapping between physical and reduced coordinates. However, the SMD can also be used more simply, by considering $\boldsymbol{\theta}_{pp}$ as an enrichment of the modal basis, composed here of the single master eigenvector $\boldsymbol{\phi}_p$. One could then derive a two-dofs reduced-order model, by projecting the general equations of motion onto these two vectors. Then, since the motions associated to the SMD are linked to non-bending modes having high frequencies, one can neglect their inertia and proceed to the static condensation of the part coming from the static modal derivative. By doing so, one would show again that the corrected cubic coefficient is still equal to Γ^p_{ppp}. Hence the static condensation of the SMD (a single vector) is thus strictly equivalent, in our simplified case of a flat structure (and considering only one master mode), to the static condensation of all coupled modes (including thickness modes).

The main result, from the SMD perspective, is that if one restricts to a single master mode p, then the SMD can be easily computed thanks to Eq. (3.18). Then the corrected cubic coefficient can be directly computed from:

$$\Gamma^p_{ppp} = \boldsymbol{\phi}_p^{\mathrm{T}} \left(\boldsymbol{F}_{\mathrm{NL}}(\boldsymbol{U}(\lambda)) - \boldsymbol{F}_{\mathrm{NL}}(\boldsymbol{U}(-\lambda)) \right) / 2\lambda^3, \tag{3.34}$$

where the imposed displacement is selected as in Eq. (3.24). This procedure allows then to find exactly the same corrected cubic coefficient of the master mode, but without resorting to the computation of all eigenvectors, as needed in the static condensation. It is thus a much more computationally efficient to use this methodology. Numerical examples are provided in Section 3.7.1.

3.6 A modified StEP for 3D elements

As observed in the previous sections, the modal ROM associated to 3D FE discretisation shows a slow convergence because of the couplings with very high frequency modes involving thickness deformations. Since these thickness modes are a peculiarity of the 3D model, they have no counterpart in plate or beam theory, which concentrate the kinematical description on the middle plane / line. Also, using the StEP with plate / beam elements show a faster convergence since one has to recover only the well-known coupling between

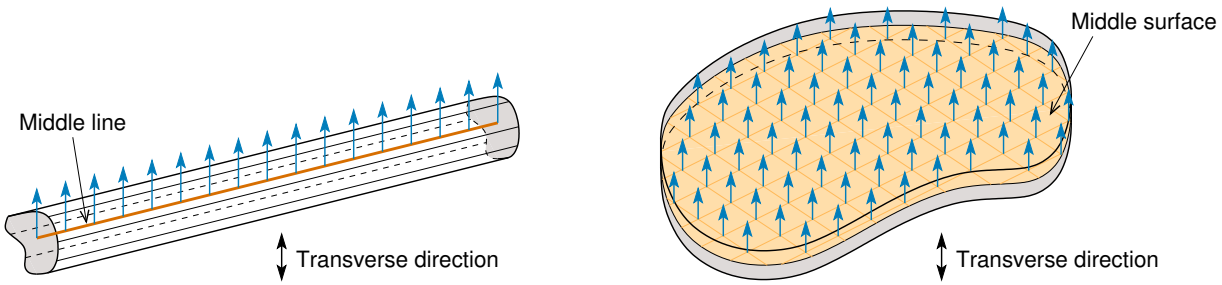


Figure 3.7: Examples of prescribed displacement field of the M-StEP, in the transverse direction and in the middle surface / line of a plate / beam

bending and in-plane motions. In order to circumvent these difficulties, we propose here to modify the StEP by prescribing the displacements only on the middle line / plane of the structure, and to let free the other degrees of freedom (Fig. 3.7). The idea is to include automatically the effects of the coupled modes, by a kind of implicit condensation of their motion, embedded into the prescribed displacement on the middle line / plane. The obtained method is called the M-StEP, for Modified-StEP. Note that a comparable idea has also been introduced in [68, 169], for 2D flat structures, where only transverse motions were prescribed, leaving the other degrees of freedom free and thus building directly a condensed model.

We show in this section that it is possible to compute directly the cubic coefficients Γ^r_{ijk} of Eq. (3.10) with a modified StEP, without having to compute all the coefficients g^k_{ij} and h^k_{ijl} beforehand. Note that in the classical StEP, the three components of the displacement field are prescribed to all the nodes of the FE mesh: the whole vector of unknown $\boldsymbol{U}$ is imposed and the FE code computation is just an evaluation of the internal force vector $\boldsymbol{F}_e = \boldsymbol{F}(\boldsymbol{U})$.

Here, we choose to apply the StEP by prescribing the displacement field only to selected nodes and for selected components. Precisely, we denote by $\mathcal{S}$ the middle plane / line of the structure and $\boldsymbol{n}$ the bending direction. To compute Γ^k_{ppp} for a given $p \in \{1, \dots N_B\}$, we choose to perform a FE computation by prescribing (i) only the transverse component of the bending mode $\boldsymbol{\phi}_p$ (ii) only on the nodes of the middle plane / line of the structure (Fig. 3.7). We then prescribe the following time independent displacement to the structure:

$$\boldsymbol{U}|_{\mathcal{S},\boldsymbol{n}} = \lambda\, \boldsymbol{\phi}_p|_{\mathcal{S},\boldsymbol{n}}, \quad \lambda \in \mathbb{R}. \tag{3.35}$$

where $\boldsymbol{U}|_{\mathcal{S},\boldsymbol{n}}$ corresponds to displacement $\boldsymbol{U}$ restricted to (i) the nodes of the FE mesh belonging to $\mathcal{S}$ and to (ii) its components along the direction defined by $\boldsymbol{n}$. In all the other nodes and directions, a zero forcing is prescribed. We then use the finite element code to solve this problem and obtain $\boldsymbol{U}$ as well as $\boldsymbol{F}(\boldsymbol{U}) = \boldsymbol{F}_e$ everywhere. Since some components of $\boldsymbol{U}$ are not prescribed, a Newton-Raphson procedure is necessary to solve this nonlinear algebraic problem. It is worth highlighting that the method is particularly suitable for flat structures meshed with hexahedral elements so that not only the middle plane / line $\mathcal{S}$ of the structure is a well define entity but it also contains a large enough

number of nodes. It will be seen that the prescribed displacement has to be representative enough of the mode of interest. This limitation of the method renders it not applicable to unstructured meshes or more complicated geometries.

To precise the method, we call master dofs the ones for which the displacement is prescribed, and slave dofs the other ones. The full displacement vector $\boldsymbol{U}$ and the internal forcing $\boldsymbol{F}$ can thus be decomposed as:

$$\boldsymbol{U} = \begin{bmatrix} \boldsymbol{U}_{\mathrm{M}} \\ \boldsymbol{U}_{\mathrm{S}} \end{bmatrix}, \qquad \boldsymbol{F} = \begin{bmatrix} \boldsymbol{F}_{\mathrm{M}} \\ \boldsymbol{F}_{\mathrm{S}} \end{bmatrix}, \tag{3.36}$$

where the index M and S are associated to the master and slave dofs, respectively. The M-StEP consists in prescribing:

$$\begin{cases} \boldsymbol{U}_{\mathrm{M}} = \lambda \boldsymbol{\phi}_p^{\mathrm{M}}, \\ \boldsymbol{F}_{\mathrm{S}} = \boldsymbol{0}. \end{cases} \tag{3.37}$$

Then, solving the static problem $\boldsymbol{F}(\boldsymbol{U}) = \boldsymbol{F}_e$ with the FE code leads to compute the internal force vector $\boldsymbol{F}_{\mathrm{M}}(\boldsymbol{U})$ on the master nodes and the displacement $\boldsymbol{U}_S$ on the slave nodes. The solution of the problem then reads:

$$\boldsymbol{U} = \begin{bmatrix} \lambda \boldsymbol{\phi}_p^{\mathrm{M}} \\ \boldsymbol{U}_{\mathrm{S}} \end{bmatrix}, \qquad \boldsymbol{F} = \boldsymbol{F}_e = \begin{bmatrix} \boldsymbol{F}_{\mathrm{M}} \\ \boldsymbol{0} \end{bmatrix}. \tag{3.38}$$

Translated in the modal space, the above computations are close to the following situation. Prescribing via $\boldsymbol{U}$ only the transverse motion in the form of $\boldsymbol{\phi}_p$, and because $\boldsymbol{\phi}_p$ is orthogonal to the other bending modes $\boldsymbol{\phi}_k$, $k \neq p$, the modal coordinate are $q_p \simeq \lambda$ and $q_k \simeq 0$. Considering the orthogonality relations associated to the stiffness matrix, this leads to assume that, for all $s \in \{1, \dots N_B\}$, $s \neq p$:

$$\boldsymbol{\phi}_p^{\mathrm{T}} \boldsymbol{K} \boldsymbol{U} \simeq \boldsymbol{\phi}_p^{\mathrm{T}} \boldsymbol{K} (\lambda \boldsymbol{\phi}_p) = \lambda \omega_p^2 m_p, \quad \boldsymbol{\phi}_s^{\mathrm{T}} \boldsymbol{K} \boldsymbol{U} \simeq \boldsymbol{\phi}_s^{\mathrm{T}} \boldsymbol{K} (\lambda \boldsymbol{\phi}_p) = 0. \tag{3.39}$$

In other words, it is assumed that the nonzero slave part $\boldsymbol{U}_{\mathrm{S}}$ of $\boldsymbol{U}$ is not involved in the orthogonality relations of the bending modes. Moreover, since the part of the displacement associated to longitudinal and thickness displacements is not prescribed by $\boldsymbol{U}$, the associated non-bending modal coordinates are not zero and their value depend on the nonlinear coupling and the geometric nonlinearities. Finally, because any non-bending eigenmode $\boldsymbol{\phi}_s$ has zero displacements on the middle plane / line in the transverse direction, the modal forcing of the non-bending modes is exactly zero:

$$\boldsymbol{\phi}_s = \begin{bmatrix} \boldsymbol{0} \\ \boldsymbol{\phi}_s^{\mathrm{S}} \end{bmatrix} \quad \Rightarrow \quad f_s = \boldsymbol{\phi}_s^{\mathrm{T}} \boldsymbol{F}_e = 0. \tag{3.40}$$

To summarize, one has:

$$\begin{cases} q_p \simeq \lambda, & \text{(3.41a)} \\ q_k \simeq 0 \qquad \forall k = 1, \dots N,\ k \neq p & \text{(3.41b)} \\ f_s = 0 \qquad \forall s = N_B, \dots, N & \text{(3.41c)} \end{cases}$$

Error estimates of those assumptions will be introduced in section 3.6.

Using the assumptions (3.41) in Eqs. (3.7,3.8) leads to:

$$\begin{cases} \lambda\omega_p^2 + \sum_{s=N_B+1}^{N} 2\lambda g_{ps}^p p_s + \lambda^3 h_{ppp}^p = \boldsymbol{\phi}_p^{\mathrm{T}} \boldsymbol{F}(\boldsymbol{U}), & \text{(3.42)} \\ \sum_{s=N_B+1}^{N} 2\lambda g_{ps}^k p_s + \lambda^3 h_{ppp}^k = \boldsymbol{\phi}_k^{\mathrm{T}} \boldsymbol{F}(\boldsymbol{U}), \qquad \forall k = 1, \dots, N_B,\ k \neq p & \text{(3.43)} \\ \omega_s^2 p_s + \lambda^2 g_{pp}^s = 0, \qquad \forall s = N_B + 1, \dots, N & \text{(3.44)} \end{cases}$$

The above Eq. (3.44) leads to:

$$p_s = -\frac{g_{pp}^s \lambda^2}{\omega_s^2}, \tag{3.45}$$

that can be condensed into (3.42),(3.43) to give:

$$\left(h_{ppp}^p - \sum_{l=N_B+1}^{N} \frac{2 g_{ps}^p g_{pp}^s}{\omega_s^2} \right) \lambda^3 = \boldsymbol{\phi}_p^{\mathrm{T}} \boldsymbol{F}(\boldsymbol{U}) - \lambda\omega_p^2, \tag{3.46}$$

$$\left(h_{ppp}^k - \sum_{l=N_B+1}^{N} \frac{2 g_{ps}^k g_{pp}^s}{\omega_s^2} \right) \lambda^3 = \boldsymbol{\phi}_k^{\mathrm{T}} \boldsymbol{F}(\boldsymbol{U}), \quad \forall k \neq p. \tag{3.47}$$

One then recognizes the terms in parenthesis as the sought corrected cubic coefficients Γ_{ppp}^i, defined by Eqs. (3.13) and (3.11), so that:

$$\Gamma_{ppp}^p = \frac{\boldsymbol{\phi}_p^{\mathrm{T}} \boldsymbol{F}(\boldsymbol{U})}{\lambda^3} - \frac{\omega_p^2}{\lambda^2}, \qquad \Gamma_{ppp}^k = \frac{\boldsymbol{\phi}_k^{\mathrm{T}} \boldsymbol{F}(\boldsymbol{U})}{\lambda^3}. \tag{3.48}$$

Consequently, all Γ_{ppp}^i, $i = 1, \dots N_B$ relies on a single nonlinear static finite elements computation, defined by Eq. (3.38). Other coefficients Γ_{ijl}^k can be obtained in the same manner, by mixing different U_{M} on several bending modes, following the classical StEP.

This above described M-StEP method is a way of automatically embed in the computation the effect of all the non-bending modes nonlinearly coupled to the bending modes associated to Γ_{ijl}^k. The essence of the method is to select the prescribed displacement $\boldsymbol{U}$ so that (i) it leaves free the degrees of freedom associated to the non-bending modes, so that the forcing f_s of the longitudinal modal coordinates in Eq. (3.44) is exactly zero and (ii) it is as orthogonal as possible to the other bending modes than the p-th.

Quality indicator for the convergence of the method

In order to be able to quantify *a priori* the quality of the computation, a main idea is to check the validity of the assumptions used in the two first equations (3.41), which are true at first order but might deteriorate in case of an incorrect selection of master dofs. Equivalently, one can verify the orthogonality of the displacement vector $\boldsymbol{U}$ to the bending modes written in Eqs. (3.39). To that purpose, let us define the following errors:

$$e_1^{pp} = \frac{\boldsymbol{\phi}_p^{\mathrm{T}} \boldsymbol{K} \boldsymbol{U}}{\lambda \omega_p^2} - 1, \qquad e_1^{pk} = \frac{\boldsymbol{\phi}_k^{\mathrm{T}} \boldsymbol{K} \boldsymbol{U}}{\lambda \omega_p^2}, \quad \forall k \neq p, \tag{3.49}$$

that should be small as compared to 1 because of Eqs. (3.39). If one wants to compute those errors with a FE in a non intrusive way, $\boldsymbol{K}\boldsymbol{U} = \boldsymbol{F}_1$ can be computed as the reaction force vector $\boldsymbol{F}_1$ of a linear static computation where $\boldsymbol{U}$ is prescribed to all the nodes of the FE mesh.

Another check can also be performed by prescribing Eq. (3.37) into a linear static computation:

$$\boldsymbol{K}\boldsymbol{U}_{\mathrm{l}} = \boldsymbol{F}_e, \tag{3.50}$$

which gives:

$$\boldsymbol{U}_{\mathrm{l}} = \begin{bmatrix} \lambda \boldsymbol{\phi}_p^{\mathrm{M}} \\ \boldsymbol{U}_{\mathrm{lS}} \end{bmatrix}. \tag{3.51}$$

Since there are no geometrical nonlinearities, imposing $\boldsymbol{\phi}_p$ on the middle line / surface in the transverse direction should result in a vector almost collinear to $\boldsymbol{\phi}_p$, that is $\boldsymbol{U}_{\mathrm{l}} \simeq \lambda \boldsymbol{\phi}_p$. In particular, the slave part $\boldsymbol{U}_{\mathrm{lS}}$ of $\boldsymbol{U}_{\mathrm{l}}$ should be very close to $\boldsymbol{\phi}_p^{\mathrm{S}}$, the slave part of $\boldsymbol{\phi}_p$. We then define the following error:

$$e(\hat{\boldsymbol{y}}, \boldsymbol{y}) = \frac{||\hat{\boldsymbol{y}} - \boldsymbol{y}||}{||\boldsymbol{y}||}, \tag{3.52}$$

where $||\cdot||$ is the norm of vector $\cdot$, and we check that $e_2^p = e(\boldsymbol{U}_l, \lambda \boldsymbol{\phi}_p)$ is very small as compared to 1.

3.7 Numerical examples

In this section, numerical examples on the three different strategies proposed in order to overcome the bias observed when using 3D elements, are given. In each case, the dominant cubic coefficient of a single mode is compared, using either the M-StEP, the static condensation of all the coupled linear modes, or the static modal derivative. Two test cases are used for the comparisons: the clamped-clamped beam of Fig. 3.1, and a clamped circular plate.

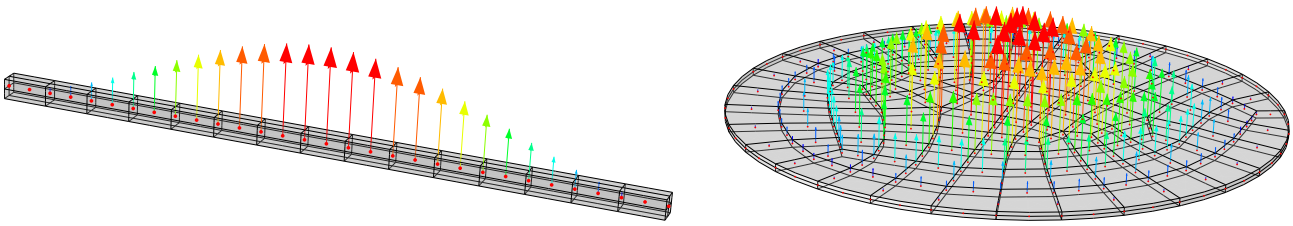


Figure 3.8: First-mode displacements prescribed on the middle line of the clamped beam and the middle surface of the circular plate. For visualisation purpose, the mesh of the plate is less fine than the one use for the computations of the ROM coefficients.

3.7.1 Application to a clamped-clamped beam

Computations of the condensed coefficients Γ^r_{ijk} are first performed with the three methods. For the M-StEP, the prescribed displacement is depicted in Fig. 3.8. The comparison made in Tab. 3.2 attests that the condensation with all the eigenmodes and the first static modal derivative are quasi equivalent, whereas the M-StEP gives very close values. The relative errors are very small (< 0.5 %) in each case. The analytical reference values present slightly larger errors, between 1 % and 5 %, probably due to unavoidable differences between the analytical beam theory and the numerical 3D computation. This could be explained by the aspect ratio $h/L = 0.03$ of the beam, which is not so small to fully verify Euler-Bernoulli assumptions.

	Corrected Coefficients				
	Γ^1_{111}	Γ^3_{111}	Γ^3_{113}	Γ^1_{333}	Γ^3_{333}
M-StEP	2.9790e+08	-2.3555e+08	2.7964e+09	-1.9044e+09	1.9235e+10
Static condensation	2.9792e+08	-2.3572e+08	2.8003e+09	-1.9083e+09	1.9288e+10
Static Modal Derivative	2.9792e+08	-2.3573e+08	2.8004e+09	-1.9084e+09	1.9288e+10
Analytic coefficients	2.9150e+08	-2.3151e+08	2.7082e+09	-1.8310e+09	1.8687e+10

Table 3.2: Corrected cubic coefficients with the three condensation methods and comparison with analytical values. Due to the symmetry of the mode shapes, the nonlinear coefficients which couple the first and the third modes have all nonzero values, and are therefore chosen for these computations.

3.7.2 Application to a clamped circular plate

In order to extend the results obtained on the beam test examples, the case of a clamped circular plate is here investigated. The selected plate has a radius $R = 0.3$ m, a thickness $h = 0.005$m, and the material properties are: density $\rho = 7800$ kg/m^3, Young's modulus $E = 210$ GPa and Poisson ratio $v = 0.3$. As for the beam cases, a coarse mesh is chosen so as to compute all the modes and apply the different proposed methodologies. Consequently,

540 HEX20 elements on the face and 2 HEX20 elements in the thickness were used, with a total of 1931 nodes and 4928 degrees of freedom.

The convergence study and appearance of thickness modes are investigated for the fundamental axisymmetric bending mode of the clamped plate, as well as the first asymmetric (1,0) mode, having one nodal line and no nodal circle. The case of the first axisymmetric mode is awaited to share the same complexity as the beam case for symmetry reasons, but the asymmetric mode might be more difficult to achieve convergence.

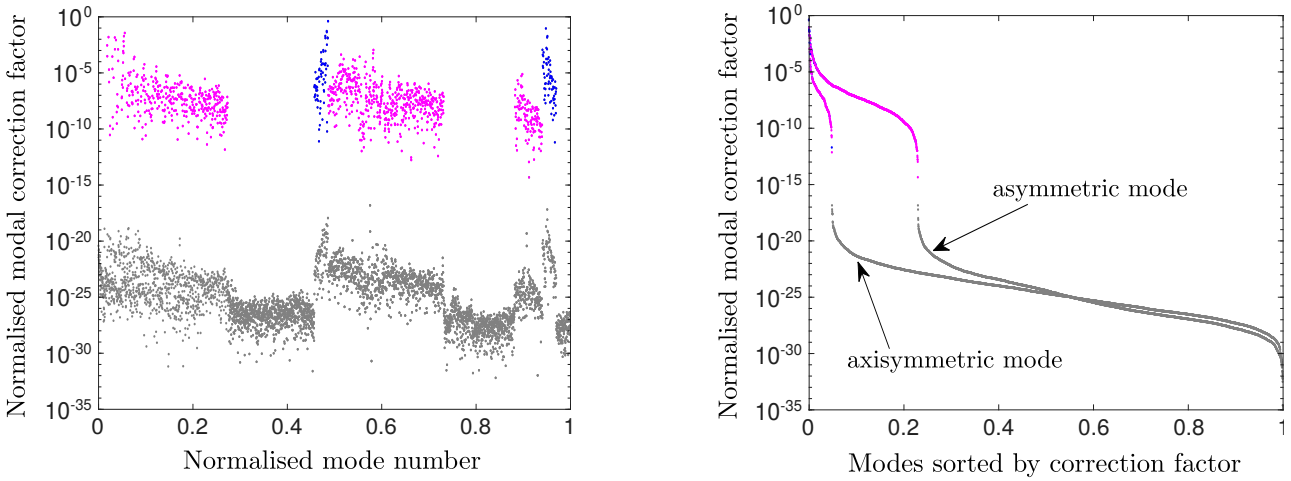


Figure 3.9: (a) Normalised modal correction factor for the clamped circular plate, as a function of the normalised mode number (normalization by the number of dofs), for the first asymmetric (1,0) mode of the plate. (b) The correction factors are now sorted by decreasing values, and two cases are shown : the case of the first asymmetic mode, corresponding to sorting (a), and the case of the first axisymmetric mode, showing a faster convergence. Grey points are negligible modes in terms of coupling, magenta points are the important in-plane coupled modes while blue points are the important thickness modes.

Fig. 3.9(a) shows the behaviour of the normalised modal correction factor $2(g^n_{pp}/\omega_n)^2/h^p_{ppp}$ used in the previous sections, where p refers to the master mode (either $p = 1$ for the first axisymmetric mode, or $p = 2$ for the first asymmetric) and $n \in \{1, N\}$ with N the number of dofs. In Fig. 3.9(a) only the case of the first asymmetric mode is shown for the sake of brevity (thus $p = 2$), but for $p = 1$ the trend was very similar. As for the beam, a strong coupling with very high frequency modes is also observed. Investigating more precisely which modes are involved in the couplings, it is found that the ones having the most important correction factor are once again thickness modes.

Table 3.3 shows the deformed shape of the first nine modes, sorted according to their correction factor, which are thus the most important in the coupling with the bending (1,0) mode. Two purely in-plane modes are found, in position 5 and 8, and all others are thickness modes. The deformed shapes can be compared to that obtained for the beam and shown in Table 3.1. Indeed, the first thickness mode having the most important correction factor shows a similar geometry for both structures. Strong similarities are also observed

between the second mode of the beam and mode (c) in Table 3.3, and the ninth mode in each case.

Fig. 3.9(b) shows the normalized correction factor now sorted by order of decreasing values, and for the two cases of the axisymmetric fundamental mode and first asymmetric mode. It shows in particular that the convergence on the correct cubic coefficient is more rapidly achieved for the axisymmetric mode, where less than 10% of the modes are needed. On the other hand, the convergence is more difficult for the first asymmetric mode. Concerning the coupling with high-frequency modes and thickness modes for these two first bending modes, it is interesting to note that the subset of coupled modes is almost exactly the same in the two cases, showing in particular that the coupling with the thickness modes is not very dependent on the selected bending mode. Indeed, more than 90% of the coupled modes are the same for the two cases investigated.

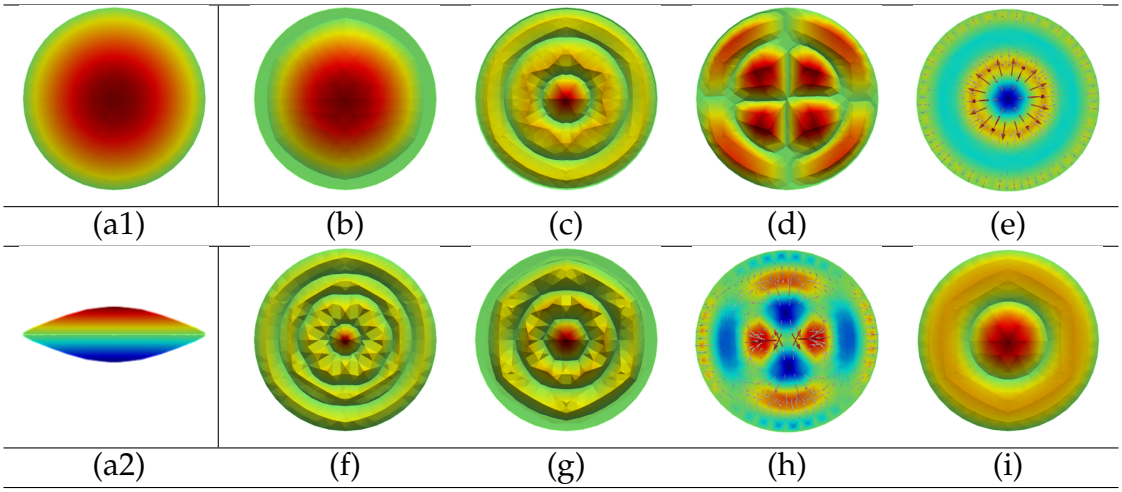


Table 3.3: Mode shapes of the 9 most relevant modes coupled with the first flexural asymmetric (1,0) mode. Only two of them are in-plane modes: (e) and (h), while all the others are thickness modes. (a2) is a side view of the top view (a1) of the first thickness mode, in order to show the strong dependence on thickness deformation.

	Corrected cubic Coefficients				
	Γ^2_{222}	Γ^4_{222}	Γ^4_{224}	Γ^2_{444}	Γ^4_{444}
M-StEP	6.4763e+10	-2.8539e+09	1.5374e+11	-57.3021	3.8776e+11
Static condensation	6.4762e+10	-2.8535e+09	1.5372e+11	5.3298e+03	3.8775e+11
SMDs condensed	6.4762e+10	-2.8536e+09	1.5372e+11	5.3080e+03	3.8775e+11

Table 3.4: Corrected cubic coefficient Γ^p_{ijk}, for two flexural modes, *i.e.* $i,j,k,p \in [2,4]$, where 2 refers to the first (1,0) asymmetric mode while 4 refers to the second (2,0) asymmetric mode; anf for three different methods : the modified StEP, the static condensation where all the coupled modes are statically condensed, and the Modal derivative where the added modal derivative is then statically condensed to the master mode.

Table 3.4 gathers the numerical results for the corrected cubic coefficient Γ^p_{ijk} defined in

Eq. (3.11), with $p = 2$ for the first asymmetric (1,0) mode and $p = 4$ for the (2,0) asymmetric mode (the first bending modes being sorted by increasing frequencies, $p = 1$ is the fundamental axisymmetric, $p = 2, 3$ for the two configurations of the (1,0) asymmetric mode and $p = 4, 5$ for the two configurations of the (2,0) mode with two nodal lines). This choice has been guided by the fact that these two asymmetric modes are coupled and thus shows important cubic coefficients that are needed if one wants to derive a reduced-order model. The three methods presented in the previous sections: M-StEP, static condensation of all the linear modes and of the modal derivative, give the same results, showing the convergence of the methods also in this case. Only Γ^2_{444} shows a different result for the M-StEP, however the value is very small as compared to the other ones so that this coefficient can be compared as negligible.

3.8 Conclusion

In this chapter, a nonlinear coupling of bending modes with thickness modes of very high frequency has been unfold as a result of geometrical nonlinearities in thin flat structures discretised with 3D finite elements. This effect adds itself to the classical longitudinal / bending coupling and is the cause of a very slow convergence of reduced order models built on the modal expansion of the nonlinear problem. It has been shown that if all eigenmodes are computed, it is possible to embed the effect of the non-bending modes into a master bending one, thus obtain a reduced order model composed of only one nonlinear Duffing oscillator. This procedure can be done either by static condensation or by a normal form reduction, equivalent to the reduction on a single nonlinear mode. Finally, two alternative methods have been proposed to overcome the problem: the use of a static modal derivative or the direct computation of the cubic coefficients by an original method, the M-StEP, inspired by the standard StEP. Those methods have been successfully verified on dedicated examples, showing equivalent results.

Most of the results presented in this chapter are restricted to the case of flat structures. Indeed, the specific shape of the equations of motion (see Eqs. (3.7),(3.8)) has been used to obtain exact equivalences between different methods. However, for more generic structures, most of the equivalences found will no longer hold.

Chapter 4

Nonlinear ROM for geometric nonlinearities and the role of the slow/fast separation assumption

The objective of this chapter is to investigate two methods for efficient reduced-order models of geometrically nonlinear structures, in order to shed light on their common aspects and better understand their limitations. The first method relies on the normal form theory that allows one to obtain a nonlinear change of coordinates for expressing the reduced-order dynamics in an invariant-based span of the phase space. The second method is the modal derivative (MD) approach, and more specifically the quadratic manifold defined in order to derive a second-order nonlinear change of coordinates. Both methods share a common point of view, willing to introduce a nonlinear mapping to better define a reduced-order model that could take more properly into account the nonlinear restoring forces. However the calculation methods are different and the quadratic manifold approach has not the invariance property embedded in its definition. Modal derivatives and static modal derivatives are investigated, and their distinctive features in the treatment of the quadratic nonlinearity is underlined. Assuming a slow/fast decomposition allows understanding how the three methods tend to share equivalent properties. While they give proper estimations for flat symmetric structures having a specific shape of nonlinearities and a clear slow/fast decomposition between flexural and in-plane modes, the treatment of the quadratic nonlinearity makes the predictions different in the case of curved structures such as arches and shells. In the more general case, normal form approach appears preferable since it allows correct predictions of a number of important nonlinear features, including for example the hardening/softening behaviour, whatever the relationships between slave and master coordinates are.

Roughly speaking, one can divide the techniques proposed in the literature into two different categories, the first one using linear change of coordinates, while in the second family nonlinear mappings are defined. When referring to linear methods, one can also distin-

guish techniques where the best orthogonal basis is computed once and for all. Modal basis [2,36,97,157], Ritz vectors [62], dual modes [69], and Proper orthogonal decomposition (POD) [3,66,73] falls into that family. The proper generalized decomposition (PGD) [26,39] under its progressive variant (pPGD) as defined in [92] also belongs to that case since additional vectors are added when the dynamics is becoming more complex. On the other hand, the linear change of coordinate can be adaptive, depending on the dynamics, the computation (single point or a whole branch of solution) or the location in phase space. Nonlinear principal component analysis (NLPCA) [65] as well as the optimized PGD (oPGD) [92] belongs to this family of improved linear methods, sometimes coined as nonlinear since the basis may change depending on some parameter.

In the third class of methods, a nonlinear change of coordinate is derived once and for all. Nonlinear normal modes [70, 101, 125, 137, 158], Spectral submanifolds [42, 119], and the quadratic manifold derived from modal derivatives [56, 127], belongs to this family. As shown in [4], when a linear method (*e.g.* POD) tries to find the best orthogonal axis fitting a learning set that have a complex shape, then the number of vectors will be larger than the number of curved subspaces one can use to describe the same datasets. In this particular example, it was shown that invariant manifolds pass exactly through the learning set thus diminishing the number of coordinates needed to describe the dynamics.

Nonlinear normal modes (NNMs) and spectral submanifolds (SSM) offer a rigorously established conceptual framework for reducing geometrically nonlinear structures. In particular, the invariance property of reduction spaces is encapsulated in their definition, ensuring that the dynamical solutions computed from a reduced-order model (ROM) also exist for the full system [43, 136, 145, 153]. This key ingredient allows deriving accurate ROMs, which, for example, are able to predict the correct hardening/softening behaviour of nonlinear structure, which is not the case for their linear counterparts [158]. More specifically, recent contributions by Haller and collaborators have shown that SSMs are unique continuations of spectral subspaces of the linear system under the nonlinear terms [42], and are thus the best mathematical object to be used in the present context. For nonlinear conservative vibratory systems, SSMs simplify to the classic Lyapunov subcenter manifolds (LSM) that are filled with periodic orbits, thus unifying a number of definitions given for NNMs in the past decades, see *e.g.* [64, 125, 136, 162].

On the other hand, modal derivatives (MDs) have been proposed independently [53, 173], and they share a number of common points with NNMs. In particular, MDs are defined by assuming that the mode shape (eigenvector) together with its eigenfrequency, have a dependence on amplitude, so that one can differentiate the classical Sturm-Liouville eigenvalue problem that defines linear normal modes, in order to make appear a quantity which is defined as the modal derivative. Symmetrically, NNMs also relies on the fact that modal quantities depend on amplitude, a key feature in nonlinear oscillations. The backbone curve and the dependence of the eigenmode shape with amplitude, is then a result from the computation of NNMs, defined as invariant manifold in phase space. However, a com-

plete comparison of both methods has not been drawn out yet. The only related paper uses the modal derivatives as a reduction method, from which the NNM, seen in this case as the family of periodic orbit in phase space –and thus reducing their information to the backbone curve only, without using the geometrical information in phase space– can be computed [143].

A recent development in the use of modal derivatives is to form a quadratic manifold for more accurate model order reduction. The properties of this nonlinear mapping are such that it is tangent to a subspace spanned by the most relevant vibration modes, and its curvature is provided by modal derivatives [56]. An idea also claimed in [127] is that such a quadratic manifold should be able to cancel the quadratic forces in the ROM. Incidentally, NNMs defined in the framework of normal form theory, as proposed in [154, 158], already present these features. Indeed, a third-order nonlinear change of coordinate is given, which has the property to be identity-tangent when the initial model is expressed in modal coordinates, thus conserving the linear modes as first approximation. Also, in case of no second-order internal resonance, the mapping exactly cancels all quadratic terms. Finally, the invariance property is directly inherited from the definition of an NNM as an invariant manifold in phase space, while the invariance of the quadratic manifold computed from MDs is not at hand.

The aim of this chapter is thus to investigate more properly the common points and differences of the two methods, and explain their advantages and drawbacks in the context of building reduced-order models for geometrically nonlinear structures. The chapter is organized as follows. Section 2 is concerned with the theoretical developments. The framework of geometrically nonlinear structures is briefly recalled, then both methods of interest, normal form theory, modal derivatives and their extension to quadratic manifold (QM), are recalled and analysed in depth. The general derivation of the QM framework for both modal derivatives (MDs) and static modal derivatives (SMDs) is highlighted, whereas previous contributions generally use the simplifying assumption of SMDs in the developments. As a consequence of this development, the distinctive treatment of the quadratic nonlinearity between MDs and SMDs is specifically underlined. Of particular interest is the comparison of methods when a slow/fast decomposition of the system can be assumed. In the course of the chapter, we will contrast the results given by MDs, SMDs and normal form and underlines that the simplifying assumption of slow/fast approximation allows retrieving partly the correct results. By doing so, an illustration of the general theorem given in [43] is thus provided for a more restrictive framework. Indeed, theorems given in [43] encompasses more generality and exact results, allowing to deal with the case of damping and forcing. We give however here more detailed comparisons, and in particular analyse how the SMD can produce incorrect predictions for structures having a strong quadratic coupling such as arches and shells. Section 3 illustrates the findings of the previous section on two simple two degrees-of-freedom (dofs) systems. Finally section 4 applies the previous results to continuous structures discretised with the finite element (FE) procedure.

4.1 Normal Form

In this thesis, the normal form theory, as defined in [154, 158], is used. The main idea is to define a nonlinear change of coordinates, from the modal coordinates to new ones defined as the *normal* coordinates. The nonlinear mapping is inherited from Poincaré and Poincaré-Dulac theorems, based on the idea of finding out a nonlinear relationship capable of eliminating as much as possible of nonlinear terms.

A visualisation of the main idea of using normal form to capture invariant manifolds is provided in Fig. 4.1. By means of a change of coordinates from modal to *normal*, the invariance broken by the nonlinear couplings is obtained in the new coordinates system. One can then use a smaller set of the new coordinates as a reduced model. The nonlinear

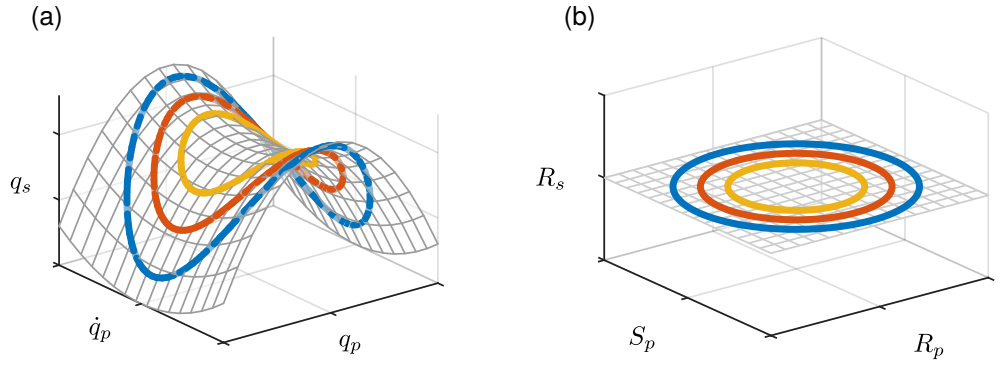


Figure 4.1: Visualisation of the change of coordinates obtained with normal form method. Plot (a): the linear invariance is broken by the nonlinear couplings between modes. Plot (b): the change of coordinates embeds all the invariance-breaking terms so that the system in normal coordinates regain the invariance property.

change of coordinates is identity-tangent, and formally reads:

$$q_p = R_p + \mathcal{P}_p(R_i, S_j), \tag{4.1a}$$

$$\dot{q}_p = S_p + \mathcal{Q}_p(R_i, S_j), \tag{4.1b}$$

where $\mathcal{P}_p$ and $\mathcal{Q}_p$ are third-order polynomials, the analytical expressions of which are given in [158] for the undamped case and in [154] for the damped case. q_p is the modal coordinate, $\dot{q}_p$ the modal velocity, and (R_i, S_j) are the new coordinates related to the invariant manifolds, and called *normal* coordinates.

The method used to derive the nonlinear mapping is based on the recognition of nonlinear resonances involving the eigenfrequencies of the system. In case where no internal resonance is present, one can show for example that all the quadratic terms can be cancelled from the normal form which is thus much simpler than the original system.

The dynamics, expressed with the newly introduced normal variables (R_i, S_j), is written in an invariant-based span of the phase space, and thus prone to open the doors to efficient

reduced-order models, as already shown in [153]. The general equation for the dynamics expressed in the new coordinates reads:

$$\begin{aligned}
&\forall\ p = 1, \dots, n : \\
&\quad \dot{S}_p + \omega_p^2 R_p + (A^p_{ppp} + h^p_{ppp}) R_p^3 + B^p_{ppp} R_p S_p^2 + \\
&\qquad + R_p \sum_{\substack{j=1 \\ j\neq p}}^{n} \left((3\, h^p_{pjj} + 2\, A^p_{jjp} + A^p_{pjj}) R_j^2 + B^p_{pjj} S_j^2 \right) + S_p \sum_{\substack{j=1 \\ j\neq p}}^{n} \left(2\, B^p_{jjp} R_j S_j \right) = 0. \qquad (4.2a) \\
&\dot{R}_p = S_p \qquad (4.2b)
\end{aligned}$$

where n is the number of master modes retained for the ROMS, $\boldsymbol{R} = (R_1, ..., R_n)$; in most cases $n \ll N$, but the formula are given for n arbitrary and can be used also for $n = N$. Note that the expression in slightly different from the one proposed in [158], a direct consequence of the choice of the representation of quadratic and cubic terms, with full summations. The coefficients A^p_{ijk} and B^p_{ijk} stems from the cancellation of the quadratic terms. Their expressions read:

$$A^p_{ijk} = \sum_{s=1}^{N} 2\, \bar{g}^p_{is} a^s_{jk}, \qquad (4.3a)$$

$$B^p_{ijk} = \sum_{s=1}^{N} 2\, \bar{g}^p_{is} b^s_{jk}, \qquad (4.3b)$$

where $\bar{g}^p_{is} = (g^p_{is} + g^p_{si})/2$ is the mean value between two adjacent terms implying the same monomial term. The coefficients a^s_{jk} and b^s_{jk} appearing in the expression of A^p_{ijk} and B^p_{ijk} are related to the quadratic terms of the change of coordinate. For the sake of illustration, we report the values of the a^s_{jk} and b^s_{jk} coefficients:

$$a^s_{jk} = g^s_{jk} \frac{\omega_j^2 + \omega_k^2 - \omega_s^2}{((\omega_j - \omega_k)^2 - \omega_s^2)((\omega_j + \omega_k)^2 - \omega_s^2)}, \qquad (4.4a)$$

$$b^s_{jk} = g^s_{jk} \frac{2}{((\omega_j - \omega_k)^2 - \omega_s^2)((\omega_j + \omega_k)^2 - \omega_s^2)}. \qquad (4.4b)$$

As known from the theory, these second-order coefficients have a singular behaviour in the vicinity of internal resonances. In this case, a strong coupling is present between the non-linear oscillators whose eigenfrequencies are commensurate, and the associated coefficient in the change of coordinate is set to zero, so that the corresponding monomial terms stay in the normal form.

From Eqs. (4.2), one can observe that invariant-breaking terms are no longer present in the equations of motion. Invariant-breaking terms are defined as quadratic monomials of the form $g^k_{pp} q_p^2$ and cubic monomials $h^k_{ppp} q_p^3$ on k-th oscillator equation. As soon as mode p has some energy, then these invariant-breaking terms directly excite oscillator k, thus

breaking the invariance of the linear mode subspace. As these terms are no longer present in Eqs. (4.2), it shows that the dynamics is now expressed in an invariant-based span. One can also note that the only monomial terms present in Eqs. (4.2) are those related to trivially resonant terms.

A ROM is simply selected by keeping in the truncation only the normal coordinates (R_p, S_p) of interest, depending on the problem at hand. By doing so, one restricts the motion in the invariant manifold described by the master normal coordinates retained, giving rise to efficient reduced models, that simulate trajectories existing in the complete phase space, and allowing to recover the correct type of nonlinearity [156,158] as well as nonlinear frequency response curves [155]. The simplest ROM is built by restricting the motion to a single NNM by keeping only one pair (R_p, S_p) and cancelling all the others: $\forall\, k \neq p, \quad R_k = S_k = 0$. In this case the nonlinear change of coordinates for the master coordinates reads:

$$q_p = R_p + a^p_{pp} R_p^2 + b^p_{pp} S_p^2, \tag{4.5a}$$

$$\dot{q}_p = S_p + \gamma^p_{pp} R_p S_p, \tag{4.5b}$$

whereas for the slave coordinates one has:

$$\begin{aligned} &\forall\, k \neq p : \\ &\quad q_k = a^k_{pp} R_p^2 + b^k_{pp} S_p^2 + r^k_{ppp} R_p^3 + u^k_{ppp} R_p S_p^2, \qquad (4.6a) \\ &\quad \dot{q}_k = \gamma^k_{pp} R_p S_p + \mu^k_{ppp} S_p^3 + \nu^k_{ppp} S_p R_p^2. \qquad (4.6b) \end{aligned}$$

Again, all the introduced coefficients, γ^p_{pp}, r^k_{ppp}, u^k_{ppp}, μ^k_{ppp} and ν^k_{ppp}, originate from the explicit expression of the polynomials $\mathcal{P}_p$ and $\mathcal{Q}_p$ of Eq. (4.1). They are all analytic and their expressions derived in [158] read:

$$r^s_{ppp} = \frac{(A^s_{ppp} + h^s_{ppp})(7\omega_p^2 - \omega_s^2) + 2B^s_{ppp}(\omega_p^4)}{(\omega_s^2 - \omega_p^2)(\omega_s^2 - 9\omega_p^2)}, \tag{4.7a}$$

$$u^s_{ppp} = \frac{6(A^s_{ppp} + h^s_{ppp}) + B^s_{ppp}(3\omega_p^2 - \omega_s^2)}{(\omega_s^2 - \omega_p^2)(\omega_s^2 - 9\omega_p^2)}, \tag{4.7b}$$

$$\mu^s_{ppp} = \frac{6(A^s_{ppp} + h^s_{ppp}) + B^s_{ppp}(3\omega_p^2 - \omega_s^2)}{(\omega_s^2 - \omega_p^2)(\omega_s^2 - 9\omega_p^2)}, \tag{4.7c}$$

$$\nu^s_{ppp} = \frac{3(A^s_{ppp} + h^s_{ppp})(3\omega_p^2 - \omega_s^2) + 2B^s_{ppp}(\omega_p^2\omega_s^2)}{(\omega_s^2 - \omega_p^2)(\omega_s^2 - 9\omega_p^2)}. \tag{4.7d}$$

Interestingly, Eqs. (4.6) describes the geometry of the invariant manifold in phase space, up to order three, but of course one can limit the development of this equation to second-order only. The dynamics on the invariant manifold (p^{th} NNM) is found by cancelling all (R_k, S_k) for $k \neq p$ in Eqs. (4.2). In the case of a single NNM motion the equation is particularly

simple and reads:

$$\ddot{R}_p + \omega_p^2 R_p + (A^p_{ppp} + h^p_{ppp}) R_p^3 + B^p_{ppp} R_p \dot{R}_p^2 \;=\; 0\,. \tag{4.8}$$

Of particular interest here is the fact that the correcting coefficients A^p_{ppp} and B^p_{ppp} appearing in this last equation are provided by the second-order terms in the nonlinear change of coordinates. Consequently, the third-order terms have no influence on this reduced dynamics, which is thus exactly the one given by the second-order truncation of the normal form nonlinear mapping.

All these formulas can be used to reconstruct the mode shape dependence on amplitude, assuming the motion is enslaved to a single NNM, *i.e.* lying in the invariant manifold associated to mode p. Assuming this single-NNM motion, the physical displacement is reconstructed from

$$\boldsymbol{U} = \sum_{k=1}^{N} q_k \boldsymbol{\phi}_k = q_p \boldsymbol{\phi}_p + \sum_{\substack{k=1 \\ k\neq p}}^{N} q_k \boldsymbol{\phi}_k, \tag{4.9}$$

where q_p is replaced using Eq. (4.5a) and q_k using Eq. (4.6a), so that one finally obtains the amplitude-dependent mode shape as :

$$\boldsymbol{U} = \left(R_p + a^p_{pp} R_p^2 + b^p_{pp} S_p^2\right) \boldsymbol{\phi}_p + \sum_{\substack{k=1 \\ k\neq p}}^{N} \left(a^k_{pp} R_p^2 + b^k_{pp} S_p^2 + r^k_{ppp} R_p^3 + u^k_{ppp} R_p S_p^2\right) \boldsymbol{\phi}_k. \tag{4.10}$$

This formula has already been used in order to represent the amplitude dependence of mode shapes on amplitude, see *e.g.* [138, 158], and will be further analysed and compared to the prediction given by the method of quadratic manifold from modal derivatives in Sect. 4.4.

Note that, as a comparison to quadratic manifold is targeted, a detailed description of the effects of order truncation in the normal form approach is in order. In the present approach of the normal form, the change of coordinates is up to order three, but the reduced-order dynamics can be considered as up to the second order, since the effect of cancelling the cubic terms to the higher-orders have not been taken into account due to the third-order truncation of all asymptotic developments. Also, most of the comparisons in the remainder will be drawn between single-mode reduced-order dynamics. In this simplified context, Eq. (4.8) clearly shows that the cancellation of the third-order non-resonant monomials have absolutely no effect on this equation which is left unchanged. Consequently, Eq. (4.8) is the reduced dynamics obtained with a second-order normal form nonlinear mapping. The only difference between second-order and third-order is in Eq. (4.6), which describes how the exact invariant manifold is approximated in phase space, and one can analyse the effect of either second-order or third-order nonlinear mapping in this respect. In the remainder, a clear attention will be devoted to these two specific truncations in order to draw out a fair comparison with the quadratic manifold approach.

We now turn to the definition of modal derivatives and the associated nonlinear mapping: the so-called quadratic manifold, before comparing the two methods in detail.

4.2 Modal derivatives

The modal derivatives have been first introduced with the aim of offering a framework taking into account the dependence of mode shapes and eigenfrequencies on amplitude for nonlinear systems. This is a common point with nonlinear normal modes, that also recognizes this fact as a major outcome that needs to be addressed correctly in the modelling. The ij-th modal derivative (MD) is defined as the derivative of $\tilde{\phi}_i$ with respect to the j-th coordinate used for the reduced basis, denoted here as R_j. For the sake of clarity, q_j is the modal coordinates, and R_j the reduced coordinates, following the notations introduced for the normal form approach. At first order, one has $q_j = R_j$, but as we consider nonlinear change of coordinates, these relationships will be enriched by higher-order terms. For the quadratic manifold approach, this will be explained in the next subsections, so that for the present definitions, one can assume $R_j = q_j$. In that context, the ij-th MD $\boldsymbol{\Theta}_{ij}$ is the derivative of $\tilde{\phi}_i$ with respect to a displacement enforced along the direction of the j-th eigenvector $\boldsymbol{\phi}_j$ as introduced in [53, 56, 127, 173].

Recalling the definition of modal derivatives from Sec. 2.3.3, the system to find the modal derivatives reads:

$$\begin{bmatrix} \boldsymbol{K} - \omega_i^2 \boldsymbol{M} & -\boldsymbol{M}\boldsymbol{\phi}_i \\ -\boldsymbol{\phi}_i^T \boldsymbol{M} & 0 \end{bmatrix} \begin{Bmatrix} \boldsymbol{\Theta}_{ij} \\ \frac{\partial \omega_i^2}{\partial R_j} \end{Bmatrix} = \begin{Bmatrix} -2\boldsymbol{G}_{ij} \\ 0 \end{Bmatrix}, \tag{4.11}$$

where the quadratic tensor $\boldsymbol{G}$ of the restoring force has been used in place of the nonlinear force. Similarly for the static modal derivative:

$$\boldsymbol{K}\boldsymbol{\Theta}_{ij}^{(S)} = -2\boldsymbol{G}_{ij}. \tag{4.12}$$

In order to compare the expressions of the reduced model obtained with modal derivatives with those of normal form, it is necessary to express them in modal coordinates. For this purpose, the ij-th MD in modal basis, denoted as $\boldsymbol{\theta}_{ij}$, is introduced as

$$\boldsymbol{\Theta}_{ij} = \boldsymbol{\Phi}\boldsymbol{\theta}_{ij} = \sum_{s=1}^{N} \boldsymbol{\phi}_s \theta_{ij}^s, \tag{4.13}$$

with the values of $\boldsymbol{\theta}_{ij}$ in modal coordinates stemming from Eq. (4.11) and reading:

$$\theta_{ij}^s = -\frac{2g_{ij}^s}{\omega_s^2 - \omega_i^2}, \qquad \text{for} \quad s \neq i, \tag{4.14a}$$

$$\theta_{ij}^i = 0, \tag{4.14b}$$

where the expression of Eq. (4.14b) stems from the second row of the system of Eqs. (4.11) and represent an enforcement of the mass-orthogonality between the i-th mode ϕ_i and the ij-th modal derivative $\mathbf{\Theta}_{ij}$. It will be shown that such orthogonality has important consequences.

Similarly for the static modal derivatives:

$$\theta_{ij}^{(S)} = -\frac{2\, g_{ij}^{s}}{\omega_s^2}. \tag{4.15}$$

In both cases, one can notice that the ij-th modal derivatives is directly proportional to the ij-th component of the quadratic tensor in modal coordinates. This clearly shows that the ij-th MD is able to retrieve the strong quadratic coupling occurring between every slave mode s and the master modes i and j.

4.3 Quadratic Manifold

The quadratic manifold approach has been introduced in [56, 127] in order to extend the use of modal derivatives in the context of model order reduction, and propose a nonlinear mapping from initial to reduced coordinates. The nonlinear mapping is quadratic in nature and does not account for nonlinear internal resonance as the normal form theory does. In this section, the derivation of reduced-order models using the quadratic manifold is given, following the previous results obtained in [56,127]. A particular attention is paid on writing the differences one can await when using the quadratic manifold with MDs and SMDs, with the comparison to the results provided by normal form theory in mind, thus giving rise to new developments. The coordinates describing the reduced-order models are denoted as R_p for all the methods in order to compare more directly the equations. One has however to keep in mind that the meaning of these coordinates is not the same for each method.

The nonlinear mapping proposed in the quadratic manifold method written for comparison in modal coordinates reads:

$$q_k = R_k + \frac{1}{2}\sum_{i=1}^{n}\sum_{j=1}^{n}\theta_{ij}^{k} R_i R_j. \tag{4.16}$$

The nonlinear mapping can then be used in order to derive the reduced-order equations by directly applying Eq. (2.98) to the original equations of motion, and using a standard Galerkin projection. For that purpose, one has to compute the derivatives of Eq. (2.98) with respect to time, and finally left-multiply the system by the tangent space as derived in Sec. 2.3.4. These derivations have already been proposed in [56,127], we refer the interested reader to these articles for details about the procedure. Here we give the reduced-order dynamics obtained once the projection realised, as a function of the modal coupling coefficients $\boldsymbol{g}$ and $\boldsymbol{h}$, a derivation that is not given in [56, 127] and will allow drawing out more direct comparisons with the normal form approach.

The dynamics for each reduced coordinates R_p finally reads, for $p = 1...n$:

$$\ddot{R}_p \; + \; \omega_p^2 R_p \; + \; \sum_{i,j=1}^{n} \left((g_{ij}^p + \frac{\omega_p^2}{2}\,\bar{\theta}_{ij}^p)\; R_i R_j \; + \; \bar{\theta}_{ij}^p\; (\dot{R}_i \dot{R}_j + R_i \ddot{R}_j) \; + \; \bar{\theta}_{pi}^j\; (\omega_j^2 R_i R_j + R_i \ddot{R}_j) \right) \; + \\ + \; \sum_{i,j,k=1}^{n} \left(\left(h_{ijk}^p + \sum_{s=1}^{N} \left(\bar{g}_{is}^p\; \bar{\theta}_{jk}^s + \bar{\theta}_{pk}^s\; (g_{ij}^s + \frac{\omega_s^2}{2}\,\bar{\theta}_{ij}^s) \right) \right)\; R_i R_j R_k \; + \; \sum_{s=1}^{N} \left(\bar{\theta}_{pk}^s\; \bar{\theta}_{ij}^s \right) (\dot{R}_i \dot{R}_j R_k + \ddot{R}_i R_j R_k) \right) \\ = \; 0, \tag{4.17}$$

where the following notations have been introduced for simplifying the expressions : $\bar{g}_{is}^p = (g_{is}^p + g_{si}^p)/2$ and $\bar{\theta}_{ij} = (\theta_{ij} + \theta_{ji})/2$. Note that this formula simplifies in the case of a symmetric quadratic tensor, which is generally the case in structural mechanics.

One can observe that the linear part is uncoupled, resulting from the fact that the first term of the quadratic manifold in Eq. (2.98) is the usual expansion onto the eigenmodes, thus implying, at linear order, uncoupled linear oscillators. The nonlinear terms can be compared to those obtained when using the normal form approach as nonlinear mapping, Eqs. (4.2). In particular, one can observe that the normal form approach completely cancels all quadratic terms, provided that no second-order internal resonance are present, a key feature embedded in the derivation which makes the distinction between resonant and non-resonant terms. On the other hand, quadratic terms are always present in (4.17). A second comment is on the presence of terms depending on accelerations in (4.17), not present in the reduced-order dynamics given by the normal form approach.

The restriction to a single master dof is provided, so that one could draw out a term-by-term comparison between the reduced-order dynamics provided by the two methods. Assuming that only mode p is present as reduced coordinates, thus $R_i = 0$, for all $i \neq p$, Eq. (4.17) simplifies to:

$$\ddot{R}_p \; + \; \omega_p^2 R_p \; + \; (g_{pp}^p + \frac{\omega_p^2}{2}\,\theta_{pp}^p)\; R_p^2 \; + \; \theta_{pp}^p\; (\dot{R}_p^2 + R_p \ddot{R}_p) \; + \; \theta_{pp}^p\; (\omega_p^2 R_p^2 + R_p \ddot{R}_p) \; + \\ + \; h_{ppp}^p R_p^3 \; + \; \sum_{s=1}^{N} \left(\bar{g}_{ps}^p\; \theta_{pp}^s\; R_p^3 \; + \; \theta_{pp}^s\; (g_{pp}^s + \frac{\omega_s^2}{2}\,\theta_{pp}^s)\; R_p^3 \; + \; \left(\theta_{pp}^s \right)^2\; (\dot{R}_p^2 R_p + \ddot{R}_p R_p^2) \right) \; = \; 0 \tag{4.18}$$

This last equation can then be used either for MD or SMD, so that one can contrast the results obtained by using one of these two strategies (modal derivatives, be they static or dynamic) with the nonlinear change of coordinates provided by normal form theory, which is the aim of the next section.

4.4 Theoretical Comparison

This section aims at comparing the different nonlinear mappings used to derive reduced-order models on the different outcomes they provide: reduced-order dynamics, and prediction of typical nonlinear features such as hardening/softening behaviour, and dependence of mode shapes on amplitude. For that purpose, we restrict ourselves to a single master mode. Moreover, from now on, we introduce the symmetry property of the quadratic tensor $\boldsymbol{g}$ that results from the fact that the internal force derives from a potential, thus leading to $g^i_{jk} = g^i_{kj}$ and $g^i_{jk} = g^j_{ki} = g^k_{ij}$. Note however that, due to our initial choice of fully populated sums and tensors without assuming commutativity of the product, the symmetry property may appear a bit different from *e.g.* [97] when equal indexes are present. Indeed, in [97] one can read for example $g^p_{ps} = 2g^s_{pp}$. This is the only consequence of the initial choice since in [97] one has $g^p_{sp} = 0$ for $s > p$. In our case, the relationship reads $g^p_{ps} = g^s_{pp}$ and $g^p_{sp} = g^s_{pp}$.

By using such symmetry property, we can also simplify $\bar{g}^p_{ps} = g^p_{ps} = g^s_{pp}$ and substituting the value of the modal derivative in modal space $\theta^s_{pp} = -2g^s_{pp}/(\omega_s^2 - \omega_p^2)$ when $s \neq p$ and $\theta^p_{pp} = 0$ in Eq. (4.18), one obtains:

$$\begin{aligned}&\ddot{R}_p \;+\; \omega_p^2 R_p \;+\; g^p_{pp}\, R_p^2 \\ &+\; h^p_{ppp} R_p^3 \;-\; \sum_{\substack{s=1\\ s\neq p}}^{N} (g^s_{pp})^2 \frac{2}{\omega_s^2 - \omega_p^2} \left(\frac{\omega_s^2 - 2\omega_p^2}{\omega_s^2 - \omega_p^2}\, R_p^3 \;-\; \frac{2}{\omega_s^2 - \omega_p^2}\, (\dot{R}_p^2 R_p + \ddot{R}_p R_p^2) \right) \;=\; 0.\end{aligned} \tag{4.19}$$

If the value of the SMD is used instead of the MD, then the reduced-order dynamics writes:

$$\begin{aligned}&\ddot{R}_p \;+\; \omega_p^2 R_p \;-\; g^p_{pp} \frac{2}{\omega_p^2}\, (\omega_p^2 R_p^2 + \dot{R}_p^2 + 2R_p \ddot{R}_p) \;+ \\ &h^p_{ppp} R_p^3 \;-\; \sum_{s=1}^{N} (g^s_{pp})^2 \frac{2}{\omega_s^2} \left(R_p^3 \;-\; \frac{2}{\omega_s^2} (\dot{R}_p^2 R_p + \ddot{R}_p R_p^2) \right) \;=\; 0.\end{aligned} \tag{4.20}$$

For the explicit comparison, we rewrite the reduced-order dynamics derived with the normal form approach, Eq. (4.8), where the A^p_{ppp} and B^p_{ppp} terms have been expanded:

$$\ddot{R}_p + \omega_p^2 R_p + h^p_{ppp} R_p^3 - \sum_{s=1}^{N} (g^s_{pp})^2 \frac{2}{\omega_s^2} \left(\frac{\omega_s^2 - 2\omega_p^2}{\omega_s^2 - 4\omega_p^2}\, R_p^3 \;-\; \frac{2}{\omega_s^2 - 4\omega_p^2}\, \dot{R}_p^2 R_p \right) \;=\; 0. \tag{4.21}$$

Note that the remark on the order of the truncations of normal form may be better understood from these single-mode reduced dynamics. Eq. (4.21) is the ROM given by normal form, be the calculation of the nonlinear change of coordinate truncated at order two or at order three. Consequently this equation gives the third-order reduced dynamics produced by truncating the normal form at second order. In the same line, Eqs. (4.19) and (4.20) are

the third-order reduced-dynamics provided by the quadratic manifold approach. Hence comparing the predictions given by these reduced dynamics is correct since the same order of asymptotic developments is at hand. The only difference one can estimate in the analysis thus relies in the nonlinear mapping, which can be pushed at third-order easily in the normal form approach since the calculation has already been proposed in the past. This means that in the comparisons, the only difference will be on the geometry of the manifold in phase space and the reconstruction formula, but not on the reduced-order dynamics.

In order to have a better view on the reduced-order dynamics for each of the methods, the general nonlinear oscillator equation describing the dynamics on the reduced subspace can be written under the general form as:

$$\ddot{R}_p + \omega_p^2 R_p + C_1 R_p^2 + C_2 \frac{\dot{R}_p^2}{\omega_p^2} + C_3 \frac{\ddot{R}_p R_p}{\omega_p^2} + C_4 R_p^3 + C_5 \frac{\dot{R}_p^2 R_p}{\omega_p^2} + C_6 \frac{\ddot{R}_p R_p^2}{\omega_p^2} \;=\; 0, \tag{4.22}$$

with C_1 to C_6 different coefficients, which values are summarized in Tables 4.1, 4.2 for the three different methods.

	C_1	C_2	C_3
MD	g^p_{pp}	0	0
SMD	-2g^p_{pp}	-2g^p_{pp}	-4g^p_{pp}
NF	0	0	0

Table 4.1: Table of coefficients of the reduced system given by the three methods

	C_4	C_5	C_6
MD	$h^p_{ppp} - \sum_{\substack{s=1 \\ s\neq p}}^{n} (g^s_{pp})^2 \frac{2(\omega_s^2 - 2\omega_p^2)}{(\omega_s^2 - \omega_p^2)^2}$	$\sum_{\substack{s=1 \\ s\neq p}}^{n} (g^s_{pp})^2 \frac{4\,\omega_p^2}{(\omega_s^2 - \omega_p^2)^2}$	$\sum_{\substack{s=1 \\ s\neq p}}^{n} (g^s_{pp})^2 \frac{4\,\omega_p^2}{(\omega_s^2 - \omega_p^2)^2}$
SMD	$h^p_{ppp} - \sum_{s=1}^{N} (g^s_{pp})^2 \frac{2}{\omega_s^2}$	$\sum_{s=1}^{N} (g^s_{pp})^2 \frac{4\,\omega_p^2}{\omega_s^4}$	$\sum_{s=1}^{N} (g^s_{pp})^2 \frac{4\,\omega_p^2}{\omega_s^4}$
NF	$h^p_{ppp} - \sum_{s=1}^{N} (g^s_{pp})^2 \frac{2(\omega_s^2 - 2\omega_p^2)}{\omega_s^2(\omega_s^2 - 4\omega_p^2)}$	$\sum_{s=1}^{N} (g^s_{pp})^2 \frac{4\,\omega_p^2}{\omega_s^2(\omega_s^2 - 4\omega_p^2)}$	0

Table 4.2: Table of coefficients of the reduced system given by the three methods

As already remarked, only the normal form approach is able to cancel the quadratic nonlinearity and produce a parsimonious, cubic-order reduced dynamics, depending on two separate coefficients only. Using SMDs creates the larger number of coefficients while only

4 are needed for MDs. Most importantly, the closeness of the results given by the three methods can be underlined in the case where a slow/fast decomposition can be assumed between the master mode p and the slave modes s. This case is often encountered in mechanical vibrations since one has often to deal with a large number of modes with very high eigenfrequencies. Let us assume that all the slave modes s are well separated from the master mode, so that for all s one has $\omega_s \gg \omega_p$. It is then very easy to verify on the coefficients given in Tables 4.1, 4.2 that those provided by the normal form and the MD method tends to the values given by the SMD approach. More specifically, C_4 and C_5 from normal form exactly match those from the SMD, so that the only difference between the two reduced-order dynamics lies in the additional terms C_1, C_2, C_3 and C_6 for the SMD method. On the other hand, using the slow/fast approximation for the coefficients provided by the MD shows that C_4, C_5 and C_6 tends exactly to the values obtained with SMDs, the only difference being in the summation, where the p term is excluded in the MD approach whereas it is not in the SMD, as a direct consequence from Eq. (4.14). Indeed for the MD, the g^p_{pp} term is not included in the reconstruction vector because of the orthogonality between $\boldsymbol{\phi}_p$ and $\boldsymbol{\Theta}_{pp}$. On the other hand for SMD, the g^p_{pp} term is taken into account in the vector defining the SMD, Eq. (4.15). This important difference between the two methods will have consequences that are commented further in the next sections, and the g^p_{pp} will be denoted further as the self-quadratic term.

In order to better understand the observed differences on the reduced-order dynamics, a fair comparison has to be given not onto a term-by-term comparison, since the meaning of the reduced variables is not the same, but on the general predictions given by each reduction method on the most important nonlinear features. The next sections are thus devoted to comparing the prediction of the type of nonlinearity provided by each method (*i.e.* the first term in the amplitude-frequency relationship that dictates the hardening or softening behaviour), as well as the mode shape dependence on amplitude.

Hardening/softening behaviour

The generic reduced-order dynamics, Eq. (4.22), can be solved with a perturbation method in order to derive the type of nonlinearity predicted by each method. Keeping the general notation with the C_i coefficients for the ease of reading, the general solution up to second order in amplitude reads:

$$R_p = a_0 \cos[\,\omega_p\, t\,(1+\Gamma a_0^2)] + a_0^2 \left(\frac{C_1 - C_2 - C_3}{6\,\omega_p^2} \cos[\,2\,\omega_p\, t\,(1+a_0^2\Gamma)] - \frac{C_1 + C_2 - C_3}{2\,\omega_p^2} \right) + \mathcal{O}(a_0^3), \tag{4.23}$$

with a_0 the amplitude, and Γ the general coefficient that dictates the hardening/softening behaviour. Indeed, one can introduce the nonlinear frequency $\omega_{\mathrm{NL}} = \omega_p(1+\Gamma a_0^2)$. If $\Gamma > 0$ then the system is hardening. The general expression for Γ with all the C_i coefficients

writes:

$$\Gamma = -\frac{1}{24\,\omega_p^4}\left(10\,C_1^2 + 10\,C_1C_2 + 4\,C_2^2 - 7\,C_2C_3 + C_3^2 - 11\,C_1C_3\right) + \frac{1}{8\,\omega_p^2}\left(3\,C_4 + C_5 - 3\,C_6\right). \tag{4.24}$$

One can note in particular that with the normal form approach, one has $C_1 = C_2 = C_3 = 0$ since the method fully cancels the quadratic terms, so that there is no second harmonic term in the reduced-order dynamics and Eq. (4.23) reduces to its first term at order two. However, since quadratic terms are present in the nonlinear change of coordinates, this simplification does not imply that the second harmonic is not present in the reconstructed displacements, as it will be shown in the next section. Once again, these two last equations show that normal form approach produces a parsimonious representation of the reduced dynamics which is generally easier to read and interpret.

Replacing the values of the C_i coefficients obtained for each method (MD, SMD or NF for normal form), one arrives at the prediction of the type of nonlinearity provided by each reduced-order model as:

$$\Gamma_{\text{MD}} = -\frac{5}{12\,\omega_p^2}\left(\frac{g_{pp}^p}{\omega_p}\right)^2 + \frac{3}{8\,\omega_p^2}\left(h_{ppp}^p - \sum_{\substack{s=1\\s\neq p}}^{n} 2\left(\frac{g_{pp}^s}{\omega_s}\right)^2\left(1 + \frac{\omega_p^2(4\,\omega_s^2 - 3\,\omega_p^2)}{3(\omega_s^2 - \omega_p^2)^2}\right)\right), \tag{4.25a}$$

$$\Gamma_{\text{SMD}} = -\frac{5}{12\,\omega_p^2}\left(\frac{g_{pp}^p}{\omega_p}\right)^2 + \frac{3}{8\,\omega_p^2}\left(h_{ppp}^p - \sum_{\substack{s=1\\s\neq p}}^{n} 2\left(\frac{g_{pp}^s}{\omega_s}\right)^2\left(1 + \frac{4\,\omega_p^2}{3\,\omega_s^2}\right)\right), \tag{4.25b}$$

$$\Gamma_{\text{NF}} = -\frac{5}{12\,\omega_p^2}\left(\frac{g_{pp}^p}{\omega_p}\right)^2 + \frac{3}{8\,\omega_p^2}\left(h_{ppp}^p - \sum_{\substack{s=1\\s\neq p}}^{n} 2\left(\frac{g_{pp}^s}{\omega_s}\right)^2\left(1 + \frac{4\,\omega_p^2}{3(\omega_s^2 - 4\,\omega_p^2)}\right)\right). \tag{4.25c}$$

One can note that the first terms of the prediction are the same, while the difference arise from the way the slave (or neglected) coordinates are taken into account in order to predict the type of nonlinearity. This feature is however key in order to give a correct prediction since there is a strong need to take properly into account the curvature of the manifolds in phase space, otherwise incorrect predictions are given [158].

In order to give more insights into Eqs. (4.25), let us first notice that in the summed terms, the first one is always the same since the different expressions all start with $1 + ...$ Let us isolate this term and introduce the following notation :

$$\mathcal{C}_{\text{SC}}^s = 2\left(\frac{g_{pp}^s}{\omega_s}\right)^2. \tag{4.26}$$

One can notice that this correction term is the one obtained by using static condensation, as

already shown for example in [139,165], thus the subscript SC. Denoting as $\mathcal{C}_{\text{MD}}$, $\mathcal{C}_{\text{SMD}}$ and $\mathcal{C}_{\text{NF}}$ the correction factors given by each method (*i.e.* the term in the summation), one can then simply compares all these terms to $\mathcal{C}^s_{\text{SC}}$ in order to have an expression depending only on the eigenfrequencies. Assuming that there is only one slave mode s in the summation in order to highlight the contribution brought by each term, the following ratios can be written:

$$\frac{\mathcal{C}_{\text{MD}}}{\mathcal{C}_{\text{SC}}} = 1 + \frac{4}{3}\frac{\rho^2 - 3/4}{(\rho^2-1)^2}, \tag{4.27a}$$

$$\frac{\mathcal{C}_{\text{SMD}}}{\mathcal{C}_{\text{SC}}} = 1 + \frac{4}{3}\frac{1}{\rho^2}, \tag{4.27b}$$

$$\frac{\mathcal{C}_{\text{NF}}}{\mathcal{C}_{\text{SC}}} = 1 + \frac{4}{3}\frac{1}{\rho^2 - 4}, \tag{4.27c}$$

where $\rho = \omega_s/\omega_p$ has been introduced in order to highlight their behaviour with respect to the fulfilment of the slow/fast partition. These expressions clearly underline the fact that each method refine the correction factor of static condensation by an additional term. One can also observe that the refinement of the $\mathcal{C}^s_{\text{SMD}}$ comes from the inertia and velocity terms C_5 and C_6, whereas the term C_4 is exactly the one from static condensation. Consequently, using SMD without quadratic manifold could lead to erroneous predictions since inertial and velocity corrections could be missed. This remark should be particularly relevant in a case of geometric nonlinearity involving inertia, as *e.g.* in the case of a cantilever beam.

To better assess the quality of the predictions given by the three methods, Eqs. (4.27) can be Taylor-expanded by using the slow/fast assumption $\omega_s \gg \omega_p$ for the slave modes s. This assumption allows introducing a small parameter ω_p/ω_s, or, equivalently, considering the expansion under the assumption $\rho \to \infty$. One then obtains:

$$\frac{\mathcal{C}_{\text{MD}}}{\mathcal{C}_{\text{SC}}} = 1 + \frac{4}{3}\frac{1}{\rho^2} + \sum_{i=2}^{\infty}\frac{3+i}{3}\frac{}{\rho^{2i}}, \tag{4.28a}$$

$$\frac{\mathcal{C}_{\text{SMD}}}{\mathcal{C}_{\text{SC}}} = 1 + \frac{4}{3}\frac{1}{\rho^2}, \tag{4.28b}$$

$$\frac{\mathcal{C}_{\text{NF}}}{\mathcal{C}_{\text{SC}}} = 1 + \frac{4}{3}\frac{1}{\rho^2} + \sum_{i=2}^{\infty}\frac{4^i}{3}\frac{}{\rho^{2i}}. \tag{4.28c}$$

These formulas show in particular that all the methods predict the same first two terms in the expansion that assumes slow/fast partition, and the limit for $\rho \to \infty$ is the same for all methods, including static condensation, since the ratios tends to 1 in this case. This means that a formal equivalence in the prediction of the type of nonlinearity is obtained only in the limit case of $\omega_s \gg \omega_p$ for all the studied methods. Fig. 4.2 illustrates this convergence and shows that it is obtained rapidly, indicating in particular that from the value $\omega_s/\omega_p \simeq 4$, all methods are almost converged in terms of type of nonlinearity, thus quantifying more properly the value from which the slow/fast partition is effective so that one can use the methods based on modal derivatives safely. In order to be a bit more quantitative, one can

remark that the relative difference between $\mathcal{C}_{\text{MD}}$ and $\mathcal{C}_{\text{NF}}$ is equal to 5% for $\rho = 3.25$ and 1% for $\rho = 4.6$, so that the proposed bound $\omega_s/\omega_p \simeq 4$ has not to be understood as a strict one. Moreover, the error on Γ will be smaller than the error on the correction factor $\mathcal{C}$, being Γ composed of other terms that are not affected by the reduction method. The conclusion is that $\rho \in [3, 4]$ can be understood as a transition region, and converged results thanks to slow/fast assumption can be faithfully obtained over 4, but below 3 caution has to be exercised.

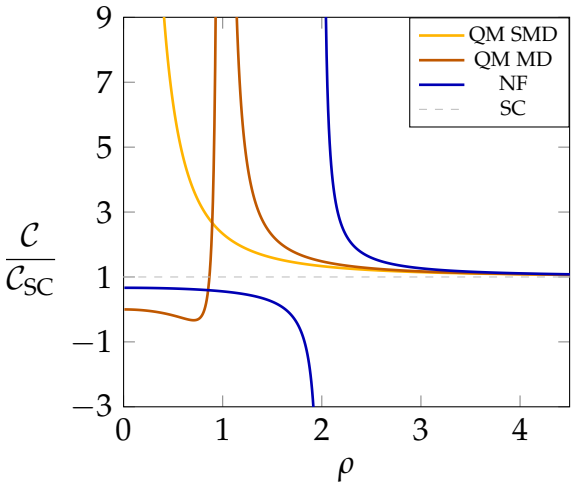


Figure 4.2: Evolution of the ratios $\frac{\mathcal{C}_{\text{MD}}}{\mathcal{C}_{\text{SC}}}$, $\frac{\mathcal{C}_{\text{SMD}}}{\mathcal{C}_{\text{SC}}}$ and $\frac{\mathcal{C}_{\text{NF}}}{\mathcal{C}_{\text{SC}}}$, defined in Eqs. (4.27), as a function of the parameter $\rho = \omega_s/\omega_p$, from which the behaviour of the type of nonlinearity defined by the Γ coefficients in Eqs. (4.25), can be directly deduced. Dashed grey line is the (constant) value predicted by static condensation (all curves are normalized with respect to this value). Yellow curve: $\frac{\mathcal{C}_{\text{SMD}}}{\mathcal{C}_{\text{SC}}}$ predicted by static modal derivatives; orange curve: $\frac{\mathcal{C}_{\text{MD}}}{\mathcal{C}_{\text{SC}}}$ computed from modal derivatives, blue curve: $\frac{\mathcal{C}_{\text{NF}}}{\mathcal{C}_{\text{SC}}}$ given by normal form theory.

Fig. 4.2 shows also other interesting features on the behaviour of the type of nonlinearity. Besides the convergence of all curves in the limit $\rho \to \infty$, important differences occur in the regions where the methods have a singularity. The normal form approach displays a singular behaviour in the vicinity of the 1:2 internal resonance when $\omega_s \simeq 2\omega_p$. This fact is logical and has already been commented in numerous prior publications. Indeed, when such a resonance exists, then a strong coupling arises between the two modes, so that reducing the dynamics to a single master mode has no meaning anymore, and the minimal model should be composed at least by these two internally resonant modes. The divergence in the behaviour of $\mathcal{C}_{\text{NF}}/\mathcal{C}_{\text{SC}}$ reflects this fact, meaning that in this zone the definition of the type of nonlinearity is of no more use since another dynamical regime takes place. Previous publications also clearly underlines that the prediction given by Γ_{NF} in Eq. (4.25c) is correct [158], which has been confirmed with comparisons to direct simulations of the full-order model, and this prediction of the type of nonlinearity has then been used for continuous structures such as cables and shells [6, 109, 120, 156].

On the other hand, the prediction given by MD displays a divergence at the 1:1 resonance,

when the slave and master modes have close eigenfrequencies, $\omega_s \simeq \omega_p$. This divergence does not rely on a firm theoretical result from dynamical systems. Indeed, even though in the case a 1:1 internal resonance exists so that the two modes need to be taken into account to study the coupled dynamics, uncoupled solutions still exist and the backbone curves of these uncoupled solutions can be computed, thus preserving the meaning of the Γ coefficients defined in Eqs. (4.25), see *e.g.* [37,90,157]. Thus the divergence of $\mathcal{C}_{\text{MD}}/\mathcal{C}_{\text{SC}}$ is interpreted as a failure of the method. Finally, for small values of ρ, one can observe that the SMD method shows a singular behaviour, and will predict unreasonably stiff behaviour. On the other hand, MD method gives a finite value, which is a bit different from the correct one given by normal form approach. All these results underline that MD and SMD can be used safely only when the assumption $\omega_s > 4\omega_p$ is fulfilled, otherwise unreliable predictions may be given by these two methods.

Drift and mode shapes

A second comparison on the global outcomes of the three method can be provided by contrasting the mode shape dependence on amplitude. Indeed, assuming a single mode motion with $R_s = 0$ for all $s \neq p$ (only master mode p participates to the vibration), allows recovering the amplitude dependence of the p-th mode shape. At small amplitude, the three methods recover the usual eigenmode, but they then differ in the way they are taking into account the cross-couplings with slave modes. Let us denote as $\boldsymbol{U}_{\text{MD}}$, $\boldsymbol{U}_{\text{SMD}}$ and $\boldsymbol{U}_{\text{NF}}$ the physical displacement following single-mode motion for each of the three methods. Using the previous formula allows one to reconstruct

$$\boldsymbol{U}_{\text{MD}}(t) = \boldsymbol{\phi}_p R_p(t) - \sum_{\substack{s=1 \\ s\neq p}}^{N} \frac{g^s_{pp}}{\omega_s^2 - \omega_p^2} R_p^2(t) \boldsymbol{\phi}_s, \tag{4.29}$$

$$\boldsymbol{U}_{\text{SMD}}(t) = \boldsymbol{\phi}_p R_p(t) - \boldsymbol{\phi}_p \frac{g^p_{pp}}{\omega_p^2} R_p^2(t) - \sum_{\substack{s=1 \\ s\neq p}}^{N} \frac{g^s_{pp}}{\omega_s^2} R_p^2(t) \boldsymbol{\phi}_s, \tag{4.30}$$

$$\begin{aligned} \boldsymbol{U}_{\text{NF}}(t) = \boldsymbol{\phi}_p R_p(t) - \boldsymbol{\phi}_p \frac{g^p_{pp}}{\omega_p^2} \frac{1}{3} \left(R_p^2(t) + \frac{2}{\omega_p^2} \dot{R}_p^2(t) \right) + \\ - \sum_{\substack{s=1 \\ s\neq p}}^{N} \frac{g^s_{pp}}{\omega_s^2} \left(\frac{\omega_s^2 - 2\omega_p^2}{\omega_s^2 - 4\omega_p^2} R_p^2(t) - \frac{2}{\omega_s^2 - 4\omega_p^2} \dot{R}_p^2(t) \right) \boldsymbol{\phi}_s. \end{aligned} \tag{4.31}$$

Comparing the mode shapes given by MD and SMD, one can already underline that the summed term given by MD reduces to that given by SMD if one considers the slow/fast assumption with $\omega_s \gg \omega_p$. However a difference persists in the two methods since with SMD an added quadratic term, depending on mode p only, is present (second term in (4.30)). This comes again from the treatment of the self-quadratic g^p_{pp} term in Eqs. (4.14),. Indeed, the g^p_{pp} term for the MD method is not present in the reconstruction, but in the dependence

of the nonlinear frequency with amplitude instead, while the SMD method distributes the influence of this g^p_{pp} term on the spatial reconstruction, but not on the amplitude-frequency relationship. This explains why the prediction of the hardening/softening behaviour appears to be more general for the MD method than for the SMD. Comparing now with the normal form approach, one can see that NF reduction gives rise to velocity-dependent terms in these formula, a feature that is not present in the other method, which is a direct consequence of the fact that NF method takes into account both independent displacement and velocity variables as it should be from a dynamical system perspective.

Again, one can also observe that the summed term in (4.32) reduces (at first significant order) to that provided by SMD when the slow/fast assumption is at hand, showing that the SMD method provides the most simplified expressions.

From the general expressions given in (4.29)-(4.32), one can isolate the constant term (zeroth harmonic) which is produced by the quadratic nonlinearity, in order to compare more closely one term of this general expansion. This constant term is known as a drift since it corresponds to the fact that due to quadratic nonlinearity, the oscillations are no more centred around zero, and it has already been compared for different reduction methods, see *e.g.* [99, 158]. One can then simply replace $R_p(t)$ by the expression given by Eq. (4.23); while the values of $R^2_p(t)$ and $\dot{R}^2_p(t)$ up to second order write:

$$R^2_p(t) = \frac{a_0^2}{2}\left(1+\cos[2\omega_{\mathrm{NL}}t]\right) + \mathcal{O}(a_0^3) \tag{4.32}$$

$$\dot{R}^2_p(t) = \frac{a_0^2}{2}\omega^2_{\mathrm{NL}}\left(1-\cos[2\omega_{\mathrm{NL}}t]\right) + \mathcal{O}(a_0^3) \tag{4.33}$$

where the nonlinear frequency $\omega_{\mathrm{NL}} = \omega_p(1+a_0^2\Gamma)$ has been introduced. Isolating the constant term leads to the following expressions for the drift d predicted by each reduction method:

$$\boldsymbol{d}_{\mathrm{MD}} = \frac{a_0^2}{2}\left(-\frac{g^p_{pp}}{\omega_p^2}\boldsymbol{\phi}_p - \sum_{\substack{s=1\\ s\neq p}}^{N}\frac{g^s_{pp}}{\omega_s^2-\omega_p^2}\boldsymbol{\phi}_s\right), \tag{4.34}$$

$$\boldsymbol{d}_{\mathrm{SMD}} = \frac{a_0^2}{2}\left(-\frac{g^p_{pp}}{\omega_p^2}\boldsymbol{\phi}_p - \sum_{\substack{s=1\\ s\neq p}}^{N}\frac{g^s_{pp}}{\omega_s^2}\boldsymbol{\phi}_s\right), \tag{4.35}$$

$$\boldsymbol{d}_{\mathrm{NF}} = \frac{a_0^2}{2}\left(-\frac{g^p_{pp}}{\omega_p^2}\left(\frac{1}{3}+\frac{2}{3}\frac{\omega^2_{\mathrm{NL}}}{\omega_p^2}\right)\boldsymbol{\phi}_p - \sum_{\substack{s=1\\ s\neq p}}^{N}\frac{g^s_{pp}}{\omega_s^2}\left(1-\frac{2(\omega^2_{\mathrm{NL}}-\omega_p^2)}{\omega_s^2-4\omega_p^2}\right)\boldsymbol{\phi}_s\right). \tag{4.36}$$

One can observe that assuming slow/fast dynamics, the drift predicted by MD reduces to that given by SMD. On the other hand, one can also see that in order to retrieve the drift predicted by SMD from $\boldsymbol{d}_{\mathrm{NF}}$, one has to assume that the deviation of the nonlinear

frequency ω_{NL} is small as compared to the linear frequency so that $\omega_{\text{NL}} \simeq \omega_p$. Hence the prediction of the mode shape dependence on amplitude given by SMD is reliable only in the case where the backbone curve does not depart severely from the linear resonance, which is a strong assumption.

In order to point out a last difference on the theoretical expressions which will have important consequences in the next sections, let us also follow the first harmonic of the solution in the reconstruction procedure. Using Eq. (4.23) to define the harmonic content of the master variable, and going back to the harmonic content of the modal coordinates q_i defined using either the QM method, Eq. (4.16), or the normal form approach, Eqs. (4.5)-(4.6), one can easily follow the first harmonic and retrieve its expression in the modal coordinates. Since p is the master mode and at lowest order $q_p = R_p$, then the most important contribution is present in q_p as compared to other q_k's. Let us denote as $[q_p^{(H1)}]_{\text{MD}}$ the first harmonic for the MD approach (and SMD and NF for the other two methods), these expressions write:

$$[q_p^{(H1)}]_{\text{MD}} = a_0 \cos(\omega_{\text{NL}} t) \left(1 + \mathcal{O}(a_0^4)\right), \tag{4.37a}$$

$$[q_p^{(H1)}]_{\text{SMD}} = a_0 \cos(\omega_{\text{NL}} t) \left(1 - a_0^2 \, \frac{2}{3} \left(\frac{g_{pp}^p}{\omega_p^2}\right)^2 + \mathcal{O}(a_0^4)\right), \tag{4.37b}$$

$$[q_p^{(H1)}]_{\text{NF}} = a_0 \cos(\omega_{\text{NL}} t) \left(1 + \mathcal{O}(a_0^4)\right). \tag{4.37c}$$

They underline the importance of the treatment of the self-quadratic g_{pp}^p term between MD and SMD method. Indeed, whereas the amplitude a_0 defined from (4.23) corresponds, for the MD and NF cases, to the amplitude of the first harmonic in q_p, this is not the case for the QM derived from SMD. In that case, the amplitude has an extra term implying the self-quadratic coupling term. Importantly, this term appears as a difference so that the amplitude of the first harmonic can tend to small values with increasing a_0. Whereas all the comparisons led in this section shows that the methods tend to be equivalent under a slow/fast assumption, this last expression highlights the fact that, for the SMD method, the amplitude of the master mode can be very different from the amplitude of the initial coordinate. The consequence of this finding will be more clearly illustrated in the next sections on examples, and will be key to understand why the SMD method can fail even under the slow/fast assumption.

4.5 Comparison on two degrees of freedom systems

In this section, the comparisons drawn out on the theoretical expressions are illustrated on two dofs systems, in order to highlight the main differences on simple cases. Two different models are selected. The first one is derived from the equations of motion of a beam, and is selected in order to mimic the nonlinearities present in a flat symmetric system, where these simplifying assumptions help in letting the methods based on SMD work properly. The second example has important quadratic couplings and better accounts

from the problems arising with curved structures such as arches and shells.

4.5.1 A two-dof model representing a flat symmetric structure

Recalling Eq. (3.3) defined in the previous chapter and referred to a two modes reduction of a von Kármán beam, here we use the model to investigate the effect that the ratio $\rho = \omega_2/\omega_1$ has on the different methods. The two-dofs system that will be used for the investigations reads:

$$\ddot{q}_1 + q_1 + 2\,\bar{G}\,\rho\,q_1 q_2 + D q_1^3 = 0, \tag{4.38}$$

$$\ddot{q}_2 + \rho^2 q_2 + \bar{G}\,\rho q_1^2 = 0, \tag{4.39}$$

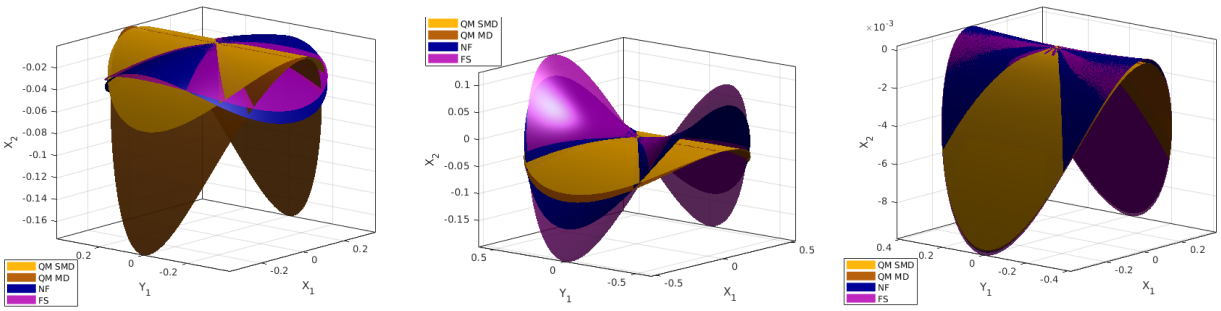
where $\bar{G} = G\,\beta^2/(4\pi\sqrt{12})$ has been introduced for the ease of reading and the ratio ρ has been substituted to the slenderness factor σ. Also the notation for the variables has been changed with $q_1 = q_1$ and $q_2 = p_4$ for the sake of simplicity. A particular feature of this system is that the coupling between master and slave mode is purely quadratic. Consequently the potential third-order tensors from the normal form approach are all vanishing. In this case, the two nonlinear mappings are thus exactly at the same order due to the very simplified shape of the starting equations.

This system is now investigated in order to see how the methods under study behaves when reducing the system to its first (flexural) mode using different nonlinear mappings. The advantage of this formulation is that all coefficients are related to a physical problem so that some insights can be given to the results obtained with this simplistic model with regard to continuous problems. In particular, the previous section underlined that all methods show a convergence on some properties when a slow/fast assumption is assumed, which has been quantified precisely on the type of nonlinearity as occurring for $\rho > 4$. Also, divergent behaviours has been underlined and explained for $\rho \simeq 1$ (case of MD) and $\rho \simeq 2$ (case of normal form). Consequently the system will be studied for three different values close to these points, namely $\rho = 1.25$, $\rho = 2.5$ and $\rho = 10$. Note that a beam is generally considered as slender if $\sigma \leq 1/20$. Thanks to Eq. (3.4), this means that $\rho \geq 40$. The consequence of this remark is that in all slender beams the slow/fast assumption is very well fulfilled, and our study concerns specific cases occurring for very thick beams. Regarding the nonlinear coefficients G and D, they only depend on the modes selected in the expansion. In our study, we will always consider the first flexural and fourth axial, so that G and D are constants since they only depend on the nondimensional shape functions of the selected modes. In the remainder of the study, we have selected $D = 2.67$, $\bar{G} = 0.63$.

Results

The comparisons between the different methods are drawn out on the geometry of the manifolds, as well as on the dynamics onto these manifolds, described by the frequency-amplitude relationship (backbone curve). All the solutions are computed thanks to a nu-

merical continuation method using the asymptotic-numerical method, implemented in the software Manlab, where the unknowns are represented thanks to the harmonic balance method [27, 41, 78]. After a convergence study, the number of harmonics retained in the computations is 7. In each case, the master mode is the fundamental one, q_1, and the slave mode q_2. The dynamics onto the reduced subspaces is given by Eq. (4.19) when using the MD approach, Eq. (4.20) if one considers SMD instead, and Eq. (4.21) with the normal form method, with R_1 the master coordinates. For the reduced models, continuation is performed on the master coordinate in order to compute the frequency-amplitude relationships. From these values, the nonlinear mappings, given either by Eqs. (4.1) for the normal form approach, or by Eqs. (4.16) for the QM method, allows to retrieve the initial modal amplitude q_1 and q_2. From all these data, one can plot either the geometry of the manifolds in phase space (q_1, p_1, q_2, p_2), or the backbone curves.



(a) $\rho = 1.25$. (b) $\rho = 2.5$. (c) $\rho = 10$.

Figure 4.3: Comparison of manifolds in phase space for the first example, and for three different values of $\rho = \omega_2/\omega_1$. The exact NNM, represented in violet (full system solution: FS), is compared to the reduction manifolds obtained by QM from MDs (dark orange), from SMDs (yellow), and normal form (blue). (a) $\rho = 1.25$, (b) $\rho = 2.5$, (c) $\rho = 10$ with slow/fast assumption fulfilled.

Fig. 4.3 shows the geometry of the manifolds obtained for this first system, when one increases the values of ρ so as to meet the slow/fast assumption. One can remark that the reduced subspaces produced by the quadratic manifold method don't show a dependence on the velocity. Increasing the values of ρ it is observed that the real manifold obtained from the full system loses this velocity dependence so that this approximation is less and less wrong. On the other hand, the manifold produced by normal form has two important advantages: it is an invariant manifold of the full system by construction, and it has this velocity dependence, hence allowing for a correct prediction of the reduction subspace, whatever the value of ρ. As a matter of fact the only limitation of the normal form approach is that it relies on a Taylor expansion, so that for large amplitudes, the solution departs from the exact manifold. But in any case the correct invariant subspace is approximated. As already remarked, due to the fact that only quadratic couplings are present between master and slave coordinates, the manifolds shown in Fig. 4.3 for the normal form are obtained thanks to the second-order expansion, the third-order terms being all equal to zero.

Fig. 4.3a shows also that the quadratic manifold produced by MD encounters a problem near the 1:1 resonance, which is here underlined since ρ has been selected close to 1. Comparison with a full order solution clearly shows that this is a failure of the method. In fact, a 1:1 internal resonance is not occurring in this case, as shown by the behaviour of the full model. If a 1:1 resonance case was tested, in each method two modes should be kept in the basis to correctly reproduce it; such case is not treated here because the system is composed of two degrees of freedom only and a two modes reduced model would be meaningless in such conditions. On the other hand, Fig. 4.3c shows that when the slow/fast assumption is verified, then all methods converge to the same reduced subspace, in line with the theoretical results.

We now turn to the prediction given on the backbone curves. First of all, one can compare the values of the Γ coefficients dictating the type of nonlinearity. Eqs. (4.25) have thus been rewritten for the present two-dofs system and now read, as a function of the ratio $\rho = \omega_2/\omega_1$:

$$\Gamma_{\text{MD}} = \frac{3D}{8} - \frac{\bar{G}^2(3\rho^2-2)\rho^2}{4(\rho^2-1)^2}, \tag{4.40a}$$

$$\Gamma_{\text{SMD}} = \frac{3D}{8} - \frac{\bar{G}^2(3\rho^2+4)}{4\rho^2}, \tag{4.40b}$$

$$\Gamma_{\text{NF}} = \frac{3D}{8} - \frac{\bar{G}^2(3\rho^2-8)}{4(\rho^2-4)}. \tag{4.40c}$$

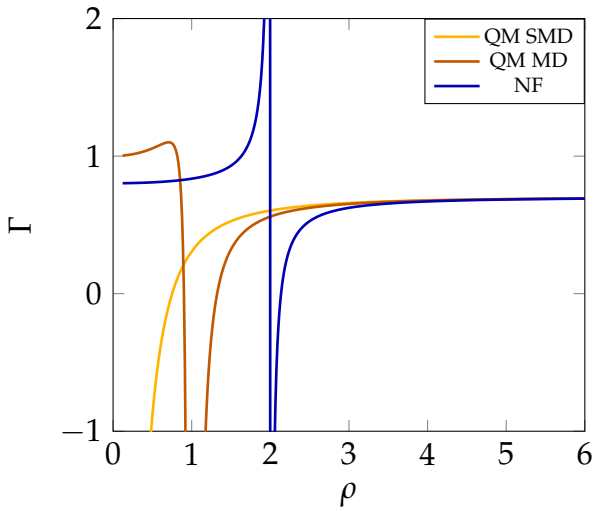
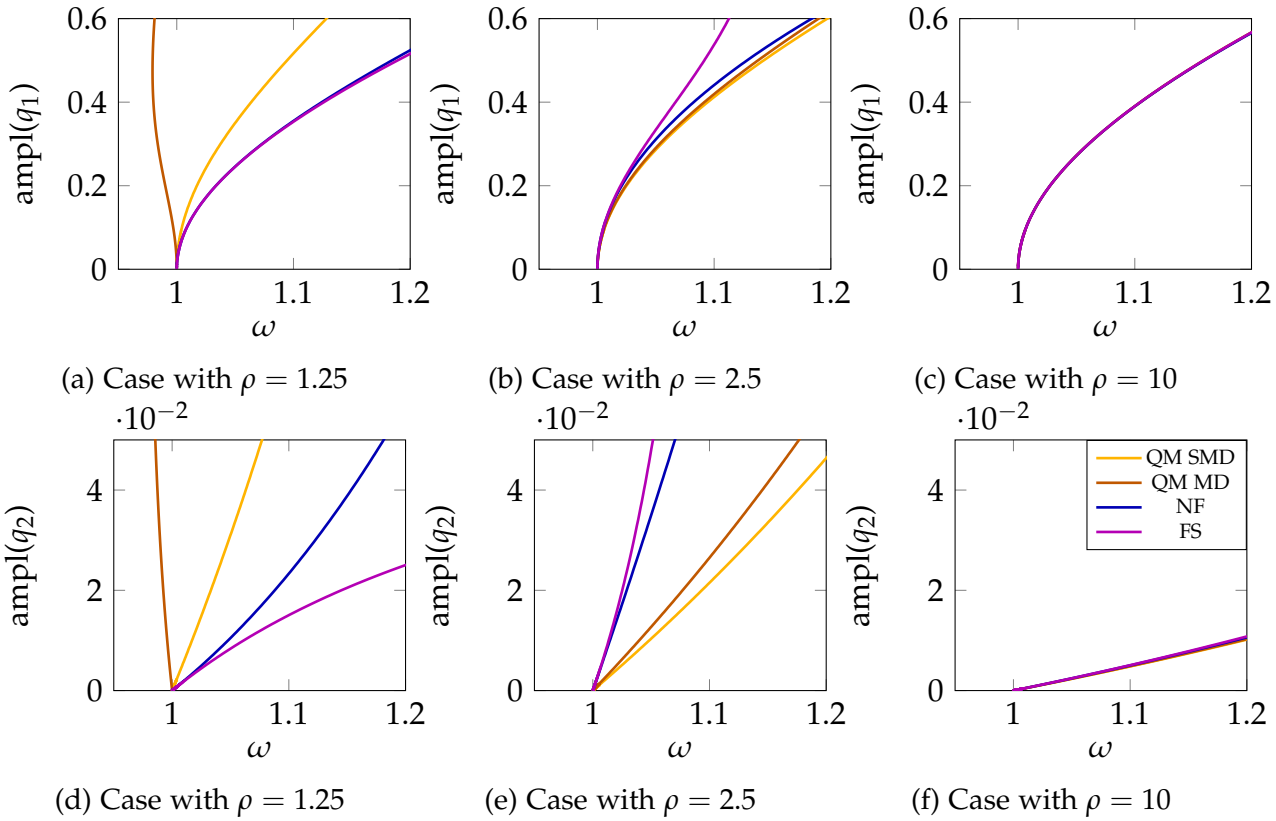


Figure 4.4: Values of the coefficient Γ dictating the hardening/softening behaviour for the first two-dofs system. Comparison of Γ_{MD}, Γ_{SMD} and Γ_{NF}, given respectively by QM with MDs, with SMDs, and normal form, Eqs. (4.40), and for varying $\rho = \omega_2/\omega_1$ ratio.

These values are represented in Fig. 4.4, which shows important similarities with Fig. 4.2. Again the same divergent behaviours are observed, and the convergence of all methods for $\rho > 4$ is clearly observed. To be more quantitative, the relative difference between Γ_{MD} and Γ_{NF} is 5% for $\rho = 2.95$ and 1% for $\rho = 3.93$. On the other hand, the difference between Γ_{SMD} and Γ_{NF} is 5% for $\rho = 3.06$, and 1% for $\rho = 4.18$, underlining clearly that $\rho \in [3, 4]$ has to be

understood as a transition zone. For very small values of ρ, the quadratic manifold based on SMD will predict incorrect result with a softening behaviour. Also, after its failure at $\rho = 1$, the MD method will also produce an incorrect prediction with a softening behaviour.



(a) Case with $\rho = 1.25$ (b) Case with $\rho = 2.5$ (c) Case with $\rho = 10$

(d) Case with $\rho = 1.25$ (e) Case with $\rho = 2.5$ (f) Case with $\rho = 10$

Figure 4.5: First mode backbone curves as a function of modal amplitude q_1 (first row), and q_2 (second row), and for different values of $\rho = \omega_2/\omega_1$. Comparisons between the exact solution (FS: full system, violet), that predicted by QM with MDs (dark orange), SMDs (yellow) and normal form (NF, blue).

Fig. 4.5 shows the backbone curves obtained from the reduced-order dynamics and compared to that obtained from the full system. The comparison is drawn on the main modal amplitude q_1, which shows the largest values (first row), but also on the slave coordinate q_2 (second row). The first case selected, just after the 1:1 resonance with $\rho = 1.25$, shows, as envisioned in Fig. 4.4, that the QM produced from MD can be very wrong in this case and predict at first order a softening behaviour. When $\rho = 2.5$, the three methods predicts a very similar behaviour and are almost undistinguishable. One can note that for large amplitude, the full system solution is less and less hardening. This is probably a consequence of the vicinity of the 2:1 internal resonance. Since $\omega_2 = 2.5\omega_1$ and the behaviour is hardening, the nonlinear frequency tends to approach the 2:1 ratio at higher amplitudes, which could explain this particular behaviour of the full system solution. Finally, for $\rho = 10$, the three methods give the same predictions which are fully aligned with the full system.

The conclusion on this first example with simple nonlinearities are in the line of the theoretical results, since all methods tends to perform well in the limit of the slow/fast assumption, again estimated as a ratio of 4 between the eigenfrequencies of the master and slave mode.

On the other hand, when this assumption is not fulfilled, the quadratic manifold is not reliable and can produce incorrect predictions, in contrary to the normal form approach, that gives a correct ROM up to the third-order, whatever the link between slave and master coordinates. These results explain also why the application of modal derivatives on slender structures that are flat and symmetric produce accurate results. Indeed, slenderness is fulfilled when ρ is larger than 40, and our numerical experiments show that the slow/fast assumption can be considered as valid as soon as $\rho > 4$.

4.5.2 A two-dof model representative of a shell structure

Equations of motion

In this section, a system composed of a mass connected to two springs representing geometric nonlinearity and sketched in Fig. 4.6, is selected. This system has been used in a number of studies so that numerous results are already present in the literature, the interested reader is referred to [158] for the derivation of the equation of motions specifying the behaviour of the springs, and to [22,121,154,158] for different results already published on this example system.

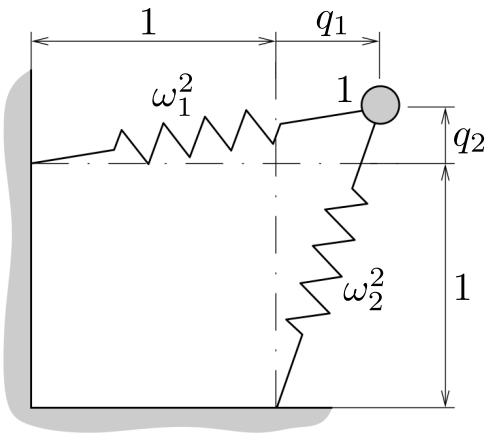


Figure 4.6: Two degrees of freedom model with quadratic springs characteristic and geometric nonlinearities.

Here we simply recall that the main idea behind this model is to replicate the behaviour of a structure with quadratic and cubic nonlinearities. For this reason, the characteristic of the springs is proportional to the quadratic difference between the equilibrium position and the deformed position. The potential energy reads:

$$\mathcal{E}_p = \frac{1}{2}\left(\omega_1^2\epsilon_1^2 + \omega_2^2\epsilon_2^2\right) \qquad \text{with } \epsilon_i = \frac{1}{2}\left(l_i^2 - 1\right) \tag{4.41}$$

and the deformed lengths l_i defined as:

$$l_1 = \sqrt{(1+q_1^2)+q_2^2} \tag{4.42a}$$

$$l_2 = \sqrt{(1+q_2^2)+q_1^2} \tag{4.42b}$$

The equations of motion of the system then read:

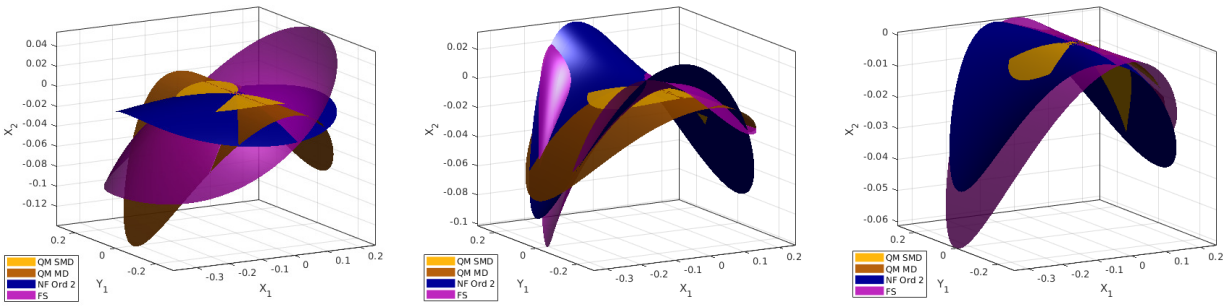
$$\begin{aligned} &\ddot{q}_1 + \omega_1^2 q_1 + \frac{\omega_1^2}{2}(3q_1^2+q_2^2) + \omega_2^2 q_1 q_2 + \frac{\omega_1^2+\omega_2^2}{2} q_1(q_1^2+q_2^2) = 0, \\ &\ddot{q}_2 + \omega_2^2 q_2 + \frac{\omega_2^2}{2}(3q_2^2+q_1^2) + \omega_1^2 q_1 q_2 + \frac{\omega_1^2+\omega_2^2}{2} q_2(q_1^2+q_2^2) = 0. \end{aligned} \tag{4.43}$$

As compared to the previous example, this system has all quadratic nonlinear terms present in the equations of motion, and all the nonlinear coefficients are expressed directly from the two eigenvalues ω_1 and ω_2, so that the problem has only two parameters. Note that this model is not derived from a continuous shell structure like the previous example was derived from the von Kármán beam equations, however it is known that curved structures display strong quadratic couplings that are found in this system. Moreover, the results will show that this model is sufficient to show important departures between the three tested methods, which are due to the way the quadratic terms are processed.

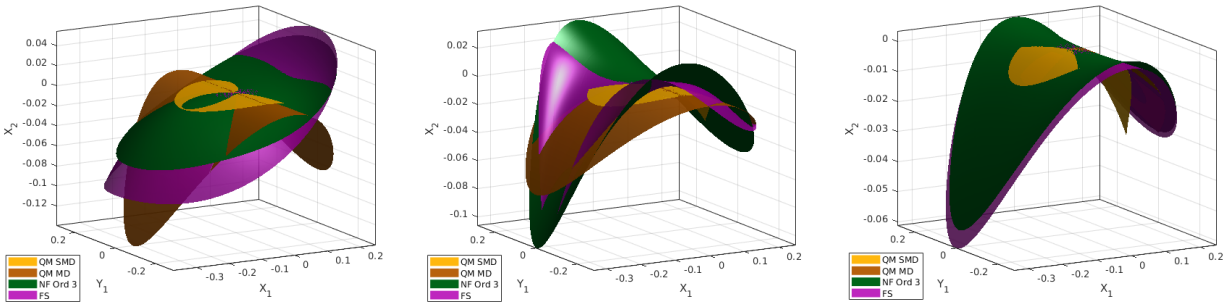
Results

As for the preceding example, comparisons are drawn out on the geometry of the manifolds and the backbone curves. Numerical continuation is used to solve out the different systems and compare their outcomes. The eigenfrequency ratio $\rho = \omega_2/\omega_1$ is also used and the same values, namely 1.25, 2.5 and 10 are selected to observe the differences between the methods when tending to fulfil the slow/fast assumption. In the computation, $\omega_1 = 1$ in all cases so that one simply have $\omega_2 = \rho$.

Fig. 4.7 shows the geometry of the manifolds in phase space, as compared to the exact invariant manifold defining the first NNM of the system. The comment on the velocity dependence, already raised in the previous example, still holds: while for small values of ρ the quadratic manifolds are not able to catch the correct curvature in this direction, for large values of ρ the velocity dependence vanishes. Note that in all the three figures, the manifold produced by the SMD method has a smaller range in amplitude. This maximal range used for the representation has been fixed from the frequency-amplitude relationships (see Fig. 4.9, when the nonlinear frequency has decreased of ten percent and reaches the value 0.9 –a softening behaviour is at hand in the considered cases–), so that all manifolds spans the same frequency range, but corresponds to different amplitudes. This underlines in particular that even if the correct manifold is approximated, which is the case for $\rho = 10$, the amplitude-frequency relationship may be not.

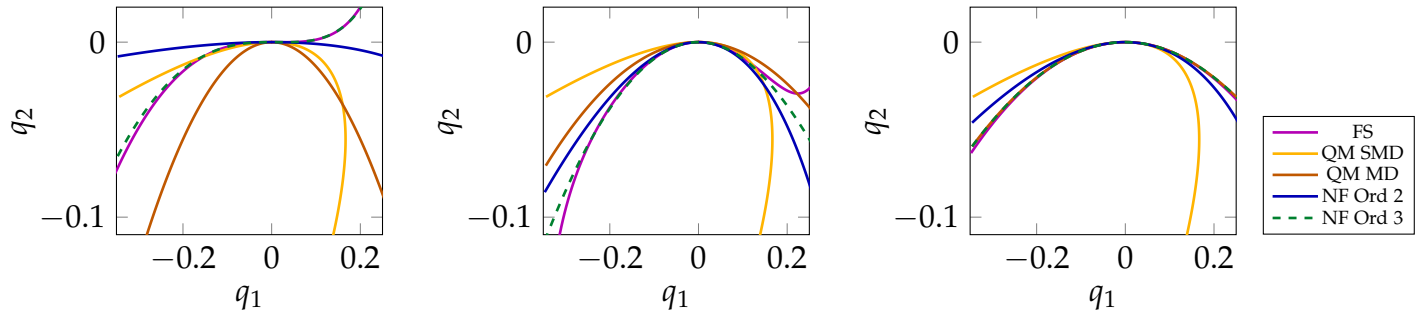


(a) Case with $\rho = 1.25$. (b) Case with $\rho = 2.5$. (c) Case with $\rho = 10$.



(d) Case with $\rho = 1.25$. (e) Case with $\rho = 2.5$. (f) Case with $\rho = 10$.

Figure 4.7: Comparison of manifolds in phase space for the second two-dofs example, and for three different values of $\rho = \omega_2/\omega_1$. The exact NNM, represented in violet (full system solution: FS), is compared to the reduction manifolds obtained by QM from MDs (dark orange), from SMDs (yellow), and normal form up to the second order (blue manifold in the first line, plots a-b-c) and third order (green manifolds, second line in plots d-e-f) are given. (a-d) $\rho = 1.25$, (b-e) $\rho = 2.5$, (c-f) $\rho = 10$ with slow/fast assumption fulfilled. In all cases $\omega_1 = 1$.



(a) Case with $\rho = 1.25$ (b) Case with $\rho = 2.5$ (c) Case with $\rho = 10$

Figure 4.8: First mode invariant manifolds cut on the $\dot{q}_1 = 0$ plane, evaluated with the quadratic manifold method (QM) (either with MD in dark orange, and SMD in yellow) and normal form (NF) approach, where the distinction between NF up to second order (blue line) and third-order (dashed green line) is reported, and compared to the numerical solution obtained with the full system (FS). In all cases $\omega_1 = 1$.

Since the only difference between second- and third-order normal form can be appreciated from the nonlinear mapping and not the reduced dynamics, Fig. 4.7 illustrates the case. In the first line, the manifold produced by the second-order normal form (in blue) is contrasted to the other methods, while the third-order is shown in the second line (in green).

One can observe that the effect of retaining the cubic term is especially important for the smallest values of $\rho = 1.25$, but then the differences between second- and third-order are barely visible. Interestingly, this example also shows that the quadratic manifolds produced by MD and SMD does not tend to the same geometries, even under the assumption of slow/fast dynamics. This can be appreciated in Fig. 4.7, but is more clearly evidenced in Fig. 4.8 where a section of the manifolds in space (q_1, q_2) is shown, without the amplitude limit given by the frequency, used in the 3d plot.

Unlike Fig. 4.7, Fig. 4.8 has been directly obtained from the manifolds expressions given by Eq. (4.16) for the QM approach, and (4.5)-(4.6) for the normal form approach, by simply prescribing the values of R_1 and compute the resulting (q_1, q_2) values. More specifically, let us underline the main difference between the MD and SMD method in this case. Using Eqs. (4.16) with (4.14), the reconstruction of (q_1, q_2) from the QM method derived from MD reads:

$$q_1 = R_1, \tag{4.44a}$$

$$q_2 = -\frac{g_{11}^2}{\omega_2^2 - \omega_1^2} R_1^2 = -\frac{\omega_2^2}{2(\omega_2^2 - \omega_1^2)} R_1^2. \tag{4.44b}$$

On the other hand, using SMD in the QM leads to:

$$q_1 = R_1 - \frac{g_{11}^1}{\omega_1^2} R_1^2 = R_1 - \frac{3}{2} R_1^2, \tag{4.45a}$$

$$q_2 = -\frac{g_{11}^2}{\omega_2^2} R_1^2 = -\frac{1}{2} R_1^2. \tag{4.45b}$$

One can first notice that for this specific example, the manifold produced with the SMD method does not depend on the parameters (ω_1, ω_2). Consequently, the cut of this manifold in (q_1, q_2) plane in Figs. 4.8(a-c) for different values of ρ, is always the same. The second comment is on the slow/fast approximation: even though the value given for q_2 tends to be the same under the slow/fast assumption $\omega_2 \gg \omega_1$, this is not the case for q_1. This is a major difference between the two methods, so that a persistent error on the manifold is done when using SMD, whereas MD tends to the solution provided by the NF and full system when ρ increases. The last interesting comment is on the fact that the manifold produced by SMD shows a constant folding point. Indeed, q_1 from Eq. (4.45a) cannot exceed the value of $1/6$ (achieved at $R_1 = 1/3$) after which the quadratic term in Eq. (4.45a) is larger than the linear one.

This is a direct consequence of the different treatment of the self-quadratic coupling term g_{11}^1, already underlined at the end of Sect. 4.4, leading to the fact that even under the slow/fast assumption, the QM built on SMD can lead to erroneous results. This point is further commented on the backbone curves comparison. First, Eqs. (4.25) are written for this specific system, leading to the following predictions, as a function of the ratio

$\rho = \omega_2/\omega_1$:

$$\Gamma_{\text{MD}} = -\frac{16\rho^4 - 27\rho^2 + 12}{16(\rho^2-1)^2}, \tag{4.46}$$

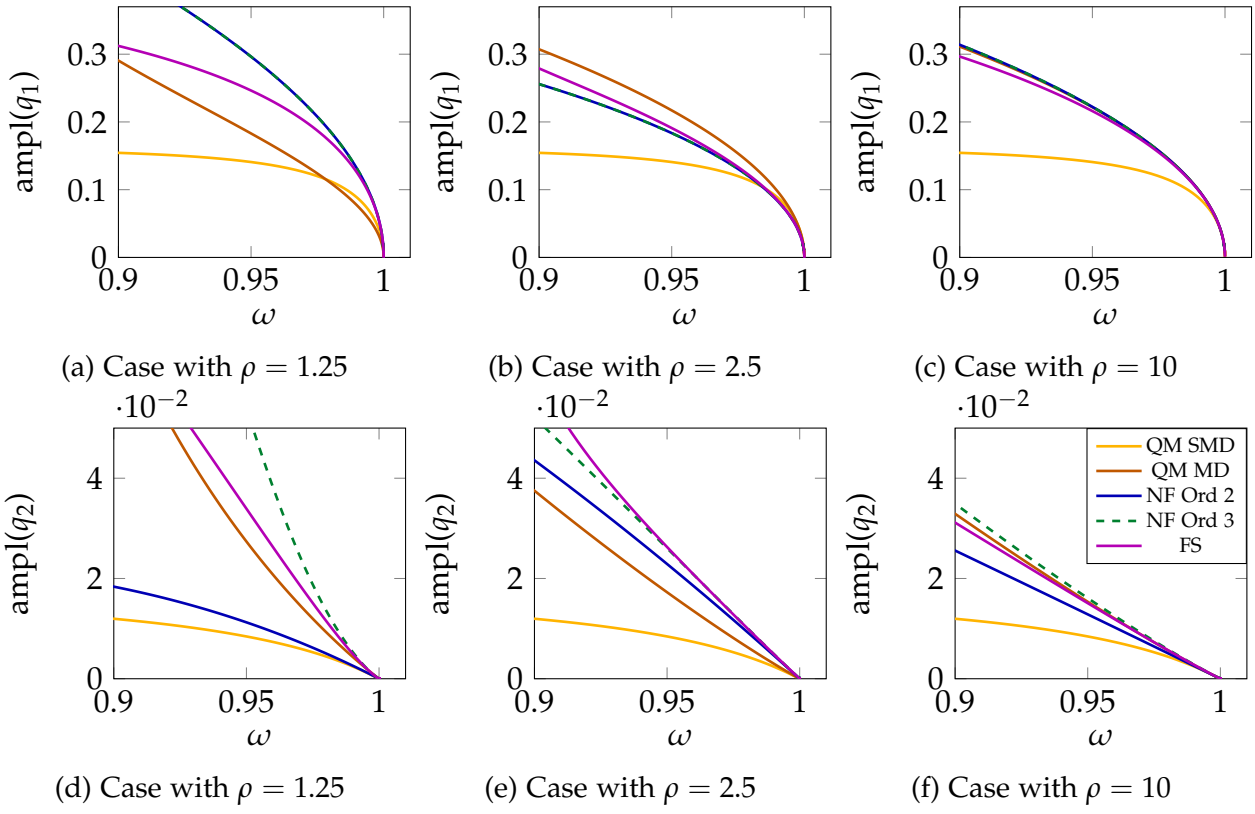
$$\Gamma_{\text{SMD}} = -1, \tag{4.47}$$

$$\Gamma_{\text{NF}} = -\frac{\rho^2 - 3}{\rho^2 - 4}. \tag{4.48}$$

In line with the constant manifold found with SMD, the method also predicts a constant type of nonlinearity, independent of the variations of the eigenfrequencies (ω_1, ω_2). Assuming slow/fast partition, $\rho \to \infty$, then all three methods tends to predict the same Γ coefficient dictating the hardening/softening behaviour. However, as underlined at the end of Sect. 4.4, the amplitude of the first harmonics for each method is different. Since in this case $g^1_{11} \neq 0$, a direct consequence of (4.37b) is that the backbone curves for the SMD method will show a saturation effect, the amplitude q_1 being unable to overcome a maximum value. This phenomenon is clearly visible in Fig. 4.9, depicting the backbone curves obtained for the three selected values of ρ. The constant value of Γ_{SMD} has for direct consequence that the backbone predicted by the SMD quadratic manifold is almost unchanged with respect to variations of ρ. When the slow/fast assumption is fulfilled for $\rho = 10$, Fig. 4.9(c), the backbone predicted by SMD QM is in line with those predicted by the other methods at small amplitude level. However, at higher amplitude the SMD backbone moves away from the others and saturates to a limit value for all cases, since the amplitude is differently computed as shown in Eq. (4.37b). On the other hand, the backbone predicted by the MD method tends to the correct values under the slow/fast approximation, while the normal form approach always produces a correct prediction. More specifically, the prediction for the master q_1 component given by the normal form is the same if one considers a quadratic or cubic normal form expansion, see Eq. (4.5). On the other hand, the slave component q_2 is affected by the order and this is illustrated in Fig. 4.9(d-e-f), where one can observe that, as for the manifold approximation in phase space, the third-order terms bring about a better estimate.

4.6 Shallow and Non-Shallow Arches

This section aims at drawing a comparison between the different methods when applied on a continuous structure discretised with three dimensional finite elements. In order to investigate how the results obtained in the previous section are confirmed in the general case, three beams are considered and shown in Fig. 4.10. They have been selected in order to fulfil different assumptions that have been highlighted on the two-dofs examples in order to achieve correct predictions from the ROMs. The first case, Fig. 4.10a, is a slender flat symmetric beam. The two other examples, Fig. 4.10b and Fig. 4.10c are arches, the first one being shallow while the third one is non-shallow. Adding curvature has two important effects. First, flexural and in-plane modes are no longer linearly uncoupled. Second, the

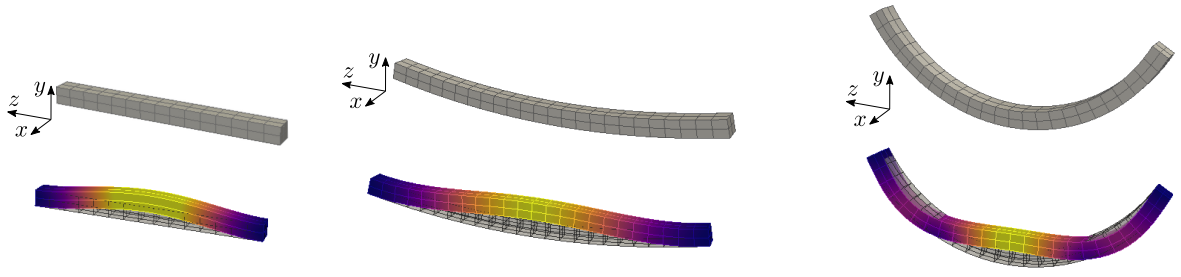


(a) Case with $\rho = 1.25$ (b) Case with $\rho = 2.5$ (c) Case with $\rho = 10$

(d) Case with $\rho = 1.25$ (e) Case with $\rho = 2.5$ (f) Case with $\rho = 10$

Figure 4.9: First mode backbone curves for the second two-dofs example with quadratic nonlinearity, as a function of modal amplitude q_1 (first row), and q_2 (second row), and for different values of $\rho = \omega_2/\omega_1$. Comparisons between the exact solution (FS: full system, violet), that predicted by QM with MDs (dark orange), SMDs (yellow) and normal form (NF, blue, NF third order, dashed green).

curvature renders the restoring force asymmetric and an important quadratic nonlinearity appears between the bending modes. This example illustrates the fact that the slow/fast assumption is not enough to guarantee that the method based on static modal derivatives will converge. The curvature will be used in order to play on the slow/fast assumption as well as on the values of the quadratic coupling terms.



(a) Flat beam. (b) Shallow arch. (c) Non-shallow arch.

Figure 4.10: Mesh and deformation along the mode under study for three different test cases: (a) a flat beam, (b) a shallow arch and (c) a non-shallow arch. For each test case the mode under study corresponds to the first flexural mode in the plane $y - z$ where the curvature is imposed if present.

In all three cases, the boundary conditions are clamped, the material parameters are se-

lected as homogeneous linear elastic with Young modulus $E = 124$ GPa, Poisson ratio $\nu = 0.3$ and density $\delta = 4400$ kgm/s^2. In each cases, an equal thickness h and width b is selected: $h = b = 5$ cm. For the flat beam, the length is $L = 0.7$ m. The arches have been built from a portion of a circle. For the shallow arch, the radius of curvature is set as 250 cm, for an angular span of $2\pi/15$, resulting in a curvilinear length of $20\pi/3 \simeq 1.05$ m. The height of the static deflection at center is 5.5 cm, *i.e.* almost equal to the thickness. For the non-shallow arch, the radius of curvature is set as 50 cm, for an angular span of $2\pi/3$, resulting in the same curvilinear length of $20\pi/3 \simeq 1.05$ m, but with a static deflection of 25 cm, *i.e.* 5 times the thickness. All beams are discretised with three-dimensional hexahedral 20 nodes finite elements. The flat beam uses 60 elements (4 in the section and 15 in the length), resulting in a total number of 1287 dofs. The two arches have 96 solid elements (4 in the section and 24 in the length) and 2097 dofs. A relative coarse mesh has been selected in order to have a limited number of degrees of freedom so that all the methods can be handled easily. Indeed, the key point here is not to look for converged and refined results on a large frequency range, but to compare the different reduction methods on the same test examples. Moreover, as already shown in [165], using 3D elements leads to couplings with very high-frequency thickness modes, so that truncations and convergence are difficult to observe in general.

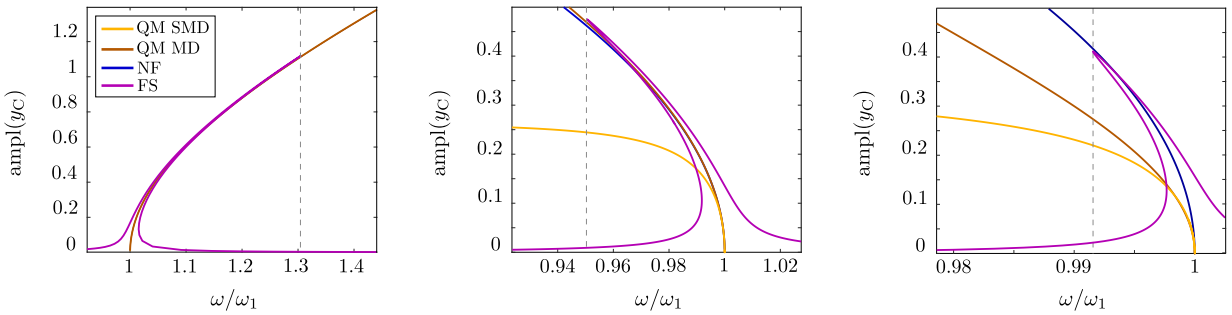
In the three cases, the nonlinear behaviour of the first flexural mode in the curvature plane is investigated. The mode shape is shown in Fig. 4.10. In the case of the flat beam, it corresponds to the first mode and its eigenfrequency is 545.60 Hz. As already underlined in Sect. 4.5.1, the most important coupling arises with the fourth in-plane mode, whose eigenfrequency is 15.19 kHz, so that the ratio ρ between the most important slave mode and the master mode is in this case equal to 27.83. Consequently the slow/fast assumption and our criterion $\rho \geq 4$ is perfectly fulfilled. This example can be seen as an extension of the first two-dofs example, with the distinctive feature that now many more modes are coupled to the first bending, all of them being of higher frequencies than the fourth axial. Also, the nonlinear coupling terms have in this case a simplified form, following the general discussion given in Sect. 4.5.1. In the case of the arches, for the shallow arch the first flexural mode corresponds to the second mode of the structure and its eigenfrequency is equal to 372.28 Hz and, for the non-shallow arch, the first flexural mode corresponds to the fourth mode of the structure and its eigenfrequency is equal to 1003.99 Hz. Contrary to the case of flat symmetric structures, the curvature renders the restoring force asymmetric and an important quadratic nonlinearity appears between the bending modes. Investigating the important couplings between the linear modes of the curved beams shows that the first bending mode is strongly coupled with the third one. While the ratio between the first and third bending modes is 5.4 in the case of the flat beam, it decreases when the curvature increases. Consequently, for the case of the shallow arch, this ratio is equal to 3.44 (eigenfrequency of third bending equal to 1283.33 Hz), and 1.66 for the non-shallow arch (eigenfrequency of third bending equal to 1665.11 Hz). These two examples have thus been built as an extension of the second two-dofs example. For the shallow arch,

the slow/fast assumption is almost fulfilled (3.44 is slightly smaller than the criterion we proposed with a limit value at 4), but now important quadratic couplings are present and in particular the self-quadratic term g^p_{pp}. Finally, the case of the non-shallow arch allows testing a case where the slow/fast assumption does not hold, and important self-quadratic terms are present.

4.6.1 Amplitude-frequency relationships

The methods are compared on their ability to predict the backbone curves. A reference solution is computed thanks to a numerical continuation on all the degrees of freedom of the structure, using a code with parallel implementation of harmonic balance method and pseudo arc-length continuation algorithm [17]. In this computation, a small amount of mass proportional damping is added under the form $\zeta\omega_p \boldsymbol{M}$ so that a frequency-response function (FRF) is computed, in the vicinity of the eigenfrequency of the master mode (first flexural). The values of ζ are 0.18%, 0.27%, and 0.1% for the flat beam, shallow, and non-shallow arches, respectively. The forcing is located in the central node of each mesh in the y-direction in order to excite the first flexural mode. The force amplitude is chosen in order to have a displacement amplitude at resonance comparable to the thickness so that its values are 5 kN, 1.5 kN, and 2.5 kN for the flat beam, shallow, and non-shallow arches, respectively. It must be noticed that in the case of curved structures the value of amplitude of vibration equal to the thickness has not been achieved and the reported FRFs excite a maximum amplitude of approximately half of it. In fact, due to the long computational time that the full model FRF requires, approximately 1 day for each FRF, and due to its high chances to undergo internal resonance with higher modes, these values have been selected in order to stay in the limit of one-mode approximation without exciting more complex dynamics. However, with this level of amplitudes, the nonlinearity is sufficiently important so that its effect is clearly visible on the backbone curves.

The ROMS are built using QM or NNM approach, and their backbone curves are computed in the same manner than in the previous section, assuming a single master mode. For the normal form approach, the third order coefficients have not been included in the computation. Indeed, the third-order tensors require the computation of huge number of coupling coefficients from the modal basis expressions, which would need for an important number of pre-computation steps. This choice has also been guided by the fact that comparing the two methods at the same order of accuracy is more meaningful. The FRF of the ROMS have not been computed since taking into account the damping of the slave modes is important to achieve good results. If the normal form theory has been developed for that purpose, see *e.g.* [154] where the effect of a small amount of damping of the slave modes on the FRF of the master mode is reported, the inclusion of the damping for the modal derivatives has not been derived theoretically yet. Hence it appears that a better comparison is given on the backbone curves only, and the FRF of the full model with a small amount of damping is used to underline if the nonlinearity is correctly addressed by the methods. Fig. 4.11 shows the numerical results obtained for the three cases. The case of the flat beam is the one



(a) Flat beam. (b) Shallow arch. (c) Non-shallow arch.

Figure 4.11: Comparison of backbone curves obtained from QM with MDs (dark orange), SMDs (yellow) and normal form approach (blue), for the three tested structures: (a) flat beam, (b) shallow arch, (c) non-shallow arch. Nondimensional amplitude of flexural displacement (along y, nondimensionalised with respect to the thickness) of the central node of each beam as a function of ω/ω_1 where ω_1 refers to the eigenfrequency of the first flexural mode studied shown in Fig. 4.10. The backbone curves are contrasted to the FRF obtained on the full system (FS, violet) with numerical continuation and a small amount of damping, see text. The vertical gray dashed lines represent the frequency at which the saddle-node bifurcation of the forced response occurs.

having the most assumptions fulfilled (slow/fast separation and no self-quadratic terms). Consequently, the three methods match very well and are all able to retrieve correctly the nonlinearity of the full model with a very good accuracy. In the case of the shallow arch, the slow/fast assumption is almost fulfilled (since being a little bit below the proposed criterion $\rho \geq 4$), and important self-quadratic coupling appears due to the curvature. The main consequence is that the QM built from SMD is not able anymore to predict the correct type of nonlinearity. As already found for the second two-dofs example, it overpredicts the softening behaviour and make appear again the saturation phenomenon in the amplitude of the backbone. On the other hand, both QM based on MD and normal form methods give a correct prediction. For the non-shallow arch, the slow/fast assumption does not hold anymore. The consequence is that the MD method does not predict the correct nonlinearity. This example again illustrates clearly that: (i) as soon as important self-quadratic terms appear (case of arches and shells), then the SMD method is not reliable anymore, whatever the slow/fast assumption is fulfilled or not, (ii) the MD can still give correct result but only if the criterion $\rho \geq 4$ for the slow/fast assumption is fulfilled. As soon as ρ gets under this value, then the solution starts departing from the full-order model, and becomes unreliable when $\rho \leq 2$.

4.6.2 Nonlinear modeshapes

The different approximations made by the three methods are finally contrasted on the mode shape dependence on amplitude, illustrating the Equations given in Sect. 4.4. Recalling Eqs. (4.29) – (4.32), it is possible to see that, for each method, the contributions to the nonlinear modeshape can be divided into (i) a deformation along the master p mode and (ii) a deformation that contains all the coupled modes but the p-th. In order to make the figures

more illustrative, and since the amplitude of the deformation along p-th mode generally gives the dominant contribution, it is decided to compare the outcomes of the methods only on the (ii) part of the solution. Also, since the normal form approach constructs the solution both with displacements and velocities, to draw a better comparison the focus will be on the time step where the reduced variable $R_p(t)$ reaches its maximum and minimum values (i.e. a turning point such that $\dot{R}_p(t) = 0$).

Under these assumptions, let us define as $\boldsymbol{U}^{\perp}$ the component of the nonlinear mode shape $\boldsymbol{U}$ that is orthogonal to $\boldsymbol{\phi}_p$. From Eqs. (4.29) – (4.32), it reads, for the three different methods:

$$\boldsymbol{U}^{\perp}_{\mathrm{MD}}(t^*) = -R_p^2(t^*) \sum_{\substack{s=1 \\ s\neq p}}^{N} \frac{g^s_{pp}}{\omega_s^2 - \omega_p^2} \boldsymbol{\phi}_s, \tag{4.49a}$$

$$\boldsymbol{U}^{\perp}_{\mathrm{SMD}}(t^*) = -R_p^2(t^*) \sum_{\substack{s=1 \\ s\neq p}}^{N} \frac{g^s_{pp}}{\omega_s^2} \boldsymbol{\phi}_s, \tag{4.49b}$$

$$\boldsymbol{U}^{\perp}_{\mathrm{NF}}(t^*) = -R_p^2(t^*) \sum_{\substack{s=1 \\ s\neq p}}^{N} \frac{g^s_{pp}}{\omega_s^2} \left(\frac{\omega_s^2 - 2\omega_p^2}{\omega_s^2 - 4\omega_p^2} \right) \boldsymbol{\phi}_s, \tag{4.49c}$$

where t^* is the time instant where R_p is either maximum or minimum.

In order to compare to the full-order solution, the deformation must be first filtered out from its component along the p-th mode. One can thus define $\boldsymbol{U}^{\perp}_{\mathrm{FS}}$ for the full system as:

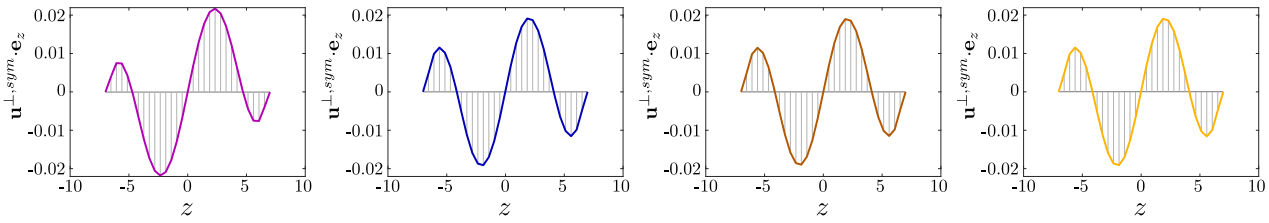
$$\boldsymbol{U}^{\perp}_{\mathrm{FS}}(t) = \boldsymbol{U}_{\mathrm{FS}}(t) - \frac{\boldsymbol{\phi}_p^{\mathrm{T}} \boldsymbol{U}_{\mathrm{FS}}(t)}{\boldsymbol{\phi}_p^{\mathrm{T}} \boldsymbol{\phi}_p} \boldsymbol{\phi}_p. \tag{4.50}$$

Finally, given the quadratic nature of the deformation computed from the reduction methods based on second-order expansions (and clearly underlined by the dependence in R_p^2 in Eqs. (4.49)), the third-order component should be also filtered out from $\boldsymbol{U}^{\perp}_{\mathrm{FS}}$ for a closer comparison. In order to cancel the odd harmonics of the full-order solution, we thus define $\boldsymbol{U}^{\perp,sym}_{\mathrm{FS}}$ as the symmetric part of $\boldsymbol{U}^{\perp}_{\mathrm{FS}}$ with respect to amplitude:

$$\boldsymbol{U}^{\perp,sym}_{\mathrm{FS}} = \frac{1}{2}(\boldsymbol{U}^{\perp}_{\mathrm{FS}}(t^{max}) + \boldsymbol{U}^{\perp}_{\mathrm{FS}}(t^{min})). \tag{4.51}$$

This value will be used as reference and compared to the prediction of the ROMS given by Eq. (4.49).

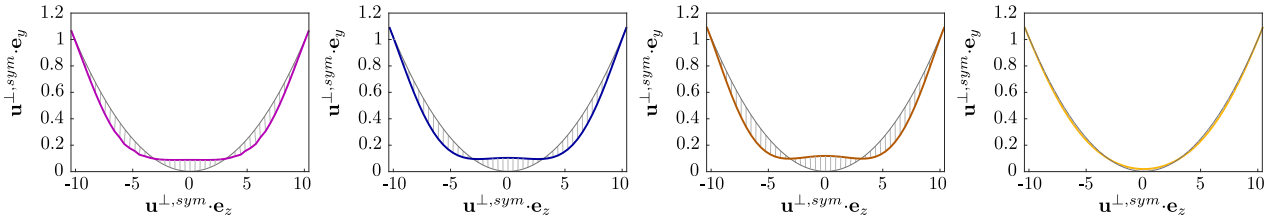
Fig. 4.12 shows the comparison between the $\boldsymbol{U}^{\perp}$ defined by Eq. (4.51) for the full-order system, and those produced by the reduced-order models, Eqs. (4.49), for the case of the flat beam. Importantly enough, since the nonlinear couplings are with in-plane modes, the contributions of the $\boldsymbol{U}^{\perp}$ along the axial z direction is shown in Fig. 4.10, since the most important contributions are along this direction. As it could be awaited from the previous



(a) Full Model. (b) Normal Form. (c) Modal Derivatives. (d) Static MD.

Figure 4.12: Comparisons of the additional terms perturbing the linear mode shape solutions (deformation orthogonal to ϕ_p) for the case of the flat beam, computed at the saddle-node bifurcation point marked in Fig. 4.11a, fixing the frequency at which they have been computed. (a) full model solution, representation of the axial component of displacement $\boldsymbol{U}_{\text{FS}}^{\perp,sym}.\boldsymbol{e}_z$ of the centre line nodes, (b) normal form: $\boldsymbol{U}_{\text{NF}}^{\perp}(t^*).\boldsymbol{e}_z$, (c) Modal derivative : $\boldsymbol{U}_{\text{MD}}^{\perp}(t^*).\boldsymbol{e}_z$, (d) Static modal derivative $\boldsymbol{U}_{\text{SMD}}^{\perp}(t^*).\boldsymbol{e}_z$.

analyses, Fig. 4.12 clearly shows that the three ROMs are all able to recover the correct spatial dependence of the contributions of coupled modes to the fundamental flexural NNM. Also, this contribution is mostly conveyed by the fourth in-plane mode, being the most importantly coupled to the fundamental flexural mode. Note that the amplitude used to construct this figure is the one corresponding to the upper saddle-node bifurcation point in the FRF of the full-order system, as shown by the gray vertical line in Fig. 4.11a. At that point, the backbones and the FRF meet so that it can be used safely for a correct comparison. It also corresponds to an amplitude of one time the thickness for the mode shape.

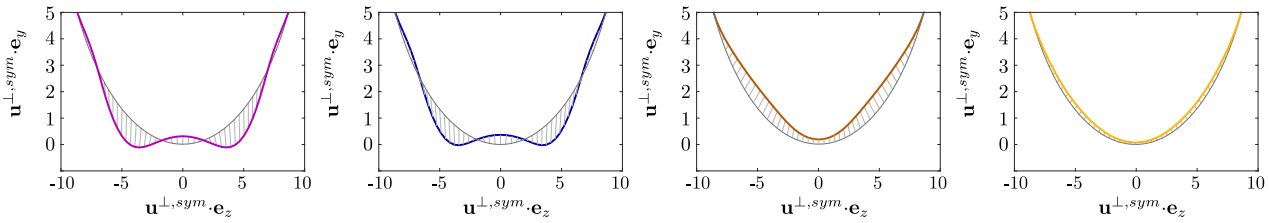


(a) Full Model. (b) Normal Form. (c) Modal Derivatives. (d) Static MD.

Figure 4.13: Comparisons of the additional terms perturbing the linear mode shape solutions (deformation orthogonal to ϕ_p) for the case of the shallow arch, computed at the saddle-node bifurcation point marked in Fig. 4.11b, fixing the frequency at which they have been computed. (a) full model solution, representation of the displacement $\boldsymbol{U}_{\text{FS}}^{\perp,sym}$ of the centre line in the $y-z$ plane; vertical axis $\boldsymbol{U}_{\text{FS}}^{\perp,sym}.\boldsymbol{e}_y$ (transverse direction) and horizontal axis $\boldsymbol{U}_{\text{FS}}^{\perp,sym}.\boldsymbol{e}_z$ (axial direction), (b) normal form: $\boldsymbol{U}_{\text{NF}}^{\perp}(t^*)$, (c) Modal derivative : $\boldsymbol{U}_{\text{MD}}^{\perp}(t^*)$, (d) Static modal derivative $\boldsymbol{U}_{\text{SMD}}^{\perp}(t^*)$. Gray lines: position of the centre line of the beam at rest. Solution amplified of factor 15.

In the case of the shallow arch, some differences are appearing due to the self-quadratic coupling term, creating a deficiency in the prediction given by the SMD. This is underlined in the nonlinear mode shape dependence in Fig. 4.13, where in this case, since the most important coupling is between bending modes, the contributions of the different $\boldsymbol{U}^{\perp}$ are represented along the transverse y direction. The amplitude used for the figure is illustrated

in Fig. 4.11b with a gray line, and still corresponds to the upper saddle-node bifurcation point in the FRF of the full-order system. One can observe in Fig. 4.13 that, in the line of the results found on the nonlinear amplitude-frequency relationships, normal form and MD methods are able to retrieve the correct spatial dependence for the contribution of the slave modes. On the other hand, the treatment of the self-quadratic term by the SMD approach prevents the correct prediction of this spatial dependence.



(a) Full Model. (b) Normal Form. (c) Modal Derivatives. (d) Static MD.

Figure 4.14: Comparisons of the additional terms perturbing the linear mode shape solutions (deformation orthogonal to ϕ_p) for the case of the non-shallow arch, computed at the saddle-node bifurcation point marked in Fig. 4.11c, fixing the frequency at which they have been computed. (a) full model solution, representation of the displacement $\boldsymbol{U}_{\text{FS}}^{\perp,sym}$ of the centre line in the $y-z$ plane; vertical axis $\boldsymbol{U}_{\text{FS}}^{\perp,sym}.\boldsymbol{e}_y$ (transverse direction) and horizontal axis $\boldsymbol{U}_{\text{FS}}^{\perp,sym}.\boldsymbol{e}_z$ (axial direction), (b) normal form: $\boldsymbol{U}_{\text{NF}}^{\perp}(t^*)$, (c) Modal derivative : $\boldsymbol{U}_{\text{MD}}^{\perp}(t^*)$, (d) Static modal derivative $\boldsymbol{U}_{\text{SMD}}^{\perp}(t^*)$. Gray lines: position of the centre line of the beam at rest. Solution amplified of factor 50.

The case of the non-shallow arch is shown in Fig. 4.14, for an amplitude of motion marked by the gray line in Fig. 4.11c. Following the observation on the frequency, one can notice that only the normal form approach is able to retrieve the correct spatial dependence. On the other hand, SMD method fails because of the incorrect treatment of the self-quadratic term, while QM constructed from MD does not produce the correct result since the slow/-fast assumption is not fulfilled anymore.

4.7 Conclusion

In this chapter, a detailed comparison of different methods recently proposed in order to define nonlinear mappings with the aim of providing accurate reduced-order models for geometrically nonlinear structures, has been made. The quadratic manifold proposed from the definitions of modal derivatives has thus been contrasted to the normal form theory, related to the definition of nonlinear normal modes as invariant manifolds in phase space. While the quadratic manifold only contains the displacements as unknowns, the normal form approach takes into account displacements and velocities, thus giving a more complete link to the geometry in phase space. Secondly, the quadratic manifold is defined up to the second-order while current expressions of normal form are up to order three and can be continued to higher orders easily. Thirdly, normal form theory relies on firm

mathematical theorems, ensuring a clean conceptual framework, while modal derivatives appear as an ad-hoc, yet efficient, method used in the vibration community.

The main outcomes of this chapter are the following. First, the theoretical derivations of the quadratic manifold using either MD or SMD, has been fully made explicit. These calculations have highlighted the fact that both methods do not handle the quadratic terms in the same manner, and especially the self-quadratic coupling terms arising between the master coordinates. This difference has been found to have important consequences on the global predictions of the methods. Secondly, detailed comparisons between the three methods have been fully analysed on the mathematical expressions: nonlinear change of coordinates, reduced-order dynamics, and main predictive outcomes of the methods such as type of nonlinearity, drift and mode shape dependence on amplitude. To illustrate the results, two two-dofs systems have been used as starting example, and the results found from these have been extended to a continuous structure: a clamped-clamped beam with varying curvature.

A main result of our investigations is that the results predicted by the QM approach with MDs converge to those provided by the normal form approach, only in the case where a slow/fast assumption between master and slave coordinates, holds. This result is fully in the line of general theorems provided in [43, 163], and thus further illustrates the general findings given in these papers where a more general framework including damping is given, together with an exact result that do not rely on asymptotic expansion. A first quantification of the limit value for the slow/fast assumption to hold has been provided, based on the predicted values for the type of nonlinearity, showing that a small gap is needed: $\omega_s > 4\omega_p$, thus justifying a posteriori the good results found by previously published papers using this method. However, the different treatment of the quadratic nonlinearity (and more specifically the self-quadratic coupling term) between MD and SMD, leads to the fact that even with a slow/fast assumption, the QM built from SMD can lead to erroneous predictions, as soon as an important self-quadratic coupling term is present. This result has important implications when one wants to build ROMs for slender curved structures such as arches and shells. This specific feature has been clearly highlighted on the two-dofs system, and found in the more general case of a non shallow arch. On the other hand, the robustness of the normal form approach has been underlined in each case.

These results argue for the use of the tools from dynamical system theory to derive safe and robust ROMS: invariant manifold, normal form theory and spectral submanifold. A limitation could be the use of these methods in the context of FE models where the need of computing, possibly in a non-intrusive manner, the nonlinear coefficients might be a difficult task, see *e.g.* all the literature related to the StEP method (Stiffness Evaluation Procedure, see *e.g* [36, 94, 97]). However recent developments show that the coefficients can be directly computed, for the case of spectral submanifold [163], or for the case of normal form in a non-intrusive manner [167] (see Ch. 5), so that this limitation does not hold anymore.

Chapter 5

Direct Normal Form for Large Scale FE Models

Model order reduction methods for geometrically nonlinear structures is an active field of research and numerous techniques have been proposed in the past [42, 94, 122, 136, 145]. Among them, nonlinear mappings and reduction to invariant manifolds attracts a special attention since they are able by nature to provide better results than any linear method [4, 119, 137]. Indeed, the invariance property is key to ensure that trajectories from the ROM also exist for the full model, and the curvature of the reduction spaces allows the use of less coordinates to describe the dynamics than any linear decomposition.

Nonlinear normal modes (NNMs) offers a framework for such reduction methods. Since their first definition by Rosenberg in the 1960s [125], they have witnessed numerous developments and definitions: family of periodic orbits [67, 162], invariant manifold tangent at the origin to the linear eigenspaces [137, 138], as well as numerous computational methods, from asymptotic developments [87, 101, 120, 137, 158] to numerical solution [18, 104, 114, 121, 142] including continuation of periodic orbits [7, 27, 86, 108]. Recently, Haller and coworkers revisited the mathematical definition of NNMs in order to settle down a unified framework [42]. They defined a spectral submanifold (SSM) as the smoothest member of an invariant manifold family, tangent to a linear eigenstructure. In the context of conservative systems, this definition reduces to the Lyapunov subcenter manifolds that are filled with periodic orbits, thus allowing unification of the different definitions given in the past, from Rosenberg to Shaw and Pierre approach.

Based on the introduction of invariant manifolds, NNMs have been used in order to derive reduced-order models for nonlinear dynamical systems and geometrically nonlinear structures, see *e.g.* [5, 114]. A real approach to normal form has also been derived in order to make clear the connection with the invariant manifold approach, and generalise the derivation of reduced-order models thanks to a complete nonlinear change of coordinates [153, 154, 158]. Successful applications to shells have been reported with this

method [155, 156]. SSMs have been developed with efficient parametrisation allowing to deal with large amplitude and produce efficient predictive models [22, 119].

Application of these methods to finite-element (FE) structures with geometric distributed nonlinearity, remains however scarce [5, 36, 160]. On the other hand, other methods have been proposed in the FE community in order to tackle geometric nonlinearity, with a particular emphasis to non-intrusive or indirect methods [94], that can be derived from any commercial FE software by using only standard operations, and thus without the need to implement new calculations at the elementary level. The StEP (Stiffness Evaluation Procedure) allows for a non-intrusive computations of the modal nonlinear coupling coefficients [97, 110], but as such is not a reduction method since it allows only projecting the equations of motion onto the linear modes basis. Improvements of the method have been proposed, see *e.g.* the dual modes proposed in [69], the combination of StEP with a POD (Proper Orthogonal Decomposition) [8], or a modified StEP where displacements are imposed on selected degrees of freedom only [68, 165]. Implicit condensation and expansion (ICE) have been proposed in order to eliminate the high-frequency components [34, 48, 74] thanks to a two-step procedure where a stress manifold is fitted after a series of static loading computations. Finally, modal derivatives, first introduced by Idelsohn and Cardona [53] have also been used with this objective of finding out a complementary projection subspace with faster convergence than linear modes [173, 176]. Recent extension proposes to use modal derivatives in a nonlinear mapping perspective to compute a quadratic manifold as reduction subspace [56, 127].

Recent studies compare all these approaches mainly developed in the computational mechanics community to invariant and spectral submanifolds in order to better understand their mathematical foundations, advantages and drawbacks. Haller and Ponsioen derived general theorems showing that condensation and modal derivatives need a slow/fast assumption between master and slave coordinates in order to ensure convergence to a correct solution [43]. Elaborating on this idea, the quadratic manifold (QM) has been compared to the normal form approach in the previous chapter, showing again how the QM tends to invariant manifold only when slow/fast assumption holds. A numerical criterion was established, stating that this slow/fast separation could be claimed as soon as the eigenfrequencies of the slave coordinates are 4 times larger than those of the master. A particular emphasis was also placed on both cases of static (SMD) and full modal derivatives (MD), showing how quadratic nonlinearities can be treated incorrectly with the SMD approach, even if the slow/fast assumption is fulfilled. The ICE method has also been compared to invariant manifolds in [139], again underlining the requirement of slow/fast separation. Importantly, ICE and QM methods produce reduction subspaces that are not velocity-dependent and neither invariant, and these simplifications become an important drawback in the prediction given by the ROMs [139].

These results advocate better application of reduction methods based on invariant manifold for FE structures as well, that would take properly into account the specificity of FE dis-

cretisation and also open the doors to possible non-intrusive procedures that could inherit the intrinsic properties of reduced subspace (*e.g.* invariance, velocity dependence). Also, a main advantage of invariant-based techniques is that they are by nature *simulation free*, *i.e.* without the need of resorting to a priori computations or outputs from the full-order model, as is the case for example for the POD or the PGD (Proper Generalized Decomposition) methods [3, 26, 73, 92]. Such an effort has been recently tackled for methods based on SSM [163]. By using a single master coordinate, the authors gave general formula, up to the third-order, allowing for a direct computation of a ROM from the physical coordinates. The proposed method is however limited to a single master mode in the proposed version. Even though the extension to multiple modes is theoretically possible, following *e.g.* [113], the procedure needs to be revised and developed further for direct computation.

The objective of this contribution is to extend the results obtained thanks to the real normal form approach [154, 158] to FE structures. A main limitation of the method as it was presented in [154, 158] is to rely on the equations of motion written in the modal basis. Since this projection step is out of reach for a number of FE problems involving very large number of degrees of freedom, the method has been completely rewritten in order to compute the needed quantities directly from the FE unknowns. In that manner, a full nonlinear mapping is introduced, allowing one to compute directly the reduced dynamics in an invariant-based span of the phase space, up to the third-order.

5.1 Normal Form

This section recalls the main results obtained in [152, 158] for a conservative system, which has then been extended in [154] in order to deal with modal damping. In these contributions, the starting point is the equations of motion in modal coordinates. The method has then been applied to partial differential equations (PDE) of beams, plate and shell models, see *e.g.* [159] and [155] respectively for beams and shells, [4] for a comparison with the POD method, [156] for the correct prediction of the hardening/softening behaviour of shallow spherical shells, and [153] for an overview.

The nonlinear mapping is defined up to the third order and is based on an asymptotic expansion that can be pushed further if needed. The theory of normal form; Poincaré and Poincaré-Dulac's theorems, lay the foundation for its derivation. It is also defined for both displacements and velocities. Previous derivations showed that the results are equivalent to the center manifold approach used by Shaw and Pierre [136]. Hence the nonlinear mapping allows one to express the dynamics in an invariant-based span of the phase space. This property is crucial in order to defined accurate ROMs. Let us denote as $\boldsymbol{p} = \dot{\boldsymbol{q}}$ the velocity vector in physical space, R_i and $S_j = \dot{R}_j$ the *normal* coordinates (respectively displacement and velocity). Let us also assume that the ROM is composed of n master modes. Even if it is generally assumed that $n \ll N$, the method is given for a free n and can also be used with $n = N$, hence defining a complete change of coordinates between modal and normal

coordinates. The nonlinear mapping reads:

$$\boldsymbol{q} = \sum_{i}^{n} \boldsymbol{e}_i R_i + \sum_{i=1}^{n}\sum_{j=1}^{n} \boldsymbol{a}_{ij} R_i R_j + \sum_{i=1}^{n}\sum_{j=1}^{n} \boldsymbol{b}_{ij} S_i S_j + \sum_{i=1}^{n}\sum_{j=1}^{n}\sum_{k=1}^{n} \boldsymbol{r}_{ijk} R_i R_j R_k + \sum_{i=1}^{n}\sum_{j=1}^{n}\sum_{k=1}^{n} \boldsymbol{u}_{ijk} R_i S_j S_k, \tag{5.1a}$$

$$\boldsymbol{p} = \sum_{i}^{n} \boldsymbol{e}_i S_i + \sum_{i=1}^{n}\sum_{j=1}^{n} \boldsymbol{\gamma}_{ij} R_i S_j + \sum_{i=1}^{n}\sum_{j=1}^{n}\sum_{k=1}^{n} \boldsymbol{\mu}_{ijk} S_i S_j S_k + \sum_{i=1}^{n}\sum_{j=1}^{n}\sum_{k=1}^{n} \boldsymbol{\nu}_{ijk} S_i R_j R_k. \tag{5.1b}$$

In these expressions, $\boldsymbol{e}_i$ represents the unit eigenvector of the modal basis, with length N, composed of zeros except for the i-th entry which is equal to 1. The full expressions of all the reconstruction tensors $\boldsymbol{a}$, $\boldsymbol{b}$, $\boldsymbol{\gamma}$, $\boldsymbol{r}$, $\boldsymbol{u}$, $\boldsymbol{\mu}$, and $\boldsymbol{\nu}$ are not reported here due to their length, but the interested reader is referred to [158] for the detailed expressions. The sole difference between these tensors and those provided in [158], lies in the treatment of the symmetric terms in the summations. In these expressions, full summations are used with lower index covering from 1 to N. The other choice, often selected in such case, is to use upper-diagonalised forms for the tensors with ordered summations ($s \geq r$ and $t \geq s$), using the fact that the usual product is commutative. This choice is not retained here since it has been found easier to handle the expressions with full summations.

The following important properties of the nonlinear mapping from Eqs. (5.1) are recalled: (i) the change of coordinate is identity-tangent in the sense that the first order is colinear to a given eigenmode. The correcting terms allows to take into account the curvature of the NNM (invariant manifold). (ii) the number of master modes n can be selected freely and in the most exhaustive case one can have $n = N$. The main advantage of these formula is that they are already defined in a multiple mode framework, so they can be directly applied to systems with internal resonances where a single mode assumption would not hold. This is in contrast with methods based either on two-dimensional invariant manifolds, see *e.g.* [19], or the recently proposed method based on SSM [163].

The reduced-order dynamics is written for the general case where no internal resonance exists between the eigenfrequencies of the system. When an internal resonance is present, some terms are vanishing in Eqs. (5.1), leading to extra terms staying in the normal form of the system. The theory is detailed in [153, 154, 158], and further comments will be provided in the next sections. In any case, the dynamics onto the third-order $2n$-dimensional invariant manifold corresponding to the n selected master modes writes, in this general case without internal resonance, $\forall r = 1...n$:

$$\begin{aligned} &\ddot{R}_r + \omega_r^2 R_r + (A^r_{rrr} + h^r_{rrr}) R_r^3 + (B^r_{rrr}) R_r \dot{R}_r^2 \\ &+ R_r \sum_{j\neq r}^{n} (A^r_{jjr} + A^r_{jrj} + A^r_{rjj} + 3h^r_{rjj}) R_j^2 + R_r \sum_{j\neq r}^{n} (B^r_{rjj}) \dot{R}_j^2 + \dot{R}_r \sum_{j\neq r}^{n} (B^r_{jjr} + B^r_{jrj}) R_j \dot{R}_j = 0. \end{aligned} \tag{5.2}$$

As clearly emphasised in Eq. (5.2) where R_r and $\dot{R}_r$ terms have been factorised, the reduced dynamics does not contain invariant-breaking terms anymore. An important remark is

also that since no internal resonance have been assumed between the eigenfrequencies, no quadratic terms are present in Eq. (5.2), only cubic terms corresponding to trivial resonance stay in the normal form. Finally, one can note the presence of velocity-dependent terms in the reduced dynamics, reflecting the velocity-dependence of the invariant manifolds. Even though displacement and velocities are used as independent variables in the process, the method can simply reduce to displacements only, one has just to replace $S_r = \dot{R}_r$ everywhere to obtain full expressions depending on displacements only. In the same line, Eq. (5.1b) allows for a better reconstruction of the velocities but is not mandatorily needed and can be deduced from (5.1a).

New fourth-order tensors $\boldsymbol{A}$ and $\boldsymbol{B}$ appear in these equations, their expressions from the modal basis can be found in [158] and are here recalled:

$$\boldsymbol{A}_{ijk} = \sum_{s=1}^{N} (\boldsymbol{g}_{is} + \boldsymbol{g}_{si}) a^s_{jk} = \sum_{s=1}^{N} 2\,\boldsymbol{g}_{is} a^s_{jk}, \tag{5.3a}$$

$$\boldsymbol{B}_{ijk} = \sum_{s=1}^{N} (\boldsymbol{g}_{is} + \boldsymbol{g}_{si}) b^s_{jk} = \sum_{s=1}^{N} 2\,\boldsymbol{g}_{is} b^s_{jk}, \tag{5.3b}$$

where the last simplification stems from the symmetry of the quadratic tensor $\boldsymbol{g}$.

In a FE context, the main problem is that applicability of this reduction procedure needs as a first step the full equations in modal basis, with all the coefficients $\boldsymbol{g}$ and $\boldsymbol{h}$ known and computed. Even though theoretically feasible by resorting to the *Stiffness Evaluation Procedure* (StEP) as described in [97], this computation is generally out of reach for much of the FE structures since the associated computational cost is prohibitively large. Also, an *a priori* selection of some of the important coupled eigenmodes, which could indicate a way of solving that dimensionality issue, is clearly out of reach, as underlined for example for 3D elements in Chapter 3, where non-negligible couplings with very high frequency thickness modes have been exhibited. Hence there is a clear need for a direct computation of the normal form from the FE discretisation, since it will allow one to take directly into account all the coupled modes without any a priori or assumptions to formulate, and will define a simulation-free method applicable for efficient reduced-order modeling with geometric nonlinearity.

5.1.1 Single mode motion coefficients

In this section, the nonlinear coefficients of the mapping given by the normal form theory are given in detail. For the sake of brevity, only the coefficients appearing in the simplified case where a single master mode p is selected in the reduced model, are recalled. The interested reader can refer to [154, 158] for most complete expressions covering all the cases, including also damping. We begin with the second-order coefficients, a^s_{pp}, b^s_{pp} and

γ^s_{pp} coefficients, with p the master mode and s a slave mode :

$$a^s_{pp} = g^s_{pp}\frac{2\,\omega_p^2 - \omega_s^2}{-\omega_s^2(4\,\omega_p^2 - \omega_s^2)}, \tag{5.4a}$$

$$b^s_{pp} = g^s_{pp}\frac{2}{-\omega_s^2(4\,\omega_p^2 - \omega_s^2)}, \tag{5.4b}$$

$$\gamma^s_{pp} = g^s_{pp}\frac{2}{4\,\omega_p^2 - \omega_s^2}. \tag{5.4c}$$

The third order nonlinear mapping coefficients are equal to zero in the specific case when $s = p$. Their full expressions for $s \neq p$ read:

$$r^s_{ppp} = \frac{(A^s_{ppp} + h^s_{ppp})(7\omega_p^2 - \omega_s^2) + 2B^s_{ppp}(\omega_p^4)}{(\omega_s^2 - \omega_p^2)(\omega_s^2 - 9\omega_p^2)}, \tag{5.5a}$$

$$u^s_{ppp} = \frac{6(A^s_{ppp} + h^s_{ppp}) + B^s_{ppp}(3\omega_p^2 - \omega_s^2)}{(\omega_s^2 - \omega_p^2)(\omega_s^2 - 9\omega_p^2)}, \tag{5.5b}$$

$$\mu^s_{ppp} = \frac{6(A^s_{ppp} + h^s_{ppp}) + B^s_{ppp}(3\omega_p^2 - \omega_s^2)}{(\omega_s^2 - \omega_p^2)(\omega_s^2 - 9\omega_p^2)}, \tag{5.5c}$$

$$\nu^s_{ppp} = \frac{3(A^s_{ppp} + h^s_{ppp})(3\omega_p^2 - \omega_s^2) + 2B^s_{ppp}(\omega_p^2\omega_s^2)}{(\omega_s^2 - \omega_p^2)(\omega_s^2 - 9\omega_p^2)}, \tag{5.5d}$$

$$\tag{5.5e}$$

where:

$$A^s_{ppp} = \sum_{l=1}^{N} 2g^s_{pl}a^l_{pp} \tag{5.6a}$$

$$B^s_{ppp} = \sum_{l=1}^{N} 2g^s_{pl}b^l_{pp} \tag{5.6b}$$

with $\boldsymbol{g}_{pl}$, the vector of quadratic coupling between the master mode p and a generic mode l of the structure.

5.2 Direct Normal Form

In this section, the normal form proposed in [152, 158] will be completely rewritten in a form that allows its computation in a non-intrusive and direct manner. To do so, one has to first rewrite the modal normal from of [152, 158] in tensorial form; then, the expressions have to be rearranged and finally their transformation from modal to physical coordinates can be obtained.

5.2.1 Second-order direct normal form

In order to introduce progressively the cubic nonlinear mapping, we begin with a first step where only the second-order terms of the normal form are computed directly from the FE discretisation. This first step allows for a better understanding of the physical meaning of the involved coefficients, as well as some short comparisons with the quadratic mapping introduced from the modal derivatives in [56, 127]. The reduced dynamics in this case will also be specified and the meanings of this assumption further detailed. In the results section, this assumption will be again discussed and highlighted on given test cases.

The quadratic mapping, deduced from Eq. (5.1), from the physical $\boldsymbol{U}$ coordinates of the FE model, reads:

$$\boldsymbol{U} = \sum_{i}^{n} \boldsymbol{\phi}_i R_i + \sum_{i=1}^{n}\sum_{j=i}^{n} \bar{\boldsymbol{a}}_{ij} R_i R_j + \sum_{i=1}^{n}\sum_{j=i}^{n} \bar{\boldsymbol{b}}_{ij} S_i S_j, \tag{5.7a}$$

$$\boldsymbol{V} = \sum_{i}^{n} \boldsymbol{\phi}_i S_i + \sum_{i=1}^{n}\sum_{j=i}^{n} \bar{\boldsymbol{\gamma}}_{ij} R_i S_j. \tag{5.7b}$$

In these expressions, n stands for the number of master modes retained for building the ROM, and $\boldsymbol{\phi}_i$ is the corresponding eigenvector. The *normal* coordinates (R_i, S_j) describe the dynamics in the same invariant-based span of the phase space. The expressions of the reconstruction vectors $\bar{\boldsymbol{a}}$, $\bar{\boldsymbol{b}}$ and $\bar{\boldsymbol{\gamma}}$, are the equivalent to those obtained in modal basis, the only difference being that the new ones can now be computed directly from the FE nodes. As already remarked, the second equation (5.7b) is not mandatorily needed for the reduction process. Indeed, (5.7b) can be deduced from (5.7a), by adding the first-order assumption $\dot{S}_p = -\omega_r^2 R_r$.

The detailed derivation of the second-order tensors in physical coordinates $\bar{\boldsymbol{a}}$, $\bar{\boldsymbol{b}}$, $\bar{\boldsymbol{\gamma}}$, is now given. We start by recalling the general formulas needed to compute the second-order tensors from the normal form in modal basis, namely $\boldsymbol{a}$, $\boldsymbol{b}$, $\boldsymbol{\gamma}$. These have been first derived in [152,158], but they are here rewritten in compact notation to allow for better understanding on how their direct form has been obtained.

The derivation of the second order tensors in modal basis, is obtained by substituting the nonlinear mapping equations for $\boldsymbol{q}, \boldsymbol{p}$ into the equations of motion for $\dot{\boldsymbol{q}}, \dot{\boldsymbol{p}}$, by replacing each $\dot{R}_r$ (and $\dot{S}_r$) term with the first order assumption $\dot{R}_r = S_r$ (and $\dot{S}_r = -\omega_r^2 R_r$), and finally by balancing the second order terms. This process will lead to four equations for each couple of indexes i, j, one for the terms multiplying $R_i R_j$, one for $S_i S_j$, one for $R_i S_j$,

and one for $S_i R_j$. The equations obtained permit to derive $\boldsymbol{a}_{ij}, \boldsymbol{b}_{ij}, \boldsymbol{\gamma}_{ij}, \boldsymbol{\gamma}_{ji}$; the system reads:

$$\begin{cases} 2\boldsymbol{a}_{ij} - 2\omega_i^2 \boldsymbol{b}_{ij} - \boldsymbol{\gamma}_{ij} = \boldsymbol{0}, \\ 2\boldsymbol{a}_{ij} - 2\omega_j^2 \boldsymbol{b}_{ij} - \boldsymbol{\gamma}_{ji} = \boldsymbol{0}, \\ -2\boldsymbol{\Omega}^2 \boldsymbol{a}_{ij} + \omega_j^2 \boldsymbol{\gamma}_{ij} + \omega_i^2 \boldsymbol{\gamma}_{ji} = \boldsymbol{g}_{ij}, \\ 2\boldsymbol{\Omega}^2 \boldsymbol{b}_{ij} + \boldsymbol{\gamma}_{ij} + \boldsymbol{\gamma}_{ji} = \boldsymbol{0}. \end{cases} \tag{5.8}$$

The solution of this system of equations in the unknown tensors can be written as:

$$\mathbf{D}_{ij} \boldsymbol{a}_{ij} = ((+\omega_i^2 + \omega_j^2)\boldsymbol{I} - \boldsymbol{\Omega}^2)\boldsymbol{g}_{ij}, \tag{5.9a}$$

$$\mathbf{D}_{ij} \boldsymbol{b}_{ij} = 2\,\boldsymbol{g}_{ij}, \tag{5.9b}$$

$$\mathbf{D}_{ij} \boldsymbol{\gamma}_{ij} = ((-\omega_i^2 + \omega_j^2)\boldsymbol{I} - \boldsymbol{\Omega}^2)2\,\boldsymbol{g}_{ij}, \tag{5.9c}$$

$$\mathbf{D}_{ij} \boldsymbol{\gamma}_{ji} = ((+\omega_i^2 - \omega_j^2)\boldsymbol{I} - \boldsymbol{\Omega}^2)2\,\boldsymbol{g}_{ij}, \tag{5.9d}$$

where the left-hand side term $\mathbf{D}_{ij}$ is the denominator of the coefficients. It makes appear the second order internal resonance relationship (small divisor problem), and reads:

$$\mathbf{D}_{ij} = ((+\omega_i + \omega_j)^2 \boldsymbol{I} - \boldsymbol{\Omega}^2)((-\omega_i + \omega_j)^2 \boldsymbol{I} - \boldsymbol{\Omega}^2). \tag{5.10}$$

If no second order internal resonance occurs, in Eqs. (5.9) the denominator matrix can be inverted and the expression for the tensors made explicit. With these expressions, one is then able to compute all the coefficients needed for the classical modal normal form.

In order to understand how the coefficients of the direct normal form can be derived from those of the modal normal form, we will illustrate the procedure on a specific term a_{ij}^s of the second order tensor $\boldsymbol{a}_{ij}$. The explicit expression for a_{ij}^s can be deduced from the previous equation or found in [158]. It reads:

$$a_{ij}^s = \frac{((+\omega_i^2 + \omega_j^2) - \omega_s^2)}{((+\omega_i + \omega_j)^2 - \omega_s^2)((-\omega_i + \omega_j)^2 - \omega_s^2)} g_{ij}^s, \tag{5.11}$$

Let us first rewrite this formula so that the denominator, which is of order four in ω, is split into two factors of order two, reminding that this denominator has a physical meaning. Indeed, the two factors represents the two possible second-order internal resonances between the modes of index i, j, s. One obtains:

$$a_{ij}^s = \left(\frac{1}{(+\omega_i + \omega_j)^2 - \omega_s^2} + \frac{1}{(-\omega_i + \omega_j)^2 - \omega_s^2} \right) \frac{g_{ij}^s}{2}. \tag{5.12}$$

This can be rewritten in a more compact form for the vector $\boldsymbol{a}_{ij}$ for all s:

$$\boldsymbol{a}_{ij} = \frac{1}{2}((+\omega_i+\omega_j)^2\boldsymbol{I}-\boldsymbol{\Omega}^2)^{-1}\boldsymbol{g}_{ij} \; + \; \frac{1}{2}((-\omega_i+\omega_j)^2\boldsymbol{I}-\boldsymbol{\Omega}^2)^{-1}\boldsymbol{g}_{ij}. \tag{5.13}$$

It is now possible to express $\boldsymbol{a}$ in terms of $\boldsymbol{K}$ and $\boldsymbol{M}$ by using the diagonalisation equations stating $\boldsymbol{\Phi}^T\boldsymbol{M}\boldsymbol{\Phi}=\boldsymbol{I}$, and $\boldsymbol{\Phi}^T\boldsymbol{K}\boldsymbol{\Phi}=\boldsymbol{\Omega}^2$, so that:

$$\boldsymbol{a}_{ij} = \frac{1}{2}((+\omega_i+\omega_j)^2\boldsymbol{\Phi}^{\mathrm{T}}\boldsymbol{M}\boldsymbol{\Phi}-\boldsymbol{\Phi}^{\mathrm{T}}\boldsymbol{K}\boldsymbol{\Phi})^{-1}\boldsymbol{g}_{ij} \; + \; \frac{1}{2}((-\omega_i+\omega_j)^2\boldsymbol{\Phi}^{\mathrm{T}}\boldsymbol{M}\boldsymbol{\Phi}-\boldsymbol{\Phi}^{\mathrm{T}}\boldsymbol{K}\boldsymbol{\Phi})^{-1}\boldsymbol{g}_{ij}. \tag{5.14}$$

Each factor in brackets can be rewritten as:

$$\left(\boldsymbol{\Phi}^{\mathrm{T}}\left(\sigma_{ij}^2\boldsymbol{M}-\boldsymbol{K}\right)\boldsymbol{\Phi}\right)^{-1} = \boldsymbol{\Phi}^{-1}\left(\sigma_{ij}^2\boldsymbol{M}-\boldsymbol{K}\right)^{-1}\boldsymbol{\Phi}^{-\mathrm{T}} \tag{5.15}$$

where for the sake of readability the term σ_{ij} replaced the summation of eigenvalues $(\pm\omega_i+\omega_j)$. One can see that the full eigenvector matrix appears twice in each factor. Consequently a simplification arises by premultiplying Eq. (5.14) by $\boldsymbol{\Phi}$, which also leads to make appear $\bar{\boldsymbol{a}}_{ij}$ since $\bar{\boldsymbol{a}}_{ij}=\boldsymbol{\Phi}\boldsymbol{a}_{ij}$. Also, by noticing that $\boldsymbol{\Phi}^{-\mathrm{T}}\boldsymbol{g}_{ij}=\boldsymbol{G}(\phi_i,\phi_j)$, the post-multiplied term can be simplified, so that a final expression involving only terms from the physical basis is obtained:

$$\bar{\boldsymbol{a}}_{ij} = \frac{1}{2}((+\omega_i+\omega_j)^2\boldsymbol{M}-\boldsymbol{K})^{-1}\boldsymbol{G}_{ij} \; + \; \frac{1}{2}((-\omega_i+\omega_j)^2\boldsymbol{M}-\boldsymbol{K})^{-1}\boldsymbol{G}_{ij}. \tag{5.16}$$

Lastly, we define the two vectors $\bar{\boldsymbol{Z}}\boldsymbol{s}_{ij}$ and $\bar{\boldsymbol{Z}}\boldsymbol{d}_{ij}$ as:

$$\bar{\boldsymbol{Z}}\boldsymbol{s}_{ij} = ((+\omega_i+\omega_j)^2\boldsymbol{M}-\boldsymbol{K})^{-1}\boldsymbol{G}_{ij}, \tag{5.17a}$$

$$\bar{\boldsymbol{Z}}\boldsymbol{d}_{ij} = ((-\omega_i+\omega_j)^2\boldsymbol{M}-\boldsymbol{K})^{-1}\boldsymbol{G}_{ij}, \tag{5.17b}$$

which are the two terms appearing in the compact expression for $\bar{\boldsymbol{a}}$. By applying a similar procedure to the other tensors $\boldsymbol{b},\boldsymbol{\gamma}$, one can show that the four tensors can all be expressed as linear combinations of $\bar{\boldsymbol{Z}}\boldsymbol{d}_{ij}, \bar{\boldsymbol{Z}}\boldsymbol{s}_{ij}$, hence only two operations are needed to derive four tensors. This underlines the fact that the second equation on $\boldsymbol{V}$ is not independent from the first one, so that in a simplified version of the method it can be neglected.

These vectors encompass all the possible second-order internal resonance thanks to the appearance of the sum $\omega_i+\omega_j$ and difference $-\omega_i+\omega_j$ of two eigenfrequencies (thus giving the names of these $\bar{\boldsymbol{Z}}$ vectors with s (summation) and d (difference) as subscripts). Indeed, the matrix to invert will become singular in case of existence of a second-order internal resonance. These terms come from the denominators of the modal normal form and vanish in case of internal resonance, see [153, 158].

Moreover, $\bar{\boldsymbol{Z}}\boldsymbol{s}_{ij}$ and $\bar{\boldsymbol{Z}}\boldsymbol{d}_{ij}$ can be computed easily by solving a linear system, thus avoiding a matrix inversion. This will be further commented in Section 5.5 where specific algorithmic

details will be highlighted.

The expressions for the three tensors $\bar{\boldsymbol{a}}$, $\bar{\boldsymbol{b}}$ and $\bar{\boldsymbol{\gamma}}$ in terms of the two $\bar{\boldsymbol{Z}}\boldsymbol{s}_{ij}$ and $\bar{\boldsymbol{Z}}\boldsymbol{d}_{ij}$ only, finally read:

$$\bar{\boldsymbol{a}}_{ij} = \frac{1}{2}(\bar{\boldsymbol{Z}}\boldsymbol{d}_{ij} + \bar{\boldsymbol{Z}}\boldsymbol{s}_{ij}), \tag{5.18a}$$

$$\bar{\boldsymbol{b}}_{ij} = \frac{1}{2\omega_i\omega_j}(\bar{\boldsymbol{Z}}\boldsymbol{d}_{ij} - \bar{\boldsymbol{Z}}\boldsymbol{s}_{ij}), \tag{5.18b}$$

$$\bar{\boldsymbol{\gamma}}_{ij} = \frac{\omega_j - \omega_i}{\omega_j}\bar{\boldsymbol{Z}}\boldsymbol{d}_{ij} + \frac{\omega_j + \omega_i}{\omega_j}\bar{\boldsymbol{Z}}\boldsymbol{s}_{ij}. \tag{5.18c}$$

Another possible procedure to express the tensors in physical coordinates, is now described in order to show why the splitting operation done in Eq. (5.12) has permitted to drastically reduce the computational cost. In fact, to derive the expression of the tensors in physical basis, the splitting operation is not strictly needed and another expression for them can be found starting from Eq. (5.11). From Eq. (5.11), the expression for $\boldsymbol{a}_{ij}$ in compact form reads:

$$\boldsymbol{a}_{ij} = ((-\omega_i + \omega_j)^2\boldsymbol{I} - \boldsymbol{\Omega}^2)^{-1}((+\omega_i + \omega_j)^2\boldsymbol{I} - \boldsymbol{\Omega}^2)^{-1}((+\omega_i^2 + \omega_j^2)\boldsymbol{I} - \boldsymbol{\Omega}^2)\boldsymbol{g}_{ij}. \tag{5.19}$$

Again, its equivalent in physical coordinates is the tensor $\bar{\boldsymbol{a}}_{ij} = \boldsymbol{\Phi}\boldsymbol{a}_{ij}$, and the equivalent of the forcing term in physical coordinates is $\boldsymbol{G}_{ij} = \boldsymbol{\Phi}^{-T}\boldsymbol{g}_{ij}$. By introducing these two equivalences into Eq. (5.19) one obtains:

$$\bar{\boldsymbol{a}}_{ij} = \boldsymbol{\Phi}((-\omega_i + \omega_j)^2\boldsymbol{I} - \boldsymbol{\Omega}^2)^{-1}((+\omega_i + \omega_j)^2\boldsymbol{I} - \boldsymbol{\Omega}^2)^{-1}((+\omega_i^2 + \omega_j^2)\boldsymbol{I} - \boldsymbol{\Omega}^2)\boldsymbol{\Phi}^T\boldsymbol{G}_{ij}. \tag{5.20}$$

This equation still presents two matrices in modal coordinates: the full eigenvectors matrix $\boldsymbol{\Phi}$ and the full eigenvalues matrix $\boldsymbol{\Omega}^2$. To eliminate these two matrices and make $\boldsymbol{K}$ and $\boldsymbol{M}$ appear, one last operation is needed. Introducing the matrix:

$$\boldsymbol{O}^2 = \boldsymbol{M}^{-1}\boldsymbol{K}, \tag{5.21}$$

one has that the relationship between $\boldsymbol{O}^2$ and $\boldsymbol{\Omega}^2$ is:

$$\boldsymbol{\Omega}^2 = \boldsymbol{\Phi}^{-1}\boldsymbol{O}^2\boldsymbol{\Phi}. \tag{5.22}$$

Finally, by substituting into Eq. (5.20), the last expression for $\boldsymbol{\Omega}^2$ and simply $\boldsymbol{\Phi}^{-1}\boldsymbol{\Phi}$ for $\boldsymbol{I}$, the direct equation for $\boldsymbol{a}_{ij}$ can be obtained:

$$\bar{\boldsymbol{a}}_{ij} = ((-\omega_i + \omega_j)^2\boldsymbol{I} - \boldsymbol{O}^2)^{-1}((+\omega_i + \omega_j)^2\boldsymbol{I} - \boldsymbol{O}^2)^{-1}((+\omega_i^2 + \omega_j^2)\boldsymbol{I} - \boldsymbol{O}^2)\boldsymbol{M}^{-1}\boldsymbol{G}_{ij}. \tag{5.23}$$

This expression of $\boldsymbol{a}$ has been given in [168] for the case of equal indexes ii. Interestingly, it bears a strong resemblance with the expression given in [163] where the ROM is built using a direct approach based on spectral submanifold (SSM).

Comparing this expression for $\boldsymbol{a}$ with the one obtained after the splitting operation (Eq. (5.16)), and bearing in mind that they are completely equivalent, one sees that from a computational point of view, Eq. (5.23) is much more expensive. In Eq. (5.16), two linear systems have to be solved to find $\bar{\boldsymbol{Z}}\boldsymbol{d}$ and $\bar{\boldsymbol{Z}}\boldsymbol{s}$ and once they are found, the four tensors $\boldsymbol{a}, \boldsymbol{b}, \boldsymbol{\gamma}$ can be obtained. In Eq. (5.23), three linear systems have to be solved, one for each -1 appearing in the formula, and these three linear systems have to be solved for each tensor, making the number of linear systems to be solved equal to twelve. However, the most computational expensive operation is not the solution of a linear system but the inversion of the matrix $\boldsymbol{M}$ needed to build the matrix $\boldsymbol{O}^2$. This cost of this operation is equivalent to the cost of solving a linear system for each degree of freedom of the structure, making procedure infeasible for any engineering application. For this reason, the splitting operation that brought to Eq. (5.16), although not strictly necessary from a theoretical point of view, is instead crucial from a computational one.

Physical interpretation of second order tensors

The tensors $\bar{\boldsymbol{a}}_{ij}$, $\bar{\boldsymbol{b}}_{ij}$ and $\bar{\boldsymbol{\gamma}}_{ij}$ can be seen as correction tensors needed to take into account the quadratic curvature of the invariant manifold. They thus share a common interpretation with the concepts of modal derivatives, as it has been introduced *e.g.* in [53, 173] . Indeed modal derivatives aimed at taking into account the nonlinear dependence of an eigenvector with respect to perturbations in other modal directions. It has been recognised that this can be linked to the Hessian of the internal force vector and represents a manifold curvature in phase space [56, 127]. In order to make the connection with *static* modal derivative (SMD) more clear, let us assume that a single master coordinate, say i, is retained for building the ROM. Restricting to a single master mode motion, then Eqs. (5.17) simplifies to:

$$\bar{\boldsymbol{Z}}\boldsymbol{s}_{ii} = ((2\omega_i)^2\boldsymbol{M} - \boldsymbol{K})^{-1}\boldsymbol{G}_{ii}, \tag{5.24a}$$

$$\bar{\boldsymbol{Z}}\boldsymbol{d}_{ii} = -\boldsymbol{K}^{-1}\boldsymbol{G}_{ii}. \tag{5.24b}$$

One can observe that Eq. (5.24b) is fully equivalent to the usual definition of static modal derivative $\boldsymbol{\Theta}^{(S)}_{ii}$ one can found *e.g.* in [56, 173], to the multiplicative factor 2, *i.e.* $\bar{\boldsymbol{Z}}\boldsymbol{d}_{ii} = 2\,\boldsymbol{\Theta}^{(S)}_{ii}$. This means that in this simplified case, $\boldsymbol{\Theta}^{(S)}_{ii}$ exactly recovers the correct direction in phase space that express the quadratic couplings. However, this is not true anymore for cross-coupled SMD $\boldsymbol{\Theta}^{(S)}_{ij}$, $i \neq j$, since SMD is not able to make appear the difference between eigenfrequencies, nor the sum.

A quite similar comment can also be addressed about $\bar{\boldsymbol{Z}}\boldsymbol{s}_{ii}$, with the additional assumption of a slow/fast separation between master and slave coordinates. Indeed, Eq. (5.24a) makes appear implicitly, in the terms of the matrix to inverse, the differences $(2\omega_i)^2 - \omega_s^2$ between the master coordinate i and all the slave modes s. The slow/fast assumption requires that the slave modes are much more stiff than the master, implying $\forall s, \quad \omega_s \gg \omega_i$. Hence if this assumption is well fulfilled, then $\bar{\boldsymbol{Z}}\boldsymbol{s}_{ii}$ will also tend to the direction pointed by $\bar{\boldsymbol{Z}}\boldsymbol{d}_{ii} = 2\,\boldsymbol{\Theta}^{(S)}_{ii}$. The quadratic manifold produced by SMD will then tend to the one

provided by direct normal form, since $\bar{\boldsymbol{a}}$ will tend to twice the SMD and $\bar{\boldsymbol{b}}$ to zero. This simple comparison underlines the common point between quadratic manifold from SMD and the one proposed from direct normal form. In the general case, one understands that the formulas given by Eqs. (5.18) are more general, and only degenerate to the formulas proposed in [56,127] when specific assumptions are met. As a conclusion, one can state that $\bar{\boldsymbol{a}}$ and $\bar{\boldsymbol{b}}$ tensors are in fact the correct corrections that would have needed to be defined as the modal derivatives, since it gives the proper curvatures of the invariant manifolds (NNMs) which are defined as the continuation of the underlying eigenmodes, tangent to the linear subspaces at origin.

Second order normal form: Reduced dynamics

In the case considered in this section where a second-order normal form is studied, it is also interesting to derive the reduced-order dynamics arising from this choice, which will express the dynamics onto second-order approximations of the invariant manifolds. This dynamics has not been treated in [152, 158] where the change of coordinates was pushed up to third order. It will be shown that reduced order models obtained with second order normal form are not necessarily worse than those obtained with third order normal form. In fact, only the change of coordinates is up to second order here, but the dynamics is still calculated up to the third. The dynamics in this case is expressed up to cubic order and reads, $\forall\, r \in [1, n]$:

$$\ddot{R}_r + \omega_r^2 R_r + \sum_i^n \sum_j^n \sum_k^n (A_{ijk}^r + h_{ijk}^r) R_i R_j R_k + B_{ijk}^r R_i \dot{R}_j \dot{R}_k = 0. \tag{5.25}$$

As compared to Eq. (5.2), this reduced dynamics does not contain quadratic terms also, as a consequence of the fact that no quadratic terms are trivially resonant. As long as no second-order internal resonance exists, these terms can be cancelled out. However all the cubic terms are present, without any simplification. This is the main contrast with Eq. (5.2), where all the non-trivial resonant monomial terms have been cancelled thanks to the third-order term in the nonlinear mapping. Consequently Eq. (5.2) contains much less cubic terms than (5.25), and in particular all the invariant coupling terms can be cancelled. This point will be further commented in sections 5.2.2. One can already note that reduced-order dynamics can be simulated with Eq. (5.25), meaning that: (i) the invariant manifolds are approximated to the second-order only, (ii) all the resonant monomial terms, including non-trivial ones, are present. This might appear interesting in certain cases where strong higher order internal resonance are present, especially when they involve resonance between the nonlinear frequencies, that one cannot easily foresee from a linear analysis. This point will be highlighted in section 5.6.1.

In the particular case where a single master mode motion is selected, it is important to notice that Eqs. (5.2) and (5.25) reduce to the same, so that the reduced-order dynamics on a single invariant manifold is equivalent with second and third-order normal form.

Assuming that the master coordinate has label r, then $\forall k \neq r,\ R_k = S_k = 0$, and the dynamics of R_r writes:

$$\ddot{R}_r + \omega_r^2 R_r + (A^r_{rrr} + h^r_{rrr}) R_r^3 + B^r_{rrr} R_r \dot{R}_r^2 \ = \ 0 \ . \tag{5.26}$$

Indeed, in this simple case, the only cubic monomial terms staying in (5.26) are trivially resonant, and cannot be cancelled by the cubic order terms from the nonlinear mapping. This means that if one is interested to the reduction to a single invariant manifold, then there is no need to compute further the cubic terms from the normal form.

The last point to address is how to directly compute the $\boldsymbol{A}$ and $\boldsymbol{B}$ tensors, expressed in Eqs. (5.3), and appearing in the reduced dynamics. Since their definitions make appear the $\boldsymbol{g}$ tensor of quadratic coefficients from the modal basis, a direct computation is needed to circumvent the problem of computing all of these coefficients. For that purpose, let us define $\bar{\boldsymbol{A}}$ and $\bar{\boldsymbol{B}}$ the equivalent tensors in physical coordinates of $\boldsymbol{A}$ and $\boldsymbol{B}$, which can be simply obtained by premultiplying $\boldsymbol{A}$ and $\boldsymbol{B}$ by $\boldsymbol{\Phi}^{-\mathrm{T}}$. On the physical point of view, they are homogeneous to forces and not to displacements. Indeed, the linear change of coordinates for displacements reads $\boldsymbol{U} = \boldsymbol{\Phi q}$, whereas for a force one has $\boldsymbol{f} = \boldsymbol{\Phi}^{\mathrm{T}} \boldsymbol{F}$, where $\boldsymbol{f}$ is the modal force and $\boldsymbol{F}$ the nodal force. Since, by definition of the quadratic tensors in modal and physical coordinates, one has $\boldsymbol{\Phi}^{-\mathrm{T}} \boldsymbol{g}_{is} = \boldsymbol{G}_{is}$, then:

$$\bar{\boldsymbol{A}}_{ijk} = \sum_{s=1}^{N} 2\, \boldsymbol{G}_{is}\, a^s_{jk}, \tag{5.27a}$$

$$\bar{\boldsymbol{B}}_{ijk} = \sum_{s=1}^{N} 2\, \boldsymbol{G}_{is}\, b^s_{jk}. \tag{5.27b}$$

To arrive at a finalised expression involving only terms from the physical basis, one has to notice that $\sum_{s=1}^{N} \phi_s a^s_{jk} = \bar{\boldsymbol{a}}_{jk}$ (and similarly for $\bar{\boldsymbol{b}}$), by again using the simple projection rule. The coefficients a^s_{jk} and b^s_{jk} can then be brought into the brackets of $\boldsymbol{G}_{is}$ leading to the final expressions:

$$\bar{\boldsymbol{A}}_{ijk} = 2\, \boldsymbol{G}(\phi_i, \bar{\boldsymbol{a}}_{jk}), \tag{5.28a}$$

$$\bar{\boldsymbol{B}}_{ijk} = 2\, \boldsymbol{G}(\phi_i, \bar{\boldsymbol{b}}_{jk}). \tag{5.28b}$$

Eqs. (5.28) show how $\bar{\boldsymbol{A}}$ and $\bar{\boldsymbol{B}}$ can be computed directly by simple manipulations of the FE code (more algorithmic details will be given in Section 5.5). Once they have been obtained, their equivalent in modal basis simply read:

$$\boldsymbol{A}_{ijk} = \boldsymbol{\varphi}^{\mathrm{T}} \bar{\boldsymbol{A}}_{ijk}, \tag{5.29a}$$

$$\boldsymbol{B}_{ijk} = \boldsymbol{\varphi}^{\mathrm{T}} \bar{\boldsymbol{B}}_{ijk}, \tag{5.29b}$$

where $\boldsymbol{\varphi}$ is the reduced matrix of the master eigenvectors, which should not be confused with $\boldsymbol{\Phi}$: $\boldsymbol{\varphi}$ contains only the n master modes extracted from $\boldsymbol{\Phi}$, whereas $\boldsymbol{\Phi}$ contains all the

N eigenvectors.

To conclude this section, we have derived general second-order formula that give rise to a quadratic mapping based on the second-order normal form theory. The expression have been derived from modal normal from and transformed into physical coordinates in a thoughtful manner, thus allowing their direct computation. The expressions have also been compared to previous works using static modal derivatives and the difference between the two methods have been underlined. In particular, it has been shown how the proposed direct normal form (DNF) computation generalise the quadratic manifold SMD approach and allows to take properly into account the internal resonance, the curvature of the phase space and the velocity dependence. In the next section, we push the method further and give the detailed formulas needed to obtain the cubic terms of the nonlinear mapping.

5.2.2 Third Order direct normal form

The computation of the third-order tensors is more difficult for two different reasons. First the expressions are longer and more tedious. Second and most importantly, at the cubic order, one has to distinguish between trivial and non-trivial internal resonance. The reader is referred to [153, 154, 158] for detailed discussions, while this section will recall important definitions. Roughly speaking, if at second-order all the terms can be cancelled as long as no order-two internal resonance exists, this is not the case anymore at the third-order, otherwise this would mean that the normal form (the reduced-order dynamics) is linear. As explained *e.g.* in [153], cubic monomial term X_p^3 on oscillator p is trivially resonant, and on the physical point of view this is meaningful since it will bend the frequency-response curves so as to produce hardening or softening behaviour [158].

The nonlinear mapping up to order three reads:

$$\boldsymbol{U} = \sum_{i}^{n} \boldsymbol{\phi}_i R_i + \sum_{i=1}^{n}\sum_{j=1}^{n} \bar{\boldsymbol{a}}_{ij} R_i R_j + \sum_{i=1}^{n}\sum_{j=1}^{n} \bar{\boldsymbol{b}}_{ij} S_i S_j, + \sum_{i=1}^{n}\sum_{j=1}^{n}\sum_{k=1}^{n} \bar{\boldsymbol{r}}_{ijk} R_i R_j R_k + \sum_{i=1}^{n}\sum_{j=1}^{n}\sum_{k=1}^{n} \bar{\boldsymbol{u}}_{ijk} R_i S_j S_k, \tag{5.30a}$$

$$\boldsymbol{V} = \sum_{i}^{n} \boldsymbol{\phi}_i S_i + \sum_{i=1}^{n}\sum_{j=1}^{n} \bar{\boldsymbol{\gamma}}_{ij} R_i S_j + \sum_{i=1}^{n}\sum_{j=1}^{n}\sum_{k=1}^{n} \bar{\boldsymbol{\mu}}_{ijk} S_i S_j S_k + \sum_{i=1}^{n}\sum_{j=1}^{n}\sum_{k=1}^{n} \bar{\boldsymbol{\nu}}_{ijk} S_i R_j R_k. \tag{5.30b}$$

Even though the second equation on $\boldsymbol{V}$ is not mandatorily needed in the reduction technique, it is given for the following reasons. First, the original method has been developed including this second equation. Even though it can be deduced from the first in order to have expressions involving only displacements, the needed approximation $\dot{S}_r = -\omega_r^2 R_r$ is just the leading-order and might encounter limitations when the third order is included. Second, giving Eq. (5.30b) allows for direct reconstruction of the velocities, without deducing it from the first with an assumption, and for a light added computational effort. Finally, full dependency on the second equation from the first could be lost in more complex cases,

as *e.g.* including the damping (see [154] for the expressions of the mapping where all the monomials are involved) or other forces in the starting equation. All these points need further analytical investigations that are beyond the scope of the present study. For all these reasons, we keep the change of coordinates with both displacements and velocities.

The expressions of the newly introduced coefficients $\bar{\boldsymbol{r}}_{ijk}$, $\bar{\boldsymbol{u}}_{ijk}$, $\bar{\boldsymbol{\mu}}_{ijk}$, $\bar{\boldsymbol{\nu}}_{ijk}$ are given in the next subsection. The presentation will first consider the simplest case of the terms corresponding to non-trivial internal resonance. These terms can always be cancelled so that no specific treatment is needed as compared to the calculations presented in the previous section. Then the trivially resonant monomials are considered. These terms should not appear in the mapping so that the corresponding monomials will stay in the reduced dynamics (normal form). This specific treatment will be detailed later in this section.

The reduced dynamics after the cubic mapping is given by Eq. (5.2) in case of no internal resonance. It differs from (5.25) (reduced dynamics after second-order normal form) only by the fact that all the non resonant cubic terms have been cancelled. In some sense the order-three reduced dynamics appears simpler after the cubic treatment, and contains less possible nonlinear interactions. As a matter of fact, since the reduced dynamics is truncated at order three, the third-order treatment shown here is somehow incomplete. Indeed, non-resonant cubic monomial terms have been discarded, but the higher-order terms stemming from the nonlinear change of coordinates (quartic and quintic terms), have not been taken into account. We will show in the results section that this might have some important consequences when dealing with higher-order internal resonance. One must keep in mind that processing the cubic terms creates quartic terms that have not been considered in the present study, thus reducing the quality of the third-order reduced dynamics. A full treatment would require to go to higher orders, for example for a correct treatment of 5:1 resonance. Hence the third-order must be viewed as the needed first step toward this achievement, which is however beyond the scope of the present study.

General treatment for non-trivially resonant monomials

In this subsection, the non-resonant terms are first considered. They correspond to the cases where none of the possible combinations of the frequencies $\pm\omega_i \pm \omega_j \pm \omega_k$ is equal to another eigenfrequency ω_s of the system. The general expressions for the fourth-order tensors $\bar{\boldsymbol{r}}$, $\bar{\boldsymbol{u}}$, $\bar{\boldsymbol{\mu}}$, $\bar{\boldsymbol{\nu}}$ appearing in Eq. (5.30) have been obtained following a similar analysis as the one shown in Sec. 5.2.1 for the quadratic terms. They are here expressed from four independent vectors $\bar{\boldsymbol{Z}}\boldsymbol{0}_{ijk}$, $\bar{\boldsymbol{Z}}\boldsymbol{1}_{ijk}$, $\bar{\boldsymbol{Z}}\boldsymbol{2}_{ijk}$ and $\bar{\boldsymbol{Z}}\boldsymbol{3}_{ijk}$ given in Eqs. (5.39), in a similar fashion as the quadratic tensors have been computed from $\bar{\boldsymbol{Z}}\boldsymbol{s}_{ij}$ and $\bar{\boldsymbol{Z}}\boldsymbol{d}_{ij}$ in the previous section. This analysis is now detailed.

A similar approach to that of Sec. 5.2.1 is used to generate the expressions of the third order tensors $\boldsymbol{r}, \boldsymbol{u}, \boldsymbol{\mu}, \boldsymbol{\nu}$. We start by recalling the general expressions from the modal approach already developed in [152, 158] .

In absence of second order internal resonances, no second order terms are present in the reduced dynamics equations and the first order assumptions ($\dot{R}_r = \dot{S}_r$ and $\dot{S}_r = -\omega_r^2 R_r$), can still be used in the derivation of the third order tensors. The system resulting from the balance of each third order term for a given triplet of indexes i, j, k reads:

$$\begin{cases} 3\boldsymbol{\mu}_{ijk} - \boldsymbol{u}_{ijk} - \boldsymbol{u}_{jki} - \boldsymbol{u}_{kij} = \boldsymbol{0}, \\ 3\boldsymbol{r}_{ijk} - \boldsymbol{\nu}_{kij} - \omega_i^2 \boldsymbol{u}_{jki} - \omega_j^2 \boldsymbol{u}_{ijk} = \boldsymbol{0}, \\ 3\boldsymbol{r}_{ijk} - \boldsymbol{\nu}_{jki} - \omega_i^2 \boldsymbol{u}_{kij} - \omega_k^2 \boldsymbol{u}_{ijk} = \boldsymbol{0}, \\ 3\boldsymbol{r}_{ijk} - \boldsymbol{\nu}_{ijk} - \omega_j^2 \boldsymbol{u}_{kij} - \omega_k^2 \boldsymbol{u}_{jki} = \boldsymbol{0}, \\ \omega_i^2 \boldsymbol{\nu}_{ijk} + \omega_j^2 \boldsymbol{\nu}_{jki} + \omega_k^2 \boldsymbol{\nu}_{kij} - 3\boldsymbol{\Omega}^2 \boldsymbol{r}_{ijk} = 3\boldsymbol{h}_{ijk} + \boldsymbol{A}_{ijk} + \boldsymbol{A}_{jki} + \boldsymbol{A}_{kij}, \\ -\boldsymbol{\nu}_{jki} - \boldsymbol{\nu}_{kij} + 3\omega_i^2 \boldsymbol{\mu}_{ijk} - \boldsymbol{\Omega}^2 \boldsymbol{u}_{ijk} = \boldsymbol{B}_{ijk}, \\ -\boldsymbol{\nu}_{ijk} - \boldsymbol{\nu}_{kij} + 3\omega_j^2 \boldsymbol{\mu}_{ijk} - \boldsymbol{\Omega}^2 \boldsymbol{u}_{jki} = \boldsymbol{B}_{jki}, \\ -\boldsymbol{\nu}_{ijk} - \boldsymbol{\nu}_{jki} + 3\omega_k^2 \boldsymbol{\mu}_{ijk} - \boldsymbol{\Omega}^2 \boldsymbol{u}_{kij} = \boldsymbol{B}_{kij}. \end{cases} \tag{5.31}$$

The expressions resulting from the solution of this system are much more lengthy than those of second order tensors but they possess a similar structure. For instance, the expression for the tensor $\boldsymbol{r}$ is in the following form:

$$\boldsymbol{D}_{ijk}^{(8)} \boldsymbol{r}_{ijk} = \boldsymbol{Q}_{ijk}^{(6)} \omega_j \omega_k \boldsymbol{B}_{ijk} + \boldsymbol{Q}_{jki}^{(6)} \omega_k \omega_i \boldsymbol{B}_{jki} + \boldsymbol{Q}_{kij}^{(6)} \omega_i \omega_j \boldsymbol{B}_{kij} + \boldsymbol{P}_{ijk}^{(6)} (\boldsymbol{A}_{ijk} + \boldsymbol{A}_{jki} + \boldsymbol{A}_{kij} + 3\boldsymbol{h}_{ijk}). \tag{5.32}$$

The *numerator* matrices $\boldsymbol{Q}^{(6)}$ and $\boldsymbol{P}^{(6)}$ that multiplies the forcing terms $\boldsymbol{A}$ and $\boldsymbol{B}$ are in the form:

$$\boldsymbol{P}_{ijk}^{(6)} = p_{ijk}^{(6)} \boldsymbol{I} + p_{ijk}^{(4)} \boldsymbol{\Omega}^2 + p_{ijk}^{(2)} (\boldsymbol{\Omega}^2)^2 + (\boldsymbol{\Omega}^2)^3, \tag{5.33}$$

$$\boldsymbol{Q}_{ijk}^{(6)} = q_{ijk}^{(6)} \boldsymbol{I} + q_{ijk}^{(4)} \boldsymbol{\Omega}^2 + q_{ijk}^{(2)} (\boldsymbol{\Omega}^2)^2 + (\boldsymbol{\Omega}^2)^3, \tag{5.34}$$

with $p_{ijk}^{(\times)}$ and $q_{ijk}^{(\times)}$, both $\times$-order polynomials in the sole parameters $\omega_i, \omega_j, \omega_k$. The numerator matrices varies for the different third order tensors.

Conversely, the denominator matrix is the same for each tensor and reads:

$$\begin{aligned} \boldsymbol{D}_{ijk}^{(8)} = &((+\omega_i + \omega_j + \omega_k)^2 \boldsymbol{I} - \boldsymbol{\Omega}^2) \cdot ((-\omega_i + \omega_j + \omega_k)^2 \boldsymbol{I} - \boldsymbol{\Omega}^2) \cdot \\ &\cdot ((+\omega_i - \omega_j + \omega_k)^2 \boldsymbol{I} - \boldsymbol{\Omega}^2) \cdot ((+\omega_i + \omega_j - \omega_k)^2 \boldsymbol{I} - \boldsymbol{\Omega}^2). \end{aligned} \tag{5.35}$$

Once again, the denominator matrix carries a physical meaning in that every possible third order internal resonance between the frequency appears in it.

Following a similar approach than that on the second order tensors, it is convenient to rewrite the expressions for the third order tensors in such a way that the denominator is split. Taking a combination of indexes ijk with no internal resonance between their eigenvalues, we can retrieve the basic vectors that represents the equivalent of $\bar{\boldsymbol{Z}}\boldsymbol{s}$ and $\bar{\boldsymbol{Z}}\boldsymbol{d}$

for the third order tensors in modal basis. If one defines:

$$\boldsymbol{Z0}_{ijk} = ((+\omega_i+\omega_j+\omega_k)^2\boldsymbol{I}-\boldsymbol{\Omega}^2)^{-1}\left(\boldsymbol{A}_{ijk}+\boldsymbol{A}_{jki}+\boldsymbol{A}_{kij}+3\,\boldsymbol{h}_{ijk}-\omega_j\omega_k\boldsymbol{B}_{ijk}-\omega_k\omega_i\boldsymbol{B}_{jki}-\omega_i\omega_j\boldsymbol{B}_{kij}\right) \tag{5.36a}$$

$$\boldsymbol{Z1}_{ijk} = ((-\omega_i+\omega_j+\omega_k)^2\boldsymbol{I}-\boldsymbol{\Omega}^2)^{-1}\left(\boldsymbol{A}_{ijk}+\boldsymbol{A}_{jki}+\boldsymbol{A}_{kij}+3\,\boldsymbol{h}_{ijk}-\omega_j\omega_k\boldsymbol{B}_{ijk}+\omega_k\omega_i\boldsymbol{B}_{jki}+\omega_i\omega_j\boldsymbol{B}_{kij}\right) \tag{5.36b}$$

$$\boldsymbol{Z2}_{ijk} = ((+\omega_i-\omega_j+\omega_k)^2\boldsymbol{I}-\boldsymbol{\Omega}^2)^{-1}\left(\boldsymbol{A}_{ijk}+\boldsymbol{A}_{jki}+\boldsymbol{A}_{kij}+3\,\boldsymbol{h}_{ijk}+\omega_j\omega_k\boldsymbol{B}_{ijk}-\omega_k\omega_i\boldsymbol{B}_{jki}+\omega_i\omega_j\boldsymbol{B}_{kij}\right) \tag{5.36c}$$

$$\boldsymbol{Z3}_{ijk} = ((+\omega_i+\omega_j-\omega_k)^2\boldsymbol{I}-\boldsymbol{\Omega}^2)^{-1}\left(\boldsymbol{A}_{ijk}+\boldsymbol{A}_{jki}+\boldsymbol{A}_{kij}+3\,\boldsymbol{h}_{ijk}+\omega_j\omega_k\boldsymbol{B}_{ijk}+\omega_k\omega_i\boldsymbol{B}_{jki}-\omega_i\omega_j\boldsymbol{B}_{kij}\right) \tag{5.36d}$$

it is possible to demonstrate that the third order tensors of modal normal form are equivalently expressed as a linear combination of the above defined vectors and their expressions read:

$$\boldsymbol{r}_{ijk} = \frac{\boldsymbol{Z0}_{ijk}+\boldsymbol{Z1}_{ijk}+\boldsymbol{Z2}_{ijk}+\boldsymbol{Z3}_{ijk}}{12} \tag{5.37a}$$

$$\boldsymbol{u}_{ijk} = \frac{-\boldsymbol{Z0}_{ijk}-\boldsymbol{Z1}_{ijk}+\boldsymbol{Z2}_{ijk}+\boldsymbol{Z3}_{ijk}}{4\omega_j\omega_k} \tag{5.37b}$$

$$\begin{aligned}\boldsymbol{\mu}_{ijk} = \big(&-(+\omega_i+\omega_j+\omega_k)\boldsymbol{Z0}_{ijk}+(-\omega_i+\omega_j+\omega_k)\boldsymbol{Z1}_{ijk}+\\&+(+\omega_i-\omega_j+\omega_k)\boldsymbol{Z2}_{ijk}+(+\omega_i+\omega_j-\omega_k)\boldsymbol{Z3}_{ijk}\big)\,/(12\omega_i\omega_j\omega_k)\end{aligned} \tag{5.37c}$$

$$\begin{aligned}\boldsymbol{\nu}_{ijk} = \big(&+(+\omega_i+\omega_j+\omega_k)\boldsymbol{Z0}_{ijk}-(-\omega_i+\omega_j+\omega_k)\boldsymbol{Z1}_{ijk}+\\&+(+\omega_i-\omega_j+\omega_k)\boldsymbol{Z2}_{ijk}+(+\omega_i+\omega_j-\omega_k)\boldsymbol{Z3}_{ijk}\big)\,/(4\omega_i)\end{aligned} \tag{5.37d}$$

It is then straightforward to express Eqs. (5.36) in physical basis by using the same strategy that we applied to the second order tensors. Also in this case, there is only one linear system to solve to find the four independent tensors relative to the triplet i,j,k and from them all the eight third order tensors $\bar{\boldsymbol{r}},\bar{\boldsymbol{u}},\bar{\boldsymbol{\mu}},\bar{\boldsymbol{\nu}}$ can be derived. As a final remark, we want to point out that an expression in physical coordinates of Eq. (5.32) could have been also derived, by replacing the matrix $\boldsymbol{\Omega}^2$ with its equivalent $\boldsymbol{\Phi}^{-1}\boldsymbol{O}^2\boldsymbol{\Phi}$ but in that case the computational cost of building all the tensors $\bar{\boldsymbol{r}},\bar{\boldsymbol{u}},\bar{\boldsymbol{\mu}},\bar{\boldsymbol{\nu}}$ would have been even higher than that of the second order one.

To simplify the presentation of the third order tensors in physical coordinated, it is convenient to define the following tensors obtained as a combination of cubic forces:

$$\bar{\boldsymbol{P}}\boldsymbol{0}_{ijk} = \bar{\boldsymbol{A}}_{ijk}+\bar{\boldsymbol{A}}_{jki}+\bar{\boldsymbol{A}}_{kij}+3\boldsymbol{H}_{ijk}-\omega_j\omega_k\bar{\boldsymbol{B}}_{ijk}-\omega_k\omega_i\bar{\boldsymbol{B}}_{jki}-\omega_i\omega_j\bar{\boldsymbol{B}}_{kij}, \tag{5.38a}$$

$$\bar{\boldsymbol{P}}\boldsymbol{1}_{ijk} = \bar{\boldsymbol{A}}_{ijk}+\bar{\boldsymbol{A}}_{jki}+\bar{\boldsymbol{A}}_{kij}+3\boldsymbol{H}_{ijk}-\omega_j\omega_k\bar{\boldsymbol{B}}_{ijk}+\omega_k\omega_i\bar{\boldsymbol{B}}_{jki}+\omega_i\omega_j\bar{\boldsymbol{B}}_{kij}, \tag{5.38b}$$

$$\bar{\boldsymbol{P}}\boldsymbol{2}_{ijk} = \bar{\boldsymbol{A}}_{ijk}+\bar{\boldsymbol{A}}_{jki}+\bar{\boldsymbol{A}}_{kij}+3\boldsymbol{H}_{ijk}+\omega_j\omega_k\bar{\boldsymbol{B}}_{ijk}-\omega_k\omega_i\bar{\boldsymbol{B}}_{jki}+\omega_i\omega_j\bar{\boldsymbol{B}}_{kij}, \tag{5.38c}$$

$$\bar{\boldsymbol{P}}\boldsymbol{3}_{ijk} = \bar{\boldsymbol{A}}_{ijk}+\bar{\boldsymbol{A}}_{jki}+\bar{\boldsymbol{A}}_{kij}+3\boldsymbol{H}_{ijk}+\omega_j\omega_k\bar{\boldsymbol{B}}_{ijk}+\omega_k\omega_i\bar{\boldsymbol{B}}_{jki}-\omega_i\omega_j\bar{\boldsymbol{B}}_{kij}. \tag{5.38d}$$

From them, one can obtain four independent cubic vectors of displacement that will be

used to build the tensors:

$$\bar{\boldsymbol{Z}}\boldsymbol{0}_{ijk} = ((+\omega_i+\omega_j+\omega_k)^2\boldsymbol{M}-\boldsymbol{K})^{-1}\bar{\boldsymbol{P}}\boldsymbol{0}_{ijk}, \tag{5.39a}$$
$$\bar{\boldsymbol{Z}}\boldsymbol{1}_{ijk} = ((-\omega_i+\omega_j+\omega_k)^2\boldsymbol{M}-\boldsymbol{K})^{-1}\bar{\boldsymbol{P}}\boldsymbol{1}_{ijk}, \tag{5.39b}$$
$$\bar{\boldsymbol{Z}}\boldsymbol{2}_{ijk} = ((+\omega_i-\omega_j+\omega_k)^2\boldsymbol{M}-\boldsymbol{K})^{-1}\bar{\boldsymbol{P}}\boldsymbol{2}_{ijk}, \tag{5.39c}$$
$$\bar{\boldsymbol{Z}}\boldsymbol{3}_{ijk} = ((+\omega_i+\omega_j-\omega_k)^2\boldsymbol{M}-\boldsymbol{K})^{-1}\bar{\boldsymbol{P}}\boldsymbol{3}_{ijk}. \tag{5.39d}$$

Note that in the computational algorithm, each of these vectors is obtained by solving a linear system of equations, and not by actually inverting the matrices, which is much more meaningful on the computational point of view. The matrices of these systems are linear combinations of $\boldsymbol{K}$ and $\boldsymbol{M}$ and, similarly to the $\bar{\boldsymbol{Z}}\boldsymbol{s}$ and $\bar{\boldsymbol{Z}}\boldsymbol{d}$ vectors of the second order, cover all the possible combinations of ω_i, ω_j, and ω_k. Four of them are needed in order to obtain all possible cases, corresponding to the splitting of the denominators appearing in the modal normal form approach. The case where one of these combinations is equal to another eigenfrequency ω_s of the system, thus making one of the matrices singular, will be specifically treated later in this section. Here we assumed that it is not the case, therefore the vectors $\bar{\boldsymbol{Z}}$ can be computed.

Finally the expressions of the cubic tensors read:

$$\bar{\boldsymbol{r}}_{ijk} = \frac{1}{12}\left(\bar{\boldsymbol{Z}}\boldsymbol{0}_{ijk}+\bar{\boldsymbol{Z}}\boldsymbol{1}_{ijk}+\bar{\boldsymbol{Z}}\boldsymbol{2}_{ijk}+\bar{\boldsymbol{Z}}\boldsymbol{3}_{ijk}\right), \tag{5.40a}$$
$$\bar{\boldsymbol{u}}_{ijk} = \frac{1}{4\omega_j\omega_k}\left(-\bar{\boldsymbol{Z}}\boldsymbol{0}_{ijk}-\bar{\boldsymbol{Z}}\boldsymbol{1}_{ijk}+\bar{\boldsymbol{Z}}\boldsymbol{2}_{ijk}+\bar{\boldsymbol{Z}}\boldsymbol{3}_{ijk}\right), \tag{5.40b}$$
$$\begin{aligned}\bar{\boldsymbol{\mu}}_{ijk} = \frac{1}{12\omega_i\omega_j\omega_k}&\left(-(+\omega_i+\omega_j+\omega_k)\bar{\boldsymbol{Z}}\boldsymbol{0}_{ijk}+(-\omega_i+\omega_j+\omega_k)\bar{\boldsymbol{Z}}\boldsymbol{1}_{ijk}\right.\\&\left.+(+\omega_i-\omega_j+\omega_k)\bar{\boldsymbol{Z}}\boldsymbol{2}_{ijk}+(+\omega_i+\omega_j-\omega_k)\bar{\boldsymbol{Z}}\boldsymbol{3}_{ijk}\right),\end{aligned} \tag{5.40c}$$
$$\begin{aligned}\bar{\boldsymbol{\nu}}_{ijk} = \frac{1}{4\omega_i}&\left(+(+\omega_i+\omega_j+\omega_k)\bar{\boldsymbol{Z}}\boldsymbol{0}_{ijk}-(-\omega_i+\omega_j+\omega_k)\bar{\boldsymbol{Z}}\boldsymbol{1}_{ijk}\right.\\&\left.+(+\omega_i-\omega_j+\omega_k)\bar{\boldsymbol{Z}}\boldsymbol{2}_{ijk}+(+\omega_i+\omega_j-\omega_k)\bar{\boldsymbol{Z}}\boldsymbol{3}_{ijk}\right).\end{aligned} \tag{5.40d}$$

Before generalizing these computations to the case of trivial internal resonance, one can note that the $\bar{\boldsymbol{Z}}$ vectors introduced in Eqs.(5.39) (where $\bar{\boldsymbol{Z}}$ is a shortcut notation for all $\bar{\boldsymbol{Z}}\boldsymbol{0}_{ijk}$, $\bar{\boldsymbol{Z}}\boldsymbol{1}_{ijk}$, $\bar{\boldsymbol{Z}}\boldsymbol{2}_{ijk}$ and $\bar{\boldsymbol{Z}}\boldsymbol{3}_{ijk}$) have some symmetry relationships:

$$\bar{\boldsymbol{Z}}\boldsymbol{0}_{ijk} = \bar{\boldsymbol{Z}}\boldsymbol{0}_{ikj} = \bar{\boldsymbol{Z}}\boldsymbol{0}_{jki} = \bar{\boldsymbol{Z}}\boldsymbol{0}_{jik} = \bar{\boldsymbol{Z}}\boldsymbol{0}_{kij} = \bar{\boldsymbol{Z}}\boldsymbol{0}_{kji}, \tag{5.41a}$$
$$\bar{\boldsymbol{Z}}\boldsymbol{1}_{ijk} = \bar{\boldsymbol{Z}}\boldsymbol{1}_{ikj} = \bar{\boldsymbol{Z}}\boldsymbol{3}_{jki} = \bar{\boldsymbol{Z}}\boldsymbol{2}_{jik} = \bar{\boldsymbol{Z}}\boldsymbol{2}_{kij} = \bar{\boldsymbol{Z}}\boldsymbol{3}_{kji}, \tag{5.41b}$$
$$\bar{\boldsymbol{Z}}\boldsymbol{2}_{ijk} = \bar{\boldsymbol{Z}}\boldsymbol{3}_{ikj} = \bar{\boldsymbol{Z}}\boldsymbol{1}_{jki} = \bar{\boldsymbol{Z}}\boldsymbol{1}_{jik} = \bar{\boldsymbol{Z}}\boldsymbol{3}_{kij} = \bar{\boldsymbol{Z}}\boldsymbol{2}_{kji}, \tag{5.41c}$$
$$\bar{\boldsymbol{Z}}\boldsymbol{3}_{ijk} = \bar{\boldsymbol{Z}}\boldsymbol{2}_{ikj} = \bar{\boldsymbol{Z}}\boldsymbol{2}_{jki} = \bar{\boldsymbol{Z}}\boldsymbol{3}_{jik} = \bar{\boldsymbol{Z}}\boldsymbol{1}_{kij} = \bar{\boldsymbol{Z}}\boldsymbol{1}_{kji}. \tag{5.41d}$$

Like the second order tensors, the third order tensors needed to build the velocity term

$\boldsymbol{V}$ are not independent from those to build $\boldsymbol{U}$. More specifically, the expression for $\bar{\boldsymbol{\nu}}_{ijk}$, $\bar{\boldsymbol{\mu}}_{ijk}$, and all the $\bar{\boldsymbol{\nu}}$ and $\bar{\boldsymbol{\mu}}$ obtained by permutations of the indexes ijk, can be expressed as a linear combination of the four linearly independent vectors $\bar{\boldsymbol{r}}_{ijk}$, $\bar{\boldsymbol{u}}_{ijk}$, $\bar{\boldsymbol{u}}_{jki}$, $\bar{\boldsymbol{u}}_{kij}$. In turn, these vectors can be unequivocally expressed as a linear combination of the four linearly independent vectors $\bar{\boldsymbol{Z}}\boldsymbol{0}_{ijk}$, $\bar{\boldsymbol{Z}}\boldsymbol{1}_{ijk}$, $\bar{\boldsymbol{Z}}\boldsymbol{2}_{ijk}$, $\bar{\boldsymbol{Z}}\boldsymbol{3}_{ijk}$. This particularly means that only four independent vectors $\bar{\boldsymbol{Z}}\boldsymbol{0}_{ijk}$, $\bar{\boldsymbol{Z}}\boldsymbol{1}_{ijk}$, $\bar{\boldsymbol{Z}}\boldsymbol{2}_{ijk}$, $\bar{\boldsymbol{Z}}\boldsymbol{3}_{ijk}$ are needed to compute 8 different vectors: $\bar{\boldsymbol{r}}_{ijk}$, $\bar{\boldsymbol{u}}_{ijk}$, $\bar{\boldsymbol{u}}_{jki}$, $\bar{\boldsymbol{u}}_{kij}$ (equation on $\boldsymbol{U}$) and $\bar{\boldsymbol{\mu}}_{ijk}$, $\bar{\boldsymbol{\nu}}_{ijk}$, $\bar{\boldsymbol{\nu}}_{jki}$, $\bar{\boldsymbol{\nu}}_{kij}$ (equation on $\boldsymbol{V}$), leading to the conclusion that equation on $\boldsymbol{V}$ is not independent from the one on $\boldsymbol{U}$.

Third-order trivial resonances

Trivial resonances are the consequence of the purely imaginary eigenspectrum $\pm i\omega_p$ of any conservative vibratory system. Then for two different indices (i,j) one is always able to create a third-order trivial internal resonance relationship since $i\omega_j = +i\omega_i - i\omega_i + i\omega_j$. The mathematical consequence is that the treatment of the third order terms is complicated by taking them into account. The physical consequence is that in vibration theory, backbone curves are bent to create either hardening or softening behaviour [153, 158].

To better present the workaround that is needed to compute the third order tensors in case of a trivial resonance in a direct way, it is far more understandable to show how to compute them in modal basis first. Then we will extend the treatment to the direct computation. Even though trivial resonance can appear only when two indices are present instead of four (for a general cubic term from a fourth-order tensor), the presentation below is given for four different (s,i,j,k). This allows to maintain generality in the derivation, as well as more simple coding since these calculations are typically run in nested loops.

Let us start by writing Eqs. (5.39) in modal basis and by component for a non-resonant row s:

$$Z0^s_{ijk} = ((+\omega_i + \omega_j + \omega_k)^2 - \omega_s^2)^{-1} P0^s_{ijk}, \tag{5.42a}$$

$$Z1^s_{ijk} = ((-\omega_i + \omega_j + \omega_k)^2 - \omega_s^2)^{-1} P1^s_{ijk}, \tag{5.42b}$$

$$Z2^s_{ijk} = ((+\omega_i - \omega_j + \omega_k)^2 - \omega_s^2)^{-1} P2^s_{ijk}, \tag{5.42c}$$

$$Z3^s_{ijk} = ((+\omega_i + \omega_j - \omega_k)^2 - \omega_s^2)^{-1} P3^s_{ijk}. \tag{5.42d}$$

In modal basis, mass and stiffness matrices reduce to simple scalars thanks to their diagonalisation, and the bar over the variables are simply removed. Let us now suppose that the s-th row is resonant, meaning that ω_s is equal to one of the combinations of ω_i, ω_j, and ω_k. Then, one of the terms at the denominator in Eqs.(5.42) will be zero and the inversion will no longer be possible. In such case, the terms Z^s_{ijk} (where again the simplified notation Z^s_{ijk} refers to $Z0^s_{ijk}$ to $Z3^s_{ijk}$) that aim at cancelling $A^s_{ijk} + h^s_{ijk}$ and B^s_{ijk} must be set equal to zero, thus avoiding the singularity (problem known as small denominator), and the above mentioned $A^s_{ijk} + h^s_{ijk}$ and B^s_{ijk}, that are no longer cancelled, must remain in the reduced dynamics.

In order to write this set of operations in compact form, one has to first define the four denominator matrices:

$$\boldsymbol{D} = (\pm\omega_i \pm \omega_j \pm \omega_k)^2\boldsymbol{I} - \boldsymbol{\Omega}^2, \tag{5.43}$$

one for each combination of $\pm$. We leave it generic because this operation will apply to each $\boldsymbol{D}$. One of these will be singular because its s-th row will be zero. In order to be able to invert all other nonzero rows while enforcing the constraint that the s-th row of $\boldsymbol{Z}$ must be zero, one has to fulfil the following system:

$$\begin{cases} \boldsymbol{D}\boldsymbol{Z} = \boldsymbol{P} - \boldsymbol{e}_s P^s, \\ \boldsymbol{e}_s^{\mathrm{T}}\boldsymbol{Z} = 0. \end{cases} \tag{5.44}$$

In this way, the s-th row of the first system is the identity $0 = 0$, the others satisfy Eqs (5.42), and the last equality ensures $\boldsymbol{Z}^s = 0$. To express this system in compact form, the matrices must be augmented by the $\boldsymbol{e}_s$ vector so that the system becomes:

$$\begin{bmatrix} \boldsymbol{Z} \\ P^s \end{bmatrix} = \begin{bmatrix} \boldsymbol{D} & \boldsymbol{e}_s \\ \boldsymbol{e}_s^{\mathrm{T}} & 0 \end{bmatrix}^{-1} \begin{bmatrix} \boldsymbol{P} \\ 0 \end{bmatrix} \tag{5.45}$$

For a non-resonant row labelled p, the system is coherent with Eqs.(5.42); and for the resonant row labelled s, the system enforces $Z^s = 0$. One must notice that not only the matrix $\boldsymbol{D}$ has been augmented by a row and a column, but also the RHS vector is made of the force vector $\boldsymbol{P}$ plus a zero on its last row, as well as the solution vector will be one row longer than the sought vector $\boldsymbol{Z}$, with the last row being the reduced dynamics term that cannot be cancelled.

The last step is then to express the same operation in physical basis. The equivalent of $\boldsymbol{D}$ in physical basis is $\bar{\boldsymbol{D}} = (\pm\omega_i \pm \omega_j \pm \omega_k)^2\boldsymbol{M} - \boldsymbol{K}$ and the equivalent of the vector $\boldsymbol{e}_s$ in physical basis is the vector $\boldsymbol{M}\boldsymbol{\phi}_s$. In fact, the constraint on $\bar{\boldsymbol{Z}}$ is expressed in physical basis by the mass orthogonality between $\bar{\boldsymbol{Z}}$ and the s-th mode $\boldsymbol{\phi}_s$. The expression for the generic $\bar{\boldsymbol{Z}}$ in direct form finally reads:

$$\begin{bmatrix} \bar{\boldsymbol{Z}} \\ P^s \end{bmatrix} = \begin{bmatrix} \bar{\boldsymbol{D}} & \boldsymbol{M}\boldsymbol{\phi}_s \\ (\boldsymbol{M}\boldsymbol{\phi}_s)^{\mathrm{T}} & 0 \end{bmatrix}^{-1} \begin{bmatrix} \bar{\boldsymbol{P}} \\ 0. \end{bmatrix} \tag{5.46}$$

This augmentation procedure thus allows one to have a direct computation of all the needed trivially resonant third-order terms. Computationally speaking, since the evaluation of the $\boldsymbol{Z}$ tensors is performed inside nested loops spanning over three indexes i, j, k, the augmentation procedure has to be actuated every time two of the three indexes are equal, say $i = j$, with the augmenting vector $\boldsymbol{\phi}_s$ being the non equal remaining index $s = k$.

5.3 Internal Resonances

When deriving the theory of normal form, as already stated in the previous sections and fully detailed in [153,154,158], one has to take care of the occurrence of internal resonance. The general relationship for nonlinear resonance is found from Poincaré and Poincaré-Dulac's theorems. In the context of nonlinear vibratory systems composed of a purely imaginary eigenspectrum, it is customary to distinguish trivial internal resonance from non-trivial one. Third-order trivial resonances always exist. Consequently the normal form contains cubic-order terms that cannot be cancelled, see Eq. (5.2). Each monomial term staying in the normal form is linked to a specific trivial internal resonance, and the previous section details how to handle these terms in the processing of the cubic terms.

Non-trivial internal resonances have not been taken into account yet since the main assumption holding from the beginning is that of a system free of these relationships. In case a third-order non-trivial internal resonance exists (*e.g.* a relationship of the form $\omega_p = \pm\omega_k \pm \omega_i \pm \omega_j$), then exactly the same procedure as the one explained in the previous section for trivial resonance has to be applied. This will let the corresponding cubic term of the nonlinear mapping to zero and make appear the corresponding monomial in the normal form. Consequently adapting the general reduced dynamics given by Eq. (5.2) to a case with *e.g.* 1:1, 1:3 or a cubic combination resonance, is not difficult. Examples with 1:1 resonance can be found for example in [4,154]. Also the case of a three master modes ROM with 1:3 and 1:1 internal resonances will be highlighted in section 5.6.1.

On the other hand, if second order internal resonance exists (*e.g.* 1:2 relationship $\omega_p = 2\omega_j$ or a combination resonance $\omega_p = \omega_j \pm \omega_i$) then a special care has to be taken. Indeed Eq. (5.2) cannot be applied directly since the change in the second-order tensors will create new and important changes in the cubic terms. At present the method needs further refinement in order to compute fully the third-order tensor, so in this case it is advised to use only the second-order DNF to create a ROM.

5.4 Damping and forcing

In most of the cases one is interested in computing frequency-response curves of nonlinear structures using a dedicated ROM, and not only to predict the backbone curve of the unforced and undamped system. This section is devoted to explain how external forcing and viscous damping can be taken into account in the proposed reduction strategy using direct normal form, based on previous results already shown in [153,154,158].

For the external forcing, the strategy had already been proposed in [153,154]. Since the reduced-order model used normal coordinates linked to the invariant manifolds that are tangent to their linear counterpart at origin, one can simply add the modal force at the right-hand side. This approximation does not lead to an exact solution since the correct formalism should take into account time-dependent manifolds. However, numerical results

reported in [59,60,112,114] clearly shows that the time-dependent variation of the manifold are negligible so that the results from unforced problem is meaningful. More recently, a mathematical proof that at the leading-order, this assumption of using a phenomenological forcing aligned with a curvilinear coordinates, is correct, has been given in [163], hence justifying again that this method can be used safely for including the forcing.

For the damping, general formulas for computing the normal form with modal damping have already been derived in [154]. However, the coefficients are more complex to handle and a number of new terms appear also in the equations, see [154] for a more detailed comparison between conservative and damped normal form. Hence deriving the general expressions for a damped system overshoot the mark of the present study and is postponed to further developments. However, in order to take into account in the ROM a meaningful damping term that aggregates the losses of all the slave modes, a simplified formula is given here and will be used in the simulation results presented in section 5.6.3. The general idea of the present development is to restrict to the case of lightly damped systems, which is meaningful since geometric nonlinearities develop more easily in this context, whereas increasing damping generally favours linear behaviours. Also, since the goal of the present work is to give a ROM strategy applicable for FE structures, a special emphasis is put on the case of Rayleigh damping which is currently used in FE codes, and general formula for a direct computation of new coefficients that take into account Rayleigh damping is derived.

The proposed strategy fully relies on the general results given in [154] that are simplified and modified in order to tackle the problem at hand. More specifically, the proposed formula are given here only for the case of the second-order normal form. Indeed, computing the third-order terms in the nonlinear mapping with damping included needs a further development that needs to be accomplished in a further work. The main assumption is that of light damping. This means that, in an asymptotic development relative to damping factors, only the leading order term is considered, thus simplifying the general formulas given in [154].

The dynamics of the structure in FE nodes now reads:

$$\boldsymbol{M}\ddot{\boldsymbol{U}} + \boldsymbol{C}\dot{\boldsymbol{U}} + \boldsymbol{K}\boldsymbol{U} + \boldsymbol{G}(\boldsymbol{U},\boldsymbol{U}) + \boldsymbol{H}(\boldsymbol{U},\boldsymbol{U},\boldsymbol{U}) = \boldsymbol{0}, \tag{5.47}$$

where the additional term $\boldsymbol{C}\dot{\boldsymbol{U}}$ is now included, and where the damping matrix $\boldsymbol{C}$ reads:

$$\boldsymbol{C} = \zeta_M \boldsymbol{M} + \zeta_K \boldsymbol{K}, \tag{5.48}$$

following the definition of Rayleigh damping, with ζ_M and ζ_K two free parameters. If expressed in the modal basis, the equations of motion for a generic mode s reads:

$$\ddot{q}_s + \zeta_s \dot{q}_s + \omega_s^2 q_s + \sum_{i=1}^{N}\sum_{j=1}^{N} g_{ij}^s q_i q_j + \sum_{i=1}^{N}\sum_{j=1}^{N}\sum_{k=1}^{N} h_{ijk}^s q_i q_j q_k = 0. \tag{5.49}$$

The parameter ζ_s can also be rewritten as $\zeta_s = 2\xi_s\omega_s$ in order to make appear the ξ_s modal damping ratio. If $\boldsymbol{C} = \zeta_M \boldsymbol{M} + \zeta_K \boldsymbol{K}$, then $\zeta_s = \zeta_M + \zeta_K \omega_s^2$ and $\xi_s = (\zeta_M/\omega_s + \zeta_K \omega_s)/2$. Note that in [154], analytical asymptotic expansions for small damping are conducted by assuming the modal damping ratio to be small, $\xi_s \ll 1$.

In order to take into account the damping, three new tensors $\bar{\boldsymbol{\alpha}}, \bar{\boldsymbol{\beta}}, \bar{\boldsymbol{c}}$ have to be added in the nonlinear mapping up to the second order, which now reads:

$$\boldsymbol{U} = \sum_{i}^{n} \boldsymbol{\phi}_i R_i + \sum_{i=1}^{n}\sum_{j=i}^{n} \bar{\boldsymbol{a}}_{ij} R_i R_j + \sum_{i=1}^{n}\sum_{j=i}^{n} \bar{\boldsymbol{b}}_{ij} S_i S_j + \sum_{i=1}^{n}\sum_{j=i}^{n} \bar{\boldsymbol{c}}_{ij} R_i S_j, \tag{5.50a}$$

$$\boldsymbol{V} = \sum_{i}^{n} \boldsymbol{\phi}_i S_i + \sum_{i=1}^{n}\sum_{j=i}^{n} \bar{\boldsymbol{\alpha}}_{ij} R_i R_j + \sum_{i=1}^{n}\sum_{j=i}^{n} \bar{\boldsymbol{\beta}}_{ij} S_i S_j + \sum_{i=1}^{n}\sum_{j=i}^{n} \bar{\boldsymbol{\gamma}}_{ij} R_i S_j. \tag{5.50b}$$

In the general case of arbitrary damping values, all the tensors are modified, meaning that $\bar{\boldsymbol{a}}, \bar{\boldsymbol{b}}, \bar{\boldsymbol{\gamma}}$ needs also to be recomputed in order to take properly into account the damping. However, as shown in [154], if light damping is considered, $\xi_s \ll 1$, then all the expressions can be simplified, and one finds that the leading-order term for the $\bar{\boldsymbol{a}}, \bar{\boldsymbol{b}}, \bar{\boldsymbol{\gamma}}$ is the same as the one in the conservative case (the first adjustment due to damping being at order ξ_s^2). On the other hand, $\bar{\boldsymbol{\alpha}}, \bar{\boldsymbol{\beta}}, \bar{\boldsymbol{c}}$ involve only even powers of the damping in the asymptotics, so that the leading order is at order ξ_s only: this term is thus now taken into account.

The expressions up to first order for the tensor $\bar{\boldsymbol{c}}$ with the assumption of Rayleigh damping reads:

$$\begin{aligned}\bar{\boldsymbol{c}}_{ij} = (\zeta_M + 3\omega_i^2\zeta_K)\bar{\boldsymbol{b}}_{ij} - (2\zeta_K)\bar{\boldsymbol{a}}_{ij} + (-\zeta_M + 2\omega_i^2\zeta_K)(\bar{\boldsymbol{Z}}\boldsymbol{ss} + \bar{\boldsymbol{Z}}\boldsymbol{dd}) \\ + (-\zeta_M + 2\omega_j^2\zeta_K)(\omega_i/\omega_j)(\bar{\boldsymbol{Z}}\boldsymbol{ss} - \bar{\boldsymbol{Z}}\boldsymbol{dd})\end{aligned} \tag{5.51}$$

with $\bar{\boldsymbol{a}}_{ij}$ and $\bar{\boldsymbol{b}}_{ij}$ given by Eq. (5.18) (conservative values), and the new terms as:

$$\bar{\boldsymbol{Z}}\boldsymbol{ss}_{ij} = ((+\omega_i + \omega_j)^2 \boldsymbol{M} - \boldsymbol{K})^{-1} \boldsymbol{M}\, \bar{\boldsymbol{Z}}\boldsymbol{s}_{ij}, \tag{5.52a}$$

$$\bar{\boldsymbol{Z}}\boldsymbol{dd}_{ij} = ((-\omega_i + \omega_j)^2 \boldsymbol{M} - \boldsymbol{K})^{-1} \boldsymbol{M}\, \bar{\boldsymbol{Z}}\boldsymbol{d}_{ij}. \tag{5.52b}$$

As one can observe, the structure of the equations are close to the undamped case, the difference being that $\bar{\boldsymbol{Z}}\boldsymbol{ss}_{ij}$ and $\bar{\boldsymbol{Z}}\boldsymbol{dd}_{ij}$ are more involved, but implying the same kind of operations as $\bar{\boldsymbol{Z}}\boldsymbol{s}_{ij}$ and $\bar{\boldsymbol{Z}}\boldsymbol{d}_{ij}$. The full expression for $\bar{\boldsymbol{c}}_{ij}$ clearly underlines that it is a first-order term on the damping coefficients. Interestingly, only the damping coefficients of the master modes i, j appear in Eq. (5.51), meaning in fact that the assumption of small damping needs only to be retained for the master modes. This is particularly significant since ROMs are generally built for low-frequency modes that have the smallest damping ratios. It underlines that the assumption of light damping should not be too restrictive since slave modes can have larger damping ratios.

From Eq. (5.51) defining $\bar{\boldsymbol{c}}_{ij}$, the computation of the two other second-order tensors simply

reads:

$$\bar{\boldsymbol{\alpha}}_{ij} = -\omega_i^2 \bar{\boldsymbol{c}}_{ij}, \tag{5.53a}$$

$$\bar{\boldsymbol{\beta}}_{ij} = \bar{\boldsymbol{c}}_{ij} - (\zeta_i + \zeta_j)\bar{\boldsymbol{b}}_{ij}. \tag{5.53b}$$

To conclude on the nonlinear mapping, in case of damping, one simply has to keep the $\bar{\boldsymbol{a}}, \bar{\boldsymbol{b}}, \bar{\boldsymbol{\gamma}}$ as in the conservative case, and compute the three new tensors $\bar{\boldsymbol{\alpha}}, \bar{\boldsymbol{\beta}}, \bar{\boldsymbol{c}}$ from (5.51)-(5.53).

The reduced-order dynamics is also modified by the damping terms. Following [154], and restricting to the case of the second-order normal form, the reduced dynamics now reads:

$$\ddot{R}_r + \left(\zeta_M + \zeta_K \omega_r^2\right) \dot{R}_r + \omega_r^2 R_r + \sum_i^n \sum_j^n \sum_k^n \left[(A_{ijk}^r + h_{ijk}^r) R_i R_j R_k + B_{ijk}^r R_i \dot{R}_j \dot{R}_k + C_{ijk}^r R_i R_j \dot{R}_k \right] = 0. \tag{5.54}$$

Apart from the linear damping term, the proposed strategy to take damping into accounts leads to the appearance of the term $C_{ijk}^r R_i R_j \dot{R}_k$. The coefficient C_{ijk}^r is a summation on all the modes including the slave ones. This added term can thus be understood as an aggregate nonlinear damping that takes into account the damping of all the slave modes in order to better approximate the losses on the invariant manifold. From [154], the new coefficient reads:

$$C_{ijk}^r = \sum_{s=1}^{N} 2\, g_{is}^r c_{jk}^s, \tag{5.55}$$

The last needed formula is the equivalent of Eq. (5.28) within the direct formulation in order to compute C_{ijk}^r, which is analogous to the fourth-order tensors $\boldsymbol{A}$ and $\boldsymbol{B}$, in order to avoid the full computation of all the g_{rs}^r appearing in (5.55). After the same kind of manipulations as those reported in section 5.2.1, explicit expression for C_{ijk}^r finally reads:

$$C_{ijk}^r = 2\, \boldsymbol{\phi}_r^{\mathrm{T}}\, \boldsymbol{G}(\boldsymbol{\phi}_i, \bar{\boldsymbol{c}}_{jk}), \tag{5.56}$$

hence allowing to express all the needed quantities so that they can be computed in a direct way from the FE discretisation.

Note that all other terms appearing in the reduced dynamics are left unchanged as compared to (5.25). In the case of a single master coordinates labelled p, then only one extra term has to be taken into account in the reduced dynamics, $C_{ppp}^p R_p^2 \dot{R}_p$. In case of more than one master coordinate, a simplified approach could have been to consider only the C_{ppp}^p terms in the reduced dynamics (*e.g.* in case of two master modes 1 and 2, only C_{111}^1, C_{222}^2 could have been added). However the cross couplings terms have been found to be important in the reduction process, this will be illustrated in Section 5.6.3.

5.5 Practical implementation and algorithm

In this section, a simplified overview of the computational algorithm is given, together with further considerations on the implementation and the non-intrusiveness of the method. In order to simplify the presentation, only the treatment of the conservative terms is made explicit. Adding the damping terms can be done easily following the guidelines given in the previous section.

In the present framework of distributed geometric nonlinearity where all the oscillator equations are fully coupled with quadratic and cubic terms, direct extractions from the finite element model of the full tensors $\boldsymbol{G}$ and $\boldsymbol{H}$ is not feasible. The proposed method is direct in the sense that only the nonlinear force tensors $\boldsymbol{G}(\phi_i, \phi_j) = \boldsymbol{G}_{ij}$ and $\boldsymbol{H}(\phi_i, \phi_j, \phi_k) = \boldsymbol{H}_{ijk}$ are required with $i, j, k \in [1, n]$ only spanning the master modes.

These can be easily obtained thanks to the known StEP method, that computes the quadratic and cubic forces generated in the structure when a displacement along a combination of eigenvectors is imposed, see *e.g.* [36, 97]. The number of StEP method calculations is then equal to $n(n+1)(n+2)/6$ (scales with n^3) for the $\boldsymbol{H}$ tensor and $n(n+1)/2$ (scales with n^2) for the $\boldsymbol{G}$ tensor if the symmetry property of the tensors are exploited.

Also one of the main advantages of the proposed method is to rely on a direct computation solely involving a selection of a priori master coordinates from usual physical considerations (on the nature of the forcing or the dynamics at hand). Since the ROM is directly expressed in the invariant-based span of the phase space, the curvatures induced by the nonlinear mapping allows to directly compute the important, non-resonant couplings. There is no extra need to seek the slave modes coupled to the master ones by a convergence study: they are directly embedded in the nonlinear mapping and thus taken into account. The consequence is that there is no need to compute the full eigenvector matrix $\boldsymbol{\Phi}$, only the master modes are needed and stored in the matrix $\boldsymbol{\varphi}$.

A simplified overview of the algorithm is shown in Alg. 1. It relies on four main separate functions: `Eig`, `StEP`, `Calc_O2` and `Calc_O3`. `Eig` is the usual eigensolver and is not explicated further. `StEP` implements the StEP method following the general and known guidelines, see for example [36, 97, 110]. The starting point of the algorithm is given by the user, with the selection of the master modes of interest, from which the matrix $\boldsymbol{\varphi}$, together with their companion eigenfrequencies, are formed. The StEP method is then applied in order to derive the quadratic and cubic terms of the master modes of interest.

The operations contained in the functions `Calc_O2` and `Calc_O3` have been already detailed in Sec. 5.2.1 and Sec. 5.2.2, but their practical implementation is yet to be discussed. For the sake of simplicity, the discussion is here restricted to the case of a single master mode, but of course the same considerations also apply to the more general case of multiple master modes.

The outputs of `Calc_O2` are the $\bar{\boldsymbol{a}}$, $\bar{\boldsymbol{b}}$, $\bar{\boldsymbol{\gamma}}$ second-order tensors. As shown in Section 5.2.1,

Algorithm 1: Direct Normal Form

Input : $\boldsymbol{K}, \boldsymbol{M}$
Functions : `Eig`, `StEP`, `Calc_O2`,`Calc_O3`
Output : $\boldsymbol{\varphi}, \boldsymbol{\omega}, \bar{\boldsymbol{a}}, \bar{\boldsymbol{b}}, \bar{\boldsymbol{\gamma}}, \boldsymbol{A}, \boldsymbol{B}, \boldsymbol{h}$
OptionalOutput: $\bar{\boldsymbol{r}}, \bar{\boldsymbol{u}}, \bar{\boldsymbol{\mu}}, \bar{\boldsymbol{\nu}}$

Compute eigenproblem only for the master modes
$\boldsymbol{\phi}_r, \omega_r \leftarrow$ `Eig` $(\boldsymbol{K}, \boldsymbol{M})$

Compute StEP method on the master modes $\boldsymbol{\varphi}$
$\boldsymbol{G}_{ij}, \boldsymbol{H}_{ijk} \leftarrow$ `StEP` $(\boldsymbol{\phi}_i, \boldsymbol{\phi}_j, \boldsymbol{\phi}_k)$

Compute second order mapping tensors $\bar{\boldsymbol{a}}, \bar{\boldsymbol{b}}, \bar{\boldsymbol{\gamma}}$
$\bar{\boldsymbol{a}}_{ij}, \bar{\boldsymbol{b}}_{ij}, \bar{\boldsymbol{\gamma}}_{ij} \leftarrow$`Calc_O2` $(\boldsymbol{K}, \boldsymbol{M}, \omega_i, \omega_j, \boldsymbol{G}_{ij})$

Compute StEP method on $\boldsymbol{\varphi}, \bar{\boldsymbol{a}}$ *and* $, \boldsymbol{\varphi}, \bar{\boldsymbol{b}}$
$\boldsymbol{G}(\boldsymbol{\phi}_i, \bar{\boldsymbol{a}}_{jk}) \leftarrow$ `StEP` $(\boldsymbol{\phi}_i, \bar{\boldsymbol{a}}_{jk})$
$\boldsymbol{G}(\boldsymbol{\phi}_i, \bar{\boldsymbol{a}}_{jk}) \leftarrow$ `StEP` $(\boldsymbol{\phi}_i, \bar{\boldsymbol{b}}_{jk})$

Obtain third order forces tensors $\bar{\boldsymbol{A}}$ *and* $\bar{\boldsymbol{B}}$
$\bar{\boldsymbol{A}}_{ijk} \leftarrow 2\,\boldsymbol{G}(\boldsymbol{\phi}_i, \bar{\boldsymbol{a}}_{jk})$
$\bar{\boldsymbol{B}}_{ijk} \leftarrow 2\,\boldsymbol{G}(\boldsymbol{\phi}_i, \bar{\boldsymbol{b}}_{jk})$

if *DNF up to Second Order* **then**
  Compute full third order reduced dynamics tensors
  $h^r_{ijk} \leftarrow \boldsymbol{\phi}_r^{\mathrm{T}} \boldsymbol{H}_{ijk}$
  $A^r_{ijk} \leftarrow \boldsymbol{\phi}_r^{\mathrm{T}} \bar{\boldsymbol{A}}_{ijk}$
  $B^r_{ijk} \leftarrow \boldsymbol{\phi}_r^{\mathrm{T}} \bar{\boldsymbol{B}}_{ijk}$
else
  Compute third order mapping tensors
  $\bar{\boldsymbol{r}}_{ijk}, \bar{\boldsymbol{u}}_{ijk}, \bar{\boldsymbol{\mu}}_{ijk}, \bar{\boldsymbol{\nu}}_{ijk} \leftarrow$ `Calc_O3` $(\boldsymbol{K}, \boldsymbol{M}, \omega_i, \omega_j, \omega_k, \bar{\boldsymbol{A}}_{ijk}, \bar{\boldsymbol{B}}_{ijk}, \boldsymbol{H}_{ijk})$
  Fill third order reduced dynamics tensors solely with trivially resonant terms
  $h^r_{ijk} \leftarrow \boldsymbol{\phi}_r^{\mathrm{T}} \boldsymbol{H}_{ijk}$
  $A^r_{ijk} \leftarrow \boldsymbol{\phi}_r^{\mathrm{T}} \bar{\boldsymbol{A}}_{ijk}$
  $B^r_{ijk} \leftarrow \boldsymbol{\phi}_r^{\mathrm{T}} \bar{\boldsymbol{B}}_{ijk}$
end

they are derived from the computation of internal variables $\bar{\boldsymbol{Z}}\boldsymbol{s}$ and $\bar{\boldsymbol{Z}}\boldsymbol{d}$. Let us detail this computation and comment its effectiveness with regard to a non-intrusive method, in the case of a single master mode i. Eqs. (5.24) gives the expressions of $\bar{\boldsymbol{Z}}\boldsymbol{s}$ and $\bar{\boldsymbol{Z}}\boldsymbol{d}$, which are written in their explicit form for a direct solution, i.e. with the unknown vectors alone on the left hand side. In the actual implementation, there is however no need to perform a

matrix inversion because, in the FE solver, a linear algebraic system is solved instead:

$$((2\omega_i)^2\boldsymbol{M} - \boldsymbol{K})\bar{\boldsymbol{Z}}\boldsymbol{s} = \boldsymbol{G}(\phi_i, \phi_i), \tag{5.57a}$$

$$\boldsymbol{K}\,\bar{\boldsymbol{Z}}\boldsymbol{d} = -\boldsymbol{G}(\phi_i, \phi_i). \tag{5.57b}$$

In Eq. (5.57b), the linear system can be solved directly by performing a linear static analysis that computes the unknown displacement vector $\bar{\boldsymbol{Z}}\boldsymbol{d}$ when the structure is subjected to the force vector $-\boldsymbol{G}(\phi_i, \phi_i)$. This type of analysis is a standard operation in every FE software and its computational cost is quite small even for very large models. The same kind of operation has already been used in the context of SMD and is considered as a non-intrusive calculation. The linear system in Eq. (5.57a) is a bit different and involves a linear combination of $\boldsymbol{K}$ and $\boldsymbol{M}$, but without an increase in the size of the system to solve. Despite this operation is not a standard one in a FE software, its computational cost is again quite low. To be able to perform this operation, the FE software must allow the user to script and to do matrix operations online. In this way, the $\boldsymbol{K}$ and $\boldsymbol{M}$ matrices are never exported from the software but only the resulting vector is.

The next steps of the algorithm is then to compute the $\bar{\boldsymbol{A}}$ and $\bar{\boldsymbol{B}}$ tensors following Eqs. (5.28). This is performed in lines 8 and 9 of the algorithm, by using the StEP function. Indeed, one can note that StEP is a calculation method, that can be applied with any input vectors needed. Even though, in its first derivation given in [97], it was only thought for a non-intrusive computation of the modal nonlinear coupling coefficients, so that the entries of the procedure were prescribed displacements along given eigenmodes, the procedure can also be used more generally, as done here with entries composed of one eigenvector and a vector $\bar{\boldsymbol{a}}_{ij}$ or $\bar{\boldsymbol{b}}_{ij}$. Once $\bar{\boldsymbol{A}}$ and $\bar{\boldsymbol{B}}$ computed, their counterpart $\boldsymbol{A}$ and $\boldsymbol{B}$ are found by using a projection involving $\boldsymbol{\varphi}$, which is needed for the reduced-order dynamics.

The last part of the algorithm distinguishes if the user only needs the second-order normal form or the third-order. In case the third-order is needed, then the function `Calc_O3` is called, producing the computations explained in Section 5.2.2.

For all our computations, the open software Code_Aster [28] has been used. All the calculations have been simply implemented using external scripts driving the master code, without the need of entering intrusively in the code.

5.6 Numerical Results

5.6.1 A clamped-clamped beam with internal resonance

The first example is a clamped-clamped straight beam, for which the amplitude-frequency backbone curves will be computed with the direct normal form approach. This example has interesting features since it presents, at high levels of vibration amplitudes, internal resonances between the nonlinear frequencies of the system. This creates resonance loops in

the backbones where strong interactions between the modes exist, see *e.g.* [67,85,108]. This salient feature shares common points with internal resonance between the eigenfrequencies of the system, for which special care needs to be taken since corresponding to a resonant monomial term in the normal form. In the present case, the resonance occurs between the nonlinear frequencies, at large amplitudes. Such a beam example has also been studied recently in [143], where these resonance loops have been reported in Frequency-Energy Plots (FEP). Consequently the results shown in [143] will serve here as a guideline in order to detect if the same behaviour can be retrieved with the DNF.

The model in [143] used simple 1D beam elements thus resorting to a simplified kinematics, and 30 elements gave the space discretisation. In order to cope with a more realistic mesh, closer to general assumptions of elasticity, 3D block elements with three displacements per nodes, have been used for meshing the clamped-clamped beam. The FE model consists of a mesh of 80 hexahedrons (20 along the axis, 2x2 in the section) with 20 nodes each, for a total number of 621 nodes, and 1863 degrees-of-freedom (dofs). The dimensions of the beam are $L = 1$ m along the z axis, $b = h = 0.01$ m. The material properties are the following: $E = 210$ GPa, $\rho = 8750$ kg/m^3, $\nu = 0.3$. The mesh is shown in Fig. 5.1 together with the eigenmodeshapes of modes 1 to 4 and 6. In the rest of the Chapter, the displacement along x will be denoted as u, while the displacement along the in-plane direction z, is denoted as w. No motion is allowed along y.

The six lowest eigenfrequencies of the beam, corresponding to bending modes, are reported in the first row of Table 5.1. In the second row, the frequency ratio with respect to mode 1 is given, showing that the eigenfrequency of mode 3 is a bit larger than 5 times the first. At the linear level, a 5:1 internal resonance does not exist. However, since the beam has a hardening behaviour, increasing the amplitude will make the fulfilment of 5:1 ratio possible, so one could expect for the first NNM, a strong interaction in 5:1 ratio with mode 3, a result that has indeed already been reported in [143]. The last row of Table 5.1 shows the frequency ratios with respect to mode 2. One can see that a 3:1 internal resonance may be excited once the hardening behaviour has sufficiently increased the nonlinear frequencies. So a 3:1 internal resonance loop with an interaction with mode 4 can be expected for NNM 2. As reported in [143], this will be indeed the case, as well as, at larger amplitudes, a 5:1 resonance with mode 6.

Mode Number	1	2	3	4	5	6
Frequency (Hz)	50.900	140.74	277.09	460.64	692.93	975.85
Frequency Ratio with mode 1	1		5.44			
Frequency Ratio with mode 2		1		3.27		6.93

Table 5.1: Linear modes frequencies and frequency ratios with mode 1 and 2.

Fig. 5.2 shows some of the components of the quadratic and cubic tensors used in the nonlinear mapping, Eq. (5.30). The first line shows quadratic $\bar{\boldsymbol{a}}_{ij}$ vectors for some specific combinations: $\bar{\boldsymbol{a}}_{11}$, $\bar{\boldsymbol{a}}_{13}$, and $\bar{\boldsymbol{a}}_{33}$, and give also a direct comparison with the corresponding

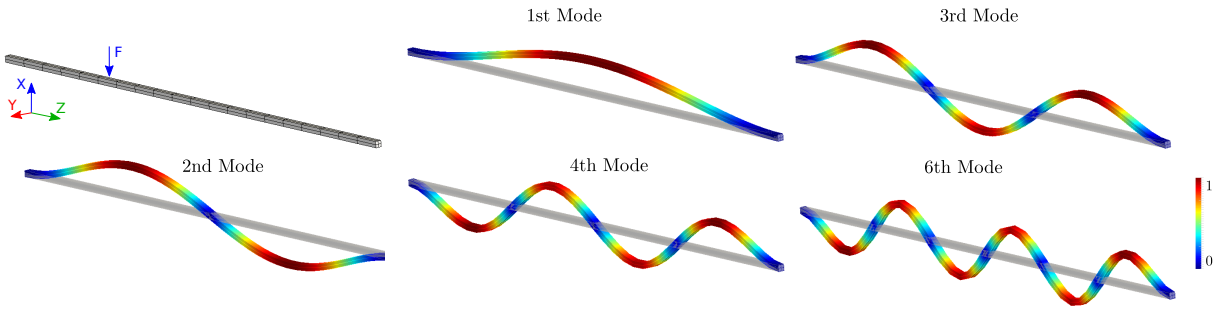


Figure 5.1: Mesh selection and geometry of the straight clamped-clamped beam, as well as eigenmode shapes corresponding to bending modes number 1 to 4 and mode 6. The bending vibration direction is along x while the in-plane direction is z.

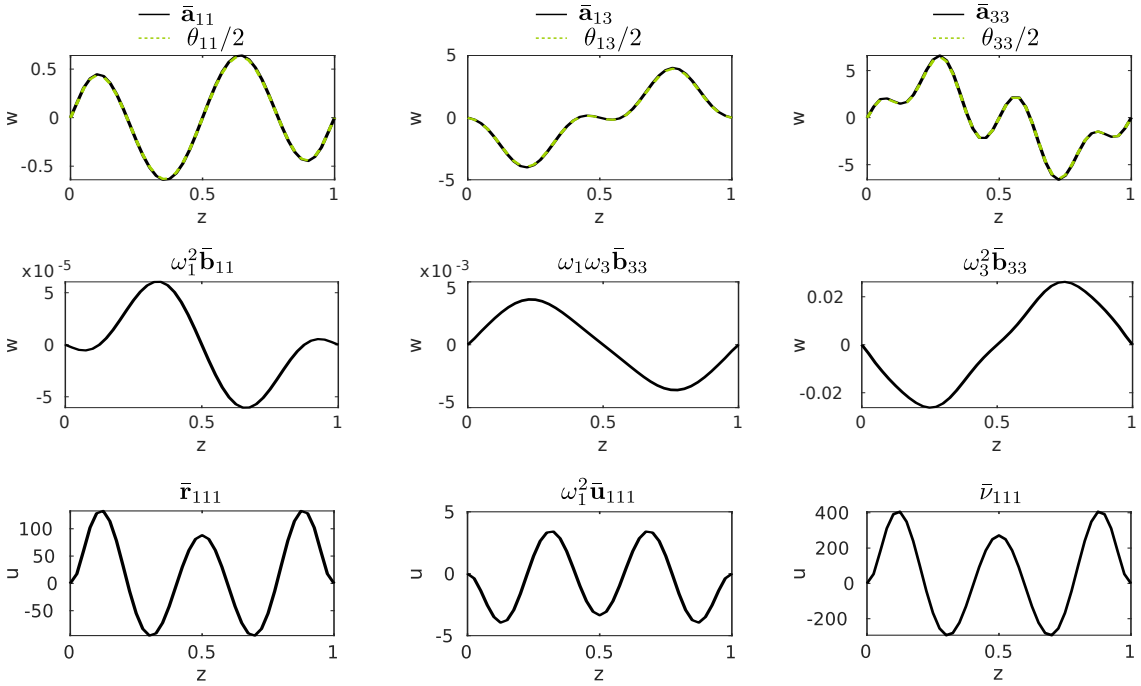


Figure 5.2: Illustration of the physical content of some of the quadratic and cubic tensors used in DNF approach. First line: $\bar{\boldsymbol{a}}_{11}$, $\bar{\boldsymbol{a}}_{13}$ (black lines) compared to static modal derivatives Θ_{11}, Θ_{13} and Θ_{33} (dashed green line). Second line: quadratic vectors $\bar{\boldsymbol{b}}_{11}$, $\bar{\boldsymbol{b}}_{13}$ and $\bar{\boldsymbol{b}}_{33}$. Third line: cubic vectors: $\bar{\boldsymbol{r}}_{111}$, $\bar{\boldsymbol{\mu}}_{111}$ and $\bar{\boldsymbol{\nu}}_{111}$.

static modal derivative (SMD) Θ_{11}, Θ_{13} and Θ_{33}. As explained in section 5.2.1, in a simplified case where a slow/fast assumption can be assumed, then $\bar{\boldsymbol{a}}_{ij}$ vectors will point to the same direction as static modal derivatives, and $\bar{\boldsymbol{b}}_{ij}$ vectors should be negligible. This property is indeed verified in this example: all three selected $\bar{\boldsymbol{a}}_{ij}$ examples are exactly the same as their SMD counterparts. Interestingly, $\bar{\boldsymbol{a}}_{ij}$ vectors are able to recover the most important quadratic couplings between eigenmodes. As analysed in Chapter 3, for flat structures such as the straight beam considered, quadratic couplings arise only in the oscillator equations governing the in-plane modes dynamics, and involve two bending modes. With this respect, one understands why the $\bar{\boldsymbol{a}}_{ij}$ vectors only involve in-plane motions, such that their main component is along w (z direction) in Fig. 5.2. Also, slow/fast assumption in order to use safely SMD has been estimated in Chapter 4 as soon as the ratio between slave and master mode is larger than 4. Here the ratio between the first bending mode and the fourth

axial mode is approximately 192.4. Second, $\bar{\boldsymbol{a}}_{11}$ allows to directly recover the fact that for the first bending mode of a beam, the most important coupling is with the 4th axial mode, see *e.g.* [36, 139] for numerical examples highlighting this result. It is thus fully logical to observe that $\bar{\boldsymbol{a}}_{11}$ have the shape of this fourth axial mode. The direct consequence is that there is no need to analyse beforehand the mode couplings, since they are automatically embedded in the added quadratic tensors. Finally, as shown in [36], bending mode 3 has a strong quadratic coupling with in-plane modes number 2, 6 and 8. Consequently, $\bar{\boldsymbol{a}}_{33}$ shows an axial deformation being a combination of these three mode shapes.

The second line of Fig. 5.2 shows the same plot as the first line but now for the $\bar{\boldsymbol{b}}_{ij}$ vectors: $\bar{\boldsymbol{b}}_{11}$, $\bar{\boldsymbol{b}}_{13}$ and $\bar{\boldsymbol{b}}_{33}$. These additional vectors are not taken into account if one uses the quadratic manifold from SMD. In this specific case of a straight beam where the slow/fast assumption is very well fulfilled, one can observe that the $\bar{\boldsymbol{b}}_{ij}$ vectors have, as anticipated, very small amplitudes, and can thus be safely neglected. These first results, highlighting how the nonlinear couplings are embedded into the additional vectors of the second-order term in the mapping, explains why in this simple case of a straight beam, the results provided by SMD are very good and allows to retrieve correct predictions, as reported in [143]. However, adding curvature to the structures and thus more complex couplings between modes and disappearance of the slow/fast assumption, it has been shown that SMD do not produce correct results anymore, as shown *e.g.* in the previous chapter. The reflection of that fact should then appear in the behaviours of $\bar{\boldsymbol{b}}_{ij}$ vectors. This specific illustration is reported to a future work but preliminary comparisons are already reported in Chapter 4.

Finally, the third line of Fig. 5.2 shows three of the third-order vectors: $\bar{\boldsymbol{r}}_{111}$, $\bar{\boldsymbol{\mu}}_{111}$ and $\bar{\boldsymbol{\nu}}_{111}$. Again, for a flat structure, cubic couplings involve only bending modes. Consequently, these correction vectors are in the x direction and involve mostly bending displacement u. Their shape also underlines the fact that, due to symmetry reasons, a clear separation exist between odd and even modes, the two families being coupled together with no cross-coupling between them. Consequently, $\bar{\boldsymbol{r}}_{111}$, $\bar{\boldsymbol{\mu}}_{111}$ and $\bar{\boldsymbol{\nu}}_{111}$ shows only combinations of odd modes and underlines why mode 1 couples only with modes 3, 5, and so on, and the same for mode 2 with mode 4, 6 and so on.

We now turn to the analysis of the backbone curves for the first and the second mode. In each case, a reference, full-order simulation, is performed thanks to numerical continuation on all the degrees of freedom of the structure. A parallel implementation using harmonic balance method and pseudo arc-length continuation, as reported in [17], is used. In this beam case, due to some limitations of this algorithm, the beginning of the backbone is numerically found by using a small amount of harmonic forcing. Then, as soon as the first points are found, forcing is removed and continuation restarted.

Fig. 5.3(a) shows the reference result for the first mode obtained with the full-order model. As anticipated, a resonance loop appears along the backbone due to the excitation of the 5:1 internal resonance between mode 1 and mode 3. Interestingly, two results from the computation of the full-order model are shown in Fig. 5.3(a). The first one has been ob-

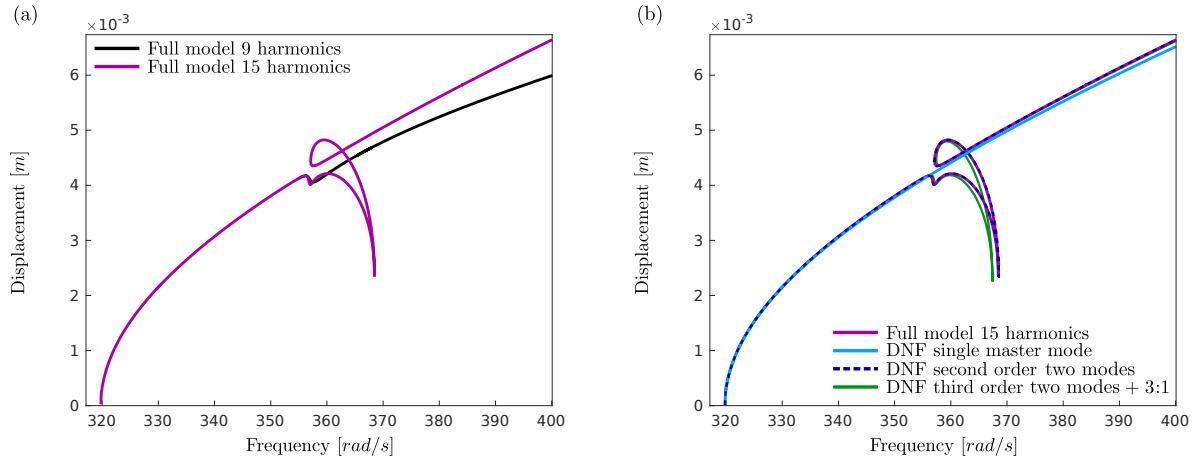


Figure 5.3: Amplitude-frequency backbone curve for the first NNM of the clamped-clamped beam. (a) reference full-order solution obtained with 9 harmonics (black line) and with 15 harmonics (purple). Stability is not reported. (b) comparison of the reference solution to different ROMs computed with the direct normal form (DNF). Light blue curve: direct normal form with a single master coordinate corresponding to mode 1. Dashed blue line: second-order direct normal form with two master coordinates 1 and 3, green line: third-order direct normal form with two master modes (1 and 3) and inclusion of the resonant monomials corresponding to 3:1 internal resonance.

tained by using 9 harmonics in the numerical solution for continuation. As observed, this solution is not converged since the complete resonance loop is partially missed, in contrast to the converged solution obtained with 15 harmonics. This result underlines that in the resonance loops, complex high-order interactions are activated between the harmonics of the solution and a too crude truncation oversimplify the analysis and misses important detail of the nonlinear dynamics.

In Fig. 5.3(b), the reference solution is compared to different ROMs computed with the direct normal form (DNF). The first ROM is obtained by retaining a single master coordinate in the reduction strategy, corresponding to mode 1 (DNF single master mode, light blue curve). As it could be expected, the single-mode solution offers a drastic reduction, is able to recover the correct hardening behaviour of the beam, but is not able to retrieve the internal resonance, since a strong interaction with mode 3 is activated. The minimal reduced model should consists of at least two master coordinates. Consequently different ROMs including two master coordinates corresponding to mode 1 and 3 are tested.

The second ROM is computed thanks to the second-order normal form presented in section 5.2.1, and two master coordinates (modes 1 and 3). The main advantage of this strategy is that all possible combinations of higher-order resonance (from order three) have not been dealt with the nonlinear mapping. Consequently they are still present in the cubic terms and can express themselves if needed. This strategy is particularly meaningful in the case considered since a 5:1 internal resonance is at hand, which would formally need to push all the normal form development up to order five, which is beyond the scope of the present study. The ROM obtained with two master modes and second order normal form is able to properly retrieve the 5:1 internal resonance, without any extra effort from the analysis.

This is explained by the fact that the second-order resonances have been correctly treated, but then stopping at this order let all other possibilities free.

On the other hand, using the third-order normal form for getting back this 5:1 relationship opens the doors to new questions. In the best setting, one should go to order five and add only the resonant monomial terms corresponding to the 5:1 relationship. Since this calculation is far more difficult, different options are considered. The first, already commented option, is to stop at second order, leaving all higher-order terms there. This option gives very good result in this case. Its main drawbacks are twofold. First an order of accuracy in the nonlinear mapping has been lost as compared to what can be easily computed, meaning that the approximation of the underlying invariant manifold is less accurate. Second, the number of cubic terms in the ROM is more important, which is not a big issue since only two modes are considered. A second option would be to select two master coordinates and use the normal form up to the third order, using the solution obtained without considering internal resonance, see Eq. (5.2) for the reduced dynamics. In this case the same solution as with a single master coordinate will be retrieved, because no invariant-breaking terms are present in Eq. (5.2).

A third option consists in adding invariant-breaking terms in order to excite the coupling and retrieve the 5:1 internal resonance loop with only cubic terms. Since internal resonance appears due to nonlinear interactions between harmonics of the solution, it is meaningful to add invariant-breaking terms related to lower-order internal resonance, in this case 3:1 and 1:1. In the first case (3:1 resonance), two terms are added to the dynamics due to 3:1 resonance: a $R_1^2 R_3$ term for the first oscillator (and all their ancillary terms involving velocities), and a R_1^3 on the second master coordinate (corresponding to mode 3, again with all its companion terms with velocities). The dynamics of these ROMs are fully explicated in Appendix B so that the reader can get a better understanding of the equations used.

The resulting backbone is shown in Fig. 5.3(b), and is named DNF third order + 3:1. Interestingly, this ROM can recover the internal resonance loop of the 5:1, with only a slight departure from the reference solution. Finally if one also considers the terms due to 1:1, it means adding the R_3^3 term on R_1 equation, and $R_1 R_3^2$ monomial on R_3 equation (see Appendix B for details). In this case the model is simply the same as the one obtained with second-order normal form, since all the cubic terms are now present. So this case is equivalent to the result already obtained with the second-order normal form, and gives a perfect match.

Fig. 5.4 shows the results obtained for the second NNM. As expected from the linear analysis and from the results already reported in [143], the full-order solution shows two successive loops, corresponding to the fulfilment of 3:1 internal resonance between the nonlinear frequencies of mode 2 and mode 4, and the 5:1 resonance between mode 2 and mode 6. Again, different reduced-order models are compared in order to better understand their capabilities. A first ROM is built using a single master coordinate corresponding to mode 2, and compared to full-order solution in Fig. 5.4(a). This ROM allows to predict the correct

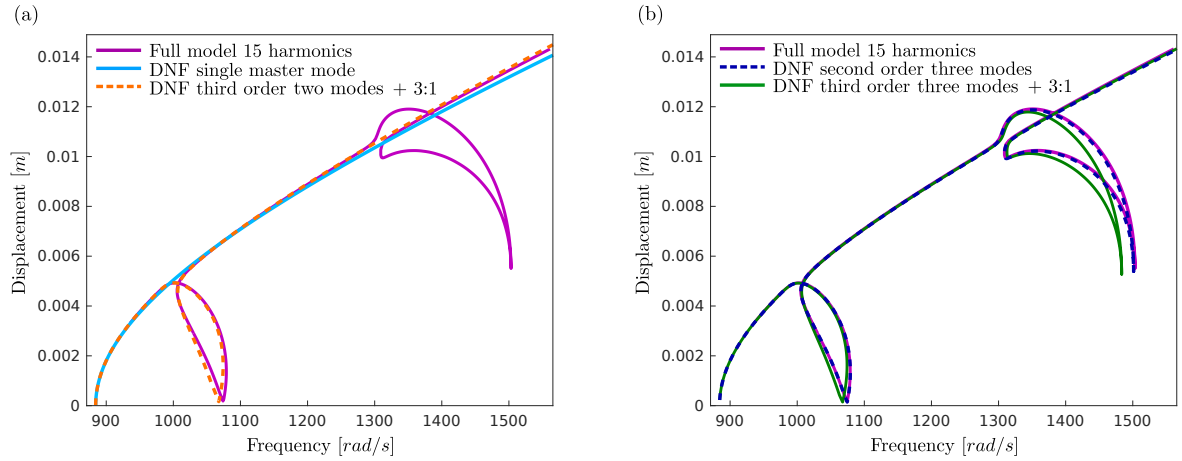


Figure 5.4: Amplitude-frequency backbone curve for the second NNM of the clamped-clamped beam. (a) Reference solution obtained with 15 harmonics (purple) compared to ROM considering only master coordinate of mode 2 (DNF single master mode, light blue), and a ROM with the third-order normal form with modes 2 and 4 and the resonant monomials corresponding to 3:1 internal resonance (DNF third-order + 3:1, dashed red curve). (b) Reference solution is compared to a ROM obtained with the second-order normal form with 3 master coordinates corresponding to modes 2, 4 and 6 (dashed blue), and to a ROM obtained with the third-order normal form, 3 master coordinates, and resonant monomials corresponding to 3:1 between mode 2 and 4 and 2 and 6.

hardening behaviour, but cannot catch the resonance loops since the resonant dynamics is intrinsically of higher dimension. A second ROM with two master coordinates corresponding to mode 2 and 4 is then built, using the third-order normal form. Since a 3:1 internal resonance is expected, the resonant monomials corresponding to 3:1 resonance between modes 2 and 4 are taken into account in this reduced dynamics. The result is shown in Fig. 5.4(a). It underlines that this ROM is capable of reproducing the loop of 3:1 internal resonance with a fair accuracy, but of course is not able to catch the second loop since a nonlinear interaction with mode 6 comes into play.

Fig. 5.4(b) compares the results provided by two ROMs composed of three master coordinates corresponding to modes 2, 4 and 6. The first one is computed with the second-order normal form. As in the case of the first NNM, it gives a perfect match to the reference solution and is able to recover the two loops of internal resonances corresponding to 3:1 resonance with mode 4 and 5:1 resonance with mode 6. Note that in some sense this ROM is minimal since only three master coordinates have been used. To our point of view, it is not possible to reproduce such backbones with less than three master coordinates since nonlinear interactions are between mode 2 and 4 and then between mode 2 and 6. On the other hand, the same behaviour has been successfully reported in [143], but their model were composed of 9 modes (3 linear modes plus 6 static modal derivatives).

The last ROM tested still contains three master coordinates and applies the third-order normal form. Resonant monomial corresponding to 3:1 resonance between mode 2 and 4 have been added to reproduce the first resonance loop. For the second loop implying a 5:1 resonance, the same problem appears as with the case of NNM 1: a perfect recov-

ering of this resonance with the normal form theory would need to push the asymptotic development up to order five. Consequently, in the line of the previous study on NNM 1, only the resonant monomials corresponding to a 3:1 resonance between mode 2 and 6 have been added. This ROM contains far less nonlinear terms in the reduced dynamics than the second-order normal form. It is able to well reproduce the two resonance loops, however with a small difference as compared to the full-order solution.

These examples clearly underline that selecting the second-order normal form is generally a very good option when odd resonances are present. Indeed, comparing in this case the reduced dynamics given by second and third-order DNF shows that the only difference is that the non-resonant terms have been removed in the dynamics for the third-order. On the other hand, the higher-order corrective terms that should come into play since the computation of normal form is intrinsically an asymptotics, have not been taken into account, based on the fact that the dynamics is truncated up to order three. This means that in the present version, the second-order normal form contains more information and is capable of reproducing higher-order resonance as shown here with the 5:1 case. The main drawback is that in the reconstruction process, the nonlinear mapping is less accurate since truncated to order two. But the gain in the reduced dynamics, which contains much more terms, seems to be more important.

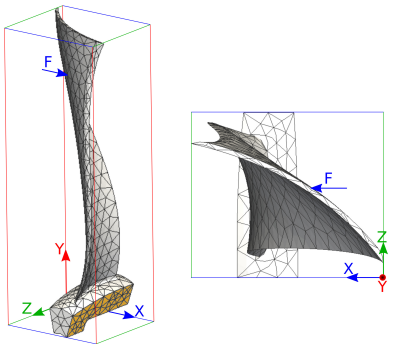
5.6.2 FE model of a fan blade

In this section, a FE model of a fan blade is selected in order to test the method with an application of high interest in engineering, with a more complex geometry and large-amplitude vibrations exciting geometric nonlinearities. The backbone curve of the first mode of the structure will be computed with the DNF approach and compared to a reference solution obtained from direct continuation of all the dofs of the structure.

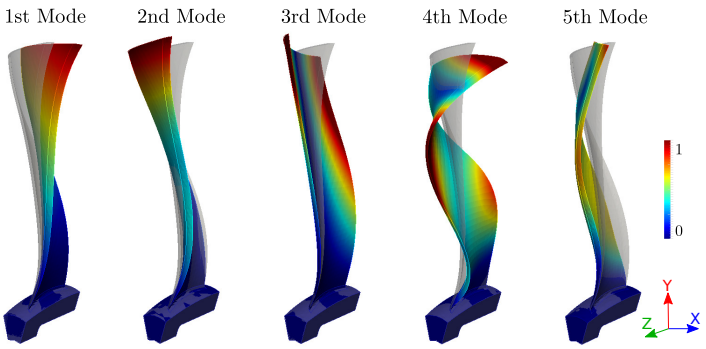
The FE model of the fan blade is shown in Fig. 5.5a, and consists of a mesh of 2041 tetrahedrons with 10 nodes each, for a total number of 3895 nodes (11685 dofs). The blade is clamped at its root as shown in Fig. 5.5a. The dimension of the bounding box containing the blade and the portion of disk at its root is: $\Delta X = 0.41$ m, $\Delta Y = 1.14$ m, $\Delta Z = 0.35$ m. The span of the blade is approximately 1.02 m, the chord measured from trailing to leading edge is 0.48 m and the thickness in the centre of the profile is 0.01 m. The material properties are the following: $E = 104$ GPa, $\rho = 4400$ kg/m^3, $\nu = 0.3$. The frequency of the first five modes are reported in Table 5.2. The mode shapes are reported in Fig. 5.5b.

Mode Number	1	2	3	4	5
Frequency (Hz)	14.592	40.571	49.055	170.36	197.03
Frequency Ratio	1	2.78	3.36	11.67	13.50

Table 5.2: First five eigenfrequencies of the fan blade and frequency ratios with the first mode.



(a) Blade mesh isometric and top view.



(b) Blade modes

Figure 5.5: Blade mesh and first five modes. In Fig. 5.5a, the blade mesh is shown from two different views. Clamped faces highlighted in yellow. In Fig. 5.5b, the first five modes of the blade are reported.

This example is challenging for a number of reasons. First the nonlinear behaviour of the blade is close to a cantilever beam, for which inertia nonlinearity plays an important role [32]. In this case, reduction methods based on static condensation are not reliable anymore since neglecting the most important phenomenon. Second, as compared to the beam, the shape of the fan is twisted and curved, making the problem closer to a shell than to a flat structure. Consequently quadratic nonlinearities are much more pronounced and slow/fast separation is less fulfilled. For all these reasons, computing the correct type of nonlinearity (hardening/softening behaviour) of this kind of structure, still remains difficult for a ROM. As a matter of fact, no clear numerical demonstration that a reduced-order model is able to accurately compute the non-linear vibration of a Fan Blade has been proposed so far. The existing methods published in literature for vibration of large 3D models cannot achieve a better accuracy that 10% of error, in the best case, as compared to the full model [9].

In Fig. 5.6, the second order tensors $\bar{\boldsymbol{a}}, \bar{\boldsymbol{b}}$ relative to the first mode of the blade are reported together with the reduced dynamics parameters of the ROM for a single mode motion. The shape of the $\bar{\boldsymbol{a}}$ vector shows that a shortening motion (proportional to R^2) takes place as the vibration amplitude of the first mode (proportional to R) increases. This is a fairly expectable behaviour occurring in every cantilever-like structure. The correction provided by $\bar{\boldsymbol{a}}$ thus serves the purpose of relaxing the stiffening effect that one would observe when this shortening motion is erroneously locked, see *e.g.* [126,127]. The relaxation provided by $\bar{\boldsymbol{a}}$ is what generates the A^1_{111} term in the reduced dynamics of the first mode. Importantly, the absolute values of A^1_{111} and h^1_{111} are nearly the same and their sum is almost vanishing, meaning that the R^3 term is small in the reduced dynamics. Unlike overconstrained structures, cantilever-like structures are isostatic therefore the slave modes quadratically coupled to the master are free to move, generating this particular behaviour that we have also observed in other cases.

Since the correction brought by A^1_{111} makes the term $A^1_{111} + h^1_{111}$ very small, one under-

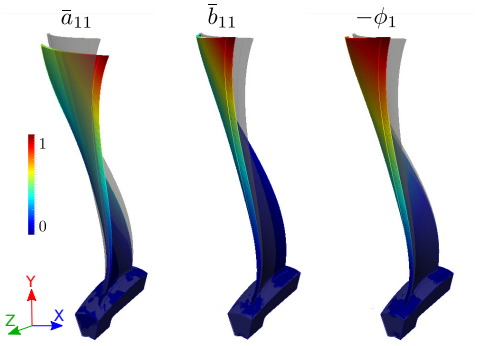
stands that much larger amplitudes needs to be reached in order to observe a remarkable curvature in the backbone curve. Secondly, the B^1_{111} term in the reduced dynamics becomes more important and convey a significant information in order to retrieve the correct hardening/softening behaviour. These remarks underline why reduction methods such as static and implicit condensation cannot catch properly the correct behaviour in this particular case of cantilever structure [68]. Indeed, since these methods neglect velocities and inertia effects in their development, referring to a static manifold instead of the correct invariant manifold, they can retrieve the relaxation on cubic term but will neglect the inertial effect appearing in B^1_{111}, linked to a $R\dot{R}^2$ monomial term. As reported in [127], static modal derivatives also encounter convergence issues with cantilever structures when taking into account two master modes in the ROM.

The computation of the full-order solution also presents some challenges. As known from nonlinear continuation analysis on such complex structures, increasing the number of harmonics can make the solution more and more difficult to achieve since more and more complex internal resonance with numerous loops appears in the backbone. This has also been the case with this fan blade. A full model computed using a harmonic balance continuation method with 5 harmonics has been found unable to achieve moderate amplitudes of vibrations, since the computation was not able to get out of numerous loops of high-order internal resonance occurring at small amplitudes.

For such complex structures with large modal density, it is known that an impressive number of high-order internal resonance are possible creating an intricate web of loops. Internal resonance has already been observed and studied on a reduced order model of a full 3D fan blade [30]. Although the dynamics observed in this paper is interesting, the selected reduced order model is too simple to validate the conclusions. The authors used indeed a reduced-order model based on two linear modes with computation of the quadratic and cubic term using the StEP method.

Also, a number of these loops occur on very short parameter range and are often not robust to *e.g.* addition of damping. It results that they can be interpreted as obstacle for full order simulation of the conservative system with continuation, that are in general not meaningful for the global observable dynamics in forced-damped case. A computation with only 3 harmonics has been able to get rid of this limitation and attains large amplitude by filtering the higher order interactions. Hence this solution will be taken as reference, and is shown in Fig. 5.7, for a vibration amplitude up to 0.18 m. Here the reported amplitude corresponds to the displacement in the x direction, at the point shown in Fig. 5.5a. Given the slenderness of the blade, $0.18m$ vibration amplitude at this point corresponds to $0.267m$ at the leading edge which is indeed a large magnitude with regard to usual applications. In this range, a softening behaviour is reported, in the line of usual results reported in different studies for fan blades, and showing the importance of the quadratic nonlinearity and shell-like behaviour of this structure.

Three different ROMs are built in order to test their ability to recover the backbone of the



Parameter	Value
A^1_{111}	-1.6166e+8
h^1_{111}	+1.6163e+8
$A^1_{111} + h^1_{111}$	-7.2077e+3
$\omega_1^2 B^1_{111}$	+2.6529e+3
$\max(\omega_1^2 \bar{\mathbf{b}}_{11})$	+4.4473e-2
$\min(\bar{\mathbf{a}}_{11})$	-1.4706e-1

Figure 5.6: Second-order correction vector shapes $\bar{\boldsymbol{a}}_{11}$ and $\bar{\boldsymbol{b}}_{11}$ used in the reduction procedure for the first mode of the fan blade ϕ_1. The vector $\bar{\boldsymbol{b}}_{11}$ presents a strong component of the mode ϕ_1, highlighting the important quadratic self-coupling term g^1_{11} due to the curvature. In the table are listed the values of the parameters needed to construct the reduced-order dynamics for the fundamental mode.

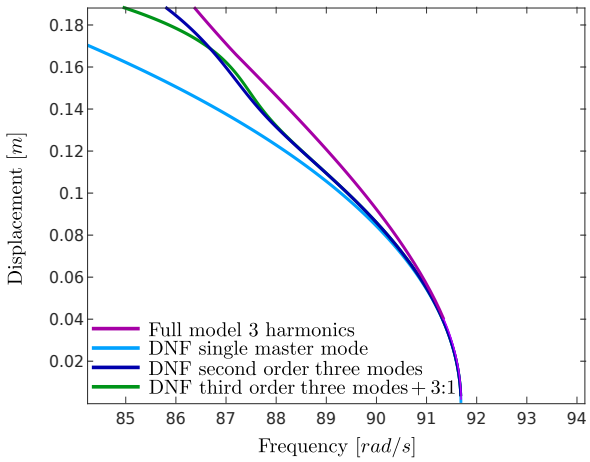


Figure 5.7: Backbone curve of the fundamental mode of the fan blade. Amplitude of vibrations (in m) computed at the node where the force vector is shown, see Fig. 5.5a, and in the same direction x.

reference solution. The first ROM is composed of a single master mode. As shown in Fig. 5.7, it recovers directly the correct softening behaviour, as it could have been expected from previous theoretical derivations [156, 158]. This good prediction is an excellent result since many reduction method encounters difficulties in retrieving such a behaviour [9, 127]. However, one can see that, when vibration amplitude at the forcing point reach values at about 0.1 m, the single NNM solution starts to depart from the reference solution, underlining that a new stiffening effect comes into play and needs to be taken into account in order to obtain a ROM prediction closer to the reference.

As shown in Table 5.2, modes 2 and 3 of the blade have close eigenfrequencies as compared to the first. Also, they are both not far from showing a 3:1 resonance relationship with the first eigenfrequency. Indeed, the ratio are respectively 2.78 and 3.36. Depending on the hardening/softening behaviour of each mode, it is likely that the exact fulfilment of 3:1 resonance might appear at larger amplitudes. Consequently, two other ROMs have been built, including these two additional modes. The first one is thus composed of mas-

ter modes 1, 2 and 3, and uses second-order normal form, while the second one selects the same master modes, but uses third-order normal form with additional resonant terms corresponding to 3:1 resonance relationships. These two ROMs predicts backbone curves that are closer to the reference, showing that the addition of these supplementary modes is meaningful for achieving a correct solution on a larger range of amplitudes. They nevertheless show a slight departure from reference at large amplitude, underlining the fact that the full-order solution is again more complex, with possibly other higher-order resonances appearing.

5.6.3 Frequency-response curve with damping and forcing

In this last section, frequency-response functions (FRFs) are computed including damping and forcing. The two structures of the previous sections, namely the straight beam and the fan blade, are used for illustrative purposes. The aim is to show how one can easily build ROM including damping and forcing from the DNF technique, using the guidelines provided in section 5.4. First the fan blade is used to highlight the efficiency of the damping model proposed, by comparing the results when using only either mass-proportional or stiffness-proportional damping. Then the beam is considered in order to show the behaviour of the FRF when approaching the 3:1 internal resonance, in the case of the second NNM.

Fan Blade

The frequency response curve of the fan blade investigated in section 5.6.2 are computed and a comparison between a full-order simulation and reduced-order models composed of a single master mode using DNF with damping and forcing, is produced. The forcing is harmonic with forcing frequency Ω and magnitude F. It is aligned with the direction x and located at the point shown in Fig. 5.5a, a few centimetres below the tip. To build the ROM, the guidelines provided in section 5.4 are applied. A single master coordinate corresponding to mode 1 is selected. A modal force corresponding to modal projection of the external forcing is added at the right-hand side of the dynamics. A linear damping term, directly deduced from the Rayleigh damping coefficients, is taken into account, as well as the additional nonlinear damping term involving the coefficient C^1_{111}, and aggregating the contributions of the damping factors of the slave modes. In the remainder, comparisons will be drawn out by considering this additional term or not.

In the first case under study, only mass-proportional damping is considered. The amplitude of the forcing is set at $F = 30N$, and the Rayleigh coefficients are such that $\zeta_M = 3 \cdot 10^{-1}$ and $\zeta_K = 0$. In the case of only mass-proportional damping, the modal damping factors reads $\xi_p = \zeta_M / 2\omega_p$, where ξ_p is the nondimensional factor appearing when expressing the linear damping term as $2\xi_p \omega_p \dot{X}_p$. Consequently this damping factor decreases with the frequency, which is not a correct representation of real structures where losses generally increases with frequency. In this specific case, the slave modes are thus less and less

damped and their influence on the master low-frequency mode that is directly excited is awaited to be negligible.

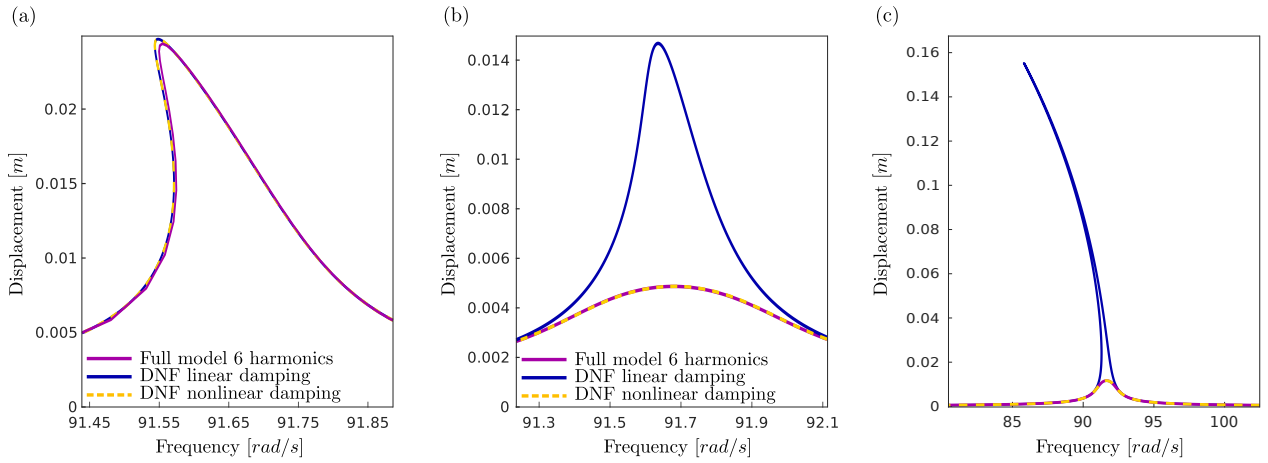


Figure 5.8: Frequency response functions of the fan blade subjected to harmonic forcing in the vicinity of the first bending eigenfrequency. (a) Only mass-proportional Rayleigh damping is taken into account, with $\zeta_M = 3 \cdot 10^{-1}$ and $\zeta_K = 0$. Amplitude of the forcing $F = 30N$. Comparison between full-order model (purple), and ROM composed of a single master mode computed with direct normal form, either with only linear damping term (DNF linear damping, blue curve), or by taking into account the nonlinear aggregated damping term (DNF nonlinear damping, yellow dashed curve). (b) Only stiffness-proportional damping with $\zeta_K = 2 \cdot 10^{-5}$ and $\zeta_M = 0$. Amplitude of forcing $F = 2N$. (c) Only stiffness-proportional damping with $\zeta_K = 10^{-5}$, $\zeta_M = 0$, amplitude of forcing $F = 10N$.

Fig. 5.8(a) shows the FRFs obtained and compares the full-order solution to two different ROMs, one where only the linear damping term $\zeta_M \dot{R}_1$ is taken into account in the ROM (DNF linear damping, blue curve), and another one where the aggregated nonlinear damping term is added (DNF nonlinear damping, dashed yellow curve). In this case the two ROMs reproduce very well the solution of the full-order model, and the difference between the two is negligible, meaning that the aggregated $C^1_{111} R_1^2 \dot{R}_1$ is very small and can be easily neglected. This is the direct consequence of the choice of only mass-proportional damping and the fact that modal damping ratios are decreasing with frequencies.

Fig. 5.8(b) and (c) shows two different cases where only stiffness-proportional damping is selected. This case is much more interesting since it corresponds to a more physically relevant situation. Also, since the modal damping factors are linearly increasing in this case, this means that the damping factors of the slave modes are more and more important, so that neglecting their effect in a ROM would lead to discrepancies. Fig. 5.8(b) shows a case of an important stiffness-proportional damping with $\zeta_K = 2 \cdot 10^{-5}$ and $\zeta_M = 0$. The forcing is set to $F = 2N$. One can now observe a very important difference between the FRFs computed by the two ROMs. Neglecting the aggregated nonlinear damping term leads to important overestimation of the amplitude of the solution in the resonant region. On the other hand, the ROM with the nonlinear damping exactly reproduces the amplitude of the full model, and enforces the structure to vibrate in an almost linear regime as it should be.

Fig. 5.8(c) shows a case with smaller value of damping, $\zeta_K = 10^{-5}$, $\zeta_M = 0$, and larger amplitude of forcing: $F = 10N$. Even in this case the behaviour of the full-order model is almost linear with a small bump close to linear resonance. Interestingly, the prediction given by taking into account only the linear damping term is completely wrong and gives amplitudes that are huge as compared to the reference. This clearly shows that neglecting the damping of the slave modes can lead to erroneous predictions. On the other hand, the nonlinear damping term exactly recovers the correct amplitude and is able to perfectly match the reference solution. These examples shows that even in a system with complex geometry and 3D elements, the proposed ROMs are able to compute with great accuracy the FRF with minimal models.

Straight beam with internal resonance

In this last example, FRFs of the straight clamped-clamped beam considered in section 5.6.1 are considered. The idea is to show how the method behaves in case of internal resonance where there is the need to take into account more than one master coordinate in the ROM. For that purpose, a harmonic forcing in the vicinity of the second eigenfrequency is considered. Two different values of forcing are selected. The first case is that of a small amplitude of forcing, such that the FRF does not enter in the loop of the 3:1 resonance. In this case, only one master mode is awaited to produce a correct prediction. A second case of larger amplitude is then selected so that the FRF enters the resonance loop where 3:1 with mode 4 is excited. In this case, ROMs built from two master coordinates will be selected. In each case the forcing is located at $z = 0.275$ from the clamp as in Fig. 5.1, and excites the beam in the x direction. Finally, only the most interesting case of only stiffness-proportional damping is considered, since it is closer to real situations and give rise to more important differences between models.

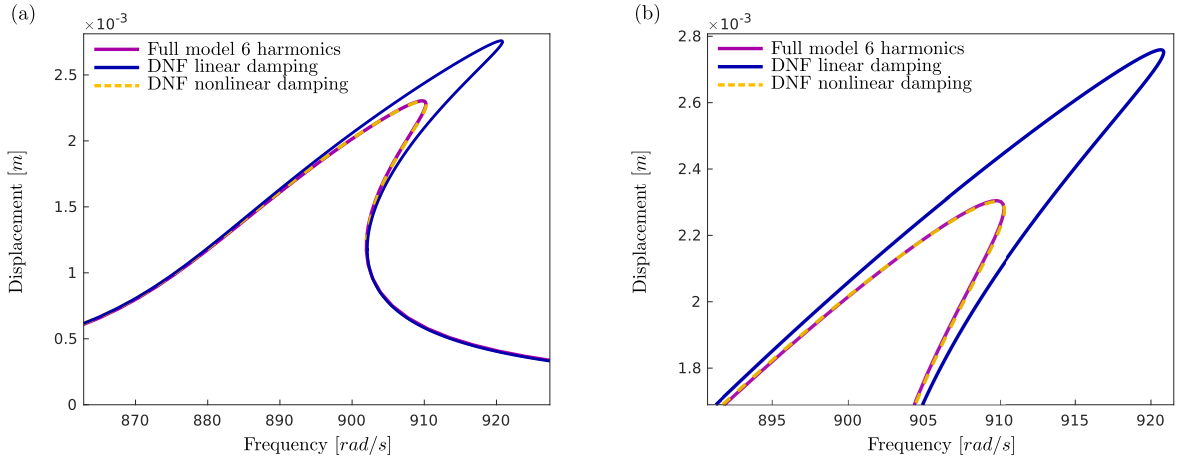


Figure 5.9: (a) Frequency response functions of the clamped-clamped beam subjected to harmonic forcing in the vicinity of the second eigenfrequency. Only stiffness-proportional damping is considered with $\zeta_K = 13 \cdot 10^{-6}$ and $\zeta_M = 0$. Amplitude of the forcing $F = 10N$. Full-order solution is compared to ROMs obtained with a single master coordinate (mode 2), with only linear damping term (blue curve) and with additional nonlinear damping term (dashed yellow curve). (b) close-up view near the maximum amplitude.

Fig. 5.9 shows the results obtained when selecting $\zeta_K = 13 \cdot 10^{-6}$ and $F = 10N$, such that the FRF is below the internal resonance loop. The reference solution is obtained by taking into account 6 harmonics in the expansion. Two different ROMs are contrasted, both containing a single master coordinate corresponding to mode 2, and one with only the linear damping term while the second one takes into account the additional nonlinear damping term. As in the previous case, the difference between the two ROMs are important and taking into account the nonlinear damping term is very important in order to correctly predict the maximum amplitude of the FRF.

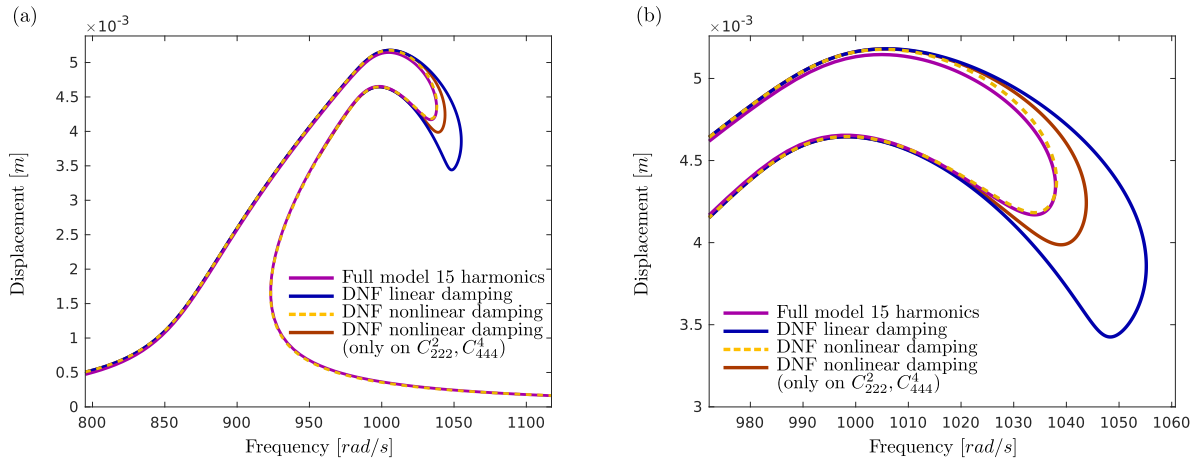


Figure 5.10: (a) Frequency response functions of the clamped-clamped beam subjected to harmonic forcing in the vicinity of the second eigenfrequency. Stiffness-proportional damping is considered with $\zeta_K = 3 \cdot 10^{-7}$ and $\zeta_M = 0$. Amplitude of the forcing $F = 30N$. Full-order solution is compared to different ROMs obtained with a two master coordinates corresponding to modes 2 and 4. Reference solution obtained with 15 harmonics (purple). All the ROMs are obtained with two modes and second-order normal form. Blue curve: only linear damping term considered. Yellow dashed curve: full consideration of nonlinear damping including cross-coupling terms. Brown curve: nonlinear damping neglecting the cross-couplings. (b) close-up view in the 3:1 resonance loop.

Fig. 5.10 now considers the case of a smaller damping coefficient $\zeta_K = 3E-7$ and a larger amplitude of forcing $F = 30N$. The reference solution now enters the loop so that the 3:1 internal resonance with mode 4 is activated. Consequently, the reference solution has been computed with a larger number of harmonics (15), in order to achieve convergence. Three different ROMs are compared, all of them being built with two master coordinates corresponding to modes 2 and 4, and second-order normal form. The first ROM contains only the linear viscous damping term. Since the underlying conservative system with second-order normal form is able to perfectly well reproduce the resonance loop of the 3:1 resonance, this solution also shows this typical feature, highlighting that the dynamics is more complex and involves more than one mode. However, the damping is not important enough, so that a slight departure is observed from the reference solution. A second ROM is built by adding nonlinear damping terms, following Eq. (5.54). However a simplification is introduced. In the summation terms involving C^p_{ijk} terms, only the self-nonlinear damping terms C^p_{ppp} are considered. This means that only two terms have been added to the reduced dynamics: $C^2_{222}R^2_2\dot{R}_2$ for the equation of mode 2 (first master coordinate) and $C^4_{444}R^2_4\dot{R}_4$ for

the equation of mode 4 (second master coordinate). The cross-coupling nonlinear damping terms involving C^p_{ijk} with different indexes have been discarded. In this case, one can observe a better behaviour as compared to the linear case, meaning that the two added terms convey important information on the damping of the slave modes, that cannot be neglected. However the result is still a bit different from the reference solution.

Finally a ROM with two modes and considering all the nonlinear damping terms including the cross-couplings one, is reproduced in Fig. 5.10, and shows an almost perfect comparison with the reference. This example shows that these cross-coupling terms also convey an important information, needed in order to reproduce with great accuracy the FRF.

5.7 Conclusions

A nonlinear mapping for the derivation of reduced-order models for geometrically nonlinear structures discretised by the FE method, has been presented. It relies on the normal form theory and presents a firm theoretical background in order to cope with nonlinear dynamics phenomena such as internal resonance. The method allows for a direct computation of the normal form, from a FE discretisation. Computational details are provided and a full algorithm has been presented with related discussion on the non-intrusiveness of the method and coding advice for practical implementation. In essence, the technique allows one to go from the physical space (nodes of the FE structure given by the original mesh) to an invariant-based span of the phase space, with a third-order approximation of the invariant manifolds (nonlinear normal modes) of the structure. It is a simulation-free method that directly computes the third-order approximation of the reduced dynamics, with no restriction on the number of selected master modes.

The main developments have been proposed for a correct estimation of the nonlinear force of the ROM, *i.e.* in a conservative framework. Two declinations of the method have been proposed: a second-order normal form and a third-order mapping, with, in each case, the associated reduced dynamics. The second-order normal form proposes a quadratic mapping approximating the underlying invariant manifold up to the second-order only. Consequently, the reduced dynamics (up to order three) contains all possible third- and higher-order internal resonances embedded, and has no quadratic nonlinearity if no second-order internal resonance are present. The third-order normal form distinguishes the trivial and non-trivial resonant terms. The main improvement consists in offering a better approximation of the invariant manifolds, and a more simplified reduced dynamics with only trivially resonant monomial cubic terms included. On the other hand, the reduced dynamics contains less terms since the higher-orders have been neglected. Consequently the dynamical solutions of the second-order DNF can produced more accurate results as highlighted in the examples.

A methodology has been proposed in order to take into account external forcing and damping in the ROM so as to produce frequency-response functions (FRF). For the damping,

the proposed technique relies on a first-order approximation of the general result derived in [154]. It has been rewritten for Rayleigh damping law, the most commonly retained assumption to model losses in FE context. The main interest relies in proposing an aggregated damping force on the reduced dynamics, taking into account the losses of all the slave (neglected) modes. In the present version, the general formulas for taking properly into account the damping have been given only for the second-order DNF.

The method has been applied to a clamped-clamped beam and a FE model of a fan blade. Backbone curves have been extracted and discussed. In particular, as known from previous studies on normal form for model order reduction, the method predicts directly the correct hardening/softening behaviour. Also, in the beam case, it has been shown that the ROM can recover internal resonance loops due to the fulfilment of an exact commensurability of nonlinear frequencies. FRF have been computed, underlining the importance of the added, aggregated damping, as well as the very good match between full and reduced models.

Future work will apply the methodology to different structures having also internal resonance between eigenfrequencies of the system, in order to test the predictions of the ROM with an increasing number of master modes. Improvements of the method can also be investigated. For example higher-order reduced dynamics can be computed by pushing the normal form up to order five for better accuracy. Taking into account the full damped version of the normal form as developed in [154] could also be helpful. Finally, different internal forces could also be taken into account by enlarging the application field to *e.g.* gyroscopic forces, electrostatic forces (for MEMs applications), non conservative follower forces (for fluid-structure interaction problems) or piezoelectric couplings.

Chapter 6

Structures with clearance nonlinearity

The main focus of this chapter is the application of nonlinear modal analysis to blade-casing interaction problems. From a phenomenological point of view, the main focus of blade-casing interaction analysis is the blade vibration. Unlike rotor stator interaction studies, in blade-casing interaction the disk and the shaft are treated as perfectly rigid bodies and only the blade possesses flexibility. In this way, the dynamics of the whole stage is fully represented by the dynamics of the single blade. To study this problem, many different approaches are possible. A vast amount of literature in this field has been produced by joint works between Snecma and the Structural Dynamics and Vibration Laboratory of McGill University in recent years [11, 80, 95, 132]. In their work, time integration is used to predict resonances in presence of contact and usually a distorted casing is used to force the system. In Fig. 6.1, the situation where a distorted casing interacts with a blade is depicted. If the amount of distortion overcomes the clearance between the casing and the blade, a forcing term whose frequency is proportional to the rotational frequency will act on the blade exciting its vibratory motion. If the frequency of the excitation is tuned to a blade's natural frequency, a resonance may occur leading to high amplitude vibration.

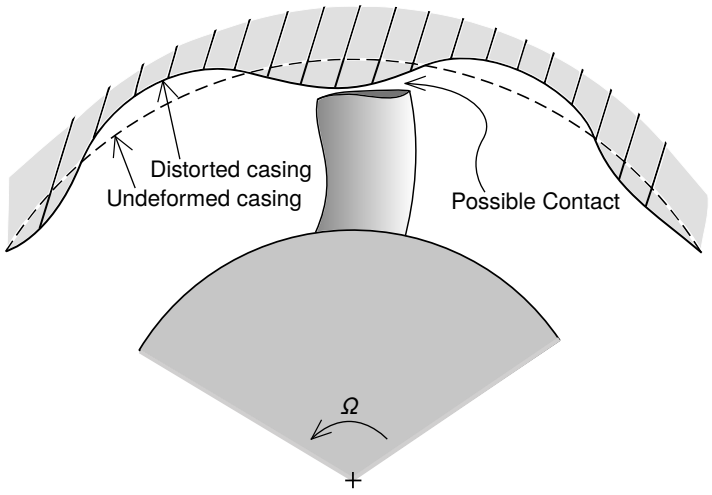


Figure 6.1: Rubbing between single blade and elastic casing

To model the contact between the blade and the rigid casing, a distinction between coated

and bare casing has to be made. In the first case, the abradable material is taken into account in the model and its elastic behaviour modelled as a spring in the normal direction [115, 117, 130]. in the second case, the casing surface is treated as an infinitely rigid wall that give rise to an impact when the first contact occur [11, 80, 132]. If the surface is elastic and responds to the structure as an elastic spring, the nonlinearity at the contact boundary is often called *clearance* nonlinearity. In fact the nonlinear force is only activated once the clearance between the structure and the surface is reached, otherwise the structure is linear. In the second case the surface is impenetrable and at the time instant of the first contact, when the impact occurs, the velocity of the structure at the contact boundary has a non-smooth variation depending on the coefficient of restitution of the contact surface. In the first case the nonlinear force is piecewise linear whereas in the second is non-smooth. Despite being consumed by the blade rubbing, the abradable material is never completely worn out therefore the bare casing condition should be considered as an extremely rare event.

In the studies where time integration is applied to analyse blade-casing interactions, the abradable material is usually modelled with an elasto-plastic law and the amount of worn material taken into account in the simulation [14, 81, 124, 174]. The evolution of the wear in time and the wear-patterns can be then studied to better understand the blade behaviour. Methods for the periodic solution are instead not capable of accounting for the wear because only the steady state solution is computed. A method to account for slow variations such as the ones produced by wear in a periodic framework has been proposed by Salles [128]. In [128], two different time scales were adopted, a fast one for the vibration cycle and a slow one for the effects of wear. Another attempt to account for wear in a periodic framework consist in the machining analogy. The idea that the mechanism underlying a blade rubbing an abradable material is assimilable to the machining of a cutting tool has been exploited by two different studies pursued by Salvat [131] and Olgac [105]. Although having been developed separately, both treated the rub problem as a machining problem and applied delay differential equations to predict self-excited vibration in the system, namely the chatter instability. The main weakness of this approach lies in the assumption of permanent contact between the blade and the abradable. Although convenient from a computational point of view, because it renders the system linear, this assumption is not physical in the majority of the cases because the blade will always have a free flight phase during its vibration cycle. The increased accuracy of the method gained by the inclusion of wear, is then diminished by the invalidity of its underlying assumption. The effects of wear on the dynamics are outside the scope of this work therefore will not be included in the following.

Here the normal response of the abradable will be treated as a linear spring in the normal direction of the contact (cfr. [117, 129]). However, the abradable material has also a tangential response, not only due to the resistance of the material to shear, which is usually very low, but also due to wear. In fact, when a small portion of abradable material is worn by the blade, its kinetic energy suddenly increase from zero to a value proportional to its

mass and the square of the tip velocity, thus exerting a tangential reaction force on the tip referred to as wipeout force in [174]. This reaction force is linearly proportional to the incursion; moreover it is always directed in the direction opposite to the tip motion, because at the tip, the component of velocity of the rotational motion is usually much higher than that of the vibratory motion. In this work, a linear dependence of the tangential force from the normal force will be assumed, with a coefficient of proportionality that will be simply referred to as a generalised friction coefficient. A contact condition of this kind is usually used in brake squeal problems [44, 46, 47, 51, 72, 82]. In brake squeal, the relative velocity between the two surfaces in contact is also much higher than the velocity attained by the component's vibration, and the friction force can be then assumed to be unidirectional. Friction induced vibrations can then be observed as a results of a mode coupling instability [51]. In this chapter, the analogy between brake squeal and tip rub will be investigated and the possibility for friction induced vibration to occur in blades studied. Similarly to the previously mentioned machining analogy, also in the treatment of brake squeal problems the contact is assumed to be permanent. In fact the brake pad is normally pushed against the disk with a great force; the linear eigenvalues analysis that is performed to identify possible instabilities in the brake, is done around the equilibrium conditions attained after the application of the said force. This prestress can be seen as a negative clearance that does not allow the disc to come out of contact. The application of the same strategy to the problem of blade casing interaction will be then flawed if the permanent contact assumption would not be removed. In this chapter, the analogy with brake squeal problems will be exploited but the permanent contact assumption removed; it will be shown that friction induced vibration not only occur in the negative clearance system but also in the positive clearance one, in the form of an isolated branch of periodic solutions.

The range of possible strategies to tackle blade casing interaction problems is incredibly vast and various. The interested reader is referred to two comprehensive literature surveys on blade-casing interaction and rotor-stator interaction phenomena [54, 89]. Here the main focus will be on nonlinear modal analysis and reduced order modelling methods. The aim is to provide a perspective on computationally fast tools that, despite relying on simplifying assumptions, can provide with important insights on the problem. As mentioned, the contact between the blade and the casing is rarely direct because the abradable material acts as an elastic spring in the direction of the incursion. However, the normal stiffness of the abradable material greatly varies depending on the operating conditions such as temperature, incursion rate, tangential velocity. As for the tangential components, they are very difficult to quantify too, because of their variability with respect to the operating conditions [16, 33, 146]. For this reason, in the preliminary stage design of blades, methods able to compute a wide range of possible stiffness values in a short computational time are to be preferred over time integration.

In the context of clearance nonlinearity, several methods to discretise the time have been used in the literature as an alternative to harmonic balance method, *i.e.* collocation [31, 63], shooting [121, 134], wavelet method [61]. In fact, when applying harmonic balance method,

if the stiffness of the contact surface is very high, a high number of harmonics is needed because of the sharp variations in the contact force thus reducing the advantages of the method. In Section 6.2, a comparison between harmonic balance method and finite element time method on a conservative system with purely normal contact is drawn and their accuracy is tested with different contact stiffness values.

The introduction of the generalised friction coefficient renders the system non-conservative and, depending on the phase of the vibratory motion at which the interaction occurs, it can either provide or take energy from the structure. The classical modal analysis can then no longer be applied and the so called extended periodic motion concept [71], introduced in Sec. 2.5.4 has to be adopted to find a steady state for the system. Dissipative frictional systems are a classical application of the extended periodic concept [71, 147]; here, this approach is instead used to detect self-sustained vibrations and to calculate the post flutter limit cycles of the self-excited system.

In terms of reduced order modelling for frictional contact nonlinearities, the Hurty/Craig-Bampton method is the standard method for such problems [13, 116]. However, in the context of nonlinear modal analysis, when the backbone curve of a particular mode is targeted and if this mode is a relatively high frequency one, the number of internal modes to be retained into the reduced model increases with the frequency of the targeted mode. Being the nonlinear forces piecewise smooth, the reduction methods presented in the previous chapters do not apply to this type of nonlinearity because their derivation is obtained in an asymptotic manner since geometric nonlinearities are polynomials. An adaptation of modal derivatives to contact problems can be found in [118, 175] where the trial vectors derivatives are proposed. The so called trial vector derivatives can be seen as an extension of modal derivatives for contact and friction problems but to the author's knowledge, not much literature apart from [118, 175] is present. In Section 6.3, a method inspired by the direct normal form method derived in the previous chapter, is adapted to the case of soft contact nonlinearities and its accuracy assessed.

6.1 Problem statement

As detailed in Chapter 2, the equation of motion of a system with contact nonlinearities reads:

$$\boldsymbol{M}\ddot{\boldsymbol{U}} + \boldsymbol{C}\dot{\boldsymbol{U}} + \boldsymbol{K}\boldsymbol{U} = \boldsymbol{F}_{\text{ext}} + \boldsymbol{T}_C(\boldsymbol{U}_C, \dot{\boldsymbol{U}}_C) \tag{6.1}$$

where, in the nonlinear force vector $\boldsymbol{T}_C$, all contact forces are included. When the structure is discretised with finite elements, the contact forces only affect the nodes at the contact boundary and they only depend on the displacement and velocity of the said nodes. One can define, for each of these nodes, a vector of length N that picks the normal degree of freedom needed to discriminate if the p-th node is in contact or not:

$$\boldsymbol{B}_n^{(p)} = \left\{0, \dots, \boldsymbol{e}_n^{(p)}, \dots, 0\right\}^{\mathrm{T}} \tag{6.2}$$

where $\boldsymbol{B}_n^{(p)}$ the normal contact vector relative to the k-th node is a vector with all zeros except for the entries relative to the three degrees of freedom of the p-th node for which it is equal to the normal unitary vector $\boldsymbol{e}_n^{(p)}$. Similarly one could define a tangential contact vector for each contact node, that picks the direction of the friction force based on the direction of the relative sliding velocity:

$$\boldsymbol{B}_t^{(p)} = \left\{0, \dots, \boldsymbol{e}_t^{(p)}, \dots, 0\right\}^{\mathrm{T}} \tag{6.3}$$

In case of regularised contact, the normal contact forces act as a unilateral spring of stiffness $k_\epsilon^{(p)}$ and at each node the clearance $g^{(p)}(t)$ defines the distance between the node and the contact surface. The vector of normal contact forces for a given node will then read:

$$\boldsymbol{T}_{C,n}^{(p)} = -\boldsymbol{B}_n^{(p)}\, k_\epsilon^{(p)}\, \max\left(0, (\boldsymbol{B}_n^{(p)})^{\mathrm{T}}\boldsymbol{U} - g^{(p)}\right) \tag{6.4}$$

Here, the normal contact force is assumed to be in the form of a unilateral spring, hence no dissipation is assumed to occur in the normal direction. This choice is motivated by simplicity reasons. In fact, if a viscous damping term was to be included as a unilateral Kelvin-Voigt element, a discontinuity in the normal force would be observed and also an non-physical pulling force during the detaching velocity phase; in [52], a modification to the classical Kelvin-Voigt element is proposed, which involves a polynomial expression for the damping term. This approach is considered unnecessary in that, not only it would complicate the numerical implementation, but it would also enlarge the parameter space with another value, the damping parameter, whose identification is non trivial. For the sake of simplicity is thus assumed here that the normal contact force is purely elastic.

As for the tangential component, if the contact surface is sliding in a given direction and if its speed is much higher than that attained by the structure due to vibration, a condition of permanent sliding will be undergone when the structure comes into contact. This condition is of particular interest in this work; in fact, in the rotational frame, the casing can be seen as an elastic surface moving in the tangential direction with a velocity proportional to the rotational speed and to the radius of the casing. As mentioned at the beginning of this chapter, the velocity of the blade in the rotational frame, being purely due to the blade vibration, is consistently smaller than the velocity of the casing, meaning that the relative velocity of the rubbings can be approximated with the sole rotational component and the vibratory one neglected. In this way, the tangential contact forces become dependent from the state only through the linear dependence from the incursion. The response of the casing can be then seen simplified as a frictional response with generalised friction coefficient $\mu^{(p)}$ that takes into account the wipeout forces, and a velocity always directed along $\boldsymbol{e}_p^{(t)}$. The vector of tangential contact forces for a given node will read:

$$\boldsymbol{T}_{C,t}^{(p)} = -\boldsymbol{B}_t^{(p)}\, \mu^{(p)}\, k_\epsilon^{(p)}\, \max\left(0, (\boldsymbol{B}_n^{(p)})^{\mathrm{T}}\boldsymbol{U} - g^{(p)}\right) \tag{6.5}$$

where the condition of permanent sliding implies that the friction force is equal to the normal force multiplied by the friction coefficient.

The equation of motion will then read:

$$\boldsymbol{M}\ddot{\boldsymbol{U}} + \boldsymbol{C}\dot{\boldsymbol{U}} + \boldsymbol{K}\boldsymbol{U} = \boldsymbol{F}_{\text{ext}} - \sum_{p \in \Sigma_C} \left(\boldsymbol{B}_n^{(p)} + \boldsymbol{B}_t^{(p)}\, \mu^{(p)} \right) k_\epsilon^{(p)}\, \max\left(0, (\boldsymbol{B}_n^{(p)})^{\mathrm{T}} \boldsymbol{U} - g^{(p)}\right) \quad (6.6)$$

To simplify the problem, let us assume that only one node of the structure belongs to the contact boundary and can therefore come into contact with the elastic contact surface. If one defines the contact stiffness matrix as:

$$\boldsymbol{K}_C = (\boldsymbol{B}_n + \boldsymbol{B}_t\, \mu)\, k_\epsilon (\boldsymbol{B}_n)^{\mathrm{T}} \quad (6.7)$$

and the forcing-like term due to the clearance as:

$$\boldsymbol{G}_C = (\boldsymbol{B}_n + \boldsymbol{B}_t\, \mu)\, k_\epsilon\, g \quad (6.8)$$

The system of Eq. (6.4) can be written as:

$$\begin{cases} \boldsymbol{M}\ddot{\boldsymbol{U}} + \boldsymbol{C}\dot{\boldsymbol{U}} + (\boldsymbol{K} + \boldsymbol{K}_C)\, \boldsymbol{U} = \boldsymbol{F}_{\text{ext}} + \boldsymbol{G}_C & \text{if } (\boldsymbol{B}_n)^{\mathrm{T}} \boldsymbol{U} > g \\ \boldsymbol{M}\ddot{\boldsymbol{U}} + \boldsymbol{C}\dot{\boldsymbol{U}} + \boldsymbol{K}\boldsymbol{U} = \boldsymbol{F}_{\text{ext}} & \text{if } (\boldsymbol{B}_n)^{\mathrm{T}} \boldsymbol{U} \leq g \end{cases} \quad (6.9)$$

In Eq. (6.9), both $\boldsymbol{F}_{\text{ext}}$ and $\boldsymbol{G}_C$ have an explicit dependence on time. In particular, if the forcing is imposed as a casing distortion, the value of $g(t)$ will be equal to a constant term g_0 denoting the constant clearance of the system, plus a fluctuating term $d(t)$ representing the periodic distortion. When the amplitude of $d(t)$ overcomes g_0, the contact surface interferes with the equilibrium position of the contact node, thus initiating the contact.

The autonomous system can be then written by assuming no external forcing and no distortion and reads:

$$\begin{cases} \boldsymbol{M}\ddot{\boldsymbol{U}} + \boldsymbol{C}\dot{\boldsymbol{U}} + (\boldsymbol{K} + \boldsymbol{K}_C)\, \boldsymbol{U} = \boldsymbol{G}_{C,0} & \text{if } \boldsymbol{B}_n^{\mathrm{T}} \boldsymbol{U} > g_0 \\ \boldsymbol{M}\ddot{\boldsymbol{U}} + \boldsymbol{C}\dot{\boldsymbol{U}} + \boldsymbol{K}\boldsymbol{U} = \boldsymbol{0} & \text{if } \boldsymbol{B}_n^{\mathrm{T}} \boldsymbol{U} \leq g_0 \end{cases} \quad (6.10)$$

If the clearance is positive $g_0 > 0$, the zero vector is an equilibrium position for the system and the eigenvalues of the linearised system around the equilibrium coincide with those of the linear system without contact. If the clearance is negative, the equilibrium position is instead:

$$\boldsymbol{U}_{\text{eq}} = (\boldsymbol{K} + \boldsymbol{K}_C)^{-1}\, \boldsymbol{G}_{C,0} \quad (6.11)$$

The equation for small oscillations around the equilibrium position in the case of negative clearance reads:

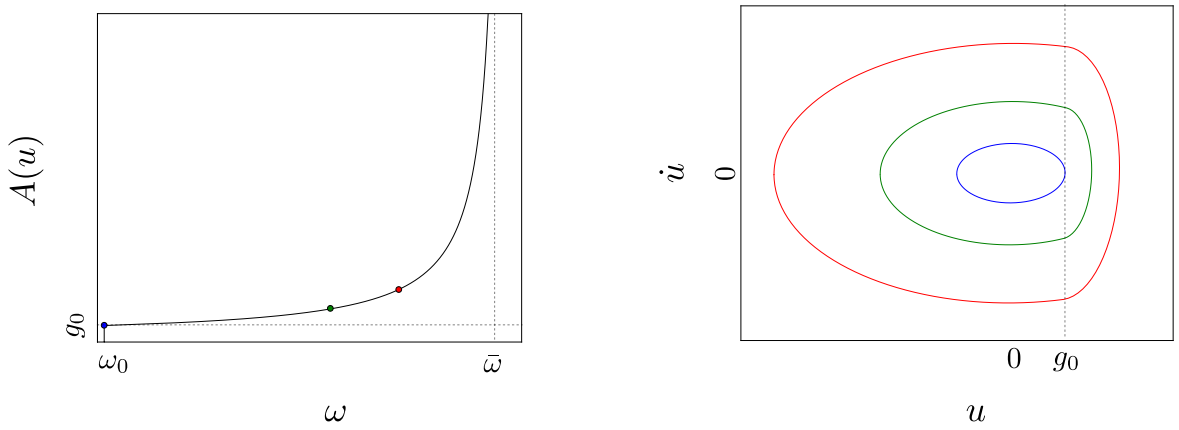
$$\boldsymbol{M}\delta\ddot{\boldsymbol{U}} + \boldsymbol{C}\delta\dot{\boldsymbol{U}} + (\boldsymbol{K} + \boldsymbol{K}_C)\, \delta\boldsymbol{U} = \boldsymbol{0} \quad (6.12)$$

where the perturbation $\delta \boldsymbol{U} = \boldsymbol{U} - \boldsymbol{U}_{\text{eq}}$ is used. In the case of negative clearance, the eigenvalues of the system linearised around the equilibrium are those obtained by adding the contact stiffness matrix $\boldsymbol{K}_C$ to the system. If friction is taken into account, this matrix is no longer symmetric, and negative damping can be observed. This case will be thoroughly discussed in Sec. 6.4.

The case of clearance equal to zero does not allow to linearise the system because the system is nonlinear at any amplitude and its jacobian not uniquely defined. The solution at zero gap though, is very important because in the conservative case, it represents an asymptote for both negative and positive clearance systems when the amplitude of the oscillations along a nonlinear mode tend to infinity. To show this behaviour, let us consider the case of a single oscillator, with purely normal contact. The conservative system reads:

$$\begin{cases} m\ddot{u} + ku + k_\epsilon u = g_0 & \text{if } u > g_0 \\ m\ddot{u} + ku = 0 & \text{if } u \leq g_0 \end{cases} \tag{6.13}$$

Treating the two conditions as two different linear systems, one can see that the natural frequency of the open system is $\omega_0 = \sqrt{k/m}$ whereas the natural frequency of the closed gap system is $\omega_\epsilon = \sqrt{(k + k_\epsilon)/m}$. The solution of the system with positive clearance is depicted in Fig 6.2. For small oscillations around the zero equilibrium position the system is linear and its natural frequency is ω_0. As soon as the amplitude of the linear oscillations reaches the value of the clearance g_0 the solution is split into a contact phase and a free flight phase. The higher the amplitude, the longer the portion of the period of the contact phase; since the value of k_ϵ is strictly positive, a longer contact phase results in a stiffening effect, that increases the nonlinear frequency. However, said stiffening effect does not increases the nonlinear frequency indefinitely, like one would observe in a Duffing oscillator; instead the nonlinear frequency reaches an asymptotic value of $\bar{\omega}$ when the amplitude tends to infinity.



(a) Frequency amplitude curve.

(b) Orbits at different amplitude.

Figure 6.2: Nonlinear mode of the single oscillator with clearance nonlinearity.

The value of this asymptotic frequency can be easily evaluated in the case of a single

oscillator in that it coincides with the nonlinear frequency of the system with zero clearance. In such system, neither stiffening nor softening effect would be observed because each orbit will have the same shape and only differs in the amplitude. The following expression is a solution of the zero clearance system for every value of A:

$$\begin{cases} u(t) = A\sin(\omega_0 t) & \text{if } t \in (0, \frac{\pi}{\omega_0}) \\ u(t) = -A\frac{\omega_0}{\omega_\epsilon}\sin(\omega_\epsilon(t - \frac{\pi}{\omega_0})) & \text{if } t \in (\frac{\pi}{\omega_0}, \frac{\pi}{\omega_0} + \frac{\pi}{\omega_\epsilon}) \end{cases} \tag{6.14}$$

Such solution is continuous in displacement, velocity and acceleration and it is periodic with period $T = \frac{\pi}{\omega_0} + \frac{\pi}{\omega_\epsilon}$. Thus, we can finally derive the final expression for the nonlinear asymptotic frequency $\bar{\omega}$ that reads:

$$\frac{2\pi}{\bar{\omega}} = \frac{\pi}{\omega_0} + \frac{\pi}{\omega_\epsilon} \tag{6.15}$$

By defining $\beta_\epsilon = k_\epsilon/k$ as the ratio between the open system stiffness and the contact one, the ratio between the asymptotic nonlinear frequency and the open system one reads:

$$\frac{\bar{\omega}}{\omega_0} = \frac{2\sqrt{1+\beta_\epsilon}}{1+\sqrt{1+\beta_\epsilon}} \tag{6.16}$$

From this last expression it is possible to see that the ratio between the asymptotic frequency and the open system one only depends on β_ϵ. For $\beta_\epsilon = 0$ the asymptotic frequency coincides with ω_0 and for $\beta_\epsilon \to \infty$ the asymptotic frequency coincides with $2\,\omega_0$.

These considerations are important in the context of blade casing interaction because they provide insights on the problem. Firstly, the range of variation of the nonlinear frequency is bounded. Even if only a one degree of freedom system has been shown, multiple dofs systems possess the same behaviour in presence of clearance nonlinearities. Therefore the resonances cannot occur outside the frequency range. Secondly, even in the case of infinitely hard contact, the value of the asymptotic nonlinear frequency cannot exceed twice the frequency of the open system. Lastly, the only parameter that defines the asymptotic nonlinear frequency is the ratio β_ϵ between the contact stiffness and the system's one. In a multiple dofs system, the low frequency modes will then be more affected by the contact than the high frequency ones because the stiffness of the former is lower than that of the latter. Even if this rule holds in general, in multiple dofs systems the identification of β_ϵ is not straightforward because it also depends on the shape of the modes other than their frequency. In fact, all the modes are coupled by the contact and one cannot simply find a direct link between the modes of the open system and those of the closed one. This concept will be further expanded in Sec. 6.3 in the framework of reduced order modelling. Before moving to the case of multiple dofs systems, a comparison between two time discretisation methods is drawn on a single oscillator testcase with a clearance nonlinearity.

6.2 Comparison of time discretisation methods

In this section the accuracy of the harmonic balance method will be investigated and compared to the time finite element method.

6.2.1 Solution with harmonic balance method

Recalling the derivation of the harmonic balance method provided in Chapter 2, the displacement can be decomposed into a series of trigonometric functions as:

$$\boldsymbol{U}(t) = (\boldsymbol{Q}(t) \otimes \boldsymbol{I}_N)\mathbb{U} \tag{6.17}$$

with the inverse Fourier transform vector defined as:

$$\boldsymbol{Q}(t) = \left\{1 \quad \cos(\Omega t) \quad \sin(\Omega t) \quad \dots \quad \cos(H\Omega t) \quad \sin(H\Omega t)\right\} \tag{6.18}$$

As anticipated in Chapter 2, an alternating frequency time procedure is necessary to compute the nonlinear forces in case of clearance nonlinearities. To do so, a discretisation of the time into a series of steps, often called AFT points, permits to calculate the nonlinear forces numerically. Discretising the period into a series of equally spaced n time steps t_i, with $t_0 = 0$ and $t_n = T$ and recalling Eq. (2.127), the numerical discretisation of the integral on the right hand side takes the form:

$$\mathbb{A}\mathbb{U} - \mathbb{F}_{\text{ext}} = \sum_{i=1}^{n} \frac{T}{n} (\boldsymbol{Q}^{\text{T}}(t_i) \otimes \boldsymbol{I}_N)\boldsymbol{F}_{\text{NL}}((\boldsymbol{Q}(t_i) \otimes \boldsymbol{I}_N)\mathbb{U}) \tag{6.19}$$

where the left hand side, representing the linear part of the residual, is left unchanged.

Normally the number of time steps n is chosen to be much higher than the number of time shape functions $2H + 1$ given by the harmonic balance method. The majority of continuation codes available (Auto, Manlab) cannot deal with piecewise smooth nonlinear functions, so in order to solve clearance nonlinearity problems, a regularisation is usually required [27] and the nonlinear force is expressed in terms of $\mathcal{C}^\infty$ functions. In this work, the nonlinear force is treated in its piecewise smooth form hence the nonlinear force is a $\mathcal{C}^0$ function. Due to the discontinuity in its derivative with respect to time, the discretisation of the force with harmonic functions generates non-physical oscillations around the discontinuity known as Gibbs phenomenon [180]. In reality, these spurious oscillations are only visible if the reconstructed solution obtained with the inverse discrete Fourier transform is performed using a number of time steps n much higher than the number of trigonometric shape functions $2H + 1$. Potentially, if one sets $n = 2H + 1$ such as the inverse discrete Fourier transform matrix is a square matrix, the Gibbs phenomenon will not be present in the solution. Obviously if the number of harmonics is low, a square inverse discrete Fourier transform matrix would produce a very coarse time mesh on the period, which is why in

the general case of smooth nonlinear forces $n \gg 2H+1$. However, when treating piecewise smooth nonlinearities the number of harmonics required to achieve a good approximation of the forces is very high, and it has to be chosen according to the stiffness of the contact surface k_ϵ. These considerations will be better detailed in the course of this chapter and a study on the effect of the number of AFT points will be shown.

6.2.2 Presentation of time finite element method

The idea behind the time finite element method is to discretise the time with shape functions whose domain is equal to one time element and then enforce the periodic motion by enforcing the periodicity of the discretisation. The high number of harmonics required when applying the harmonic balance method to stiff problems has led many researchers to investigate whether other methods could be more efficient. Shooting method ([121, 134]), collocation method [63], wavelet method [61], have been tested and compared to harmonic balance method in the case of stiff nonlinearities. In this work, we investigate the capabilities of time finite element method and compared them with those of harmonic balance method for the problem of clearance nonlinearity. The reason for this choice lies in the very good performances that the time finite element method showed when applied to stiff problems. In [171] higher order shape functions produced very accurate results when applied to clearance nonlinearities; moreover in the study from Meingast [91] it is shown how the method performs better than HBM and collocation when applied on a non-smooth system with impact and when coupled with Lemke's algorithm. Its suitability to impacts problems has also been demonstrated in the context of time stepping schemes by Capobianco [25].

Time finite element method ([20, 21, 49, 50]) is a Galerkin method in which the trial and weighting functions are polynomial shape functions whose domain of existence is limited to one element of the discretised period of interest. It can be applied to a general time boundary value problem, not necessarily periodic, as long as the boundary condition at $t_0 = 0$ and $t_n = T$ are known.

The method is based on a weak form of Hamilton's law of varying action, known as Hamilton's Weak Principle:

$$\int_0^{t_F} \delta\mathcal{L} dt + \int_0^{t_F} \delta\mathcal{W} dt = \left[\delta \boldsymbol{q}^T \frac{\delta \mathcal{L}}{\delta \dot{\boldsymbol{q}}}\right]_0^T \tag{6.20}$$

with $\mathcal{L}$ lagrangian of the system, $\delta\mathcal{W}$ work of the non conservative forces and the term on the right hand side, flux of energy entering the boundary of the time period. For a generic dynamical system, (6.20) can be written as:

$$\int_0^T \delta \boldsymbol{U}(t)^T \left(-\boldsymbol{M}\ddot{\boldsymbol{U}} - \boldsymbol{C}\dot{\boldsymbol{U}} - \boldsymbol{K}\boldsymbol{U} + \boldsymbol{F}_{\text{ext}} + \boldsymbol{F}_{\text{NL}}(\boldsymbol{U})\right) dt = \left[\delta \boldsymbol{U}^{\text{T}} \left(\boldsymbol{p} - \boldsymbol{M}\dot{\boldsymbol{U}}\right)\right]_0^T \tag{6.21}$$

where $\boldsymbol{p}$ is the vector of generalised momenta $\boldsymbol{p} = \boldsymbol{M}\dot{\boldsymbol{U}}$ imposed as a boundary condition. The term on the RHS of 6.21 is analytically equivalent to zero but it can differ from zero numerically; the numerical solution of (6.21) can be seen in this perspective as the the

solution of the equations of motion plus the natural enforcing of the boundary conditions on the velocity.

Let us discretise the period of time with n equally spaced elements and let us assume the trial and weighting functions $W_i(t)$ to be standard linear hat functions:

$$\boldsymbol{U}(t) = \sum_{i=0}^{n} W_i(t)\hat{\mathbb{U}}_i = (\boldsymbol{W}(t) \otimes \boldsymbol{I}_N)\,\hat{\mathbb{U}}\,. \tag{6.22}$$

By plugging Eq. (6.22) into Eq. (6.21), the weak formulation of the problem is the system of $N \times n + 1$ algebraic nonlinear equations:

$$\hat{\mathbb{A}}\hat{\mathbb{U}} = \hat{\mathbb{F}}_{\text{ext}} + \hat{\mathbb{F}}_{\text{NL}}(\hat{\mathbb{U}}) + \hat{\mathbb{P}} \tag{6.23}$$

where the dynamic stiffness matrix has been introduced and reads:

$$\hat{\mathbb{A}} = \hat{\boldsymbol{L}}_2 \otimes \boldsymbol{M} + \hat{\boldsymbol{L}}_1 \otimes \boldsymbol{C} + \hat{\boldsymbol{L}}_0 \otimes \boldsymbol{K} \tag{6.24}$$

with $\hat{\boldsymbol{L}}_2$ a tridiagonal matrix whose band is equal to $\{1/\Delta t,\ -2/\Delta t,\ 1/\Delta t\}$, first row is equal to $\{-1/\Delta t,\ 1/\Delta t,\ 0,\ \ldots,\ 0\}$ and last row equal to $\{0,\ \ldots,\ 0,\ 1/\Delta t,\ -1/\Delta t\}$; $\hat{\boldsymbol{L}}_1$ a tridiagonal matrix whose band is equal to $\{-1/2,\ 0,\ 1/2\}$, first row is equal to $\{-1/2,\ 1/2,\ 0,\ \ldots,\ 0\}$ and last row equal to $\{0,\ \ldots,\ 0,\ -1/2,\ 1/2\}$; $\hat{\boldsymbol{L}}_0$ a tridiagonal matrix whose band is equal to $\{\Delta t/6,\ 4\Delta t/6,\ \Delta t/6\}$, first row is equal to $\{2\Delta t/6,\ \Delta t/6,\ 0\ \ldots,\ 0\}$ and last row equal to $\{0,\ \ldots,\ 0,\ \Delta t/6,\ 2\Delta t/6\}$.

The flux vector reads:

$$\hat{\mathbb{P}} = \left\{\boldsymbol{p}_0^{\mathrm{T}},\ \boldsymbol{0},\ \cdots,\ \boldsymbol{0},\ -\boldsymbol{p}_n^{\mathrm{T}}\right\}^{\mathrm{T}} \tag{6.25}$$

where al the internal entries are zero due to the enforcing of the continuity of $\boldsymbol{p}$ at each node.

When the periodic solution is sought, the periodicity is enforced by imposing $\hat{\mathbb{U}}_0 = \hat{\mathbb{U}}_n$ and $\boldsymbol{p}_0 = \boldsymbol{p}_n$, thus reducing the size of the unknown vector from $N \times n + 1$ to $N \times n$. The number of equations is also reduced by summing the first and last rows of the system of Eq. (6.23) into one single equation. By doing so, the flux term becomes zero and the differentiation matrices $\hat{\boldsymbol{L}}$ become circulant matrices $\boldsymbol{L}$ whose internal rows are not changed and whose first and last rows become: for $\boldsymbol{L}_2$ the first row becomes equal to $\{-2/\Delta t,\ 1/\Delta t,\ 0,\ \ldots,\ 0,\ 1/\Delta t\}$ and the last row $\{1/\Delta t,\ 0,\ \ldots,\ 0,\ 1/\Delta t,\ -2/\Delta t\}$; for $\boldsymbol{L}_1$ the first row becomes equal to $\{0,\ 1/2,\ 0,\ \ldots,\ 0,\ -1/2\}$ and the last row $\{1/2,\ 0,\ \ldots,\ 0,\ -1/2,\ 0\}$; for $\boldsymbol{L}_0$ the first row becomes equal to $\{4\Delta t/6,\ \Delta t/6,\ 0\ \ldots,\ 0,\ \Delta t/6\}$ and the last row $\{\Delta t/6,\ 0,\ \ldots,\ 0,\ \Delta t/6,\ 4\Delta t/6\}$.

The algebraic system of equation with enforced periodicity will finally read:

$$\mathbb{A}\mathbb{U} = \mathbb{F}_{\text{ext}} + \mathbb{F}_{\text{NL}}(\mathbb{U}) \tag{6.26}$$

where the hat superscript has been removed to denote the fact that the system is different from the original one. This system can be solved with classical continuation algorithm such as predictor corrector in the variable $\mathbb{U}$ and in one parameter of the system.

A great advantage of the method is that the stability can be easily computed and the so called monodromy matrix is almost a by-product of the method. It has been shown that the passage from the original system of Eq. (6.23) to the periodic one of Eq. (6.26) is straightforward. In turn, also the opposite passage is, which means that once the system of Eq. (6.26) has been solved, one can easily reconstruct the original system for which the first and last timesteps are split. Let us assume that $\mathbb{U}^*$ is a solution of Eq. (6.26), then the vector $\hat{\mathbb{U}}^*$ can be build by appending the first N entries of $\mathbb{U}^*$ at the end of the vector. In this way, $\hat{\mathbb{U}}^*$ will be a solution of Eq. (6.23). By expanding Eq. (6.23) in Taylor series around $\hat{\mathbb{U}}^*$ up to first order one has:

$$\left(\hat{\mathbb{A}} - \hat{\mathbb{J}}_{\mathrm{NL}}(\hat{\mathbb{U}}^*)\right) \Delta\hat{\mathbb{U}}^* = \Delta\hat{\mathbb{P}}^* \tag{6.27}$$

with $\hat{\mathbb{J}}_{\mathrm{NL}}$ Jacobian of the nonlinear force vector with respect to $\hat{\mathbb{U}}$.

From this system the relation that links $\Delta\hat{\mathbb{U}}_0^*$ and $\Delta\hat{\mathbb{U}}_n^*$ with $\Delta\hat{\mathbb{P}}_0^*$ and $\Delta\hat{\mathbb{P}}_n^*$ can be obtained by condensation, leading to:

$$\begin{bmatrix} \mathbb{\Xi}_{00} & \mathbb{\Xi}_{0n} \\ \mathbb{\Xi}_{n0} & \mathbb{\Xi}_{nn} \end{bmatrix} \begin{Bmatrix} \Delta\hat{\mathbb{U}}_0^* \\ \Delta\hat{\mathbb{U}}_n^* \end{Bmatrix} = \begin{Bmatrix} \Delta\hat{\mathbb{P}}_0^* \\ \Delta\hat{\mathbb{P}}_n^* \end{Bmatrix} \tag{6.28}$$

Lastly, the relation between the initial conditions $\Delta\hat{\mathbb{U}}_0^*$ and $\Delta\hat{\mathbb{P}}_0^*$ with the final conditions $\Delta\hat{\mathbb{U}}_n^*$ and $\Delta\hat{\mathbb{P}}_n^*$ can be derived:

$$\begin{Bmatrix} \Delta\hat{\mathbb{U}}_n^* \\ \Delta\hat{\mathbb{P}}_n^* \end{Bmatrix} = \begin{bmatrix} -\mathbb{\Xi}_{0n} & \mathbf{0} \\ -\mathbb{\Xi}_{nn} & \boldsymbol{I} \end{bmatrix}^{-1} \begin{bmatrix} \mathbb{\Xi}_{00} & -\boldsymbol{I} \\ \mathbb{\Xi}_{n0} & \mathbf{0} \end{bmatrix} \begin{Bmatrix} \Delta\hat{\mathbb{U}}_0^* \\ \Delta\hat{\mathbb{P}}_0^* \end{Bmatrix} \tag{6.29}$$

The matrix in Eq. (6.29) represents the linear approximation of the effect that a perturbation of the initial conditions on a given solution of the periodic system will have on the final conditions. This is by definition the monodromy matrix of the system and its eigenvalues can determine the stability of the found periodic solution. If the eigenvalues of the monodromy matrix are inside the unit circle, *i.e.* their absolute values are lower than one, the found solution is stable, otherwise it unstable. In the framework of continuation, the solution of the system as a control parameter varies is of interest. If for two consecutive values of the control parameter, the found solutions are stable and unstable respectively, a bifurcation has occurred. In particular, if one eigenvalue of the monodromy matrix crossed the unit circle along the real and positive axis, a transcritical, cyclic-fold or symmetry-breaking bifurcation has occurred. If the crossing is along the real and negative axis, a period-doubling bifurcation has occurred. Else, if the eigenvalues crossing have an imaginary component the bifurcation is called a secondary Hopf or a Neimark-Sacker bifurcation [98].

6.2.3 Comparison on a single oscillator testcase

The two methods will be now compared on the single oscillator testcase of Eq. (6.13) . In order to obtain the periodic solution of this system, time finite element method (FET) and harmonic balance method (HBM) have been implemented in Fortran and coupled with continuation algorithm. The nonlinear mode of a system with $k = 1, m = 1, g_0 = 1$ and $k_\epsilon = (1, 4.5, 15)$ is firstly studied. In Fig. 6.3, the frequency amplitude curve computed with FET and HBM are reported against the reference solution. In order to compare the results of harmonic balance method and time finite element method, the number of degrees of freedom of the nonlinear algebraic system of equations is set to the same value for both methods: $n = 25$ harmonics in the HBM simulation and $2n + 1 = 51$ time elements in the FET simulation. Moreover, to better understand the role that the number of sampling points of the alternating frequency time procedure (AFT) plays in HBM, this number is chosen to be either equal to or four times the number of FET nodes.

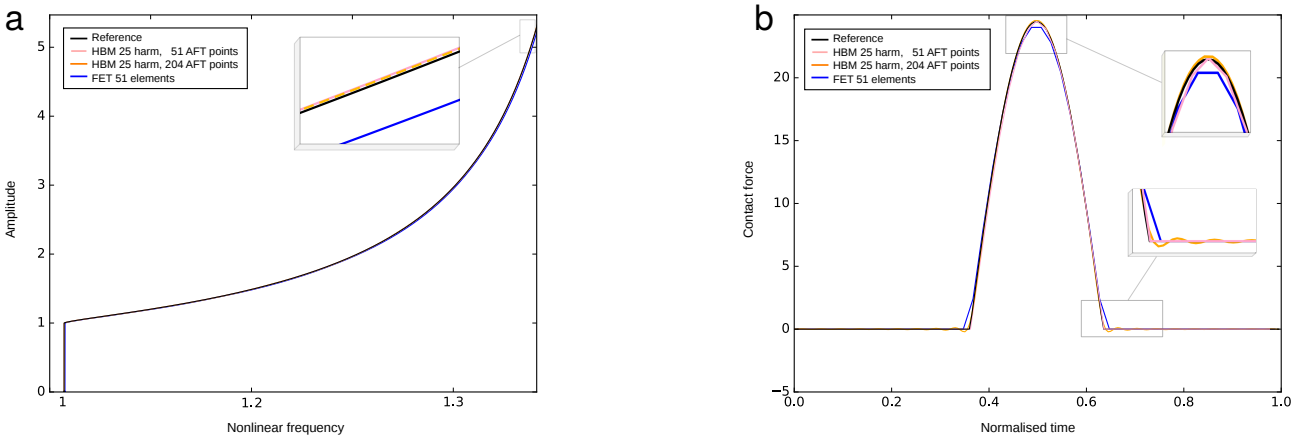


Figure 6.3: Comparison on a softer contact case. Conservative solution of the nonlinear mode with $\beta_\epsilon = 4.5$. Frequency amplitude curve (a) and contact force at $\omega = 1.35$ (b).

For a relatively low value of the contact stiffness, and a relatively fine discretisation of the period, FET method performs worse than HBM in both cases. One can see that the case of AFT points equal to the harmonic unknowns lead to a suppression of the Gibbs phenomenon, at the expenses of a worse visualisation of the solution. The maximum value of contact force is also better captured by the HBM than the FET. A higher and a lower value of the contact stiffness have been tested keeping the size of the system constant. In Table 6.1, the error on the maximum value of contact force is reported for the different methods. It is possible to see that the error of FET is between 5 and 20 times higher than HBM in any case. The main conclusion is in fact that HBM has always to be preferred when the contact is soft and the number of harmonics required not very high.

To give an idea of how HBM performs for low values of the contact stiffness, in Table 6.2, the values of the asymptotic nonlinear frequency computed for different values of β_ϵ and harmonic balance method with only 2 and 5 harmonics respectively are reported. Even in the case of a relatively high contact stiffness and an asymptotic nonlinear frequency ratio of 1.54, the error of HBM is less than 1% with only two harmonics.

	FET (51)	HBM (25,51)	HBM (25,204)
$\beta_\epsilon = 1$	6.102 %	0.329%	0.440%
$\beta_\epsilon = 4.5$	1.867%	0.366%	0.460%
$\beta_\epsilon = 15$	2.371%	0.178%	0.596%

Table 6.1: Error on the maximum value of contact force for different values of β_ϵ.

		HBM (2,200)	HBM (5,200)
$\beta_\epsilon = 2$	$\bar{\omega}/\omega_0 = 1.27$	0.065%	0.00068%
$\beta_\epsilon = 3$	$\bar{\omega}/\omega_0 = 1.33$	0.145%	0.00178%
$\beta_\epsilon = 5$	$\bar{\omega}/\omega_0 = 1.42$	0.340%	0.00302%
$\beta_\epsilon = 10$	$\bar{\omega}/\omega_0 = 1.54$	0.737%	0.00410%

Table 6.2: Error of HBM on the asymptotic nonlinear frequency for different value of β_ϵ.

Since the accuracy of harmonic balance method with soft contact has shown to be very high, the last testcase of this comparison is chosen to have a very high contact stiffness $\beta_\epsilon = 50$. Also, in this case, the excitation is provided by a moving clearance with time behaviour $d(t) = g_0 + d_0 \sin(\Omega t)$. The equation of motion in this case reads:

$$\begin{cases} m\ddot{u} + c\dot{u} + ku + k_\epsilon u = g_0 + d_0 \sin(\Omega t) & \text{if } u > g_0 + d_0 \sin(\Omega t) \\ m\ddot{u} + c\dot{u} + ku = 0 & \text{if } u \leq g_0 + d_0 \sin(\Omega t) \end{cases} \tag{6.30}$$

The simulations are run for values of the geometrical parameters $d_0 = 0.015$, $g_0 = 0.013$ and the amplitude of the response plotted is the one normalised with respect to the interference value $d_0 - g_0 = 0.002$. The results of a simulation with damping value $c = 0.16$ are shown in Fig. 6.4. The forced response function displays a main resonance for $\Omega > 1$ and super-harmonic resonances for $\Omega < 1$.

As regards to the amplitude of the oscillations, it is possible to see that a very small interference can generate high amplitude vibrations in the system. Close to the resonance at $\lambda = 0.583$ for example the amplification factor is ≈ 8 and can reach the value of ≈ 46 for the fundamental resonance.

The results obtained with the two methods are in strong agreement as can be seen from the forced response functions of Fig. 6.4; the results of FET with 31 and 151 time elements are comparable to those of HBM with respectively 15 and 75 harmonics and 62 and 302 sampling points (double respect to the FET elements).

The solution at $\lambda = 0.46$ evaluated with 151 DOFs shows a good match in terms of displacement (see Fig. 6.5,(a)). In Fig. 6.5,(b), it is possible to see that the error on displacement with respect to time integration (obtained with a central difference scheme with 10^4 points) of the HBM decreases with the number of points of the AFT with rate of convergence

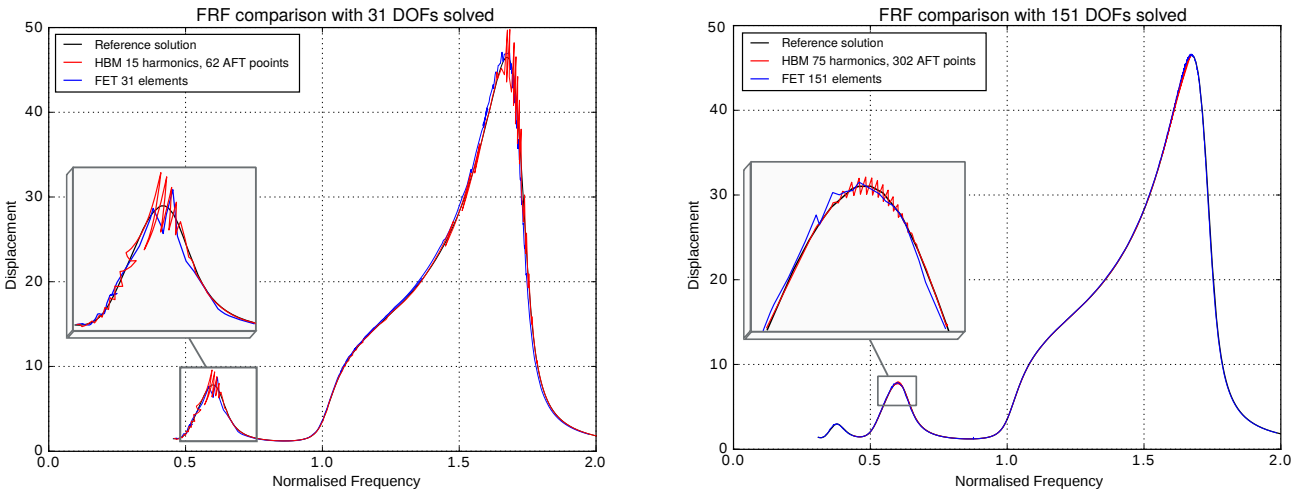


Figure 6.4: Comparison between the forced response function evaluated with HBM and with FET: (left) 31 DOFs, (right) 151 DOFs

$p_{AFT} \approx 2.5$; when the number of sampling points is 302 the error is comparable with the one of FET with 151 elements. In all cases the error on displacement displays a similar behaviour being uniformly distributed over the whole period with fluctuations that follow the solution ones, indicating that for both methods the error on displacement is the results of a difference in phase and amplitude between the reference solution and the approximated one.

Conversely, by evaluating the contact force, some differences in the behaviour of the two methods can be observed. Referring to plot b and c of Fig. 6.5, it is possible to see that the maximum relative error on the contact force is almost 10 times higher than the one on the displacement; this is due to the fact that the displacement is a $\mathcal{C}^2$ function whereas the force is $\mathcal{C}^0$ due to the discontinuity in the derivative at the two extremal points of the penetration phase.

The magnitude of the error is comparable between the two methods and the maximum error of FET is lower than the one of HBM with 151 AFT points but higher than the one of HBM with 302 points; the convergence of the error of HBM with the number of sampling points is not observed here as no significant reduction is showed with the increase of sampling points from 302 to 604.

As regards to the distribution of the error over the period, it is very different between the two methods; in particular, the error on the contact force with FET is localised over few elements around the discontinuity whereas with HBM it is spread over the whole period with the highest values close to the discontinuity points. The spreading of the error of HBM comes from the fact that, being a spectral method, each shapefunction is defined over the whole domain whereas FET shapefunctions have a compact support.

This error localisation around the discontinuities, for FET results from the fact that a sharp variation occurs inside a time step discretised with a linear function that is not able to

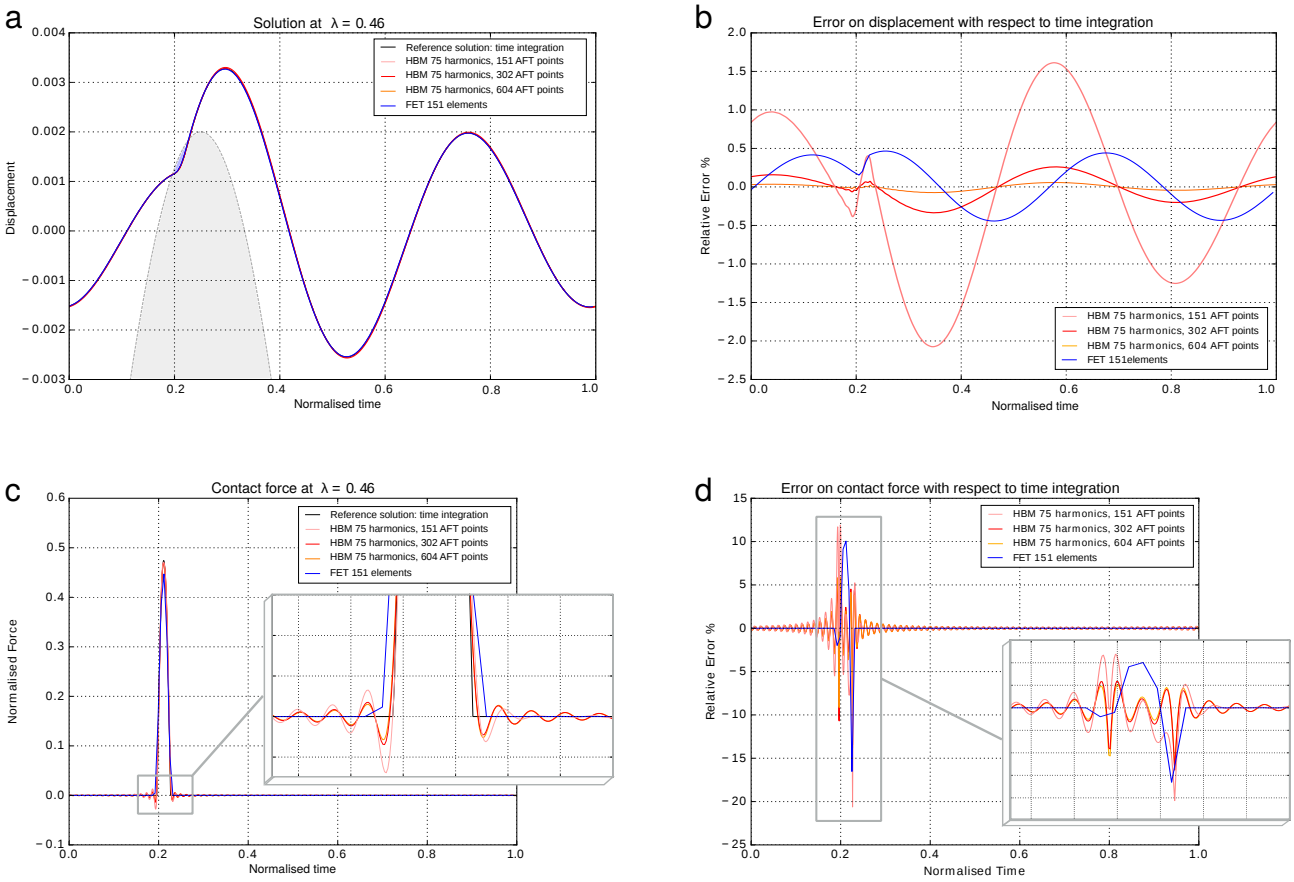


Figure 6.5: Comparison between the solution evaluated at $\lambda \approx 0.46$ with HBM and with FET: (a) Displacement over time, (b) relative error on displacement with respect to time-integration, (c) contact force over time, (d) relative error on contact force with respect to time-integration

reproduce the variation; for HBM with number of AFT points higher than the harmonic unknowns, it is instead the result of Gibbs phenomenon.

Simulations at the same frequency 0.46 have been computed with 31, 71, 151, 401, 801 DOFs and similar behaviour of the error has been observed. In Fig. 6.6, the convergence of the total error (norm-1) with the number of DOFs shows that for both methods the rate of convergence is almost constant $p_{DOF} \approx 2$. The rate of convergence with the number of AFT points of HBM displays the same behaviour for all the simulations: it is almost constant and $p_{AFT} \approx 2.5$ for what regards the error on displacement but it reaches a saturation in terms of error on the contact force. Moreover, while the total error on displacement of FET with $2N+1$ elements is always lower than HBM with N harmonics and $2N+1$ AFT points but always higher than HBM with N harmonics and $2(2N+1)$, the total error on the contact force of FET is lower than that of HBM regardless the number of AFT points. Nonetheless, the convergence with the number of harmonics of the error on the contact force is still ensured and the rate of convergence is similar to the one of FET.

The simplified model adopted does not aim at representing the behaviour of a full structure; it must be seen instead as a test-case for the implemented numerical method in which

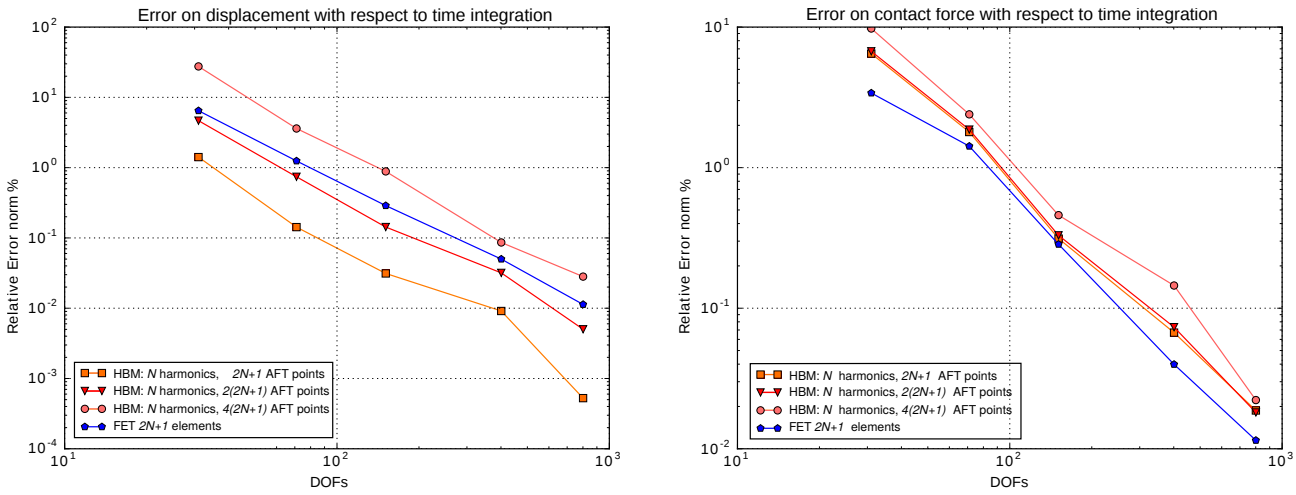


Figure 6.6: Convergence of the error with the DOFs: error on displacement (left) and error on contact force (right)

the choice of the parameters is done for testing the method under extreme conditions. In particular these conditions are favourable for the FET method more than for the HBM. In fact, in a structure with many dofs and only few in contact, the solution on the internal dof is much smoother than that at the contact dofs. In fact, the contact dofs sees a force which is $\mathcal{C}^0$ in time, and their displacement is $\mathcal{C}^2$. The force that they transmit to the neighbour internal dofs will be smoother than that they see, thus making the solution of the internal dofs smoother. Since the HBM works very well with smooth functions, the case of a single oscillator is the most unfavourable for the method. In light of this, recent work from [134] have proposed a mixed method for inelastic impacts where the internal degrees of freedom were solved with HBM and only at the contact nodes other bvp method were adopted, in that case the shooting method. In this section we have shown that the accuracy of HBM is always comparable with that of FET, even under very hard contact conditions. Similar results on a single oscillator with clearance nonlinearity had been shown by [63], where HBM was compared to collocation method. The higher accuracy shown by FET method in [25, 91] was obtained in case of non-smooth contacts; however, as shown in this section, this gain in accuracy does not apply to piecewise linear contact conditions. Lastly, we want to point out that the values of contact stiffness used in this section were intentionally much higher than those of common engineering applications. For this reason, using HBM on both internal and contact nodes is the strategy that we chose to use in the remainder.

6.3 Reduced order modelling for clearance nonlinearity

In the previous section, we showed that for relatively soft contact interactions, the accuracy of the harmonic balance method even with a very low number of harmonics is very high. However, this accuracy has been tested on a single oscillator and the case of large structures has not been treated yet. In fact, the ratio β_ϵ between the characteristic stiffness of the system and that of the contact is a well defined quantity in the case of a single oscillator

but its generalisation to a generic large FE model is not straightforward. In this section, a reduced order modelling method for soft contact interaction is proposed. It will be shown that the accuracy of the proposed method is directly linked to that of harmonic balance method with 2 harmonics. The applicability of the proposed method is therefore restricted to contact conditions for which a 2 harmonics solution would provide accurate results.

In light of this link, a quantification of the hardness of the contact in the case of a generic FE structure is necessary. Under the quasi-static assumption, and if the structure has only one node in contact, the Shur complement of the stiffness matrix relative to that degree of freedom can be used to quantify the stiffness of the structure as the ratio between a force applied to that dof over its static displacement. Splitting the stiffness matrix entries into those relative to the internal degrees of freedom and those relative to the single contact dof, the Shur complement k_S reads:

$$k_S = \boldsymbol{K}_{bb} - \boldsymbol{K}_{bi}\boldsymbol{K}_{ii}^{-1}\boldsymbol{K}_{ib} \tag{6.31}$$

This quantity can be then used to define the ratio β_ϵ as the ratio between the stiffness of the contact k_ϵ and the characteristic stiffness of the structure k_S. In this section, the proposed reduced order model will be applied on a structure with $\beta_\epsilon \approx 2$, for which the harmonic balance method with 2 harmonics is highly accurate (see Table 6.2). In future developments, higher values of the contact stiffness and the investigation of range of applicability of the proposed method can be studied.

The proposed method stems from the conjunction between the idea of trial vector derivatives proposed in [118,175] and the findings of Ch. 5 of this thesis. In particular in [118,175] the idea of static modal derivatives is applied to jointed structures with frictional contact. Recalling the definition of static modal derivatives given in Eq. (2.90), and assuming that only one nonlinear mode is of interest, one has:

$$\boldsymbol{\theta}^{(S)} = \boldsymbol{K}^{-1}\frac{\partial^2 \boldsymbol{F}_{\mathrm{NL}}}{\partial q^2}\bigg|_{\mathbf{0}}. \tag{6.32}$$

with q modal amplitude of the mode of interest and $\boldsymbol{\theta}^{(S)}$ static modal derivative relative to it. The resulting vector is referred to as trial vector derivative in [175]. The trial derivative is then used to construct the reduction matrix of the change of coordinates, thus producing a way building an a priori reduced order model.

In this section we extend this definition and propose a variation of this approach based on the observation of Ch. 5 and inspired by the direct normal form method. We will then test the reduced model under normal contact condition on a FE structure and compare the results with the classical Hurty/Craig-Bampton method ones.

6.3.1 Contact derivatives

Let us assume the case of a generic FE structure with only one contact node and the case of purely normal contact and positive clearance. The equation of motion of the conservative system reads:

$$\begin{cases} \boldsymbol{M}\ddot{\boldsymbol{U}} + (\boldsymbol{K} + \boldsymbol{K}_C)\,\boldsymbol{U} = \boldsymbol{G}_{C,0} & \text{if } \boldsymbol{B}_n^{\mathrm{T}}\boldsymbol{U} > g_0 \\ \boldsymbol{M}\ddot{\boldsymbol{U}} + \boldsymbol{K}\boldsymbol{U} = \boldsymbol{0} & \text{if } \boldsymbol{B}_n^{\mathrm{T}}\boldsymbol{U} \leq g_0 \end{cases} \tag{6.33}$$

The main purpose of the proposed method is to build an a priori reduced order model that is able to accurately compute the nonlinear mode of the structure with the least amount of degrees of freedom to be solved for. To this end, the reduction will be done on a basis that includes the linear mode of interest plus additional vectors that take into account the nonlinearity introduced by the contact. Since the contact couples all the modes of the structure, an efficient way of accounting for all their component is sought and the static modal derivative is the first candidate for this purpose. However, being the contact forces piecewise linear, the derivative of these forces with respect to the modal amplitude needed to compute the modal derivative might not be well defined. For example in the case under investigation here, when the clearance is positive, the application of Eq. (6.32) will return a zero vector for $\boldsymbol{\theta}^{(S)}$.

To overcome this issue, a procedure based on finite difference is proposed; the second order derivative of a nonlinear force with respect to a certain modal amplitude q relative to the mode $\boldsymbol{\phi}$, reads:

$$\frac{\partial^2 \boldsymbol{F}_{\mathrm{NL}}}{\partial q^2} \approx \frac{\boldsymbol{F}_{\mathrm{NL}}(+\lambda\boldsymbol{\phi}) + \boldsymbol{F}_{\mathrm{NL}}(-\lambda\boldsymbol{\phi})}{\lambda^2} \tag{6.34}$$

with λ a selected modal amplitude. This procedure is equivalent to those of the StEP method for geometric nonlinearities. In that case, the procedure will not be approximated but exact because the nonlinear forces are polynomials up to cubic order therefore the choice of λ is only driven by numerical considerations [36]. Conversely, here the choice of λ has to be made in such a way that the displacement imposed along the mode of interest is enough to overcome the positive clearance and activate the nonlinear forces. Under this condition, the approximate second order derivative of the nonlinear contact forces will read:

$$\frac{\partial^2 \boldsymbol{F}_{\mathrm{NL}}}{\partial q^2} = -\frac{\boldsymbol{K}_{\mathrm{C}}\boldsymbol{\phi}}{\lambda} \tag{6.35}$$

and, in turn, the trial vector derivative will be:

$$\boldsymbol{\theta}^{(S)} = -\frac{1}{\lambda}\boldsymbol{K}^{-1}\boldsymbol{K}_{\mathrm{C}}\boldsymbol{\phi} \tag{6.36}$$

This newly defined vector is dependent from the arbitrarily chosen amplitude λ. However, since this vector will be kept in the basis and will therefore have its own amplitude, we are only interested in its direction and we can then just assume that $\lambda = 1$.

In Ch. 5, it is shown that the second order tensor of direct normal form $\boldsymbol{Zd}$ is equivalent to the static modal derivative. In the direct normal form method, also the vector $\boldsymbol{Zs}$ is necessary if one wants to build the reduced order model in a correct way. Let us call the trial derivative vector $\boldsymbol{\psi}^{(0)}$ and let us just define a new vector $\boldsymbol{\psi}^{(2)}$, in a fashion equivalent to $\boldsymbol{Zs}$ for contact forces:

$$\boldsymbol{\psi}^{(0)} = -\boldsymbol{K}^{-1}\boldsymbol{K}_{\mathrm{C}}\boldsymbol{\phi} \tag{6.37}$$

$$\boldsymbol{\psi}^{(2)} = ((2\omega_n)^2\boldsymbol{M} - \boldsymbol{K})^{-1}\boldsymbol{K}_{\mathrm{C}}\boldsymbol{\phi} \tag{6.38}$$

The reduced order model proposed is then built by using the eigenvector of the mode of interest, plus the two additional vectors accounting for the nonlinear behaviour. The reduced matrix will then read:

$$\boldsymbol{R} = \begin{bmatrix} \boldsymbol{\phi} & \boldsymbol{\psi}^{(0)} & \boldsymbol{\psi}^{(2)} \end{bmatrix} \tag{6.39}$$

The reduced dynamics matrices will be then obtained by projecting the equation of motion onto $\boldsymbol{R}$ in a Galerkin fashion. The reduced dynamics will be composed only by three degrees of freedom, no matter which nonlinear mode one is solving. This is indeed the main advantage of the proposed method as compared to Hurty/Craig-Bampton (HCB) method. In fact, if a high mode is of interest, say the fourth, a high number of internal modes have to be included in the reduction matrix of the HCB method. With the proposed method the number of degrees of freedom will instead remain three.

Although derived in an empirical way, a more theoretical derivation of the validity of the method could be given. Let us assume that the solution along the nonlinear mode of the mode of interest, is composed by a strong component of the underlying linear mode plus a nonlinear correction that has to take into account all the modes that start to contribute as long as the nonlinear force is activated. Let us write it as:

$$\boldsymbol{U} = \boldsymbol{\phi}q + \sum_k \boldsymbol{\psi}_k u_k \tag{6.40}$$

where $\boldsymbol{\phi}$ is the linear master mode with its amplitude q and u_k a generalised amplitude that multiplies the correction vector $\boldsymbol{\psi}_k$.

Since the motion along the nonlinear mode is dominated by the contribution of the underlying linear component, we assume that in the calculation of the nonlinear contact force, the dependence on $\boldsymbol{U}$ can be simplified as:

$$\boldsymbol{F}_{\mathrm{NL}}(\boldsymbol{U}) \approx \boldsymbol{F}_{\mathrm{NL}}(\boldsymbol{\phi}q) \tag{6.41}$$

Now, we assume that the solution in time can be decomposed into an infinite series of harmonics whose unknown period is ω and each correction vector refers to a given harmonic

$k \neq 1$. Also, we assume that the modal amplitude q is dominated by the first harmonic. The generic harmonic projection of the equation of motion reads:

$$(-(k\omega)^2\boldsymbol{M} + \boldsymbol{K})\boldsymbol{\psi}_k + \boldsymbol{K}_C\boldsymbol{\phi}\int_{t=t_C} q\cos(k\omega t)dt = \mathbf{0} \tag{6.42}$$

where the integral of the modal amplitude q projected on the generic harmonic k is defined only for the contact interval t_C. Since we assumed that q is dominated by the first harmonic, $q = q^{(1S)}\sin(\omega t)$, in the evaluation of the contact force one has that the portion of time in contact, when the vibration amplitude is much higher than the gap and thus the gap can be considered zero, is the first half of the period. The integral of Eq. (6.42) then reads:

$$\int_{t=t_C} q\cos(k\omega t)dt = q^{(1S)}\int_0^{T/2}\sin(\omega t)\cos(k\omega t)dt = \frac{q^{(1S)}}{\omega}\frac{1+(-1)^k}{(1-k^2)} \tag{6.43}$$

for which the most responding terms are $k = 0$ and $k = 2$. The vectors $\boldsymbol{\psi}_k$ for $k = 0$ and $k = 2$ are exactly the above defined vectors $\boldsymbol{\psi}^{(0)}$ and $\boldsymbol{\psi}^{(2)}$ and the proposed method will be then equivalent to assume the ansatz for the displacement as:

$$\boldsymbol{U} = \boldsymbol{\phi}q + \boldsymbol{\psi}^{(0)}u_0 + \boldsymbol{\psi}^{(2)}u_2 \tag{6.44}$$

From this perspective, the condition of applicability of the method are restricted to the cases where the harmonic balance method with only two harmonic would produce accurate results if applied on the full model. The consequence of this is that the condition of soft contact has to be fulfilled. As we observed in the previous section, the error of HBM with 2 harmonics on a case with $\beta_\epsilon = 10$ was below 1%. So the requirement for the contact to be soft might not be so stringent in quantitative terms. However, a thorough assessment of the range of applicability of the method is not presented in this work and will be the subject of future developments.

6.3.2 Presentation of the testcase

A blade-like structure with a contact node at the trailing edge will be used to present the result of the proposed method and compare them with HCB method. In this structure, the value of k_S for the degree of freedom along the X direction at the trailing edge (TE) is of $1.87E5$. To fulfil the assumption of soft contact the chosen value of contact stiffness k_ϵ is equal to $4E5$; the resulting value of the stiffness ratio is $\beta_\epsilon = 2.14$. The geometry of the tested structure is showed in Fig. 6.7.

The first and fourth nonlinear modes representing a bending and a torsional mode of this structure are computed within the FE software *code_aster* [28] in which a harmonic balance method formulation combined with continuation is available through the command *MODE_NON_LINE* [96]. The formulation allows to choose a different number of harmonics for the nodes in contact. Here, the results are obtained with 15 harmonics on the internal

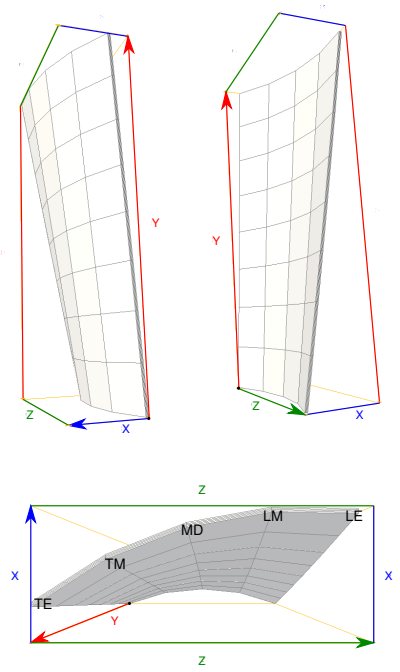
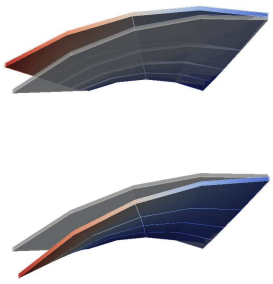
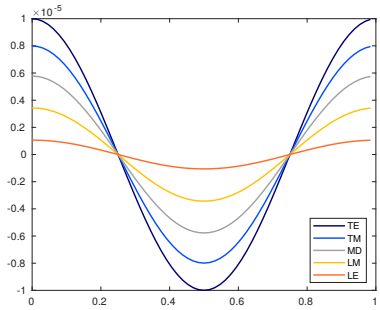


Figure 6.7: Blade-like structure under test. Discretisation and axis orientation. Bounding box size: $(\Delta X, \Delta Y, \Delta Z) = (79.84, 40.07, 200)mm$. Positioning of nodes along the chord: from trailing edge (TE) to leading edge (LE).



(a) Deformation at $t = 0$ and $t = T/2$.

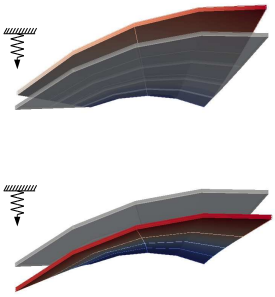


(b) Response of tip nodes.

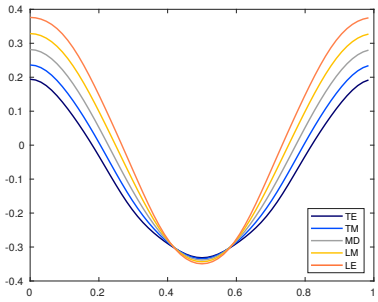
Figure 6.8: Solution of mode 1 at low amplitude vibration. Linear solution at amplitude lower than the clearance.

dofs and 150 on the contact dof. Due to the long computational time that the solution of the full model requires, we have chosen to mesh the structure with a very coarse mesh of 8 linear hexahedral elements along the span, 4 along the chord and 4 along the thickness, for a total of 675 degrees of freedom. The runtime of the computation of the nonlinear mode for the full model is of approximately one hour.

The solution of the nonlinear modes from the full model computation are reported in Figs. 6.8, 6.9, 6.10. In Fig. 6.8 solution at low amplitude vibration, before the clearance is overcome and thus the system is still fully linear, is reported. The maximum deformation and the time response of the tip nodes is displayed. The same plots are shown in Fig.6.9

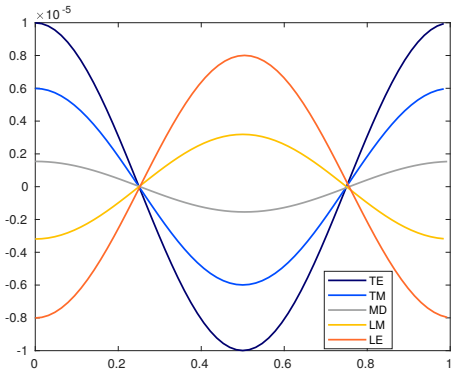


(a) Deformation at $t = 0$ and $t = T/2$.

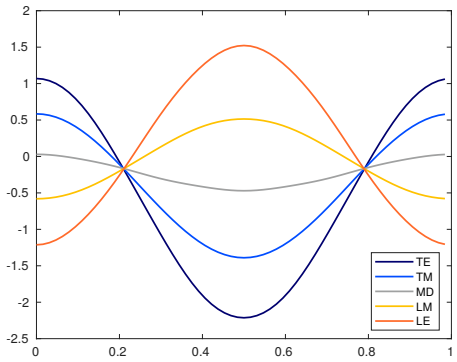


(b) Time response of tip nodes.

Figure 6.9: Solution of nonlinear mode 1 at high amplitude vibration. Solution close to asymptotic nonlinear frequency.



(a) Linear response at low amplitude



(b) Nonlinear response at high amplitude

Figure 6.10: Time response of tip nodes along nonlinear mode 4.(a) Linear solution at amplitude lower than the clearance. (b) Solution close to asymptotic nonlinear frequency.

for a solution at high amplitude vibration. At this point the nonlinear mode is very close to its nonlinear asymptotic frequency $\bar{\omega}$. The linear frequency of the first mode is around 1175 rad/s and the asymptotic frequency of the first nonlinear mode is around 1337 rad/s; the stiffening introduced by the contact is of $+14\%$ of the linear frequency. As for the fourth mode, the time responses at low and high amplitude are reported in Fig. 6.10. For this mode, the linear frequency is around 7006 rad/s and the asymptotic one around 7066 rad/s; the stiffening introduced by the contact is of $+0.8\%$. Since the contact conditions are the same for both modes, the low frequency mode is much more affected by the contact than the higher frequency one. Not only the nonlinear frequency is more affected, but also the mode shape as one can see from the time responses of Figs. 6.8, 6.9, 6.10, where the variation for example of the leading edge response from the linear to the nonlinear case is much more evident in the first mode than in the fourth.

As for the shape of the response, it is possible to see that the assumptions of response dominated by the underlying linear mode and modal amplitude dominated by the first harmonic, are both fulfilled for the two modes under investigation.

6.3.3 Comparison with Hurty/Craig-Bampton method

The results obtained with the proposed method are here compared with those obtained by the HCB method. In Fig. 6.11 the frequency amplitude plots of the first nonlinear mode are reported. The three solutions are almost overlapped and the difference is only visible in the zoomed sections. Both the proposed method and the HCB method have the same size of reduced model, 3 degrees of freedom each; in the proposed method the degrees of freedom are the modal amplitude of the linear mode and the amplitudes of the correction vectors ψ. As for HCB, the three dofs are composed by the amplitude of the static mode plus the amplitude of the first two internal modes of the system (see Sec.2.3).

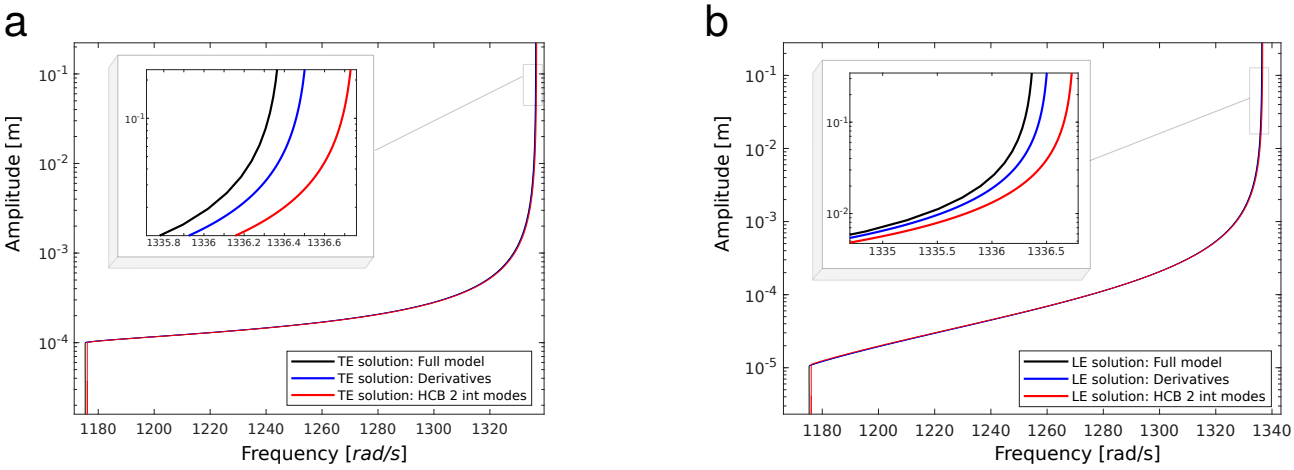


Figure 6.11: Frequency amplitude plot of nonlinear mode 1 obtained with: full model (black), proposed method based on derivatives (blue), Hurty/Craig-Bampton method with 2 internal modes (red). Amplitude at trailing edge (a) and leading edge (b).

In Fig. 6.12, the frequency amplitude plots relative to the fourth nonlinear mode are reported. In this case, two internal modes were not enough for HCB to capture the correct linear frequency of the mode, and 5 internal modes for a total of 6 dofs in the reduced dynamics have been used. Despite having a size double to that of the proposed method, the results of HCB are still worse than those obtained with the contact derivatives. The main problem in this case is that the underlying linear mode is not present in the basis of HCB, thus making it difficult for the method to provide the correct value of the linear frequency. The shape of the curve is in fact correct meaning that HCB is able to retrieve the correct hardening behaviour, but the shift in the linear frequency affect the whole solution.

Overall, the error of HCB is still minimum given that the frequency deviation between HCB and the reference solution is below 0.5%; the error on the linear frequency of HCB with only two internal modes would have been around 5%.

Another important consideration about this comparison lies in the application of the proposed method. The size of the reduced dynamics obtained with the proposed method is of three dofs for each nonlinear mode under investigation. If a multiple mode response was sought, for example if a random excitation in a certain frequency range was imposed, the

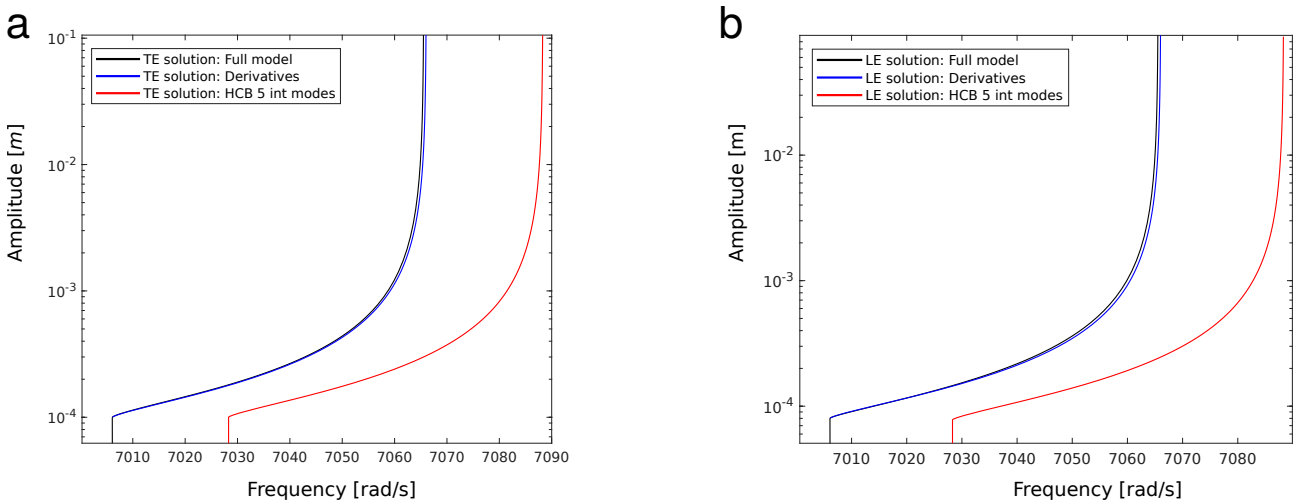


Figure 6.12: Frequency amplitude plot of nonlinear mode 1 obtained with: full model (black), proposed method based on derivatives (blue), Hurty/Craig-Bampton method with 5 internal modes (red). Amplitude at trailing edge (a) and leading edge (b).

size of the reduced system would be proportional to the number of modes in the range. In this work, the focus is on nonlinear modal analysis hence the case of multiple modes is not treated. In this context, the method provides a better minimal model for the behaviour of the structure than that obtained with HCB and also allows to isolate the mode of interest from others. In the framework of blade casing interaction, the proposed method offers a quick way of assessing the individual response of each mode to certain contact condition. The runtime of the method is in the order of seconds to build the reduction matrix and less than a minute to run the continuation on the reduced model. The information of the asymptotic frequency could then provide an important quantification about the sensitivity of each mode to the interaction.

6.4 Damped nonlinear modes for self-excited vibration

After having assessed the validity of harmonic balance method for soft contact interactions, we now move to the case of frictional contact conditions. In particular, the aim of this section is to investigate the existence of friction-induced vibrations due to flutter in a positive clearance system with permanent sliding friction condition. The aim is to assess the conditions under which a sustained regime of high amplitude vibrations driven by friction forces can be attained as a result of the mode coupling by means of the contact interaction.

Self-excited vibrations are known to occur in systems such as drum brakes, even with a constant value of the friction coefficient, as a result of flutter instability. In the study of these systems, it is common to assume that a permanent contact exist between the two bodies. This condition translates into a negative clearance system whose equilibrium position can become unstable for values of the friction coefficient above the critical limit. Conversely, in the framework of blade-casing interaction, a permanent contact cannot be assumed because the clearance between the tip of the blade and the casing, although small, is always positive.

Since the equilibrium position for positive clearance systems is always stable, self-excited solutions will not occur as a result of a bifurcation from the equilibrium branch, as in the negative clearance systems, but instead they will appear as isolated branches coexisting with the equilibrium one.

6.4.1 2DOFs Model

Most of the existing literature on blade-tip casing interaction is focused on the study of a single blade excited by a radial distortion of the casing that overcomes the tip clearance and acts as a periodic forcing term. Conversely, the possibility of high-amplitude vibrations in absence of a periodic excitation has not been considered yet. In the context of brake systems, friction-induced vibrations due to flutter instability have been extensively studied [46,47,72].

Simple self-excited mechanisms, such as the one proposed by Hamabe [44] consisting in a two degrees of freedom system pushed against a belt, are able to capture the geometrical coupling of the degrees of freedom and to analyse the Hopf bifurcation occurring in the system for a critical value of the friction coefficient. The post-Hopf behaviour in such systems depends on the nonlinearities taken into account in the model. If the amplitude of the oscillations overcomes the negative clearance imposed by the normal load, the system may detach from the belt giving rise to nonlinear limit cycle involving free flights and contact phases [82].

From a blade-casing interaction standpoint, the coupling between two blade modes can also occur due to the interaction with the casing, although the clearance between the two components in this case is always positive. The aim of this section is to study the possibility that self-excited vibrations exist in a positive clearance system in the form of an isolated branch of periodic solution that, instead of bifurcating from the equilibrium branch as in the case of the negative clearance system, coexists with the equilibrium branch. To this end, a two degrees of freedom system interacting with a frictional belt is adopted here to model, in the rotating frame, two modes of a blade interacting with a casing. This minimal model is the smallest possible model to observe this behaviour but the considerations that will be made could apply to bigger models, such as those obtained from a model reduction of a real blade finite element model.

The dynamics of a blade of a turbomachine involves several factors such as the complexity of the blade geometry, the possible coupling with adjacent blades through the disk, the centrifugal effects due to rotation. Even under simplifying assumptions, a full 3D model of the blade would still be necessary to correctly simulate the blade dynamics. The simplified model proposed here is then far from being representative of a real blade. Nevertheless, from a qualitative perspective, the phenomena observed can also occur in real blades.

The two degrees of freedom model of Fig. 6.13 is adopted here to study the coupling of two modes as a result of the interaction with a moving belt with velocity V. Two orthogonal

springs of stiffness k_1 and k_2 sustain the mass m. The damping is assumed to be mass proportional. The system is inclined with respect to the belt of the angle α_2 and the clearance between the system and the belt is the constant and positive parameter g. The interaction with the belt is regularised with the normal contact stiffness k_ϵ and the tangential contact force is expressed with a Coulomb friction law. We assume here that only sliding occur being the velocity of the belt much higher than that due to vibration of the system.

The relevance of this system for blade-case interaction problems is linked to that of the negative clearance system for brake squeal problems. Two modes with different natural frequencies and different radial to tangential displacement ratio of their modeshapes could be represented by the two degrees of freedom model of Fig. 6.13 if their tip trajectories are orthogonal. In this perspective, the inclination angle of the two degrees of freedom system could represent the lean angle of the blade and the two modes of the minimal model could represent a bending dominated and an axial dominated modes of the blade. It is important to remark, however, that the minimal model proposed in this section must be seen as a proof of concept for the sought phenomena to occur, more than a simulation of a real blade-casing interaction scenario.

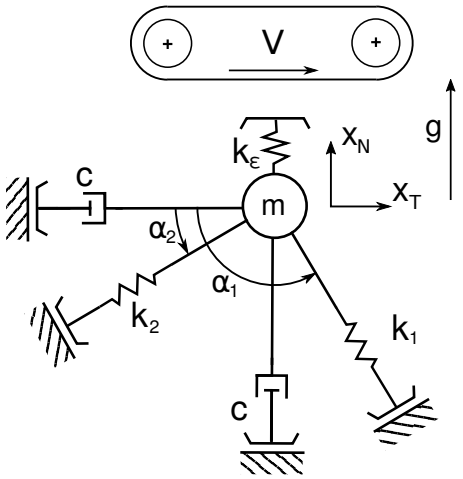


Figure 6.13: 2-DOFs simplified system.

We now define the equation of motion of the system of Fig. 6.13. The displacement vector is organised as:

$$\boldsymbol{U} = \begin{Bmatrix} x_N \\ x_T \end{Bmatrix} \tag{6.45}$$

By defining the contact stiffness matrix under the assumption of permanent sliding:

$$\boldsymbol{K}_{\mathrm{C}} = \begin{bmatrix} k_\epsilon & 0 \\ -\mu k_\epsilon & 0, \end{bmatrix} \tag{6.46}$$

and the gap vector as:

$$\boldsymbol{g} = \begin{Bmatrix} g \\ 0, \end{Bmatrix} \tag{6.47}$$

the equations of motion of the system read:

$$\begin{cases} \boldsymbol{M}\ddot{\boldsymbol{U}} + \boldsymbol{C}\dot{\boldsymbol{U}} + (\boldsymbol{K} + \boldsymbol{K}_{\mathrm{C}})\,\boldsymbol{U} = \boldsymbol{K}_{\mathrm{C}}\,\boldsymbol{g} & \text{if } x_N > g \\ \boldsymbol{M}\ddot{\boldsymbol{U}} + \boldsymbol{C}\dot{\boldsymbol{U}} + \boldsymbol{K}\boldsymbol{U} = \boldsymbol{0} & \text{if } x_N \leq g \end{cases} \tag{6.48}$$

Since we assumed orthogonality between the springs, $\alpha_1 = \alpha_2 + \pi/2$, the stiffness matrix only depends on the parameters k_1, k_2, α_2.

Before showing the results obtained on the positive clearance system, some observations on the negative clearance one have to be made.

6.4.2 Negative clearance system

When the clearance is negative ($g < 0$), the system has an equilibrium position at:

$$\boldsymbol{U_0} = (\boldsymbol{K} + \boldsymbol{K}_{\mathrm{C}})^{-1}\boldsymbol{K}_{\mathrm{C}}\,\boldsymbol{g} \tag{6.49}$$

Due to the asymmetry of the matrix $\boldsymbol{K}_{\mathrm{C}}$, Hopf bifurcation is known to occur in such system as a result of flutter instability for a critical value of the friction coefficient μ.

The stability of the system can be simply studied by computing the eigenvalues of the system rewritten in first order formulation and linearised around the equilibrium position.

It can be demonstrated that for Hopf bifurcation to occur, the condition $k_2 > k_1$ has to be fulfilled. We will then assume that $k_2 > k_1$. Under this assuption, the critical value of the friction coefficient at which Hopf bifurcation occur reads:

$$\mu_{\mathrm{cr}} = \tan(\alpha_2) + \frac{(k_2 - k_1 - k_\epsilon)^2}{2(k_2 - k_1)k_\epsilon \sin(2\alpha_2)} + \frac{2\frac{c^2}{m}(k_2 + k_1 + k_\epsilon)}{2(k_2 - k_1)k_\epsilon \sin(2\alpha_2)} \tag{6.50}$$

From Equation (6.50) it is possible to observe that the critical value of the friction coefficient for $k_\epsilon = k_2 - k_1$ and no damping is simply $\mu_{cr} = \tan\alpha_2$. Hopf bifurcation can be attained at very small values of the friction coefficient when c and α_2 are small; conversely for any value of $k_\epsilon \neq k_2 - k_1$, the critical value of the friction coefficient will be higher $\mu_{cr} > \tan\alpha_2$.

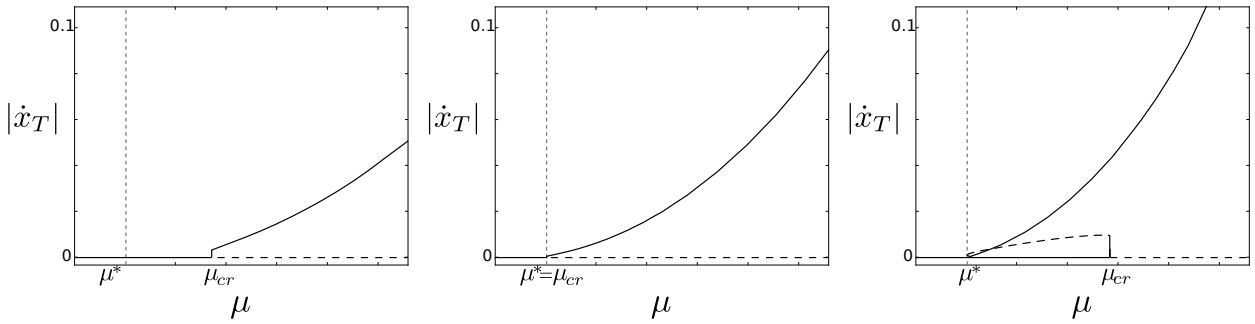
For a given geometry of the system, i.e. for k_1, k_2, α_2, m, c fixed, the contact stiffness k_ϵ^* can be defined:

$$k_\epsilon^* \triangleq k_2 - k_1 \tag{6.51}$$

If the contact stiffness is equal to k_ϵ^*, the critical friction coefficient will be the minimum possible for a given geometry. We will denote this value as μ^*:

$$\mu^* \triangleq \mu_{cr}(k_\epsilon^*) = \tan\alpha_2 + \frac{2\frac{c^2}{m}(k_2 + k_1 + k_\epsilon)}{2(k_2 - k_1)k_\epsilon \sin(2\alpha_2)} \tag{6.52}$$

For a system with parameters $m = 1$, $c = 0.01$, $\alpha_2 = \pi/15, k_1 = 1, k_2 = 5, g = -0.05$, bifurcation diagrams for different values of k_ϵ have been computed (Fig. 6.14). The three different values of k_ϵ corresponds to three different values of μ_{cr}, coinciding with the point where the periodic solutions branches bifurcates from the equilibrium. It is confirmed that the lowest possible value of μ_{cr} is attained when $k_\epsilon = k_\epsilon^*$ (Fig. 6.14b). For $k_\epsilon \neq k_2 - k_1$, the critical friction coefficient is always higher $\mu_{cr} > \mu^*$; however, if for the system with $k_\epsilon < k_\epsilon^*$ (Fig. 6.14a) this also coincides with the minimum value for periodic solutions to exist, this is no longer true for the system with $k_\epsilon > k_\epsilon^*$ (Fig. 6.14c): in this case, the bifurcation diagram, after bifurcating at $\mu_{cr} > \mu^*$, comes back to the critical value μ^* and then goes forth again. This means that the critical value of μ given by the eigenvalues analysis is not the minimum possible value for self-excited vibration to occur. Interestlingly, this phenomenon cannot be captured with a linear analysis that consider only the eigenvalues of the linearised system.



(a) $k_\epsilon < k_\epsilon^*$ (b) $k_\epsilon = k_\epsilon^*$ (c) $k_\epsilon > k_\epsilon^*$

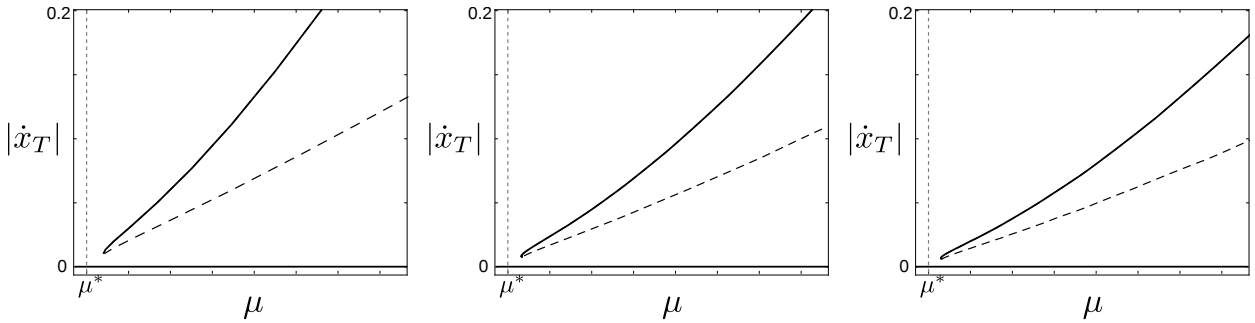
Figure 6.14: Bifurcation diagram of the negative clearance system: isolated branches of periodic solution and stable equilibrium branches for different values of k_ϵ.

6.4.3 Open clearance system

Unlike the negative clearance system studied in the previous section, the equilibrium branch of a positive clearance system will always be stable. The question addressed here is whether another stable branch of periodic solution may coexist with the equilibrium branch. If some disturbances make the system vibrates at an amplitude higher than the clearance, an interaction can occur. During the interaction, if the tangential forces make enough positive work on the system, they will increase its vibrational energy and pave the way for the next interaction to occur. In this case, a sustained regime of self-excited vibration could exist.

For the same system with parameters $m = 1$, $c = 0.01$, $\alpha_2 = \pi/15, k_1 = 1, k_2 = 5$ but now positive clearance $g = 0.05$, time integration with initial conditions that allow the system overcome the clearance has been performed to simulate an accidental disturbance. A periodic regime of self-sustained vibration is attained after the transient is damped out. The periodic solution found is used as initial point of the bifurcation diagrams of Fig. 6.15 obtained for three different values of k_ϵ. For each value, an isolated branch of periodic

solution not connected to the equilibrium branch appears. The existence of these branch means that, for a given value of μ, three possible states can exist: the stable equilibrium of the mass at rest, an unstable periodic solution, and a stable one. Moreover, there is a wide set of initial conditions for which the stable periodic solution is an attractor as can be seen from the enlarging area enclosed between the stable and unstable branches.



(a) $k_\epsilon < k_\epsilon^*$ (b) $k_\epsilon = k_\epsilon^*$ (c) $k_\epsilon > k_\epsilon^*$

Figure 6.15: Bifurcation diagram of the positive clearance system: isolated branches of periodic solution and stable equilibrium branches for different values of k_ϵ.

Unlike the negative clearance system, in the positive clearance one, it seems that regardless the value of k_ϵ, the minimum value of μ for which a self-excited solution exist is a constant value μ_{min}, slightly higher than μ^*.

To better understand the occurrence of self-excited solution in this system, the backbone curves for a value of $\mu > \mu_{min}$ and $k_\epsilon = k_2 - k_1$ have been computed.

The amplitude-frequency plots for the two nonlinear modes of the system evaluated for a given friction coefficient is reported in Fig.6.16a (red line); the two solution of the damped self-excited branch evaluated in the previous section are also reported (black crosses).

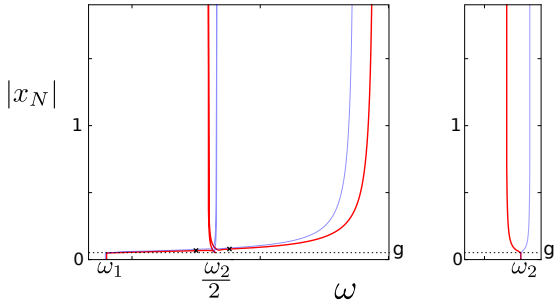
From Fig.6.16a, it is possible to see that an internal resonance between first and second mode occurs when the frequency of the first nonlinear mode coincides with half of the frequency of the second mode. The two self excited solution lie on the first nonlinear mode in the vicinity of the internal resonance. From the trajectory reported in Fig.6.16b (pre-internal resonance solution) and in Fig.6.16c (post-internal resonance solution) it is clear that the self-excited solution (black) and the nonlinear mode at that point (red) share the same shape but different phase shift between x_T and x_N. The self-excited solutions appear to be an extension of the nonlinear mode when the damping is different from zero but the tangential forces are able to compensate the energy loss. At different damping values in fact these solutions still exist and maintain the same shape but higher phase shift.

Another consideration is that the trajectory of the solution before and after the internal resonance radically changes. Moreover, by looking at the nonlinear mode evaluated at $\mu < \mu_{min}$ (clue) it is possible to observe that: first, an internal resonance also occurs but self-excited solutions do not; second, the shape change also occur but the shape the solutions seems having opposite tangential direction respect to the nonlinear mode at $\mu > \mu_{min}$; third,

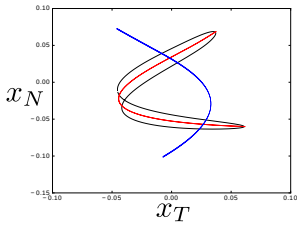
the tangential component of these solution is always lower than the one of the nonlinear mode at $\mu > \mu_{min}$. Moreover, the second mode presents a hardening effect rather than a softening. This last consideration is crucial given the fact that the value of μ^* at which μ_{min} is very close, also correspond with the value for which the eigenvalues of the negative clearance system are:

$$\lambda_{1,2}(\mu^*) = \pm \mathrm{i}\sqrt{\frac{k_1 + k_\epsilon}{m}} \qquad \lambda_{3,4}(\mu^*) = \pm \mathrm{i}\sqrt{\frac{k_2}{m}} \tag{6.53}$$

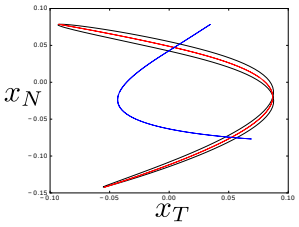
$\lambda_{1,2}(\mu^*)$ is always higher than the first eigenvalue of the free open system $\pm \mathrm{i}\sqrt{\frac{k_1}{m}}$, thus justifying the hardening effect of the first nonlinear mode for both values of μ; $\lambda_{3,4}(\mu^*_{cr})$ is instead exactly equal to the second eigenvalue of the open system which means that the value of μ^*_{cr} is the limit at which the second nonlinear mode neither soften nor harden due to the interaction. Although further investigations are required, this behaviour suggests that the necessary requirements for self-excited vibration to exist in such system may be this softening effect induced by friction forces on the higher mode.



(a) Nonlinear modes of the system at $\mu > \mu_{min}$ (red) and at $\mu < \mu_{min}$ (blue), and self-excited solutions in the vicinity of the internal resonance (black crosses).



(b) Trajectory of post-critical (red) and pre-critical (blue) NNMs, and self-excited solution pre-internal resonance (black).



(c) Trajectory of post-critical (red) and pre-critical (blue) NNMs, and self-excited solution post-internal resonance (black).

Figure 6.16: Nonlinear modes of the system and trajectories in the vicinity of the internal resonance 1:2

The study of the undamped NNM have shown that self-excited solutions lie underneath the internal resonance between the modes. Here, the extended periodic motion concept is now used to find the branch of all possible self-excited solutions for various levels of damping, *i.e.* to approximate the damped nonlinear mode of the system (dNNM). As detailed in Sec. 2.5.4, the dNNM is computed by adding a damping matrix to the system premultiplied by a damping ratio ζ, and by performing continuation on an enlarged system for which also ζ is an unknown. When applied to dissipative nonlinear forces [147], the found damping ratio ζ is positive and its absolute value provides a measure of the dissipation introduced by said forces. Here, the computation of dNNM is done on a system that displays self-excited vibration, so a negative value of damping ratio will be found, and its absolute value will be a measure of the amount of energy that the interaction with the belt is injecting into the system.

By computing the dNNM of the system, a whole branch of self-excited solutions is found to lie underneath the internal resonance 1:2 between the first and second mode of the system as reported in Fig. 6.17. When the system is augmented with the parameter ζ, the undamped nonlinear mode in red coincides with the one previously computed for $\zeta = 0$. In the vicinity of the internal resonance, a pitchfork bifurcation in the parameter ζ occurs and two branches detaching from the main branch of undamped solutions are generated. The continuation of the said detached branches permitted to compute two dNNM, one with positive and one with negative values of ζ. The solutions along the branch with negative damping ratio represents self-excited vibration whereas those along the positive damping ratio branch damped vibration. At each point along the branches the two solutions are identical, the only difference being the direction of the motion along the orbits. For this reason, the two branches are completely overlapped in Fig. 6.17. Focussing on the negative damping ratio branch, in Fig. 6.17 it is shown that the absolute value of the damping ratio is zero at the bifurcation points and increases towards the centre, up to a value of $\zeta = -3.45$. Being this value the multiplier of the mass proportional damping matrix with $c = 0.01$, the interaction can sustain vibration up to a value of $c = 0.0345$ but not higher than that.

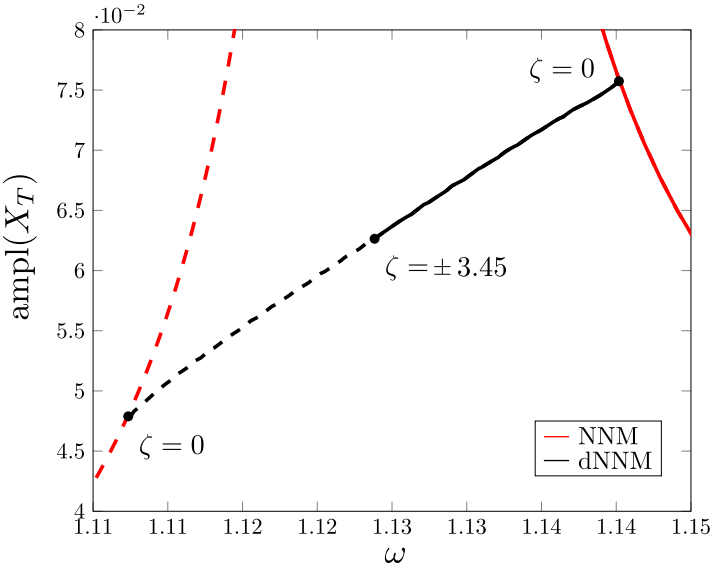


Figure 6.17: Branch of self-excited solution underneath the internal resonance 1:2 between first and second mode of the system. Stable (solid) and unstable (dashed) branches of undamped (red) and damped (black) nonlinear mode.

A consideration regarding the link between positive and negative clearance systems studied here can now be drawn. In the negative clearance system, the effect of the interaction is to increase the frequency of the lowest mode and decrease that of the highest one; in absence of damping a proper mode coupling instability occur at the critical value of friction coefficient, and the frequencies of the two modes of the closed system become equal. In the positive clearance system the same effect occur but since for a portion of the period the system is open, the change in frequency is much less pronounced. The interaction can although still occur as a result of a 1:2 resonance; in the range of frequency underneath the internal resonance both nonlinear modes exist, thus creating the conditions for the

interaction to occur.

In the general case of a multiple dofs system, a similar behaviour could be replicated by two nonlinear modes of the structure. Nonlinear modal analysis applied on such structures could potentially identify internal resonances generated by the contact interactions and, in presence of friction, could detect isolated branches of self-excited vibration. Although in the present form, the results obtained in this section cannot be directly translated to a real blade-casing interaction scenario, further developments of the minimal model could make it more applicable to realistic cases. Moreover, theoretical analyses on the the occurrence of friction induced vibration in correspondence with an internal resonance, could assess the generality of the findings obtained numerically in this section.

6.5 Conclusions

In this chapter, nonlinear modal analysis is applied to contact nonlinearities. In the first part of the chapter the case of purely normal contact is treated. The harmonic balance method is compared to time finite element method in various conditions and it is found that the applicability of harmonic balance method especially in the case of soft contact interaction has better performance than time finite method. Based on these considerations, a reduced order modelling method inspired by the direct normal form method and adapted to the case of contact nonlinearities has been proposed. The applicability of the method is linked to that if harmonic balance method with two harmonics which is found to be accurate for relatively soft contact conditions. The reduced model obtained has been compared to the classical Hurty/Craig-Bampton method in the context of nonlinear modal analysis and has shown the capabilities to follow the hardening behaviour of the nonlinear mode.

In the second part of the chapter, a system exhibiting flutter instability when pushed against a belt is tested under the condition of positive clearance. The possibility for self-excited oscillations to exist in the positive clearance system has been showed. A branch of self-excited oscillations have been found to coexist with the equilibrium branch. The condition for this branch to exist requires further investigation but from the analysis done in this Chapter it results that the softening effect of friction forces on the system dynamics are the reason for its existence. The branch of friction induced oscillations in the positive clearance system is found to occur underneath the internal resonance 1:2 between two modes. This branch is found by application of the extended periodic motion concept in order to compute the damped nonlinear mode. In the context of blade-casing interaction, this study opens the possibility for such oscillations to be observed in a real blade of a turbomachine, in case two modes of a blade undergo an internal resonance due to frictional contacts with the casing. In such an event, the existence of friction induced vibrations would mean that, for some initial conditions of the blade vibratory motion, a sustained regime of intermittent rubbing events may be undergone by the blade even in absence of any excitation source. Being this regime stable, the protracted vibration of the blade may threaten its structural

integrity. Future developments of the methods proposed in this chapter are (i) the extension of the reduction method proposed to the nonconservative case where friction is present and (ii) the inclusion of multiple modes in the reduction. In this way, the phenomena observed in the second part of the chapter could be observed in a real blade application where only the interacting modes are isolated from the others, thus filtering their behaviour.

Chapter 7

Conclusion

This thesis has been devoted to the investigation and development of reduced order modelling techniques for nonlinear vibration of complex structures like blades, with a high number of degrees of freedom. Most of the work done in this dissertation has been focused on nonlinear reduction methods for structures vibrating with large amplitudes, thus displaying geometric nonlinearities.

Three dimensional finite elements have been used throughout the whole dissertation and they are the main focus of this work. "In contrast to 1D and 2D elements, these elements are geometrically exact; furthermore, they are more suitable for discretisation of complex geometries as compared to other geometrically exact methods, such as those based on beam theory. Not only 3D finite elements are the standard in industrial applications but they can also be useful to tackle academic problems such as simple structures in large rotations.

7.1 Scientific Contributions

Recalling the research questions of Sec. 1.3.2, this work has provided an answer to many of them, though has left some others open. Here, we want to summarise the main achievements of this thesis before focusing in Sec. 7.4 on the questions that still remain open.

In Chapter 3, we showed that when discretised with three dimensional finite elements, even simple structures like a geometrically nonlinear beam can exhibit a great deal of nonlinear couplings between low frequency bending modes and high frequency ones. Modal ROMs, like normal form (NF) and static condensation (SC), that are usually based on a *a priori* identification of these couplings can no longer be used because they would require the knowledge of the full eigenvector matrix to be applied. If it is possible to compute this matrix for relatively small systems, in the case of large structures with a high number of degrees of freedom its computation is out of hand. We showed that the static modal derivative (SMD) can capture all the coupled modes into one single vector, computed with

a single static computation. If statically condensed the static modal derivative is then a viable solution to solve the problem. We also proposed another strategy that we called M-StEP method, based on the application of the StEP method only on selected degrees of freedom, leaving the other degrees of freedom related to the coupled modes free. With this strategy, we demonstrated that similar results to those obtained by static condensation of the SMD were obtained. Both proposed strategies, however, only provide accurate results when the structure is flat and symmetric because they are intrinsically equivalent to a static condensation. When applied to a simple cantilever beam, we showed that SC is not able to capture the correct behaviour of the structure due to the exclusion of the inertia terms.

Conversely in the quadratic manifold method (QM), the SMD is used to construct a nonlinear mapping of displacement that, when introduced into the equation of motion, can retrieve inertial terms in acceleration and velocity. This method is though affected by a different problem, which consists in the assumption that the nonlinear mapping is velocity independent. In Chapter 4, we showed that this assumption is valid if a slow/fast separation between the master mode and the slave modes is present. By showing the expression of all the terms of the reduced dynamics obtained with both QM and NF, we were able to quantify the concept of slow/fast assumption and provide a measure for the ratio between the frequency of the master mode and that of the closest slave mode, based on which the slow/fast separation has to be considered fulfilled or not. In particular, we considered a ratio of three to four between these frequencies to be the transition zone after which the slow/fast assumption can be considered accurate.

The main findings stemming from the comparison between the methods discussed in this thesis, *i. e.* the Static Condensation (SC) method, the quadratic manifold (QM) methods using modal derivatives (MD) or static modal derivatives (SMD), and the normal form (NF), are summarised in Table 7.1.

From the theoretical point of view, the three methods propose reduction to a curved subspace, in the attempt of approximating the invariant manifold of the system. Among them, only NF relies on a rigorous mathematical foundation for invariant manifolds parametrisation, which is the key feature that allows it to produce accurate and reliable ROMs in all the testcases presented. Indeed, methods like the quadratic manifold, rely on a projection in a Galerkin fashion of the equation of motion to obtain the reduced dynamics, a projection that is not required when using DNF. Such projection does not ensure that the reduced dynamics is fully representative of the actual dynamics on the invariant manifold, thus leading to incorrect results when the velocity independent manifold predicted with QM is too different from the actual invariant manifold. When a slow/fast separation between master and slave coordinates is present, the invariant manifold can be assumed to be velocity independent and the QM method is able to predict correct results.

The methods have been compared on FE-based beam examples. In the straight clamped-clamped beam, all the methods provide accurate results thanks to the fulfilment of the slow/fast assumption. Conversely, on the cantilever beam testcase, SC method cannot

catch the correct behaviour due to the lack of inertial terms in the derivation. When a small curvature is added to a clamped-clamped beam, the quadratic manifold method based on SMD fails due to its wrong representation of the self-quadratic term. If the curvature component is high, important nonlinear quadratic couplings appear with slave modes in the vicinity of the master mode, thus the slow/fast assumption is unfulfilled, and also quadratic manifold based on MD provided wrong results. The normal form method can retrieve the correct behaviour in all the mentioned cases, being derived in a more mathematically rigorous framework.

One of the achievement of this thesis is in the thorough derivation, analysis, implementation and comparison between the methods, that provided a better understanding of the reason for their failure thus allowing a generalisation of the found results.

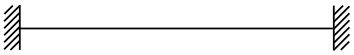
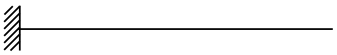
Structure type \ Method	SC	QM-SMD	QM-MD	NF
	√	√	√	√
	χ	√	√	√
	χ	χ	√	√
	χ	χ	χ	√

Table 7.1: Cases and methods capabilities.

From these results, we deduced that the use of the normal form method is always to be preferred to approximate methods. The limitation of the normal form in its classical formulation is though that, being a modal method, it requires the full eigenvector matrix to be computed beforehand. Its applicability is then limited to relatively small structures. The main achievement of this thesis is considered to be the derivation of the direct normal form method that, being defined directly in physical coordinates, allows for direct and non-intrusive computations in any finite element code. In Chapter 5, we showed that for a single master mode, only two static computations are necessary to compute the second order tensors needed to build the reduced dynamics, one of which coincides with the static modal derivatives. The direct normal form method has been applied on a large finite element model of a fan blade and it has been shown that the only limitation of the method is in the order of the asymptotic expansion. We also showed that not only two dimensional invariant manifolds can be computed but also higher dimensional ones. Higher dimensional manifolds are in fact needed when an internal resonance occurs in the system; in this context, the method was able to completely reproduce the resonant loops computed with the full model.

In Chapter 6, systems with contact nonlinearities have been treated. A method based on an empirical extension of the direct normal form to the case of clearance nonlinearities has been proposed to reduce the size of the system in a nonlinear modal analysis context. The method based on the so-called contact derivatives has shown a good accuracy when tested under relatively soft contact conditions. Compared to reduced models obtained with Hurty/Craig-Bampton method, the reduced model obtained with contact derivatives is always composed of three degrees of freedom when a single master mode is of interest; this feature renders the reduced model built with this method usually smaller than those build with HCB, especially when a relatively high frequency mode is of interest.

In terms of time discretisation, the Time Finite Elements method has been proposed as an alternative to Harmonic Balance method to treat the case of piecewise linear contact forces, in order to circumvent the Gibbs phenomenon encountered in HBM for hard contact conditions. When the same number of time variables is used, the two methods behave similarly in the case of hard contact, but HBM outperforms in the case of soft contact. However, the case of non-smooth contact conditions has not been reported; further tests in this respect could highlight the superiority of FET in dealing with non-smooth problems.

Lastly, the inclusion of friction forces in the problem has been treated. A minimal model aimed at simplifying the interaction between two modes of a blade has been studied and the existence of friction induced vibrations in a positive clearance system demonstrated. Such phenomenon has never been treated in the literature; also, the link between internal resonances and friction induced vibrations has not been explored, not even in the more classical case of negative clearance where the mode-coupling could be seen as a 1:1 internal resonance. To be studied in a real engineering application, this phenomenon would require an ad hoc reduced order modelling strategy, so the generality of the presented findings in a real blade testcase cannot be directly extrapolated by those on the two degrees of freedom model.

We now summarise the main novel results of this dissertation:

- A strong quadratic coupling between thickness and bending modes in flat and symmetric clamped-clamped structures modelled with 3D finite elements has been discovered and numerically investigated
- The mathematical equivalence between static condensation of all the modes of a structure and the static condensation of the static modal derivative has been proven
- The M-StEP method has been proposed and the conditions for its applicability mathematically justified in the case of flat structures with meshed neutral fibre
- A term-by-term expression of the reduced dynamics and nonlinear mapping provided by the quadratic manifold method has been presented
- A multiple scales based demonstration of the conditions of failure of the quadratic manifold method has been derived

- Based on the term-by-term reconstruction of the solution, the failure of the quadratic manifold with SMD for self-quadratic structures (like arches and shells) has been demonstrated
- A quantification of the slow/fast separation between modes required for the quadratic manifold method to be accurate has been given
- The method of Direct Normal Form has been developed by reformulating the classical normal form in modal basis
- The so-called second-order DNF has been proposed as a computational valid alternative to the third order one and a justification for its better behaviour when dealing with internal resonances provided
- A numerical comparison between Time Finite Element method and HBM when dealing with clearance nonlinearities is drawn
- The so-called contact derivatives are proposed and their empirical justification provided
- The phenomenon of friction induced vibration in positive clearance system is numerically captured
- A link between friction induced vibration and internal resonance is numerically shown

During the course of the PhD, three papers have been produced; the first one [165], whose majority of content is contained in Chapter 3; the second one [166], whose results are reported in Chapter 4; and a third one [167] which is reported in Chapter 5.

Moreover, the developments produced in this work have led to additional contributions; an article [141] in which the quadratic manifold method, direct normal form method, and implicit condensation and expansion method are compared and tested on different structures; an article [106] where an intrusive implementation of the DNF, reformulated for increased computational efficiency, is tested on MEMS structures in large rotations; a review paper [161] that includes some of the results from this thesis.

7.2 Industrial contribution

The inherent cantilever structure of blades together with their 3D shape makes all the tested ROMs apart from DNF, not suitable for this problem. Conversely, the direct normal form method provides a reliable tool that is able to correctly approximate the nonlinear behaviour of blades in large amplitude vibration.

In the context of blade casing interaction, the tip displacement of each nonlinear mode can then be computed employing the DNF method to allow for more accurate contact detection.

A more correct approximation of the radial component of tip displacement for each mode, *i.e.* the so-called clearance consumption, that is considered in the literature to be a key parameter for minimisation of rub induced vibration can be then computed by means of the DNF without relying on slow full model simulations.

Due to the different nature of geometric and contact forces, a unified treatment of the combined action of these two types of force has not been possible. For this reason, the case of contact nonlinearities has been treated separately. However, an adaptation of the direct normal form method to contact nonlinearities has been proposed. In this way, a step towards the unification of the methodologies has been taken and future developments in this respect might lead to the possibility of studying the combined effect of both forces.

Recalling the considerations done in Sec. 1.3.1 and the typical workflows presented in Fig. 1.5, we want to highlight the contributions of this thesis in terms of recommendations in an industrial perspective. The industrial approach to blade-casing interaction problems relies on heavy time integration simulations of the full model with geometric nonlinearities and time integration simulations of large HCB reduced models. The results of such simulations are not easy to interpret and their interpretation is based on the extraction of modal contributions from time signals. However, the nonlinearities in the model couple many modes of the structure, so that a linear mode projection could lead to misleading observations. We have proposed a more insightful approach based on nonlinear modal analysis, that permits to isolate and understand a single nonlinear mode behaviour or a multiple modes behaviour in the case of internal resonances.

In this respect, we proposed two main tools; the first one, DNF, that extend rigorous math foundation to large structures and permits to study blades in large amplitude vibration thus replacing the calculation of the tip trajectory from the full model; it would also allow individuating internal resonances purely driven by the geometric nonlinearities; the second, inspired by the first but more empirical, the contact derivatives, that can treat clearance nonlinearity, however not yet friction, and that has shown promising results when coupled with nonlinear modal analysis. Both methods do not include the effect of rotation so in order to apply to blade-casing interaction problems, such extension would be necessary. In both cases, the inclusion of a non-zero equilibrium position would be possible with a relatively small modification to the methods, thus allowing for centrifugal effects to be taken into account.

Although not been attempted in this thesis, we advise for the combined use of the above mentioned reduction methods coupled with Harmonic Balance method and nonlinear modal analysis. We believe that this fast but mathematically thoughtful approach would be particularly useful in the preliminary design stages of a blade when speed has to be preferred to accuracy and interpretability plays a big role.

7.3 Code development and integration

In terms of code development, several methods have been implemented during the course of this thesis but only the more industrially and scientifically relevant have been made public or have been integrated into the industrial workflow.

Recalling Sec. 2.6, all the reduced order modelling methods used in this thesis have been implemented in Code Aster [28]: StEP method, Static Condensation, M-StEP method, Modal Derivatives, Static Modal Derivatives, Quadratic Manifold, Normal Form, Direct Normal Form, Contact Derivatives, Hurty/Craig-Bampton method. The HBM computation of the reduced order models with geometric nonlinearities has been implemented in the code ManLab [27]. All these scripts have been shared with the collaborators of the work. The coupled Code Aster / ManLab routines for model order reduction with Quadratic Manifold and Direct Normal Form have been made public by the author [164].

A pseudo-code for the Direct Normal Form has been shared with the industrial sponsor and it will be integrated into the proprietary software SC03 by the relator of this project. In the case of contact nonlinearities, the code *fortran fun* for time discretisation with Time Finite Element detailed in Fig. 2.7 and in Appendix C will be integrated in the software FORSE by the author.

7.4 Open questions and future developments

The work presented in this thesis has left some of the stated research questions open and has also opened new questions. The main open question remains whether it is possible to unify the treatment of contact and geometric nonlinearities in an *a priori* reduced order modelling framework. As per the new questions that have been opened, some of them have led to new directions and further developments.

In terms of ROMs for geometric nonlinearities, the work done in this thesis has shown that the DNF has great capabilities as compared to existing methods. The main limitation of DNF lies in the order of the asymptotic expansion: ongoing developments in this direction, from the author and collaborators, are directed towards an arbitrary order expansion. Also, the inclusion of centrifugal effects in the method would require modifications to the method to include a non-zero equilibrium position; the author and collaborators are working in this direction, in order to render the method applicable to rotating systems. Furthermore, since the clearance consumption is a by-product of the method being the nonlinear modeshape given directly by the nonlinear tensors, the DNF could be applied directly on blades in the design stage to study the influence of the shape parameters (such as lean, sweep, and twist) on the clearance consumption; the author and collaborators are working in this direction together with the industrial sponsor Rolls-Royce and future developments could couple this analysis with optimisation tools.

As per ROMs for contact nonlinearities, the contact derivatives have shown promising results in the tested conditions but their applicability is still limited; future developments of this tool could include the treatment of friction, multiple modes and multiple contact nodes in the method. Also, unlike the DNF that provides a minimal model by introducing a nonlinear mapping, the contact derivatives rely on a linear mapping; future developments of the method could exploit the idea of contact derivatives in a nonlinear mapping framework.

As for the new questions that arose, they mostly regard the enlargement of the capabilities of the DNF to make it applicable to new challenges. The inclusion of other smooth nonlinear forces in the method, be they in the form of aerodynamic, gyroscopic, or piezoelectric forces, could make the method capable of solving new important problems with an inherent multiphysics nature. The inclusion of material nonlinearities could for instance make the method applicable to composite blades, which could replace metallic blades in new-generation fans. From an even broader perspective, the idea of the method could be reformulated from an equation-driven approach to a data-driven one, thus making it directly applicable to experimental data.

Bibliography

[1] Eugene L. Allgower and Kurt Georg. *Introduction to Numerical Continuation Methods*, volume 45. 2003.

[2] M. Amabili. Reduced-order models for nonlinear vibrations, based on natural modes: the case of the circular cylindrical shell. *Philosophical Transactions of the Royal Society A: Mathematical, Physical and Engineering Sciences*, 371(1993):20120474, 2013.

[3] M. Amabili, A. Sarkar, and M. P. Païdoussis. Reduced-order models for nonlinear vibrations of cylindrical shells via the proper orthogonal decomposition method. *Journal of Fluids and Structures*, 18(2):227–250, 2003.

[4] M. Amabili and C. Touzé. Reduced-order models for non-linear vibrations of fluid-filled circular cylindrical shells: comparison of pod and asymptotic non-linear normal modes methods. *Journal of Fluids and Structures*, 23(6):885–903, 2007.

[5] P. Apiwattanalunggarn, C. Pierre, and D. Jiang. Finite-element-based nonlinear modal reduction of a rotating beam with large-amplitude motion. *Journal of Vibration and Control*, 9:235–263, 2003.

[6] H. N. Arafat and A. H. Nayfeh. Non-linear responses of suspended cables to primary resonance excitation. *Journal of Sound and Vibration*, 266:325–354, 2003.

[7] R. Arquier, S. Bellizzi, R. Bouc, and B. Cochelin. Two methods for the computation of nonlinear modes of vibrating systems at large amplitudes. *Computers & Structures*, 84(24):1565 – 1576, 2006.

[8] M. Balmaseda, G. Jacquet-Richardet, A. Placzek, and D.-M. Tran. Reduced order models for nonlinear dynamic analysis with application to a fan blade. In *Proceedings of ASME Turbo Expo 2019*, Paper No. GT2019-90813, June 17–21, Phoenix, Arizona, 2019.

[9] M. Balmaseda, G. Jacquet-Richardet, A. Placzek, and D.-M. Tran. Reduced order models for nonlinear dynamic analysis with application to a fan blade. *Journal of Engineering for Gas Turbines and Power*, 142(4), 2020.

[10] A. Batailly, M. Legrand, An. Millecamps, and F. Garcin. Numerical-experimental Comparison in the Simulation of Rotor/stator Interaction Through Blade-tip/abradable Coating Contact. *Journal of Engineering for Gas Turbines and Power, American Society of Mechanical Engineers*, 2012.

[11] A. Batailly, M.B. Meingast, M. Legrand, and J. Ousty. Rotor-stator Interaction Scenarios for the Centrifugal Compressor of a Helicopter Engine. *Proceedings of the ASME 2013 International Design Engineering Technical Conferences and Computers and Information in Engineering Conference*, 2013.

[12] A. Batailly and A. Millecamps. Minimising Clearance Consumption: a Key Factor for the Design of Blades Robust to Rotor-stator Interactions? *Proceedings of ASME Turbo Expo 2016: Turbomachinery Technical Conference and Exposition*, 2016.

[13] Alain Batailly, Mathias Legrand, Patrice Cartraud, and Christophe Pierre. Assessment of reduced models for the detection of modal interaction through rotor stator contacts. *Journal of Sound and Vibration*, 329(26):5546–5562, December 2010.

[14] Alain Batailly and Sherbrooke West. HIGH-PRESSURE COMPRESSOR BLADE DYNAMICS UNDER AERODYNAMIC AND BLADE-TIP UNILATERAL CONTACT FORCINGS. *Proceedings of ASME Turbo Expo 2014: Turbine Technical Conference and Exposition*, pages 1–8, 2014.

[15] S. Bellizzi and R. Bouc. An amplitude-phase formulation for nonlinear modes and limit cycles through invariant manifolds. *Journal of Sound and Vibration*, 300(3-5):896–915, 2007.

[16] B. Berthoul, A. Batailly, L. Stainier, M. Legrand, and P. Cartraud. Phenomenological modeling of abradable wear in turbomachines. *Mechanical Systems and Signal Processing, Elsevier*, 98:770–785, 2018.

[17] J. Blahoš, A. Vizzaccaro, F. El Haddad, and L. Salles. Parallel harmonic balance method for analysis of nonlinear dynamical systems. In *Proceedings of ASME Turbo Expo 2020*, Paper No. GT2020-15392, Sep 21–25, London, UK, 2020.

[18] F. Blanc, C. Touzé, J.-F. Mercier, K. Ege, and A.-S. Bonnet Ben-Dhia. On the numerical computation of nonlinear normal modes for reduced-order modelling of conservative vibratory systems. *Mechanical Systems and Signal Processing*, 36(2):520 – 539, 2013.

[19] N. Boivin, C. Pierre, and S. Shaw. Non-linear normal modes, invariance, and modal dynamics approximations of non-linear systems. *Nonlinear Dynamics*, 8:315–346, 1995.

[20] M. Borri and C. Bottasso. A general framework for interpreting time finite element formulations. *Computational Mechanics*, 13:133–142, 1993.

[21] C.L. Bottasso. A new look at finite elements in time: a variational interpretation of Runge-Kutta methods. *Applied Numerical Mathematics*, 25:355–368, 1997.

[22] T. Breunung and G. Haller. Explicit backbone curves from spectral submanifolds of forced-damped nonlinear mechanical systems. *Proceedings of the Royal Society A: Mathematical, Physical and Engineering Sciences*, 474(2213):20180083, 2018.

[23] Olivier Brüls, Vincent Acary, and Alberto Cardona. *On the Constraints Formulation in the Nonsmooth Generalized- Method*. 01 2018.

[24] T.M. Cameron and J.H. Griffin. An Alternating Frequency/Time Domain Method for Calculating the Steady-State Response of Nonlinear Dynamic Systems. *Journal of Applied Mechanics, American Society of Mechanical Engineers*, 1989.

[25] G. Capobianco and S. R. Eugster. Time finite element based moreau-type integrators. *International Journal for Numerical Methods in Engineering*, 114(3):215–231, 2018.

[26] F. Chinesta, P. Ladeveze, and E. Cueto. A short review on model order reduction based on proper generalized decomposition. *Archives of Computational Methods in Engineering*, 18(4):395, 2011.

[27] B. Cochelin and C. Vergez. A high order purely frequency-based harmonic balance formulation for continuation of periodic solutions. *Journal of Sound and Vibration*, 324(1):243 – 262, 2009.

[28] Electricité de France. Finite element *code_aster*, analysis of structures and thermomechanics for studies and research. Open source on www.code-aster.org, 1989–2017.

[29] V. Denis, M. Jossic, C. Giraud-Audine, B. Chomette, A. Renault, and O. Thomas. Identification of nonlinear modes using phase-locked-loop experimental continuation and normal form. *Mechanical Systems and Signal Processing*, 106:430–452, 2018.

[30] N. Di Palma, A. Martin, F. Thouverez, and V. Courtier. Nonlinear harmonic analysis of a blade model subjected to large geometrical deflection and internal resonance. In *Proceedings of ASME Turbo Expo 2019*, Paper No. GT2019-91213, June 17–21, Phoenix, Arizona, 2019.

[31] E. J. Doedel. Auto: A program for the automatic bifurcation analysis of autonomous systems. *Congr Numer*, 30, 11 1980.

[32] H. Farokhi and M. H. Ghayesh. Geometrically exact extreme vibrations of cantilevers. *International Journal of Mechanical Sciences*, 168:105051, 2020.

[33] N. Fois, M. Watson, J. Stringer, and M. Marshall. An investigation of the relationship between wear and contact force for abradable materials. *Proceedings of the Institution of Mechanical Engineers, Part J: Journal of Engineering Tribology*, 229(2):136–150, 2015.

[34] A. Frangi and G. Gobat. Reduced order modelling of the non-linear stiffness in MEMS resonators. *International Journal of Non-Linear Mechanics*, 116:211 – 218, 2019.

[35] M. Géradin and D. Rixen. *Mechanical Vibrations: Theory and Applications to Structural Dynamics*. J. Wiley & Sons, 3rd edition, 2015.

[36] A. Givois, A. Grolet, O. Thomas, and J.-F. Deü. On the frequency response computation of geometrically nonlinear flat structures using reduced-order finite element models. *Nonlinear Dynamics*, 97(2):1747–1781, 2019.

[37] A. Givois, J.-J. Tan, C. Touzé, and O. Thomas. Backbone curves of coupled cubic oscillators in one-to-one internal resonance: bifurcation scenario, measurements and parameter identification. *Meccanica*, 2020.

[38] Ch. Glocker. *Set-Valued Force Laws, Dynamics of Non-Smooth Systems*. Lecture Notes in Applied Mechanics, Springer-Verlag Berlin, 2001.

[39] A. Grolet and F. Thouverez. On the use of the proper generalised decomposition for solving nonlinear vibration problems. In *ASME 2012 International Mechanical Engineering Congress and Exposition, American Society of Mechanical Engineers*, pages 913–920, 2012. no. 45202.

[40] Aurélien Grolet. *Dynamique non-linéaire des structures mécaniques : application aux systèmes à symétrie cyclique*. PhD thesis, Ecole centrale de Lyon 2013, 2013. 2013ECDL0049.

[41] L. Guillot, B. Cochelin, and C. Vergez. A generic and efficient taylor series–based continuation method using a quadratic recast of smooth nonlinear systems. *International Journal for Numerical Methods in Engineering*, 119(4):261–280, 2019.

[42] G. Haller and S. Ponsioen. Nonlinear normal modes and spectral submanifolds: existence, uniqueness and use in model reduction. *Nonlinear Dynamics*, 86(3):1493–1534, 2016.

[43] G. Haller and S. Ponsioen. Exact model reduction by a slowfast decomposition of nonlinear mechanical systems. *Nonlinear Dynamics*, 90:617–647, 2017.

[44] T. Hamabe, I. Yamazaki, K. Yamada, H. Matsui, S. Nakagawa, and M. Kawamura. Study of a method for reducing drum brake squeal. *SAE paper*, (1999-01-0144):53–60, 1999.

[45] À. Haro, M. Canadell, J.L. Figueras, A. Luque, and J.M. Mondelo. *The Parameterization Method for Invariant Manifolds: From Rigorous Results to Effective Computations*. Applied Mathematical Sciences. Springer International Publishing, 2016.

[46] B. Hervé, J.J. Sinou, H. Maheé, and L. Jezéquel. Analysis of friction-induced self-generated vibrations originated from mode-coupling in clutches. *Int. J. Pure Appl. Math.*, 42(3):369, 2008.

[47] N. Hoffmann, M. Fischer, R. Allgaier, and L. Gaul. A minimal model for studying properties of the mode-coupling type instability in friction induced oscillations. *Mech. Res. Commun.*, 29(4):197–205, 2002.

[48] J. J. Hollkamp and R. W. Gordon. Reduced-order models for non-linear response prediction: Implicit condensation and expansion. *Journal of Sound and Vibration*, 318:1139–1153, 2008.

[49] T.J.R. Hughes and G.M. Hulbert. Space-time finite element methods for elastodynamics: Formulations and error estimates. *Computer Methods in Applied Mechanics and Engineering*, 66(3):339–363, 1988.

[50] G.M. Hulbert. Time finite element methods for structural dynamics. *International Journal for Numerical Methods in Engineering*, 33(September 1990):307–331, 1992.

[51] J. Hultén. Brake squeal - a self-exciting mechanism with constant friction. *SAE Technical Paper*, (932965), 1993.

[52] K. H. Hunt and F. R. E. Crossley. Coefficient of Restitution Interpreted as Damping in Vibroimpact. *Journal of Applied Mechanics*, 42(2):440–445, 06 1975.

[53] S. R. Idelsohn and A. Cardona. A reduction method for nonlinear structural dynamic analysis. *Computer Methods in Applied Mechanics and Engineering*, 49(3):253 – 279, 1985.

[54] G. Jacquet-Richardet, M. Torkhani, P. Cartraud, F. Thouverez, T. Nouri Baranger, M. Herran, C. Gibert, S. Baguet, P. Almeida, and L. Peletan. Rotor to Stator Contacts in Turbomachines. Review and Application. *Mechanical Systems and Signal Processing, Elsevier*, 40(2):401–420, 2016.

[55] Martin Jahn, Merten Stender, Sebastian Tatzko, Norbert Hoffmann, Aurlien Grolet, and Jrg Wallaschek. The extended periodic motion concept for fast limit cycle detection of self-excited systems. *Computers & Structures*, 227:106139, 2020.

[56] S. Jain, P. Tiso, J. B. Rutzmoser, and D. J. Rixen. A quadratic manifold for model order reduction of nonlinear structural dynamics. *Computers and Structures*, 188:80–94, 2017.

[57] L. Jezéquel and C.H. Lamarque. Analysis of non-linear dynamical systems by the normal form theory. *Journal of Sound and Vibration*, 149(3):429–459, 1991.

[58] L. Jezéquel and C.H. Lamarque. Nonlinear modal synthesis based on normal form theory. *Proceedings of the Ninth International Modal Analysis Conference, Florence, Italy*, pages 101–108, 1991.

[59] D. Jiang. *Nonlinear modal analysis based on invariant manifolds. Application to rotating blade systems*. PhD thesis, University of Michigan, 2004.

[60] D. Jiang, C. Pierre, and S. Shaw. Nonlinear normal modes for vibratory systems under harmonic excitation. *Journal of Sound and Vibration*, 288(4-5):791–812, 2005.

[61] S. Jones and M. Legrand. Forced vibrations of a turbine blade undergoing regularized unilateral contact conditions through the wavelet balance method. *International Journal for Numerical Methods in Engineering, Wiley*, 101(5):352–374, 2014.

[62] R. K. Kapania and C. Byun. Reduction methods based on eigenvectors and ritz vectors for nonlinear transient analysis. *Computational Mechanics*, 11(1):65–82, 1993.

[63] Sami Karkar, Bruno Cochelin, and Christophe Vergez. A comparative study of the harmonic balance method and the orthogonal collocation method on stiff nonlinear systems. *Journal of Sound and Vibration*, 333(12):2554 – 2567, 2014.

[64] A. F. Kelley. Analytic two-dimensional subcenter manifolds for systems with an integral. *Pac. J. Math.*, 29:335–350, 1969.

[65] G. Kerschen and J.-C. Golinval. Non-linear generalization of principal component analysis: from a global to a local approach. *Journal of Sound and Vibration*, 254(5):867 – 876, 2002.

[66] G. Kerschen, J.-C. Golinval, A. F. Vakakis, and L. A. Bergmann. The method of proper orthogonal decomposition for dynamical characterization and order reduction of mechanical systems: An overview. *Nonlinear Dynamics*, 41(1):147–169, 2005.

[67] G. Kerschen, M. Peeters, J.C. Golinval, and A.F. Vakakis. Non-linear normal modes, part I: a useful framework for the structural dynamicist. *Mechanical Systems and Signal Processing*, 23(1):170–194, 2009.

[68] K. Kim, V. Khanna, X.Q. Wang, and M.P. Mignolet. Nonlinear reduced order modeling of flat cantilevered structures. In *Proceedings of the 50th Structures, Structural Dynamics, and Materials Conference*, AIAA Paper AIAA-2009-2492., May 4–7, Palm Springs, California, 2009.

[69] K. Kim, A. G. Radu, X.Q. Wang, and M. P. Mignolet. Nonlinear reduced order modeling of isotropic and functionally graded plates. *International Journal of Non-Linear Mechanics*, 49:100 – 110, 2013.

[70] M. Krack, L. Panning von Scheidt, and J. Wallaschek. A method for nonlinear modal analysis and synthesis: Application to harmonically forced and self-excited mechanical systems. *Journal of Sound and Vibration*, 332(25):6798 – 6814, 2013.

[71] Malte Krack. Nonlinear modal analysis of nonconservative systems: Extension of the periodic motion concept. *Computers & Structures*, 154:59–71, 2015.

[72] S. Kruse, M. Tiedemann, B. Zeumer, P. Reuss, H. Hetzler, and N. Hoffmann. The influence of joints on friction induced vibration in brake squeal. *Journal of Sound and Vibration*, 340:239–252, 2015.

[73] P. Krysl, S. Lall, and J. E. Marsden. Dimensional model reduction in non-linear finite element dynamics of solids and structures. *International Journal for Numerical Methods in Engineering*, 51(4):479–504, 2001.

[74] R. J. Kuether, B. J. Deaner, J. J. Hollkamp, and M. S. Allen. Evaluation of geometrically nonlinear reduced-order models with nonlinear normal modes. *AIAA Journal*, 53(11):3273–3285, 2015.

[75] D. Laxalde and M. Legrand. Nonlinear Modal Analysis of Mechanical Systems with Frictionless Contact Interfaces. *Nonlinear Modal Analysis of Mechanical Systems with Frictionless Contact Interfaces. Computational Mechanics, Springer Verlag*, 2011.

[76] D. Laxalde and F. Thouverez. Complex Non-Linear Modal Analysis for Mechanical Systems : Application to Turbomachinery Bladings With Friction Interfaces. *Journal of Sound and Vibration, Elsevier*, 2009.

[77] Denis Laxalde, Loic Salles, Laurent Blanc, and Fabrice Thouverez. Non-linear modal analysis for bladed disks with friction contact interfaces. *ASME. Paper No. GT2008-50860*, 2008.

[78] A. Lazarus and O. Thomas. A harmonic-based method for computing the stability of periodic solutions of dynamical systems. *Comptes Rendus Mécanique*, 338(9):510 – 517, 2010.

[79] A. Lazarus, O. Thomas, and J.-F. Deü. Finite element reduced order models for nonlinear vibrations of piezoelectric layered beams with applications to NEMS. *Finite Elements in Analysis and Design*, 49:35–51, 2012.

[80] M. Legrand, A. Batailly, B. Magnain, P. Cartraud, and C. Pierre. Full Three-dimensional Investigation of Structural Contact Interactions in Turbomachines. *Journal of Sound and Vibration*, 331:2578–2601, 2012.

[81] M. Legrand, A. Batailly, and C. Pierre. Numerical Investigation of Abradable Coating Removal in Aircraft Engines Through Plastic Constitutive Law. *Journal of Computational and Nonlinear Dynamics*, 7(1):011010, 2012.

[82] R. I. Leine, B. Brogliato, and H. Nijmeijer. Periodic motion and bifurcations induced by the painlevé paradox. *European Journal of Mechanics - A/Solids*, 21(5):869–896, 2002.

[83] Remco Leine, Vincent Acary, and Olivier Brüls. *Advanced Topics in Nonsmooth Dynamics: Transactions of the European Network for Nonsmooth Dynamics*. 06 2018.

[84] Remco I. Leine and Henk Nijmeijer. *Dynamics and Bifurcations of Non-Smooth Mechanical Systems*. Lecture Notes in Applied and Computational Mechanics, Vol. 18, Springer-Verlag Berlin, 2004.

[85] R. Lewandowski. Computational formulation for periodic vibration of geometrically nonlinear structures, part I: theoretical background. *International Journal of Solids and Structures*, 34:1925–1947, 1997.

[86] R. Lewandowski. Computational formulation for periodic vibration of geometrically nonlinear structures, part II: numerical strategy and examples. *International Journal of Solids and Structures*, 34:1949–1964, 1997.

[87] X. Liu and D. J. Wagg. Simultaneous normal form transformation and model-order reduction for systems of coupled nonlinear oscillators. *Proceedings of the Royal Society A: Mathematical, Physical and Engineering Sciences*, 475(2228):20190042, 2019.

[88] A. M. Lyapunov. The general problem of the stability of motion. *International Journal of Control*, 55(3):531–534, 1992.

[89] H. Ma, F. Yin, Y. Guo, X. Tai, and B. Wen. A Review on Dynamic Characteristics of Blade-casing Rubbing. *Nonlinear Dynamics*, 84:437–472, 2016.

[90] A. I. Manevitch and L. I. Manevitch. Free oscillations in conservative and dissipative symmetric cubic two-degree-of-freedom systems with closed natural frequencies. *Meccanica*, 38(3):335–348, 2003.

[91] M.B. Meingast, M. Legrand, and C. Pierre. A Linear Complementarity Problem Formulation for Periodic Solutions to Unilateral Contact Problems. *International Journal of Non-Linear Mechanics*, 66:18–27, 2014.

[92] L. Meyrand, E. Sarrouy, B. Cochelin, and G. Ricciardi. Nonlinear normal mode continuation through a proper generalized decomposition approach with modal enrichment. *Journal of Sound and Vibration*, 443:444 – 459, 2019.

[93] M. Mignolet and C. Soize. Stochastic reduced-order models for uncertain geometrically nonlinear dynamical systems. *Computer Methods in Applied Mechanics and Engineering*, 197:3951–3963, 2008.

[94] M. P. Mignolet, A. Przekop, S. A. Rizzi, and S. M. Spottswood. A review of indirect/non-intrusive reduced order modeling of nonlinear geometric structures. *Journal of Sound and Vibration*, 332:2437–2460, 2013.

[95] A. Millecamps, A. Batailly, M. Legrand, and F. Garcin. Snecma's Viewpoint on the Numerical and Experimental Simulation of Blade-tip/casing Unilateral Contacts. *Proceedings of ASME Turbo Expo 2015: Turbine Technical Conference and Exposition*, pages 1–11, 2015.

[96] El Hadi Moussi. *Analyse de structures vibrantes dotées de non-linéarités localisées à jeu à l'aide des modes non-linéaires*. PhD thesis, Aix-Marseille Université, 2013.

[97] A. A. Muravyov and S. A. Rizzi. Determination of nonlinear stiffness with application to random vibration of geometrically nonlinear structures. *Computers and Structures*, 81(15):1513–1523, 2003.

[98] A. H. Nayfeh and B. Balachandran. *Applied Nonlinear Dynamics*. John Wiley & sons, New-York, 1995.

[99] A. H. Nayfeh and W. Lacarbonara. On the discretization of distributed-parameter systems with quadratic and cubic non-linearities. *Nonlinear Dynamics*, 13:203–220, 1997.

[100] A. H. Nayfeh and D. T. Mook. *Nonlinear oscillations*. John Wiley & sons, New-York, 1979.

[101] A. H. Nayfeh and S. A. Nayfeh. On nonlinear normal modes of continuous systems. *Trans. ASME/Journal of Vibration and Acoustics*, 116:129–136, 1994.

[102] N. M. Newmark. A method of computation for structural dynamics. *Journal of the Engineering Mechanics*, 85:67–94, 1959.

[103] J. Nitsche. Über ein variationsprinzip zur lösung von dirichlet-problemen bei verwendung von teilräumen, die keinen randbedingungen unterworfen sind. *Abhandlungen aus dem Mathematischen Seminar der Universität Hamburg*, 36:9–15, 1971.

[104] D. Noreland, S. Bellizzi, C. Vergez, and R. Bouc. Nonlinear modes of clarinet-like musical instruments. *Journal of Sound and Vibration*, 324(3):983 – 1002, 2009.

[105] N. Olgac, U. Zalluhoglu, and A.S. Kammer. On blade/casing rub problems in turbomachinery: An efficient delayed differential equation approach. *Journal of Sound and Vibration*, 333(24):6662–6675, 2014.

[106] A. Opreni, A. Vizzaccaro, A. Frangi, and C. Touzé. Model order reduction based on direct normal form: application to large finite element MEMS structures featuring internal resonance. *Nonlinear Dynamics*, accepted, 2021.

[107] A.M. Panunzio, C. Schwingshackl, L. Salles, and M. Gola. Asymptotic Numerical Method and Polynomial Chaos Expansion for the Study of Stochastic Non-linear Normal Modes. *Proceedings of ASME Turbo Expo 2015: Turbine Technical Conference and Exposition*, 2015.

[108] M. Peeters, R. Viguié, G. Sérandour, G. Kerschen, and J.C. Golinval. Non-linear normal modes, part II: toward a practical computation using numerical continuation techniques. *Mechanical Systems and Signal Processing*, 23(1):195–216, 2009.

[109] F. Pellicano, M. Amabili, and M. P. Païdoussis. Effect of the geometry on the nonlinear vibration of circular cylindrical shells. *International Journal of Non-linear Mechanics*, 37:1181–1198, 2002.

[110] R. Perez, X. Q. Wang, and M. P. Mignolet. Nonintrusive Structural Dynamic Reduced Order Modeling for Large Deformations: Enhancements for Complex Structures. *Journal of Computational and Nonlinear Dynamics*, 9(3), 2014.

[111] R. Perez, X.Q. Wang, and M. P. Mignolet. Prediction of displacement and stress fields of a notched panel with geometric nonlinearity by reduced order modeling. *Journal of Sound and Vibration*, 333(24):6572 – 6589, 2014.

[112] E. Pesheck. *Reduced-order modeling of nonlinear structural systems using nonlinear normal modes and invariant manifolds*. PhD thesis, University of Michigan, 2000.

[113] E. Pesheck, N. Boivin, C. Pierre, and S. Shaw. Nonlinear modal analysis of structural systems using multi-mode invariant manifolds. *Nonlinear Dynamics*, 25:183–205, 2001.

[114] E. Pesheck, C. Pierre, and S. Shaw. A new Galerkin-based approach for accurate non-linear normal modes through invariant manifolds. *Journal of Sound and Vibration*, 249(5):971–993, 2002.

[115] E. P. Petrov. Analysis of Bifurcations in Multiharmonic Analysis of Nonlinear Forced Vibrations of Gas Turbine Engine Structures With Friction and Gaps. *Journal of Engineering for Gas Turbines and Power*, 138(10):102502, 2016.

[116] E.P. Petrov. A High-Accuracy Model Reduction for Analysis of Nonlinear Vibrations in Structures With Contact Interfaces. *Journal of Engineering for Gas Turbines and Power*, 133(10):102503, 2011.

[117] E.P. Petrov. Multiharmonic Analysis of Nonlinear Whole Engine Dynamics With Bladed Disc-Casing Rubbing Contacts. *Proceedings of ASME Turbo Expo 2012*, 2012.

[118] F. Pichler, W. Witteveen, and P. Fischer. Reduced-order modeling of preloaded bolted structures in multibody systems by the use of trial vector derivatives. *ASME. J. Comput. Nonlinear Dynam.*, 12(5: 051032), 2017.

[119] S. Ponsioen, T. Pedergnana, and G. Haller. Automated computation of autonomous spectral submanifolds for nonlinear modal analysis. *Journal of Sound and Vibration*, 420:269 – 295, 2018.

[120] G. Rega, W. Lacarbonara, and A. H. Nayfeh. Reduction methods for nonlinear vibrations of spatially continuous systems with initial curvature. *Solid Mechanics and its applications*, 77:235–246, 2000.

[121] L. Renson, G. Kerschen, and B. Cochelin. Numerical computation of nonlinear normal modes in mechanical engineering. *Journal of Sound and Vibration*, 364:177 – 206, 2016.

[122] A. Roberts. *Model emergent dynamics in complex systems*. SIAM, Philadelphia, 2014.

[123] Ignacio Romero. A comparison of finite elements for nonlinear beams: the absolute nodal coordinate and geometrically exact formulations. *Multibody System Dynamics*, 20(1):1573–272X, 2008.

[124] M. Ronchi, R.J. Williams, and P. Pennacchi. An Improved Simulation Method for Blade-casing Interaction Phenomena. In *Institution of Mechanical Engineers - 10th International Conference on Vibrations in Rotating Machinery*, volume 1, pages 303–312. Woodhead Publishing Limited, 2012.

[125] R. M. Rosenberg. The normal modes of nonlinear n-degree-of-freedom systems. *Journal of Applied Mechanics*, 29:7–14, 1962.

[126] J. B. Rutzmoser. *Model order reduction for nonlinear structural dynamics: simulation-free approaches*. PhD thesis, Technischen Universität München (TUM), 2018.

[127] J. B. Rutzmoser, D. J. Rixen, P. Tiso, and S. Jain. Generalization of quadratic manifolds for reduced order modeling of nonlinear structural dynamics. *Computers and Structures*, 192:196–209, 2017.

[128] L. Salles, L. Blanc, F. Thouverez, and A.M. Gouskov. Dynamic analysis of fretting-wear in friction contact interfaces. *International Journal of Solids and Structures*, 48(10):1513–1524, may 2011.

[129] L Salles, C Peng, and C Schwingshackl. ANALYSIS OF BLADE-TIP CASING INTERACTION USING HARMONIC BALANCE METHOD. *Euromech proceeding*, pages 2–3, 2015.

[130] Loïc Salles, Bernard Staples, Norbert Hoffmann, and Christoph Schwingshackl. Continuation techniques for analysis of whole aeroengine dynamics with imperfect bifurcations and isolated solutions. *Nonlinear Dyn.*, 86(3):1897–1911, 2016.

[131] N. Salvat, A. Batailly, and M. Legrand. Modeling of Abradable Coating Removal in Aircraft Engines Through Delay Differential Equations. *ASME Journal of Engineering for Gas Turbines and Power*, 135(10), 2013.

[132] N. Salvat, A. Batailly, and M. Legrand. Two-dimensional Modeling of Shaft Precessional Motions Induced by Blade/casing Unilateral Contact in Aircraft Engines. *Proceedings of ASME Turbo Expo 2014: Turbine Technical Conference and Exposition*, 2014.

[133] E. Sarrouy. Phase driven modal synthesis for forced response evaluation. In *7 th International Conference on Nonlinear Vibrations, Localization and Energy Transfer*, Marseille, France, Jul 2019.

[134] F. Schreyer and R.I. Leine. A mixed shooting harmonic balance method for unilaterally constrained mechanical systems. *Archive of Mechanical Engineering*, LXIII(2), 2016.

[135] A. Sénéchal. *Réduction de vibrations de structure complexe par shunts piézoélectriques. Application aux turbomachines*. PhD thesis, Conservatoire National des Arts et Métiers, Paris, France, 2011.

[136] S. W. Shaw and C. Pierre. Non-linear normal modes and invariant manifolds. *Journal of Sound and Vibration*, 150(1):170–173, 1991.

[137] S. W. Shaw and C. Pierre. Normal modes for non-linear vibratory systems. *Journal of Sound and Vibration*, 164(1):85–124, 1993.

[138] S. W. Shaw and C. Pierre. Normal modes of vibration for non-linear continuous systems. *Journal of Sound and Vibration*, 169(3):85–124, 1994.

[139] Y. Shen, N. Béreux, A. Frangi, and C. Touzé. Reduced order models for geometrically nonlinear structures: assessment of implicit condensation in comparison with invariant manifold approach. *European Journal of Mechanics, A/Solids*, submitted, 2020.

[140] Y. Shen, N. Béreux, A. Frangi, and C. Touzé. Reduced order models for geometrically nonlinear structures: comparison of implicit condensation and nonlinear normal modes. *Computers and Structures*, page submitted, 2020.

[141] Y. Shen, A. Vizzaccaro, N. Kesmia, T. Yu, L. Salles, O. Thomas, and C. Touzé. Comparison of reduction methods for finite element geometrically nonlinear beam structures. *Vibrations*, 4(1):175–204, 2021.

[142] J.C. Slater. A numerical method for determining nonlinear normal modes. *Nonlinear Dynamics*, 10(1):19–30, 1996.

[143] C. S. M. Sombroek, P. Tiso, L. Renson, and G. Kerschen. Numerical computation of nonlinear normal modes in a modal derivative subspace. *Computers & Structures*, 195:34 – 46, 2018.

[144] V. Sonneville, A. Cardona, and O. Brüls. Geometrically exact beam finite element formulated on the special euclidean group se(3). *Computer Methods in Applied Mechanics and Engineering*, 268:451–474, 2014.

[145] A. Steindl and H. Troger. Methods for dimension reduction and their applications in nonlinear dynamics. *International Journal of Solids and Structures*, 38:2131–2147, 2001.

[146] J. Stringer and M.B. Marshall. High speed wear testing of an abradable coating. *Wear*, 294-295:257–263, 2012.

[147] Yekai Sun, Jie Yuan, Luca Pesaresi, Enora Denimal, and Loic Salles. Parametric study and uncertainty quantification of the nonlinear modal properties of frictional dampers. *Journal of Vibration and Acoustics*, 142(5):051102, 2020.

[148] Yekai Sun, Jie Yuan, Alessandra Vizzaccaro, and Loic Salles. Comparison of different methodologies for the computation of damped nonlinear normal modes and resonance prediction of systems with non-conservative nonlinearities. *Nonlinear Dynamics*, 104(4):3077–3107, 2021.

[149] O. Thomas, A. Sénéchal, and J. F. Deü. Hardening/softening behaviour and reduced order modelling of nonlinear vibrations of rotating cantilever beams. *Nonlinear dynamics*, 86(2):1293–1318, 2016.

[150] O. Thomas, C. Touzé, and A. Chaigne. Non-linear vibrations of free-edge thin spherical shells: modal interaction rules and 1:1:2 internal resonance. *International Journal of Solids and Structures*, 42(11-12):3339–3373, 2005.

[151] P. Tiso, E. Jansen, and M. Abdalla. Reduction method for finite element nonlinear dynamic analyses of shells. *AIAA Journal*, 49(10):2295 – 2304, 2011.

[152] C. Touzé. A normal form approach for non-linear normal modes. Technical report, Publications du LMA, numéro 156, (ISSN: 1159-0947, ISBN: 2-909669-20-3), 2003.

[153] C. Touzé. Normal form theory and nonlinear normal modes: theoretical settings and applications. In G. Kerschen, editor, *Modal Analysis of nonlinear Mechanical Systems*, pages 75–160, New York, NY, 2014. Springer Series CISM courses and lectures, vol. 555.

[154] C. Touzé and M. Amabili. Non-linear normal modes for damped geometrically nonlinear systems: application to reduced-order modeling of harmonically forced structures. *Journal of Sound and Vibration*, 298(4-5):958–981, 2006.

[155] C. Touzé, M. Amabili, and O. Thomas. Reduced-order models for large-amplitude vibrations of shells including in-plane inertia. *Computer Methods in Applied Mechanics and Engineering*, 197(21-24):2030–2045, 2008.

[156] C. Touzé and O. Thomas. Non-linear behaviour of free-edge shallow spherical shells: effect of the geometry. *International Journal of Non-linear Mechanics*, 41(5):678–692, 2006.

[157] C. Touzé, O. Thomas, and A. Chaigne. Asymmetric non-linear forced vibrations of free-edge circular plates, part I: theory. *Journal of Sound and Vibration*, 258(4):649–676, 2002.

[158] C. Touzé, O. Thomas, and A. Chaigne. Hardening/softening behaviour in non-linear oscillations of structural systems using non-linear normal modes. *Journal of Sound and Vibration*, 273(1-2):77–101, 2004.

[159] C. Touzé, O. Thomas, and A. Huberdeau. Asymptotic non-linear normal modes for large amplitude vibrations of continuous structures. *Computers and Structures*, 82(31-32):2671–2682, 2004.

[160] C. Touzé, M. Vidrascu, and D. Chapelle. Direct finite element computation of non-linear modal coupling coefficients for reduced-order shell models. *Computational Mechanics*, 54(2):567–580, 2014.

[161] C. Touzé, A. Vizzaccaro, and O. Thomas. Model order reduction methods for geometrically nonlinear structures: a review of nonlinear techniques. *Nonlinear Dynamics*, accepted, 2021.

[162] A. F. Vakakis, L. I. Manevitch, Y. V. Mikhlin, V. N. Philipchuck, and A. A. Zevin. *Normal modes and localization in non-linear systems*. Wiley, New-York, 1996.

[163] Z. Veraszto, S. Ponsioen, and G. Haller. Explicit third-order model reduction formulas for general nonlinear mechanical systems. *Journal of Sound and Vibration*, 468:115039, 2020.

[164] A. Vizzaccaro. Rom for geomnl. *https://github.com/Avizzaccaro/ROM_for_geomNL*, 2021.

[165] A. Vizzaccaro, A. Givois, P. Longobardi, Y. Shen, J.-F. Deü, L. Salles, C. Touzé, and O. Thomas. Non-intrusive reduced order modelling for the dynamics of geometrically nonlinear flat structures using three-dimensional finite elements. *Computational Mechanics*, 2020.

[166] A. Vizzaccaro, L. Salles, and C. Touzé. Comparison of nonlinear mappings for reduced-order modeling of vibrating structures: normal form theory and quadratic manifold method with modal derivatives. *Nonlinear Dynamics*, 2020.

[167] A. Vizzaccaro, Y. Shen, L. Salles, J. Blahos, and C. Touzé. Direct computation of nonlinear mapping via normal form for reduced-order models of finite element nonlinear structures. *Computer Methods in Applied Mechanics and Engineering*, 284:113957, 2021.

[168] A. Vizzaccaro, Y. Shen, L. Salles, and C. Touzé. Model order reduction methods based on normal form for geometrically nonlinear structures: a direct approach. In *proc. of Euromech Non-linear Dynamics Conference, ENOC 2020*, Lyon, July 2020.

[169] X.Q. Wang, P.J. O'Hara, M.P. Mignolet, and J.J. Hollkamp. Reduced-order modeling with local enrichment for the nonlinear geometric response of a cracked panel. *AIAA Journal*, 57(1):421–436, 2019.

[170] X.Q. Wang, G. P. Phlipot, R. A. Perez, and M. P. Mignolet. Locally enhanced reduced order modeling for the nonlinear geometric response of structures with defects. *International Journal of Non-Linear Mechanics*, 101:1 – 7, 2018.

[171] Y. Wang. Dynamics Of Unsymmetric Piecewise-Linear/Non-linear Systems Using Finite Elements In Time. *Journal of Sound and Vibration*, 185(1):155–170, 1995.

[172] O. Weeger, U. Wever, and B. Simeon. Nonlinear frequency response analysis of structural vibrations. *Computational Mechanics*, 54(6):1477–1495, 2014.

[173] O. Weeger, U. Wever, and B. Simeon. On the use of modal derivatives for nonlinear model order reduction. *International Journal for Numerical Methods in Engineering*, 108(13):1579–1602, 2016.

[174] R.J. Williams. Simulation of Blade Casing Interaction Phenomena in Gas Turbines Resulting From Heavy Tip Rubs Using an Implicit Time Marching Method. *Proceedings of ASME Turbo Expo 2011*, 2011.

[175] W. Witteveen and F. Pichler. Efficient model order reduction for the dynamics of nonlinear multilayer sheet structures with trial vector derivatives. *Shock and Vibration*, 2014, 2014.

[176] L. Wu and P. Tiso. Nonlinear model order reduction for flexible multibody dynamics: a modal derivatives approach. *Multibody Syst Dyn*, 36:405–425, 2016.

[177] Vladislav Yastrebov. *Numerical methods in contact mechanics*. ISTE/Wiley, 2013.

[178] C. Yoong, A. Thorin, and M. Legrand. The wave finite element method applied to a one-dimensional linear elastodynamic problem with unilateral constraints. *Proceedings of the ASME 2015 International Design Engineering Technical Conferences and Computers and Information in Engineering Conference.*, 6: 11th International Conference on Multibody Systems, Nonlinear Dynamics, and Control. Boston, Massachusetts, USA.:V006T10A022. ASME., 2015.

[179] O. C. Zienkiewicz, R. L. Taylor, and J. Z. Zhu. *The Finite Element Method: Its Basis and Fundamentals*. Elsevier, 2005.

[180] A. Zygmund. *Trigonometrical series*. Dover books on intermediate and advanced mathematics. Dover Publications, 1955.

Appendix A

Details of the derivation of von Kármán beam model

In this appendix, we give the detailed calculation for obtaining all the coefficients von Kármán beam model. As described in Ch. 3, we only refer to the coupling between the first flexural mode and the fourth axial mode of a clamped clamped beam. The eigenfunctions and eigenvalues of these two modes can be found solving the linear eigenproblem for respectively flexural and longitudinal vibrations.

Recalling Eqs. (3.1) and focusing only on their linear part, reads:

$$\ddot{W}(X,T) + \frac{EI}{\delta S} W''''(X,T) = 0, \tag{A.1a}$$

$$\ddot{U}(X,T) - \frac{E}{\delta} U''(X,T) = 0. \tag{A.1b}$$

Eq. (A.1a), can be solved assuming:

$$W(X,T) = Q(T)\Phi(X), \tag{A.2}$$

where $\Phi(X)$ has to respect the clamped clamped boundary conditions, namely $\Phi(0) = \Phi(L) = \Phi'(0) = \Phi'(L) = 0$. The first three conditions are respected by the eigenfunction $\Phi(X)$ of arbitrary amplitude A:

$$\Phi(X) = A(\cos kX - \cosh kX)(\sin kL - \sinh kL) - A(\sin kX - \sinh kX)(\cos kL - \cosh kL), \tag{A.3}$$

whereas the last condition gives rise to the wavelength equation:

$$\cos kL \cosh kL = 1. \tag{A.4}$$

The first value of $k > 0$ that verifies the transcendental Eq. (A.4) is the dimensional wavelength k_1 of the first flexural mode. Its eigenfrequency is then obtained by solving Eq. (A.1a)

and reads:

$$\omega_{1f}^2 = \frac{EI}{\delta S} k_1^4. \tag{A.5}$$

As for the fourth longitudinal mode, a similar approach is followed. Imposing the separation of variables on U:

$$U(X,T) = P(T)\Psi(X), \tag{A.6}$$

and imposing the clamped clamped boundary conditions $\Psi(0) = \Psi(L) = 0$ one can find the eigenfunction that has now a simpler form being Eq. (A.1b) a second order differential equation in X. The first boundary condition is verified by:

$$\Psi(X) = B \sin \kappa X, \tag{A.7}$$

and the second one by the wavelength equation:

$$\sin \kappa L = 0. \tag{A.8}$$

The dimensional wavelength of the fourth axial mode is fourth value of $\kappa > 0$ that respects Eq. (A.8) equal to $\kappa_4 = 4\pi/L$. The eigenfrequency of the fourth axial mode is then obtained from Eq. (A.1b) and reads:

$$\omega_{4a}^2 = \frac{E}{\delta} \frac{(4\pi)^2}{L^2}. \tag{A.9}$$

Before operating the reduction that will produce the 2 dofs system of ODEs, it is convenient to make Eq. (A.1) non-dimensional with the following identities:

$$\begin{aligned} X &= xL, \\ T &= tT_0, \\ W &= wh, \\ U &= uh, \\ Q &= qh, \\ P &= ph, \end{aligned}$$

and by introducing the additional quantities:

$$\begin{aligned} c &= \sqrt{E/\delta}, \\ \beta &= k_1 L, \\ \sigma &= h/L, \\ T_0 &= 1/\omega_{1f} = \sqrt{12} L^2/(ch\beta^2), \end{aligned}$$

where the rectangular section assumption has been used in the last equation to simplify $I/S = h^2/12$. It is now possible to rewrite Eqs. (3.1) with respect to the new variables

x, t, w, u as:

$$\frac{h}{T_0^2}\left(w_{,tt} + \frac{1}{\beta^4}w_{,xxxx} - \frac{12}{\beta^4\sigma}\left(u_{,x}w_{,x}\right)_{,x} - \frac{6}{\beta^4}\left({w_{,x}}^3\right)_{,x}\right) = 0, \tag{A.10a}$$

$$\frac{h}{T_0^2}\left(u_{,tt} - \frac{12}{\beta^4\sigma^2}u_{,xx} - \frac{12}{\beta^4\sigma}w_{,x}w_{,xx}\right) = 0. \tag{A.10b}$$

which coincides with Eqs. (3.2) multiplied by the nonzero factor h/T_0^2.

This system of equations can be reduced to a system of ODEs using the equations for w and u now in their non-dimensional form:

$$w(x,t) = q_1(t)\Phi_{1f}(x), \tag{A.11}$$

$$u(x,t) = p_4(t)\Psi_{4a}(x), \tag{A.12}$$

with:

$$\Phi_{1f}(x) = \alpha_1(\cos\beta x - \cosh\beta x)(\sin\beta - \sinh\beta) - (\sin\beta x - \sinh\beta x)(\cos\beta - \cosh\beta)$$
$$\Psi_{4a}(x) = \alpha_4 \sin 4\pi x,$$

by projecting Eq. (A.10a) on the shapefunction Φ_{1f} and Eq. (A.10b) on the shapefunction Ψ_{4a}.

The Galerkin projection of Eqs. (A.10) leads to:

$$q_{1,tt} + q_1 - \frac{2}{\sigma}Gq_1\,p_4 + Dq_1^3 = 0, \tag{A.13a}$$

$$p_{4,tt} + \frac{12(4\pi)^2}{\beta^4\sigma^2}p_4 - \frac{1}{\sigma}Cq_1^2 = 0. \tag{A.13b}$$

With the coefficients G, D, C being equal to:

$$G = -\frac{6}{\beta^4}\left(\frac{\int_0^1 \Phi\left(\Psi_{,x}\Phi_{,x}\right)_{,x}dx}{\int_0^1 \Phi^2 dx}\right) \tag{A.14}$$

$$C = -\frac{12}{\beta^4}\left(\frac{\int_0^1 \Psi\left(\Phi_{,x}\Phi_{,xx}\right)dx}{\int_0^1 \Psi^2 dx}\right) \tag{A.15}$$

$$D = -\frac{6}{\beta^4}\left(\frac{\int_0^1 \Phi\left({\Phi_{,x}}^3\right)_{,x}dx}{\int_0^1 \Phi^2 dx}\right) \tag{A.16}$$

If the arbitrary amplitudes α_1 and α_4 are chosen to have mass normalised eigenfunctions:

$$\alpha_1 : \int_0^1 \Phi^2 dx = 1,$$
$$\alpha_4 : \int_0^1 \Psi^2 dx = 1,$$

the quadratic coupling coefficients are symmetric $G = C = 1.23$, the cubic coefficient is $D = 2.67$ and Eqs. 3.3 are finally retrieved.

Appendix B

Reduced-order models for two modes motion

This appendix gives the detailed equations governing the reduced-order dynamics in the beam case, in order to better understand which terms are present in the different ROMs, and which one are added when taking internal resonances into account. The discussion is restricted to the case of the the first NNM, where the main interesting feature is the presence of a 5:1 internal resonance (involving the nonlinear frequencies) between mode 1 and mode 3. Consequently ROMS have been built including these two modes as master coordinates. In the remainder, R_1 and R_3 will thus refer to the normal coordinates linked respectively to mode 1 and mode 3.

The simplest case is that of the ROM composed of a single master coordinate R_1. The reduced dynamics reads, following Eq. (5.26):

$$\ddot{R}_1 + \omega_1^2 R_1 + (A^1_{111} + h^1_{111}) R_1^3 + B^1_{111} R_1 \dot{R}_1^2 \;=\; 0\,. \tag{B.1}$$

The second case discussed in section 5.6.1 is that of a third-order normal form composed of modes 1 and 3, without taking into account any other terms due to the presence of an internal resonance. In this case the reduced dynamics deduces from Eq. (5.2) and directly reads:

$$\begin{aligned}\ddot{R}_1 + \omega_1^2 R_1 + (A^1_{111} + h^1_{111}) R_1^3 + B^1_{111} R_1 \dot{R}_1^2 \\ + \left(A^1_{331} + A^1_{313} + A^1_{133} + 3h^1_{133}\right) R_1 R_3^2 + B^1_{133} R_1 \dot{R}_3^2 + \left(B^1_{331} + B^1_{313}\right) \dot{R}_1 R_3 \dot{R}_3 = 0,\end{aligned} \tag{B.2a}$$

$$\begin{aligned}\ddot{R}_3 + \omega_3^2 R_3 + (A^3_{333} + h^3_{333}) R_3^3 + B^3_{333} R_3 \dot{R}_3^2 \\ + \left(A^3_{113} + A^3_{131} + A^3_{311} + 3h^3_{311}\right) R_3 R_1^2 + B^3_{311} R_3 \dot{R}_1^2 + \left(B^3_{113} + B^3_{131}\right) \dot{R}_3 R_1 \dot{R}_1 = 0.\end{aligned} \tag{B.2b}$$

These equations does not contain any invariant-breaking terms. Consequently they are unable to create a coupling between the invariant manifolds dynamics of mode 1 and 3. Since the ROM wants to follow the backbone curve of mode 1, adding the second equation on mode 3 without any invariant-breaking term is in this case meaningless, and this ROM will produce exactly the same backbone as Eq. (B.1). In order to counteract this property, the resonant monomials corresponding to the 1:3 internal resonance can be added to these equations, leading to the ROM with two modes and inclusion of new resonant terms. The reduced dynamics of this ROM now reads:

$$\begin{aligned}\ddot{R}_1 + \omega_1^2 R_1 + (A^1_{111} + h^1_{111})R_1^3 + B^1_{111}R_1\dot{R}_1^2 \\ + \left(A^1_{331} + A^1_{313} + A^1_{133} + 3h^1_{133}\right) R_1 R_3^2 + B^1_{133}R_1\dot{R}_3^2 + \left(B^1_{331} + B^1_{313}\right)\dot{R}_1 R_3 \dot{R}_3 \\ + \left(A^1_{311} + A^1_{113} + A^1_{131} + 3h^1_{113}\right) R_1^2 R_3 + B^1_{311}R_3\dot{R}_1^2 + \left(B^1_{113} + B^1_{131}\right) R_1\dot{R}_1\dot{R}_3 = 0,\end{aligned} \tag{B.3a}$$

$$\begin{aligned}\ddot{R}_3 + \omega_3^2 R_3 + (A^3_{333} + h^3_{333})R_3^3 + B^3_{333}R_3\dot{R}_3^2 \\ + \left(A^3_{113} + A^3_{131} + A^3_{311} + 3h^3_{311}\right) R_1^2 R_3 + B^3_{311}R_3\dot{R}_1^2 + \left(B^3_{113} + B^3_{131}\right) R_1\dot{R}_1\dot{R}_3 \\ + (A^3_{111} + h^3_{111})R_1^3 + B^3_{111}R_1\dot{R}_1^2 = 0.\end{aligned} \tag{B.3b}$$

As explained in the main text, the only extra terms added to this ROM are the third line in each oscillator equation. For Eq. (B.3a), the cubic resonant monomial corresponding to 1:3 resonance is $R_1^2 R_3$. This term needs to be accompanied with all his ancillary ones conveying the same resonance but with the velocity terms $\dot{R}_1$ and $\dot{R}_3$, resulting in the addition of the other resonant monomials $R_3\dot{R}_1^2$ and $R_1\dot{R}_1\dot{R}_3$. For the second equation (B.3b), the resonant monomial implying displacements only is R_1^3, which must also be complemented with all its companion terms sharing the same frequency resoannce and involcing velocities, thus the $R_1\dot{R}_1^2$ term. One can note that R_1^3 on the second equation is an invariant-breaking term. Consequently this system is prone to activate the resonance and break the invariance property of the single-mode manifold.

The last system investigated includes as extra terms those corresponding to the 1:1 reso-

nance. This final two-dofs reduced dynamics finally reads:

$$\begin{aligned}
&\ddot{R}_1 + \omega_1^2 R_1 + (A^1_{111} + h^1_{111}) R_1^3 + B^1_{111} R_1 \dot{R}_1^2 \\
&\qquad + \left(A^1_{331} + A^1_{313} + A^1_{133} + 3h^1_{133}\right) R_1 R_3^2 + B^1_{133} R_1 \dot{R}_3^2 + \left(B^1_{331} + B^1_{313}\right) \dot{R}_1 R_3 \dot{R}_3 \\
&\qquad + \left(A^1_{311} + A^1_{113} + A^1_{131} + 3h^1_{113}\right) R_1^2 R_3 + B^1_{311} R_3 \dot{R}_1^2 + \left(B^1_{113} + B^1_{131}\right) R_1 \dot{R}_1 \dot{R}_3 \\
&\qquad + +(A^1_{333} + h^1_{333}) R_3^3 + B^1_{333} R_3 \dot{R}_3^2 = 0, \qquad \text{(B.4a)} \\
&\ddot{R}_3 + \omega_3^2 R_3 + (A^3_{333} + h^3_{333}) R_3^3 + B^3_{333} R_3 \dot{R}_3^2 \\
&\qquad + \left(A^3_{113} + A^3_{131} + A^3_{311} + 3h^3_{311}\right) R_1^2 R_3 + B^3_{311} R_3 \dot{R}_1^2 + \left(B^3_{113} + B^3_{131}\right) R_1 \dot{R}_1 \dot{R}_3 \\
&\qquad + \left(A^3_{331} + A^3_{313} + A^3_{133} + 3h^3_{133}\right) R_1 R_3^2 + B^3_{133} R_1 \dot{R}_3^2 + \left(B^3_{331} + B^3_{313}\right) \dot{R}_1 R_3 \dot{R}_3 \\
&\qquad + (A^3_{111} + h^3_{111}) R_1^3 + B^3_{111} R_1 \dot{R}_1^2 = 0. \qquad \text{(B.4b)}
\end{aligned}$$

This system now contains all the possible cubic monomials. Consequently it is fully equivalent to the system obtained by applying the second-order normal form only.

Appendix C

Detailed description of the *fortran fun* library

This appendix is devoted to the description of the classes of the fortran library *fortran fun*.

In Fig. C.1, the variables and subroutines belonging to the class *read mk file* are reported. This class reads the input file containing the physical description of the system, such as mass, stiffness, damping matrices, location of contact nodes, and excitation force parameters.

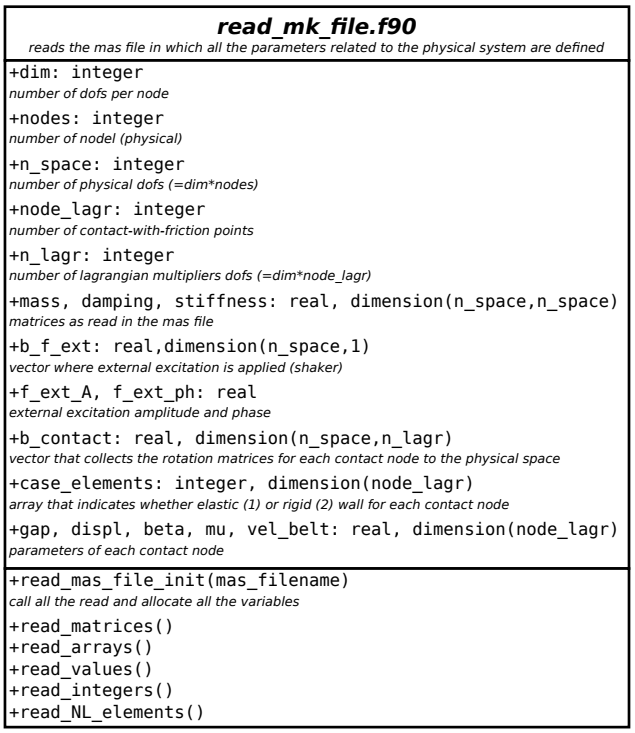


Figure C.1: Class read mk file

In Fig. C.2, the variables and subroutines belonging to the class *build physical system* are reported. This class builds the physical system matrices and vectors needed to write the

system in the form:

$$\boldsymbol{M}\ddot{\boldsymbol{U}} + \boldsymbol{C}\dot{\boldsymbol{U}} + \boldsymbol{K}\boldsymbol{U} = \boldsymbol{F}_{\text{ext}} + \boldsymbol{T}_{\text{C}}(\boldsymbol{U}_{\text{C}}, \dot{\boldsymbol{U}}_{\text{C}}). \tag{C.1}$$

or, if the contact is handled by means of Lagrangian multipliers, in the form:

$$\boldsymbol{M}\ddot{\boldsymbol{U}} + \boldsymbol{C}\dot{\boldsymbol{U}} + \boldsymbol{K}\boldsymbol{U} = \boldsymbol{F}_{\text{ext}} + \boldsymbol{B}_{\lambda}\boldsymbol{\lambda} \tag{C.2a}$$

$$\boldsymbol{\lambda} = \boldsymbol{f}(\boldsymbol{B}_{\text{X}}\boldsymbol{U}, \boldsymbol{B}_{\text{X}}\dot{\boldsymbol{U}}, \boldsymbol{\lambda}) \tag{C.2b}$$

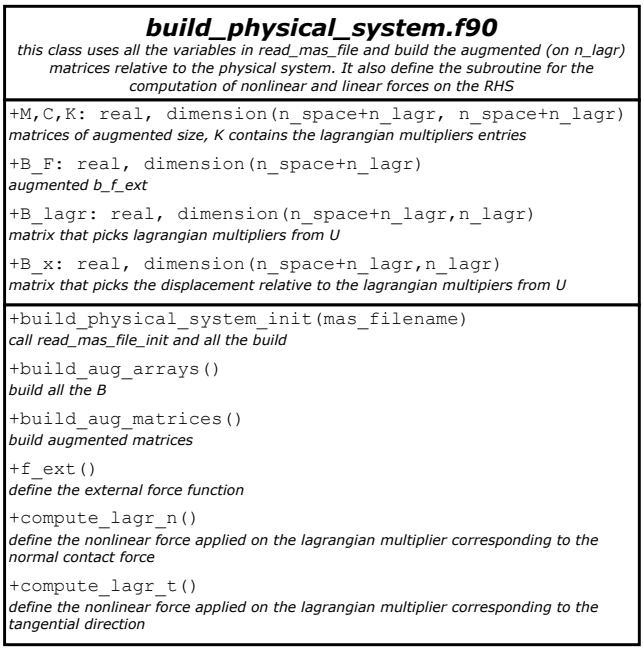


Figure C.2: Class build physical system

In Fig. C.3, the variables and subroutines belonging to the class *time discretisation* are reported. This class reads the input file where the parameters of the time discretisation are defined, such as the method used (HBM or FET), the number of harmonics and AFT points or the number of time steps and the number of Gauss Lobatto points for quadrature integration of the functions over the time element. It then defines the differentiation matrices ($\hat{\boldsymbol{L}}$) needed for the time derivatives and the direct and inverse fourier matrices needed in HBM.

In Fig. C.4, the variables and subroutines belonging to the class *initialisation* are reported. This class create the matrices and vector in the algebraic form (see Sec. 6.2 for more details on their definition):

$$\mathbb{A}(\Omega)\mathbb{U} = \mathbb{F}_{\text{ext}} + \mathbb{F}_{\text{NL}}(\mathbb{U}) \tag{C.3}$$

and also the Jacobian of the nonlinear forces $\mathbb{J}_{\text{NL}}(\mathbb{U})$ and the derivative of the dynamic stiffness matrix $\mathbb{A}$ with respect to the continuation parameter Ω.

In Fig. C.5, the variables and subroutines belonging to the class *dynamical functions* are

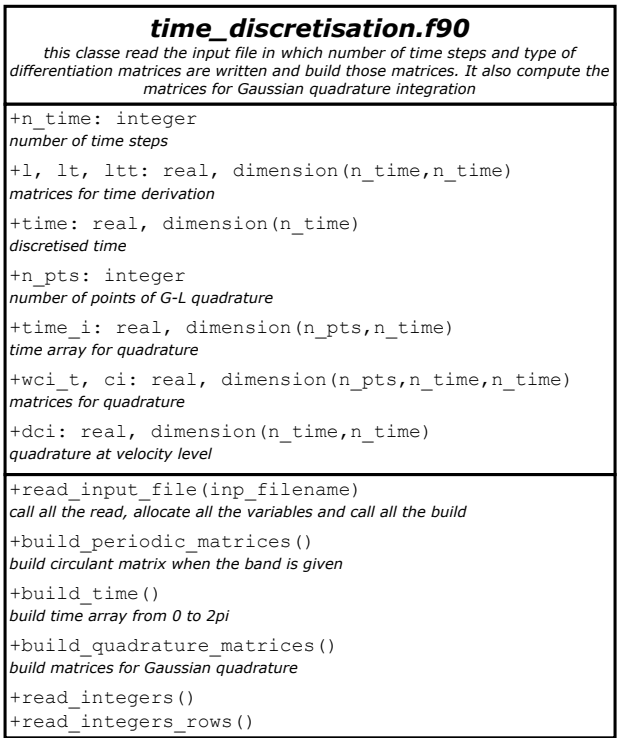


Figure C.3: Class time discretisation

reported. This class defines the residual $\mathbb{R}$ as a function of the unknown parameters $\mathbb{U}$ and Ω, the jacobian of the residual with respect to $\mathbb{U}$, and the derivative of the residual with respect to the scalar continuation parameter Ω. This class is called from the python continuation code at each continuation step.

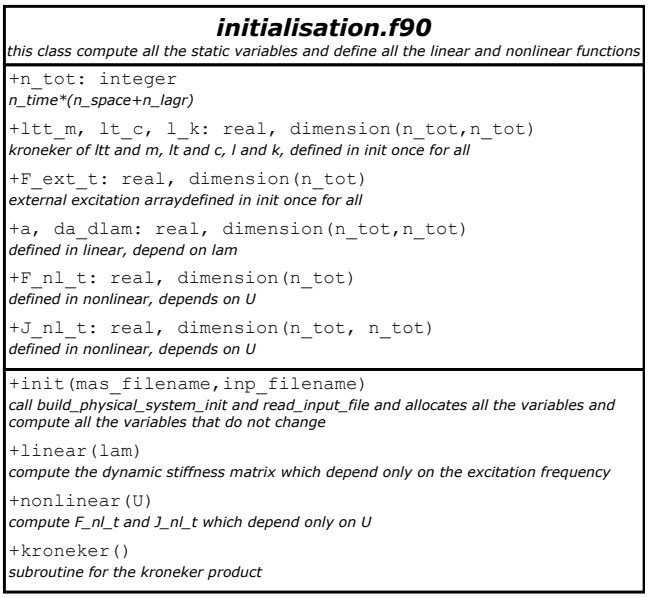


Figure C.4: Class initialisation

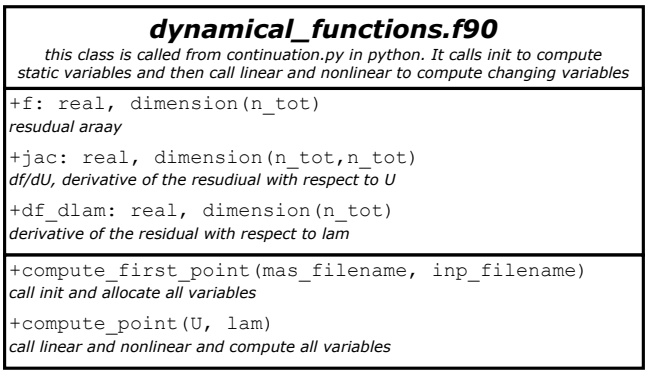


Figure C.5: Class dynamical functions